The University Of Sheffield.

Additive manufacturing magnetostrictive sensors for structural health monitoring of CFRP

By Nisar Ahmed

A thesis submitted to The University of Sheffield

Department of Materials Science and Engineering

Faculty of Engineering

For the degree of

Doctor of Philosophy

September 2023

Abstract

Magnetostriction is an inherent magnetic property that changes the volume of a magnetic material when a magnetic field is applied, and vice versa when a strain is applied the magnetisation within the magnetic material rotates and therefore changes the measured magnetic field. Therefore, this property could be used for structural health monitoring (SHM) of aircraft grade carbon fibre structure to study the changes in strain due to damage. Magnetostrictive materials are functional materials that have previously provided high resolution to detect defects or delamination in carbon fibre reinforced polymer (CFRP). Soft magnetic materials such as stainless steel 17/4 ph, Fe_3O_4 and Ni, are ideal as they have low coercivity, high saturation magnetisation and high anisotropy field. Additive manufacturing of functional materials has been an area of interest in science and engineering to exploit 3D and 4D designs, which saves cost and materials. Therefore, this project studied the design and printing of magnetostrictive material sensors to detect damage on CFRP. Two different types of printing were explored, metal extrusion (desktop metal bound deposition printer) and inkjet printing (JetLab IV) for different soft magnetic materials. Magnetic characterisation of the soft magnetic materials included using a superconducting quantum interference device (SQUID) magnetometer to measure the magnetic hysteresis loop. Structural characterisation included using scanning electron microscopy (SEM), energy dispersive X-ray spectroscopy (EDS) and fourier-transform infrared spectroscopy (FT-IR). It was found that printing stainless steel 17/4 ph by a desktop bound metal deposition printer was unsuitable for printing large, thin structures as fractures occurred due to thermal fluctuation and warping during the sintering process.

The Joule magnetostriction and the Villari effect were measured to test the sensor's performance under magnetic field and under strain respectively. The magnetic response to strain by bending was measured using an inductance coil and a Hall probe. Bending rigs with radius of curvature of 600 mm, 500 mm, 400 mm, 300 mm, 200 mm and 100 mm were used to strain the sensor. The change in magnetic field was measured using a coil inductor with various turns of copper wire. For inkjet printing, five factors were used to assess the print, which were: material choice (ink), print direction, design choice, substrate selection and additive layering. It was found that the magnetite coil design between 10 and 20 layers gave the best response to the change in field as a function of strain.

SHM of CFRP was evaluated by impact testing a defined weight onto a CFRP sheet. The inductance generated from the dropped weight was analysed by testing the inductor coil on a polycarbonate sheet. It was found that printing magnetite directly on CFRP rather than on a substrate, increased the measured inductance and performance during impact. A magnetite line was printed across the sheet to test the

SHM before and after impact on CFRP. Multiple layers of magnetite provided a better response to SHM during impact; however, to detect defects near impact, the level of change in inductance would not be suitable for service. Future work will continue to develop new materials for printing and testing on CFRP to replicate SHM technique on aircraft.

Acknowledgements and funding

Acknowledgements

I would like to thank my supervisor Professor Nicola Morley who has supported me throughout my PhD. In addition, her invaluable experience and dedication guided me through the covid pandemic and delays in experimental work, making sure. Nicola's role as a supervisor has been brilliant, always there when I needed advice and her calmness approach to dealing with problems.

I would like to thank Dr Zhao Yuan Leong for training me on magnetoelastic measurements such as measuring inductance and supported me through the whole of my PhD.

It has a been a privilege to be a part of the functional magnetic materials research group at the university of Sheffield. Sharing our problems and joy has been uplifting and encouraging. Our group meetings have been full of ideas and inspirations.

I would like to acknowledge Dr Robert Deffley for allowing me to use the Desktop metal bound deposition printed for my PhD work and to manufacture the printed gird designs.

I am grateful for Dr Patrick Smith at the department of mechanical engineering for allowing me to use his JetLab inkjet printing system. I like to thank the team Dr Vimanyu Beedasy and Dr Busra Karas for training me on the printing system and Mr Jack Leach for training me on composite manufacturing.

I would like to thank Dr Bodan Kundys and his team for training me on measuring magnetostriction at the Institute Physical and Chemistry Materials De Strasbourg.

My parents Iftitkhar Ahmed and Hamida Ahmed cared and loved me through my PhD. My siblings Shamaila Ahmed, Waqar Ahmed and Abrar Ahmed supported me throughout my studies.

Funding

This research was funded under the DSTL Anglo-French studentship scheme and the Henry Royce Institute for Advanced Materials, funded through EPSRC grants EP/R00661X/1, EP/S019367/1, EP/P02470X/1 and EP/P025285/1, for the Desktop Metal printer and SQUID access at the University of Sheffield. Collaboration between the University of Strasbourg, Institute Physical and Chemistry Materials De Strasbourg for measuring magnetostriction.

Conferences and Publications

Conferences

Materials Research Exchange 2020- Poster

IOP 2021 Poster

Intermag 2021-Poster- online

UK/France PhD 2021-Presentation- online

Intermag 2022- Online Presentation

Animate Materials Workshop Birmingham 2022: 4D Printing and Metamaterials- Presentation

UK-French PhD Conference DSTL Portsmouth 2022- Presentation

Publications

Ahmed, N., Deffley, R., Kundys, B. and Morley, N.A. (2023) '3D printing of magnetostrictive property in 17/4 ph stainless steel', *Journal of Magnetism and Magnetic Materials*, 585, p. 171115. Available at: https://doi.org/10.1016/j.jmmm.2023.171115.

Contents

Figures

Equations

Tables

Nomenclature

Units

A	Ampere
F	Farad
Kg	Kilograms
H	Henry
Hz	Herts
J	Joules
K	Kelvin
m	Meters
Ω	Ohms
T	Tesla
cm^{-1}	Wavenumber

Symbols

θ	Angle
L_m	Angular momentum
H_k	Anisotropy field
A_r	Area
C	Capacitance
q	Charge
H_c	Coercive field

E_y^H	Compliance coefficient at constant field strength
θ_c	Contact angle
T_c	Curie temperature
I	Current
Ze	Current in loop
η	Damping component
α_d	Damping constant
N_d	Demagnetisation factor
H_d	Demagnetising field
ρ	Density
S_{ed}	Devatonic stress/strain relation
d	Diameter
β	Direction of measured saturation magnetisation
γ	Direction of applied stress
∪	Dissipation factor
λ_{100}	Easy axis in cubic crystal direction
H_{eff}	Effective field
E_s	Elastic modulus at magnetic saturation
E_{sub}	Elastic modulus of the substrate
E_f	Electrical field
S	Electron spin

J_{ex}	Exchange energy
A_{ex}	Exchange stiffness constant
G	Gauge factor
g_c	Gravitational constant
V_H	Hall voltage
λ_{111}	Hard axis in cubic crystal direction
h	Height
L	Inductance
F_i	Impact force
L_f	Langevin function
l	Length
γ_{ls}	Liquid/ solid surface tension
γ_{lv}	Liquid/ vapour surface tension
H_m	Magnetic field
B	Magnetic induction
χ_m	Magnetic susceptibility
m_m	Magnetic moment
M	Magnetisation
E_A	Magnetocrystalline energy
E_σ	Magnetoelasticity
m	Mass

Rp	Maximum peak height
T_m	Melting temperature
E_0	Minimum elastic modulus
N	Newton
y	Neutral axis
d_o	Orifice diameter
Pa	Pascale
μ	Permeability
d_{33}	Piezomagnetic coefficient
e_{HS}	Piezomagnetic coupling at constant strain
d_{HT}	Piezomagnetic coupling at constant stress
μ_0	Permeability in free space
v_s	Poisson's ratio of substrate
μ_{rS}	Relative magnetic permeability measured at constant strain
μ_{rT}	Relative magnetic permeability measured at constant stress
r	Radius
R	Radius of curvature
Rt	Range of collected roughness value in data
M_r	Remanence magnetisation
Rq	Root mean squared roughness from mean line
Ra	Roughness average
λ_s	Saturation magnetostriction

γ_t	Surface tension
γ_{sv}	Solid/ vapour surface free energy
α	Saturation magnetic moment direction
B_s	Saturation magnetic induction
M_s	Saturation magnetisation
t_s	Substrate thickness
ε	Strain
σ	Stress
J_s	Saturation polarisation
αΔT	Temperature coefficient
t	Time
τ	Torque
Rv	Valley depth below the mean line
μ_v	Viscosity of ink
v	Velocity
E	Young's modulus
Z	Z number
E_z	Zeeman energy

Abbreviations

AM	Additive manufacturing
AC	Alternating current
AP	As-printed

AR As-received

ATR Attenuated total reflection

CFRP Carbon fibre reinforced polymer

CTE Coefficient of thermal expansion

CAD Computer aided design

CCT Continuous cooling transformation

DAQ Data acquisition

DC Direct current

DMBD Desktop metal bound disposition

DPI Drops per inch

DED Direct energy deposition

EMF Electromotive force

EDX/S Energy dispersive x-ray spectroscopy

FEA Finite element analysis

FT-IR Fourier transform infrared spectroscopy

HEA High entropy alloys

LCR Inductance, capacitance and resistance

KE Kinetic energy

PDMS Polydimethylsiloxane

PET/E Polyethylene terephthalate

PTFE Polytetrafluoroethylene

PP Polypropylene

PVC Polyvinylchloride

PZT Lead zirconate titanate

MSMA Magnetic shape memory alloy

MOD Metal-organic decomposition

NP Nanoparticle

PBF Powder bed fusion

Ph Precipitation hardened

RPM Revolution per minute

RT Room temperature

SEM Scanning electron microscope

SLM Selective laser melting

SLS Selective laser sintering

SS Sintered steel

SHM Structural health monitoring

SQUID Superconducting quantum interference device

TMA Thermomechanical analysis

VED Volumetric energy density

UV Ultraviolet

Chapter 1

Introduction

1 Structural health monitoring

Carbon fibre reinforced polymer (CFRP) composites are increasingly used for structural applications such as aircrafts or in the automotive sector. Composite structures provide high stiffness/ toughness and are lightweight, which gives an advantage over conventional materials such as aluminium or steel. Aircrafts are designed to operate in hostile environments, which experience large stresses and strains that can cause barely visible impact damage (BVID) to composite structure that could lead to a loss of strength and end in failure. Failure to an aircraft structure then leads to costly repairs and maintenance over time. Damages on aircraft composite structure can occur due to environmental effects (hygrothermal cycling), time based effects (lamination or cure), direct impact or from manufacturing defects (Archer and McIlhagger, 2014). Therefore, greater importance has been given to developing sensors for structural health monitoring (SHM) in aircraft composite structures. There are a number of different non-destructive inspection methods such as optical, electromagnetic, acoustic, piezoelectric sensors (Christopoulos *et al.*, 2014). Smart materials for sensing applications have increased in the past decade due to their intrinsic properties. Where an applied strain results in a change in electromagnetic properties such as electrical or magnetic field. A magnetostrictive material works by the conversion of a magnetic field into a change in volume, as first shown by James Prescott Joule in 1842. The inverse method known as the Villari effect is the conversion of change in strain to magnetic field. Thus, Villari effect could be useful for damage detection to monitor the change in magnetic field and due to the strain during flight. On the composites, a change in magnetic field could be measured using an inductor coil or a Hall sensor. Research has shown that magnetostrictive materials can be used as a sensor and actuators (Downey and Flatau, 2006). Magnetostrictive materials have been found to show a good level of sensitivity therefore could be used as a sensor and actuator for CFRP composite structures.

Soft magnetic materials can contain transitional elements such as iron, nickel and cobalt, and are important for sensing application. Typically, they have small coercivity that enable them to be easily magnetised and demagnetised. This allows for rapid changes in magnetisation in an alternating applied field. Therefore, for magnetostriction applications, soft magnets are favourable as the saturation

magnetisation is reached quickly for applied fields or strains. Magnetic materials such as Terfenol-D and Galfenol have high magnetostrictive constant λ = 200-300 ppm, so are ideal for sensors, however they are uncommon as they contain expensive elements and rare earth elements such as dysprosium and gallium. Natural materials such as magnetite are ideal due to lower cost and easy manufacturing. In addition, they have low coercivity and high saturation field, which makes them ideal for sensing applications.

Magnetostrictive sensors are currently limited to the shape of wires, tapes, films and bulk alloys. This is because manufacturing complex sensors are difficult using traditional methods. Printing magnetostrictive materials allows for flexible designs at relatively low cost and can improve the sensor by enhancing magnetisation/ magnetostriction by controlling printer parameters. However, printing metallic materials is relatively new and is used to make niche components, therefore there is a balance between cost and sensitivity of the sensor. Therefore, the motive for this project will be to explore different forms of additive manufacturing processes to produce cost effective magnetostrictive sensors for SHM.

Printing magnetostrictive materials poses a challenge, which this project will explore further. One of the biggest challenges is the choice of magnetic material. In most cases such as in extrusion or inkjet printing, the magnetic materials are synthesised with a binder or doped to maintain printability. Printing by laser melting can have issues in post treatment for example, the final design can be affected, by shrinkage, porosity, thermal history and microstructure defects, which can affect the magnetic properties such as increasing the magnetocrystalline anisotropy or decreasing the saturation magnetisation.

Recent advances in extrusion and inkjet printing of magnetic materials has shown viability in printing magnetostrictive materials. In both cases they were able to control the magnetisation, which could be useful for SHM applications. However, printed magnetostrictive material designs have not yet been tested for SHM of CFRP.

Therefore, the main goal of this research is to answer these questions:

1. How does printing magnetic materials affect the magneto-mechanical properties of the magnetostrictive sensor?

2. What could improve the magnetic properties during the manufacturing process?

3. Which design is ideal for a sensor?

4. Is a printed magnetostrictive sensor suitable for SHM of aircraft grade CFRP?

1.1 Thesis outline

The thesis is organised into 8 chapters as follows:

Chapter 1 begins with the introduction into the need for detecting and monitoring damages of aircraft CFRP structures and outlines the main issues in detecting defects or delamination in carbon fibre composite structure. The chapter introduces magnetostrictive materials and their potential to be used for sensing and monitoring damages. The main challenges during this PhD were discussed including printing magnetic materials and detecting changes in field when strain is applied.

Chapter 2 explores the current theory and background knowledge in magnetism, relevant to this PhD project. The chapter covers the MAZE energy includes magnetostatic, magnetocrystalline anisotropy, Zeeman and exchange energy, therefore a brief description of each was stated. The origin of magnetostriction including the Joule and Villari effect was mentioned. The effects of MAZE energy on magnetostriction was discussed.

Chapter 3 explores the state of the art of structural health monitoring of CFRP, including how and why failure occurs in CFRP and whether other SHM techniques are suitable or effective to use to detect BVD. A selection of material suitable for magnetostrictive sensors are explored and ways of detecting magnetostriction (directly and indirectly) were also discussed from literature. Printing magnetic materials from the current state of the art was explored. Further discussion were made on 3D printing (SLM and extrusion) and inkjet printing. Current issues and breakthroughs was discussed.

Chapter 4 outlines the methods used during this PhD project from simulation to experimental work. The methods for printing magnetic materials by desktop (extrusion) and inkjet printing (JetLab 4) are shown step by step from pre-printing to post printing techniques. Composition characterisation and morphology in pre and post printing were measured by SEM/EDS, SQUID magnetometer, Contour elite, Magcam, TGA and FT-IR techniques. Modelling magnetostrictive sensors was achieved by using COMSOL multiphysics 5.6 software. Experimental methods on strain using known radii was discussed including the details of the measurement techniques to measure the magnetic field such as using a Hall probe and coil inductor.

Chapter 5 shows the results and discusses the sensor performance of desktop-printed stainless steel 17/4 ph and its applicability for use in SHM of CFRP. The process of printing by desktop metal bound disposition printer was shown. Comparison between as-build and post-sintered structure was presented. The results include characterisation of steel by FT-IR and SEM of both as build and sintered structure. A SQUID magnetometer was used to characterise the magnetic properties in plane and out of plane

directions of both as build and sintered structure. An inductor coil was used to measure the field as the sintered structure were strained, and then conclusions are made.

Chapter 6 shows the results and discusses the sensor performance of inkjet-printed magnetite and nickel ink and their applicability for use in SHM of CFRP. The inks are characterised by optical microscope, SEM/EDS and contour elite for their morphology and composition. SQUID magnetometer was used to characterise the magnetic properties of the ink for both the in plane and out of plane directions. Different types of substrate were explored for their printability. The viscosity of nickel and magnetite ink was measured for its printability. A coil inductor was used to measure the magnetic flux as the print was strained over a known radius of curvature bend rig. Different types of designs were tested and selected based on their sensitivity to strain. An error analysis and signal to noise (SNR) of the coil with different turns has been explored.

Chapter 7 evaluates the SHM performance of inkjet-printed magnetite directly on CFRP. Bending test of magnetite coil, printed directly on CFRP, was shown to have a change in inductance as force or strain was applied. For impact testing, a control test was performed on an empty polycarbonate sheet (PC) to measure the level of noise of the inductor coil from the impact in order to select a weight with reduced noise and increased damage. A magnetite line was printed across the CFRP sheet to test the change in inductance from impact and SHM of CFRP before and after impact. A cross section for 6, 5 and 4 layers of CFRP sheet was examined and analysed to see the effect damage from 0.5 kg weight impact on each layer. Simulation using COMSOL multiphysics was employed to calculate the motion of magnetic field during impact of 0.5 kg weight for different layers of CFRP.

Chapter 8 outlines and draws the main conclusion by summarising SHM of CFRP in this work and the proposed future work.

Chapter 2

Theory of magnetic materials

2 Theory of magnetic materials

2.1 Introduction to magnetic material

Magnetic materials are fundamental to our 21st century technology from automotives, computers to healthcare. They can be classified into groups depending on their magnetic properties. Permanent magnetic materials are known as hard magnetic materials have a large coercivity and high remanence magnetisation at zero applied field, which makes them useful for applications such as motors. Soft magnetic materials have small coercivity and small remanence magnetisation at zero field, which makes them useful for sensors or transformers. The magnetic behaviour depends on the following core fundamental energies called MAZE energy (Hayward, 2019) (O'Handley, 1999):

- Magnetostatic energy
- Anisotropy energy including magnetocrystalline and magnetostrictive
- Zeeman energy
- Exchange energy

The origin of these core fundamental behaviour comes from the spin orbital interaction, which is the interaction between the magnetic moment of the electron and nucleus in an atom due to the spin and angular momentum in an orbit, effectively forming a magnetic dipole (Grunwald, 2007)(Duc and Brommer, 2014) (Grössinger, Turtelli and Mehmood, 2014). As the electron orbits the nucleus it creates a current loop where the negative and positive charges form an electrostatic field, therefore generating a magnetic field. The magnetic flux generated in the electron frame is shown in Equation 2.1 (Nave, 2000a).

Equation 2.1 Magnetic flux in the electron frame (Left) and orbital angular momentum (Right) (Nave, 2000a)

$$B = \frac{\mu_0 Zev}{4\pi r^2} \rightarrow B = \frac{\mu_0 Ze\vec{L}}{4\pi r^2} \qquad (2.1)$$

where B is induction, μ_0 is the permeability in free space, Ze is the current in loop and L is the angular momentum.

As electrons have a spin, this creates a magnetic spin dipole moment, thus the electron induces spin angular momentum as shown in Fig. 2.1 (Dapino, 2002) (left). Torque is produced on the electron as a magnetic field is applied. As the field is applied, the magnetic dipoles rotate and align towards the field, therefore creating a change in strain and deformation in a certain direction within a crystal lattice. In a crystal lattice structure, the neighbouring atoms interact with each other therefore creating a preferred direction, which leads to magnetocrystalline anisotropy. Fig. 2.1 (right) (Duc and Brommer, 2014) shows the charge difference as the magnetic dipole is orientated therefore creating a positive or negative charge difference in a lattice.

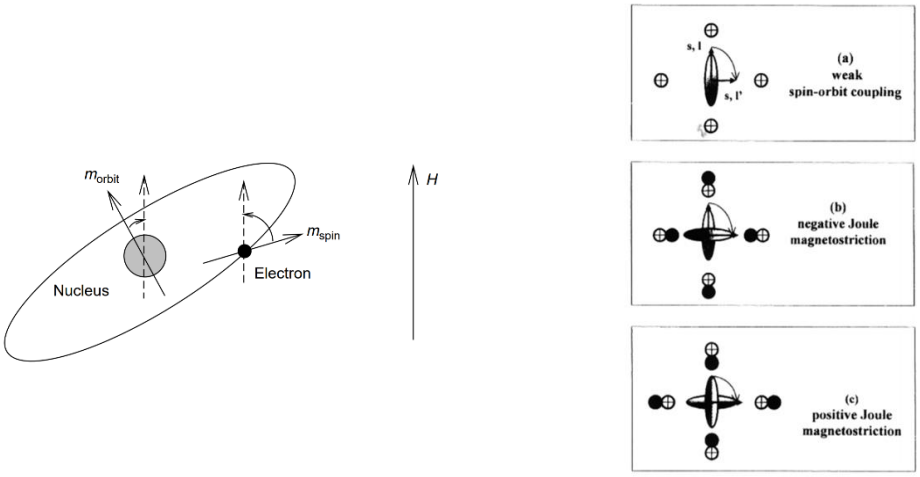

Figure 2.1 Diagram showing spin orbital coupling where electron and nucleus align creating magnetic moment by current loop (left) taken from (Dapino, 2002) and the change magnetic dipole in lattice (right) taken from (Duc and BROMMER, 2014)

Materials can be classed into diamagnetic, paramagnetic, ferromagnetic, ferrimagnetic and anti-ferromagnetic materials. These are classed based on their atomic magnetic moment direction, where the alignment of the magnetic dipoles for each domain are shown in Fig. 2.2 (Spaldin, 2012). As the electron spins and orbits around the nucleus, this creates a current loop, therefore a magnetic field is created due to the angular momentum of both electron and nucleus aligning and creating a magnetic dipole.

Paramagnetic materials have randomly orientated moments whereas ferromagnetic materials have moments aligned in the same direction. Anti-ferro and ferrimagnetic materials have magnetic moments opposite to each other, cancelling net alignment of moment as seen in Fig. 2.2. However, for ferrimagnetic materials, the moments are larger in a certain direction, thus creating a slight net magnetic moment in a specific direction. Diamagnetic materials don't have an atomic magnetic moment.

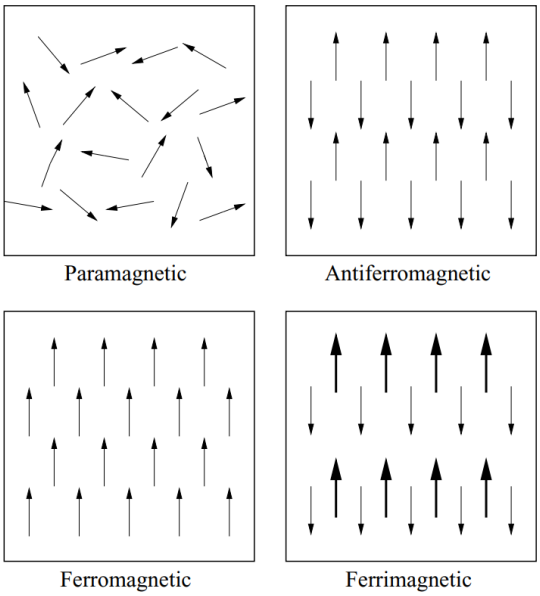

Figure 2.2 Ordering of the magnetic dipoles in magnetic materials (Spaldin, 2012)

Susceptibility of a material is the ratio of magnetisation (M) to applied field (H) per unit volume. This determines how easy it is to magnetise a material in an applied field, where $X_m < 0$ is diamagnetic and $X_m > 0$ is paramagnetic or ferromagnetic.

Equation 2.2 Susceptibility (Spaldin, 2012)

$$X_m = \frac{M}{H_m} \qquad (2.2)$$

Permeability μ is the ratio of magnetic induction B and field H_m, which indicates the level of magnetic flux within the material under a magnetic field.

Equation 2.3 Permeability (Spaldin, 2012)

$$\mu = \frac{B}{H_m} \qquad (2.3)$$

Table 2.1 from (McHugh, 2011) shows different classes of magnetic materials and how susceptible and permeable they are. It shows that transitional elements such as Fe, Ni and Co have large susceptibility and permeability compared to other elements like Cu or Ag which are diamagnetic as they have negative and small susceptibility.

Table 2.1 Types of magnetic materials (McHugh, 2011)

Magnetisation	Susceptibility to induced Magnetic Field	Permeability	Example
Diamagnetic	Negative and Small	< -1	Cu, Ag, Au
Paramagnetic	Positive and Small	> 1	Mg, Li
Ferromagnetic	Positive and very large	>> 1	Fe, Ni, Co
Anti-ferromagnetic	Positive and small	< 1	NiO
Ferrimagnetic	Positive and Large	>> 1	Fe_2O_3

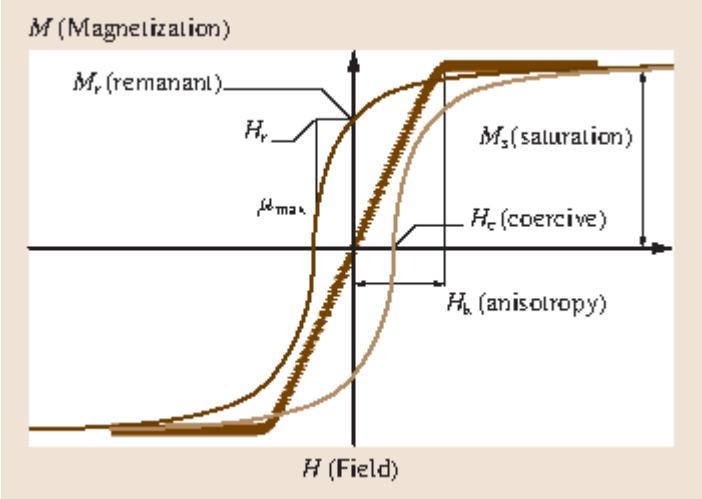

Figure 2.3 Hysteresis loop obtained for an arbitrary angle φ, between the magnetic field and the anisotropy axis (easy axis) (Tannous and Gieraltowski, 2017)

Fig. 2.3 shows magnetic hysteresis loops (M-H curve), which can be measured using a magnetometer by applying a magnetic field (H) and measuring the magnetic moment/ magnetisation (M). Magnetic properties such as saturation magnetization (M_s), remanence magnetisation (M_r), coercivity (H_c), anisotropy field (H_k) and initial susceptibility can be obtained (Tannous and Gieraltowski, 2017). This can give information on whether the domains are aligned along the hard axis or easy axis.

Temperature can affect the magnetisation, when the temperature rises above the Curie temperature (T_c), the spontaneous magnetisation disappears and becomes disordered. There is a magnetic transition from paramagnetic to ferromagnetic as the material is cooled below the T_c, where the magnetic moments

become spontaneously aligned. This is important for materials that are operating close to the T_c, as they will have reduced magnetic properties.

2.2 Maze energy

2.2.1 Zeeman energy

Zeeman energy is the amount of energy required to orientate the atomic magnetic moments into applied field direction as seen in Equation 2.4 (Nave, 2000c; Hayward, 2019) where E is the total energy, μ_0 is the permeability of free space, H is the field, m is the moment and θ is the angle between the moment and magnetic field. It is essentially the interaction of the magnetic field with the magnetic moment, therefore creating a torque, as the moment is energetically favourable to align towards the magnetic field as seen in Fig 2.4. Thus creating angular momentum resulting in potential energy.

Equation 2.4 Zeeman energy

$$E_z = -\mu_0 H_m m \cos(\theta) \qquad (2.4)$$

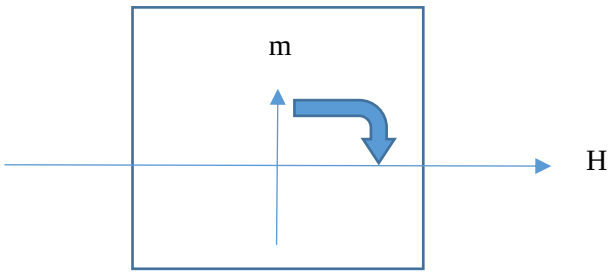

Figure 2.4 Zeeman effect on the interaction between field and magnetisation(Butcher, 2004)

Therefore, the magnetic moment will either align parallel or anti parallel to the field. If the magnetic field is anti-parallel to the moment, then this is energetically unfavourable, as more energy is required to rotate the dipole. Therefore, the angle of the moment to the applied field affects the amount of torque required and energy to magnetise a material as expressed in Equation 2.5 below.

Equation 2.5 Torque generated

$$\tau = -\mu_0 H_m m \sin(\theta) \qquad (2.5)$$

where μ_0 is the permeability of free space, H is the applied field and m is the magnetic moment at an angle θ.

2.2.2 Exchange energy

The exchange energy refers to the interaction between the alignment of 2 electrons spin. In 1928, Heisenberg discovered the exchange interaction of 2 hydrogen atoms coming together. As an anti-parallel spin of electrons creates a stable molecule, a parallel spin creates a repelling force of two atoms. The interaction can be described by the Coulomb repulsion between electrons and the Pauli exclusion principle. The exchange interaction can be used to describe the magnetism of a material as seen in Equation 2.6 (O'Handley, 1999; B.D.Cullity and C.D.Graham, 2009) known as the Heisenberg exchange interaction. Exchange energy depends on the direction and angle of atomic magnetic moments adjacent to each other. For ferromagnetism the alignment of electrons is parallel to each other (J > 0) therefore the exchange energy is positive whereas anti parallel direction (J < 0) will result in negative energy, which results in anti-ferromagnetic material.

Equation 2.6 Exchange interaction between 2 electron spin (B.D.Cullity and C.D.Graham, 2009)

$$E_{ex} = -2J_{ex}S \cdot S\cos\Phi \quad (2.6)$$

Equation 2.7 Exchange energy for discrete (left) and continuous microscopic form (right) (O'Handley, 1999)

$$E_{ex} = A_{ex}(\frac{\partial\theta}{\partial x})^2 = A_{ex}\sum_{i=l}^{3}(\frac{\nabla M_i}{M_s})^2 \qquad (2.7)$$

where J_{ex} is the exchange integral between 2 electrons, S is the total electron spin of each electron, M is the magnetisation of the electron, θ is the angle of magnetisation, x is the change with distance and A_{ex} is the exchange stiffness constant.

2.2.3 Magnetostatic energy

Magnetostatic energy is the interaction between the materials magnetisation (M) and magnetic field (H). The magnetic field outside the material in free space as seen in Equation 2.9 can change due to the difference in flux density (Equation 2.8). When a magnet has a field without any applied field, this is known as having a permanent field or demagnetising field, which depends on the magnetisation and magnetic dipole of the magnet.

Equation 2.8 Magnetic flux density

$$B = \mu_0(M + H_m) \qquad (2.8)$$

Equation 2.9 Magnetic field intensity

$$H_m = \frac{B}{\mu_0} - M \qquad (2.9)$$

where H is the magnetic field, M is the magnetisation, B is the flux density and μ_0 is permeability of free space.

To see the relation between the magnetic field and the magnetisation, Fig. 2.5 (Bertotti, 1998) shows a diagram of demagnetising field and magnetisation direction within the material. The magnetic field in free space (demagnetising field) opposes the direction of magnetisation inside the material, as this is energetically favourable as the magnetic dipole align to each other (from north to south) seen in Fig. 2.5. Where M is the magnetisation and magnetic dipole, H_M is the demagnetising field and B_M is the flux density inside the magnet.

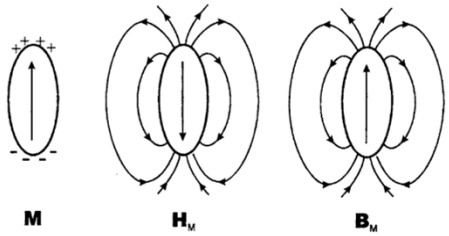

Figure 2.5 Demagnetising field (Bertotti, 1998)

The shape of the material affects the alignment and magnetisation of a magnet. The demagnetising factor (N_d) as shown in (Equation 2.10) represents the ratio of magnetisation direction in relation to the shape. Where N_a, N_b and N_c are demagnetisation factors for the principal axes for example in the X, Y and Z plane.

Equation 2.10 Demagnetising field (Spaldin, 2012)

$$H_d = N_d M \qquad (2.10)$$

The shape is linked to magnetic anisotropy where it is favourable for the magnetisation to orientate towards an axis when magnetised. For example, a magnet bar magnetised along the long side (in plane) is favourable than magnetising the bar along the short side (out of plane). Shape anisotropy is where the shape of the structure can have an effect on the direction of magnetisation. Spherical shape has no shape anisotropy therefore the magnetisation is the same in all directions along the radius of the sphere as shown in Equation 2.11 (Spaldin, 2012). For non-spherical shapes the demagnetising factor is

important. It is proportional to the geometry of the material. Therefore, as the N_d ratio is smaller, then the anisotropy will be larger (Spaldin, 2012).

Equation 2.11 Principle axis for spherical shape (Spaldin, 2012)

$$N_A = N_B = N_C \qquad (2.11)$$

Domains are important in magnetic materials as they are how the atomic magnetic moments align within the material as seen in Fig. 2.6 (i). As more domains are added as seen in (ii), the demagnetising field reduces. This increases the exchange energy as the moments are opposite to each other between domains. In (iii), shows closure of domains where it shows no magnetostatic energy but the exchange energy is increased (DoITPoMS- University of Cambridge, 2004). Therefore, magnetostatic energy is inversely proportional to the number of domains.

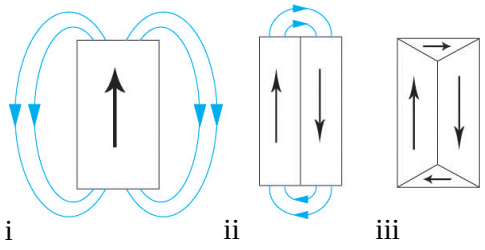

Figure 2.6 Addition of domains to reduce magnetostatic energy (DoITPoMS- University of Cambridge, 2004)

Other effects such as defects, voids, dislocations and inclusions can influence magnetic properties such as anisotropy, by restricting domain wall motion. Therefore, increasing energy is required to pass the energy barrier e.g. higher field. Domain de-pinning leads to sudden changes in volume of the domains therefore changes in magnetisation called Barkhausen noise. For example, the domains re-orientate towards the field, but where defects or voids are present, it will be harder to magnetise.

2.2.4 Magnetocrystalline anisotropy

Magnetocrystalline anisotropy is directional magnetisation within the crystal lattice (Moskowitz, 1991). Magnetocrystalline energy depends on the spin orbit interaction (electron and nucleus of each atom) and the crystal electric field. Therefore, this produces a preferred orientation as the spin orbit coupling in the lattice are energetically favourable to align in a certain direction, known as the easy direction. Other directions where the atomic moments would prefer not to align are known as the medium and hard directions. For a body centred cubic (BCC) crystals such as iron, the magnetic moments can be aligned in the [100], [110] and [111] directions. In BCC, the alignment in the [100] direction requires less energy (lower field) to align and saturate, as the atoms in the cubic crystal further apart whereas the [111] direction the atoms are close together therefore, requires more energy to align, thus the [100]

is the easy direction. For an FCC lattice structure such as magnetite as seen in Fig. 2.7, the easy direction is in the [111] direction and hard direction is in the [100]. This is different to iron, as the structure is different (FCC) which has a preferred direction in the [111] instead of [100] due to the atoms being further apart in the [111] crystal direction.

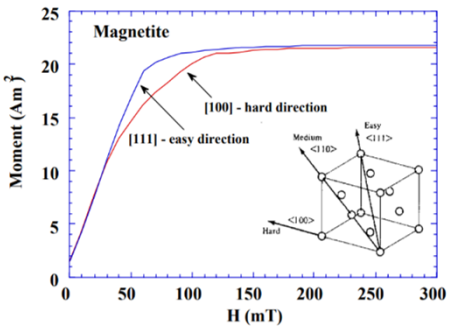

Figure 2.7 Effect of easy and hard axis in a FCC structure and magnetisation (Moskowitz, 1991)

In 1929, Akulov showed that magnetocrystalline anisotropy energy can be expressed by saturation magnetisation and crystal axis with anisotropy constant. For directions in between the crystallographic directions, Equation 2.12 (B.D.Cullity and C.D.Graham, 2009) shows the calculation for the materials magnetocrystalline anisotropy energy. Crystal direction for magnetisation is expressed as α with angle in cosines. Therefore, this will calculate a difference in each direction, as higher E will result in higher magnetocrystalline anisotropy.

Equation 2.12 Cubic magnetocrystalline anisotropy energy (B.D.Cullity and C.D.Graham, 2009)

$$E_a = K_0 + K_1 (\alpha_1^2 \alpha_2^2 + \alpha_2^2 \alpha_3^2 + \alpha_3^2 \alpha_1^2) + K_2 (\alpha_1^2 \alpha_2^2 \alpha_3^2) \text{ ..... } (2.12)$$

where E_a is the energy density, K is the anisotropy constant and $\alpha_1, \alpha_2, \alpha_3$ are the magnetisation vector with axis of X, Y, Z direction in cosine (θ). K_0 is just a constant, does not depend on the angle, and can be ignored form the equation. The easy and hard direction depends on K_1 and K_2, for example, K_1 is negative for nickel therefore $E_{111} < E_{110} < E_{100}$ this mean that the easy direction for nickel is in the [111] direction.

2.3 Dynamic micromagnetics

The MAZE energy has so far described the energy in a steady state environment. Dynamic micromagnetics describes the MAZE energy as a function of time and is useful in finite element modelling and applications such as applying an AC field or magnetic sensing devices. This is due to the magnetic moments consistently changing and moving the domain walls thus producing a dynamic MAZE energy interaction (Abert, 2013; de Laire, 2020, 2022). In (Landau and Lifshitz, 1935) they first

proposed the idea of dynamic modelling where the moment is in precessional motion as seen in Equation 2.13.

Equation 2.13 Landau and Lifshitz

$$\frac{dM}{dt} = -\gamma M \times H_{eff} \qquad (2.13.1)$$

$$\text{Where} \quad H_{eff} = -\frac{1}{\mu_0 M_s}\frac{dU}{dm} \qquad (2.13.2)$$

where M is the magnetisation, M_s is saturation magnetisation, t is time, γ is the geometric ratio of an electron, U is the dissipation factor and H_{eff} is the effective field which is the sum of demagnetising field and applied external field. The Landau and Lifshitz equation has shown the motion of the moment around the H_{eff} field in an undamped magnetisation field as seen in Fig. 2.8 (a). Gilbert then formed an additional damping behaviour of the magnetic moment as seen in (Gilbert, 2004) which forms a Landau–Lifshitz–Gilbert equation, describing the magnetic moment damping motion where the moment experiences a torque and relaxes to align towards the H_{eff}, as seen in Equation 2.14 and Fig. 2.8 (b) and (c). Where the damping component η is the damping effect added to the Landau and Lifshitz equation.

Equation 2.14 Landau–Lifshitz–Gilbert

$$\frac{dM}{dt} = -\gamma\left(M \times H_{eff} - \eta M \times \frac{dM}{dt}\right) \qquad (2.14)$$

where $\eta = \frac{\alpha_d}{M_s}$ and α_d is the damping constant.

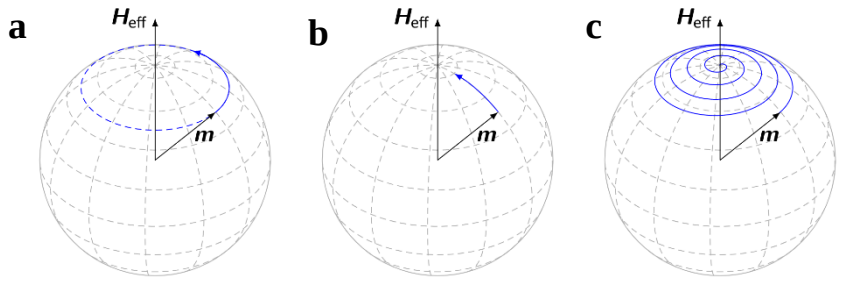

Figure 2.8 (a) Precessional motion around the effective field. (b) Damped motion. The magnetization relaxes towards the effective field. (c) Resulting motion including precession and damping taken from (Abert, 2021)

2.4 Magnetostriction theory

2.4.1 Background

In 1842, James Prescott Joule discovered the magnetostriction property. He observed that a sample of ferromagnetic material, i.e. iron, changes its length in the presence of a magnetic field. This is because magnetic domains rotate, which increases the volume. This discovery led to applications for magnetostriction such as transformers and sensors, (Yu, 2021). The theory behind magnetostriction is that the change in magnetic moment is due to the spin orbital coupling as shown in chapter 2.1 (Grunwald, 2007), (Duc and Brommer, 2014), (Grössinger, Turtelli and Mehmood, 2014).

This is useful in applications such as sensors or actuators that require/expose to mechanical stresses and strain. Therefore, a simple equation and a graph can be produced like in Equation 2.15 and Fig. 2.9 which shows change in strain in response to the magnetic field (Grunwald, 2007), (Dapino, 2004) known as the Joule effect. The equation can be rearranged to show the field and stress relation to strain as seen in Equation 2.16 (Calkins, Flatau and Dapino, 2007; Flatau, 2019).

Equation 2.15 Change in length (Grunwald, 2007)

$$\lambda_s = \frac{\Delta L}{L} \qquad (2.15)$$

where λ_s is saturation magnetostriction, L is the length of the material.

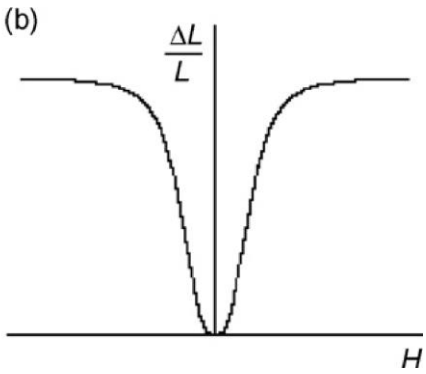

Figure 2.9 Change in length of a material in applied magnetic field (Grunwald, 2007)

Equation 2.16 1D linear Joule effect (Flatau, 2019)

$$\varepsilon = \sigma \,/\, E_y^H + d_{33}H + \alpha\Delta T \qquad (2.16)$$

where ε is strain, σ is stress, E_y^H is compliance coefficient at constant field strength, d_{33}= dε/dH (strain/field) and αΔT is the temperature coefficient and change in temperature.

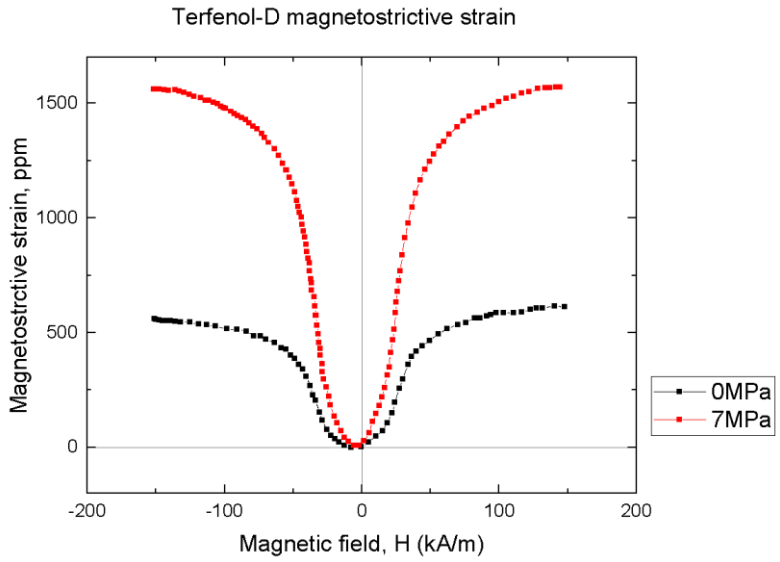

Figure 2.10 Magnetostrictive strain of Terfenol-D (Grunwald, 2007)

When a constant stress is applied to a magnetostrictive material like in Fig. 2.10 (Grunwald, 2007), this then produces strain within the material, which changes the response in an applied field. This is known as the inverse magnetostriction or the Villari effect as seen in Equation 2.17 (Calkins, Flatau and Dapino, 2007; Flatau, 2019).

Equation 2.17 1D linear Villari effect (Flatau, 2019)

$$B = d_{33}\sigma + \mu^{\sigma}H + P\Delta T \qquad (2.17)$$

where B is the magnetic flux density (T), d_{33} = dB/dσ (induction/stress) which is the magnetostrictive constant, μ^{σ} is the permeability at constant mechanical stress, H is the magnetic field and $P\Delta T$ is the temperature coefficient and change in temperature.

The Joule and Villari effects are reversible, so the materials can return to the same geometry as before when the external field or stress is removed as seen in Fig. 2.11 and 2.12 below (Wilson *et al.*, 2007).

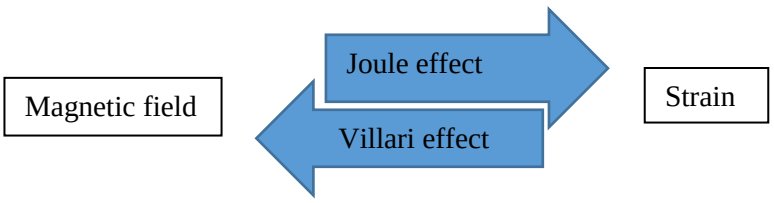

Figure 2.11 Direction of change between joule and Villari magnetostriction effect (Wilson *et al.*, 2007)

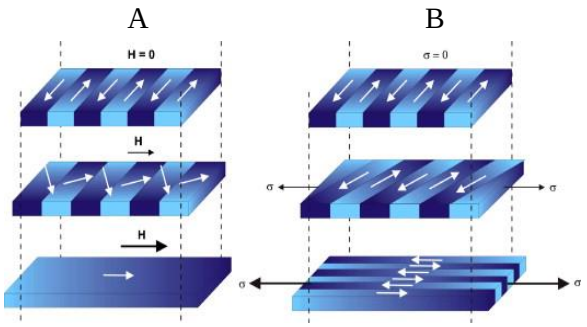

Figure 2.12 Diagram showing the rotation of domains before and after exposed to magnetic field (Joule magnetostriction) and stresses (Villari effect) (Wilson *et al.*, 2007)

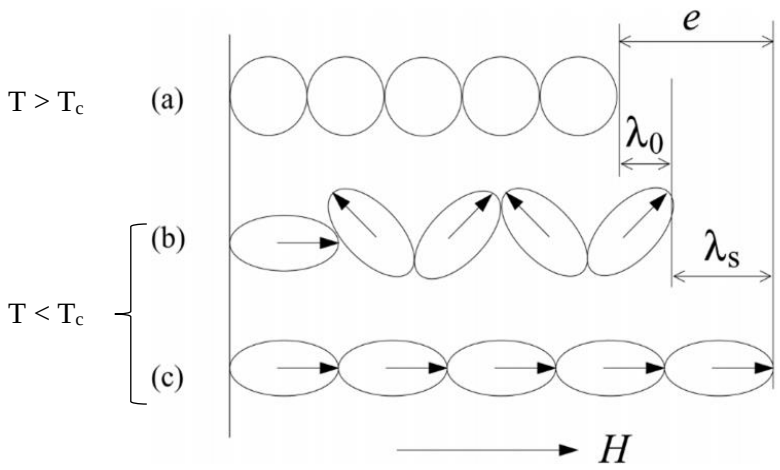

Figure 2.13 Magnetic field applied on ferromagnetic material from (a) paramagnetic $T>T_c$ to (b) spontaneous magnetostriction $T<T_c$ to (c) saturated magnetostriction $T<T_c$ (Dapino, 2004)

In Fig. 2.13, the magnetostriction can be expressed as the change in length by domain orientation from (a) to (c). (a) has no defined moment orientation (paramagnetic state) which is where the material is above the Curie temperature. (b) where the magnetic moment is unaligned (below the Curie temperature). (c) is where the domains are orientated towards the applied field and are fully saturated. In (Dapino, 2004) (Datta *et al.*, 1984), they express in Equation 2.18 the isotropic magnetostriction:

Equation 2.18 Isotropic magnetization (Dapino, 2004)

$$\lambda_s = e - \lambda_0 = \frac{2}{3}e = 2\lambda_0 \qquad (2.18)$$

where e is the total strain from (paramagnetic to saturation), λ_0 is the total strain from paramagnetic to spontaneous orientation (cooled below Curie temperature) and λ_s is when strain from spontaneous to field applied (when domains are aligned to the field).

To express the magnetostriction further, each domain is randomly orientated. Therefore, the angle between the applied field and the orientation of the domain is expressed in the Equation 2.19 (Dapino, 2004).

Equation 2.19 Orientation of domains(Dapino, 2004)

$$\lambda_s(\theta) = \frac{2}{3}\lambda_s(cos^2\theta - \frac{1}{3}) \qquad (2.19)$$

where θ is the angle between the field and domains. This can be expressed as the difference between magnetostriction in the parallel ($\lambda_{s||}$) and perpendicular angle ($\lambda_{s\dashv}$). Therefore, angles of 0 and 90 degrees are substituted in the equation above which gives the expression in Equation 2.20 (Dapino, 2004).

Equation 2.20 Ratio of parallel and perpendicular magnetization (Dapino, 2004)

$$\lambda_{s||} - \lambda_{s\dashv} = \lambda_s + \frac{1}{2}\lambda_s = \frac{3}{2}\lambda_s \qquad (2.20)$$

where $\lambda_{s||}$ is angle parallel with the field and $\lambda_{s-|}$ is the angle perpendicular to the field. With this expression, materials that exhibit magnetostriction can be compared and selected in terms of their saturation magnetostriction as shown in Equation 2.21 (Dapino, 2004).

Equation 2.21 Magnetostriction at saturation (Dapino, 2004)

$$\lambda_s = \frac{3}{2}\lambda_{100}\left(\alpha_1^2\beta_1^2 + \alpha_2^2\beta_2^2 - \frac{1}{3}\right) + 3\lambda_{111}(\alpha_1\alpha_2\beta_1\beta_2 + \alpha_2\alpha_3\beta_2\beta_3 + \alpha_3\alpha_1\beta_3\beta_1) \qquad (2.21)$$

where α is the direction along which the magnetic moments are saturated and $\beta\ is$ the direction in which the saturation magnetization is measured. In a single crystal structure, the saturation magnetostriction can be calculated by the [100] and [111] crystal direction magnetostriction constants, when moment and magnetisation are changed as shown in (Dapino, 2004). However, for materials that have multiple crystals (polycrystal) this becomes difficult to calculate the angle of the saturation. Instead an average is taken which is shown in Equation 2.22 (Dapino, 2004).

Equation 2.22 Average saturation magnetostriction in polycrystalline (Dapino, 2004)

$$\overline{\lambda_s} = \frac{2}{5}\lambda_{100} + \frac{3}{5}\lambda_{111} \qquad (2.22)$$

As stress is applied to the material, the change in magnetic field depends on the material's strength and stiffness (Young's modulus). The stress changes the direction of moment therefore Equation 2.23 below shows the relation between the magnetostriction and the strength of the material known as magnetoelasticity (E_σ), where stress (σ) is applied separately to each crystal direction for [100] (λ_{100})

and [111] (λ_{111}), cosine direction of magnetisation (α) and applied stress (γ) as shown in (Tholeke, 1993).

Equation 2.23 Magnetoelasticity of polycrystalline material (Tholeke, 1993)

$$E_\sigma = -\frac{3}{2}\sigma\lambda_{100}\sum_{i+j}^{3}\alpha_I^2\gamma_j^2 - 3\sigma\lambda_{111}\sum_{i+j}^{3}\alpha_i\gamma_i\alpha_j\gamma_j \qquad (2.23)$$

Other effects include the ΔE effect, which is when a change in elasticity (by stress strain or magnetoelatiscity) changes the anisotropy of the material as seen in Equation 2.24 (Dapino, 2004). The inverse of this is when the magnetic field changes the elasticity. Wiedemann effect is when a helical magnetic field is created when a magnetic field creates a torque to a current-carrying ferromagnetic wire. The inverse is called the Matteuci effect, where torque generates helical magnetic field. The magnetovolume effect is when there is a change in volume in an applied field, occurs near the T_c, the inverse is the Nagaoka-Honda effect where the magnetic field changes as the volume changes (Dapino, 2004).

Equation 2.24 ΔE effect (Dapino, 2004)

$$\Delta E = (E_s - E_0)/E_0 \qquad (2.24)$$

where E_0 is the minimum elastic modulus and the E_s is the elastic modulus at magnetic saturation.

2.4.1.1 Effects of MAZE energy on magnetostriction

Magnetostriction depends on several factors that restrict both the Joule and Villari effects. Both of these effects depend on the MAZE energy, which determines the energy to orientate magnetic moments and domains. The MAZE energy (Hayward, 2019) as mentioned in chapter 2.1 are Zeeman, exchange, magnetocrystalline anisotropy and magnetostatic energy.

Zeeman is the amount of energy required to orientate magnetic moments to the applied field direction. If the magnetic field is anti-parallel to the magnetic moment of the material, then this is energetically unfavourable. This results in increasing the external magnetic field towards saturation. Therefore, magnetostriction depends on the Zeeman energy due to the potential energy to align the moments.

Exchange energy is the interaction between two atomic moments. If the moment is an anti-parallel state then this can have an effect on magnetostriction as it could produce close to net zero magnetostriction as it is energetically unfavourable (O'Handley, 1999). Moments that are aligned to each other is favourable as anisotropic material would be favourable to align moments in a certain direction.

Magnetostatic energy is favourable when the magnetisation is orientated toward the long axis to reduce the demagnetisation field. Therefore, the magnetostatic energy is inversely proportional to the number

of domains. Magnetostriction is affected by the orientation of domains as less energy is required to orientate the domains and align the moments, this will increase the magnetostriction coefficient. For example, the shape anisotropy alters the alignment of moments by increasing or reducing the demagnetisation factor. The demagnetising factor is important for magnetostriction, depending on the shape of the material. For example, a thin flat shape will have low coercive force and higher magnetisation when magnetostatic energy is higher in the short end (depth), which is due to the higher number of poles. The manufacturing processes such as annealing and cold rolling can affect the Magnetostatic energy. For example, cold rolling will elongate grains and will orientate magnetic domains, which will produce directionality in the structure. Induced magnetic anisotropy can be used to lower the coercive field and produce a soft magnet that is useful for sensors like in Fig. 2.14 (Tumanski, 2016). An ideal magnetostrictive material will have a low coercive field and high saturation magnetisation. This is because for a sensor and actuator, they require quick switching of the magnetisation and strain instead of slow orientation and restricted switching.

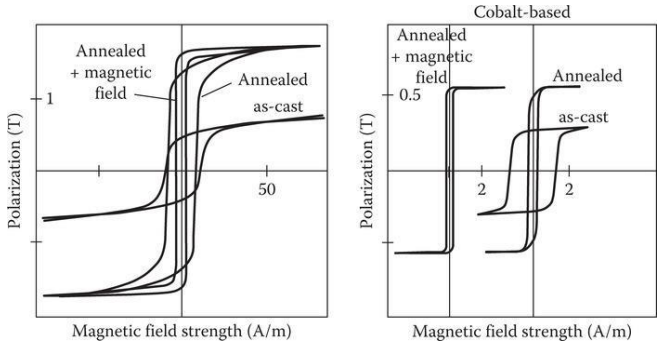

Figure 2.14 Annealing metglas in magnetic field (Tumanski, 2016)

The intrinsic magnetisation direction depends on the shape and crystal structure of the material which is due to spin orbital coupling within the crystal lattice (Moskowitz, 1991), therefore leads to magnetocrystalline anisotropy as seen in chapter 2.2.4. Magnetocrystalline anisotropy has the biggest effect on magnetostriction as having a preferred direction in the crystal lattice greatly increases magnetostriction constant. Fig. 2.7 shows a hysteresis loop of FCC magnetite, which is shown to have an easy direction in the [111] and hard direction in the [100]. Magnetocrystalline energy has an easy and hard direction where it is preferred that domains orientate in the easy direction because less energy is required as moments are aligned, hence greater anisotropy.

Chapter 3

Literature review

3 Literature Review

3.1 Background

Carbon fibre reinforced polymer (CFRP) composite have been used in aircrafts for over a decade. The amount of composite material used in commercial and military aircrafts is increasing and replacing traditional materials such as aluminium and steel (Woon, 2015) (Drahansky *et al.*, 2016). Both largest aircrafts manufacturers, Boeing and Airbus have increased composite materials within their aircrafts. For example, from Boeing 777 to the new 787 there has been an increase of 38% of composite materials and a 30% reduction of aluminium (Fig. 3.1).

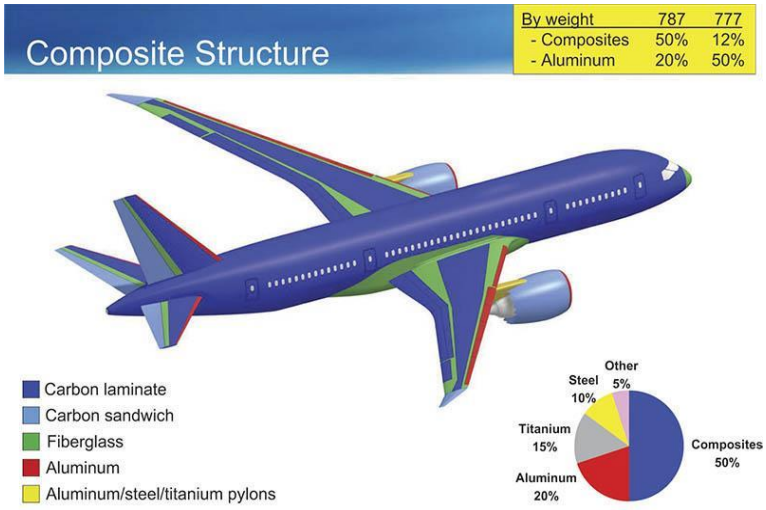

Figure 3.1 Composite structure of commercial aircraft (Drahansky *et al.*, 2016)

However, CFRP are susceptible to fracture due to fatigue and impact during use. Fig. 3.2 (Güemes *et al.*, 2020) shows that without structural health monitoring (SHM), structures can lead to failure when exposed to high fatigue over time. Time scheduled maintenance reduces the likelihood of failure significantly, but with a cost, as repeated replacement of parts over time will increase the cost of maintenance to a point where it is unsustainable. Corrective maintenance is to maintain parts when they

fail under low stress or loads. This saves cost and time, however it is dangerous to allow parts to be in service when the likelihood of failure is increased. By monitoring damages using a sensor (condition based maintenance) allows defect to be detected before they fail or reduce the performance of CFRP. This saves time, cost and prevents failure to parts that are critical to the function of the aircraft.

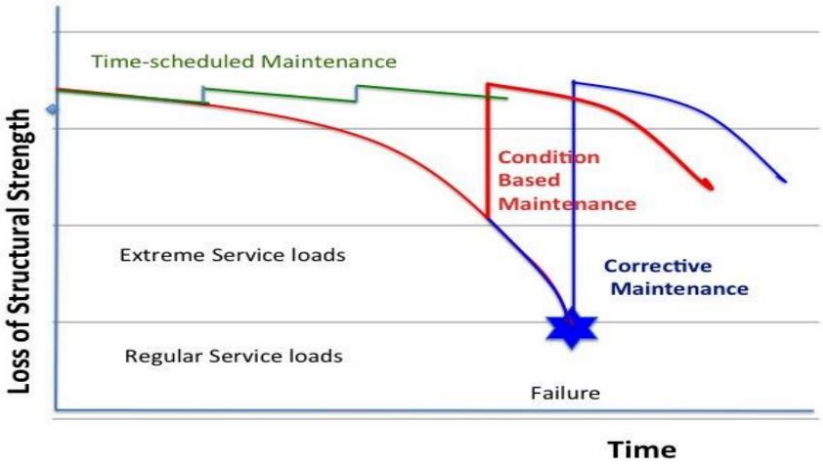

Figure 3.2 Maintenance strategies with/without structural health monitoring (SHM)

The failure in composite materials can occur by various mechanisms, as discussed in (Amafabia, Daerefa-a Mitsheal Montalvão, David-West and Haritos, 2017) where common damage types are barely visible impact damage (BVID) seen in Fig. 3.3 (Roach *et al.*, 2013). This includes matrix cracking, where crack forms between layers that are parallel to the fibre in the ply as seen in Fig. 3.4 (Ziadoon and Chwei, 2016).

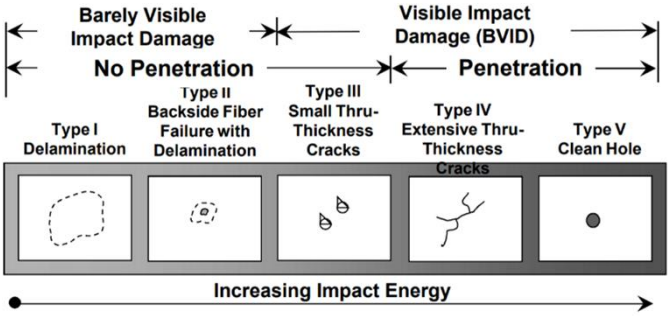

Figure 3.3 Types of damages in aircraft composite structure (Roach *et al.*, 2013)

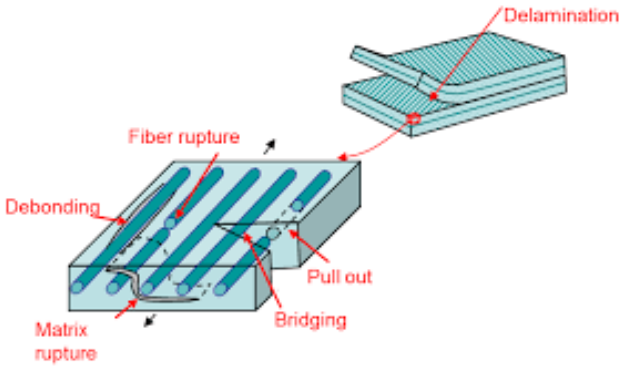

Figure 3.4 Types of failure in composites (Ziadoon and Chwei, 2016)

Matrix cracking can accelerate other damage mechanisms as the composite starts to deteriorate. Fibre fracture occurs when fibres break apart, therefore reduces strength under buckling. Debonding can occur when there is interfacial stress concentration, therefore adhesion can weaken around the fibres. Delamination can occur when there is separation of two layers due to reduced adhesion in the interface, which then propagates as the stress is increased. Fibre pull-out is when the fibre is broken, this leaves a gap in the composite, therefore reduces the interfacial strength. Damage in CFRP in aircrafts is complex as they can have multiple damage nucleation due to stresses and strain, which can be seen in Fig 3.5 (Speckmann, 2007).

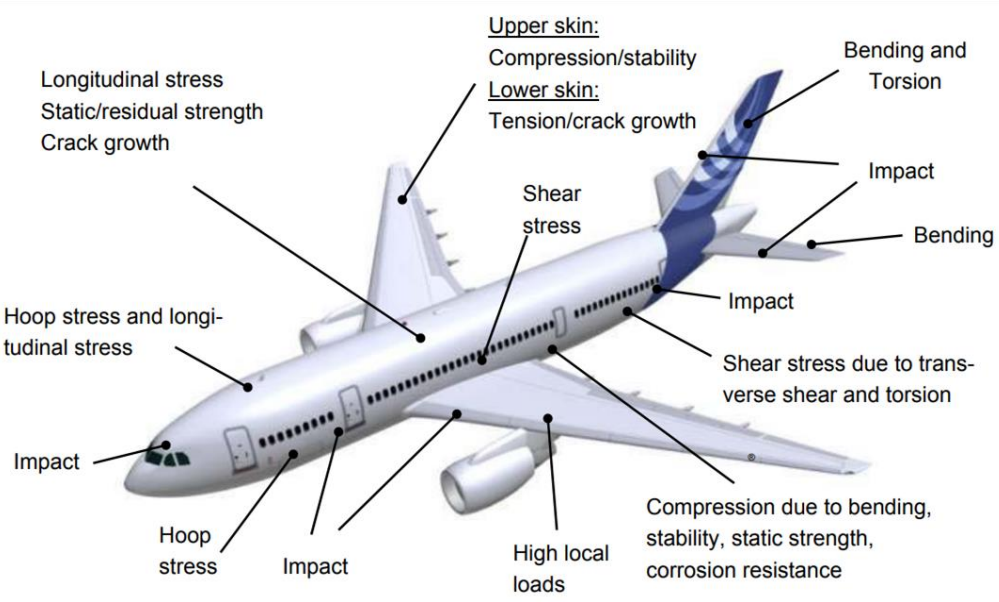

Figure 3.5 Damage location on aircraft (Speckmann, 2007)

3.2 Introduction to SHM sensors

The first known SHM for laminates structure apart from visual inspection, is the coin tap method as seen in Fig. 3.6 (Cawley and Adams, 1988) where force and time were measured. Today there are a range of sensors for SHM which can be used in applications such as monitoring bridges or aircraft (Wilson *et al.*, 2007).

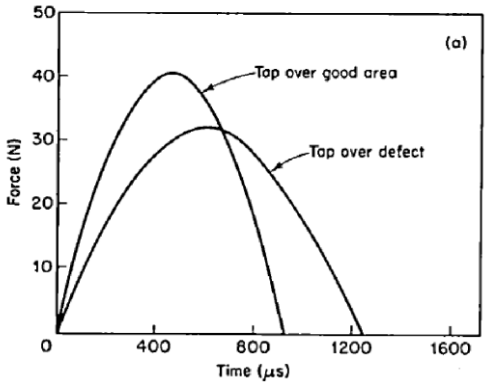

Figure 3.6 Coin tap method for SHM (Cawley and Adams, 1988)

Developing a sensor for an aircraft requires effective damage detection without reducing the performance over time. In Fig. 3.7a (Giannakeas, Khodaei and Aliabadi, 2022) shows an example of developing a SHM sensor to be installed on aircrafts. In addition to the sensor printed, an effective installation such as bonding and protective layer to secure the sensor is needed. A sensor is one part of the SHM process as seen in Fig. 3.7b (Sundaram *et al.*, 2016), where a data acquisition/software is used to interpret the signal. The data is sent to the processor via wire or wireless, which filters the raw data and information such as location of the sensor and time of detection etc. The location of the sensor is important as the location of impact and strain can be predicted as seen in Fig. 3.5 where impact damages are typically towards the front and strain (tension or compression) is focused along the wing or joints. Then a dedicated software of a specific type for the sensor measures and displays the health of the structure. The process repeats until there is a defect that alerts the user to the extent of the damage.

a

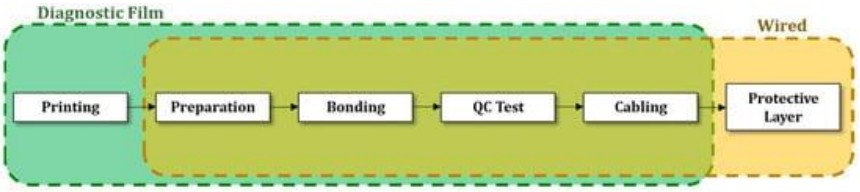

b

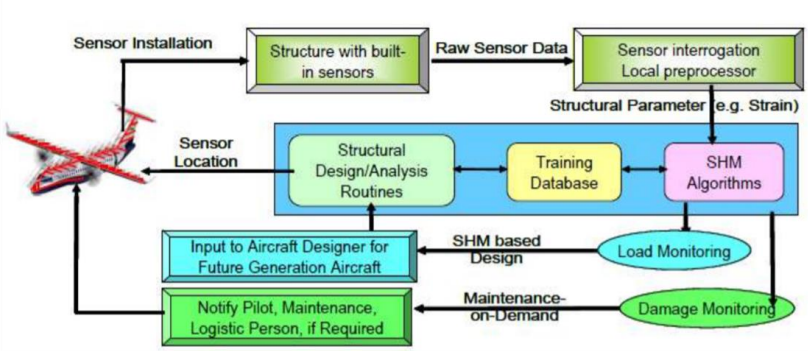

Figure 3.7 Sensor installation (a) SHM structure and design (b) (Giannakeas, Khodaei and Aliabadi, 2022) *and* (Sundaram *et al.*, 2016)

For aircrafts, there are a range of SHM sensors such as magnetostrictive, piezoelectric, electrical resistance in CFRP, optical fibre, ultrasonic testing, X-ray radiography, eddy current, acoustic emission and magnetic shape memory. There is no unified SHM sensor, which can be used in all setting and conditions e.g. geometry and calibration. Therefore, there are a number of factors to consider as shown in (Shieh *et al.*, 2001), before selecting sensors used for SHM such as:

- Resolution
- Range/coverage
- Sensitivity
- Accuracy
- Cost
- Weight
- Size
- Manufacturing
- User training and calibration

Piezoelectric sensor materials are a class of materials that generate electrical current when mechanical load is applied. One of the most common piezoelectric materials is lead zirconate titanate (PZT), which can be used as a sensor and an actuator. The actuator generates an elastic wave field (lamb waves), which propagates through the material. As the wave passes through the defect, the PZT sensor picks up a disturbance in the wave hence detection of the defect, by converting the mechanical wave into electrical energy.

Fibre optics are used to detect a defect through a change in refraction in the Bragg grating sensor. The light that is transmitted through the Bragg grating sensor changes direction therefore reduces the intensity, which is measured (Christopoulos *et al.*, 2014). Fig. 3.8 shows the optical fibre Bragg grating (FBGS, 2020) under strain, which shifts the wavelength of the light passing through, therefore the length of strain can be measured and detected.

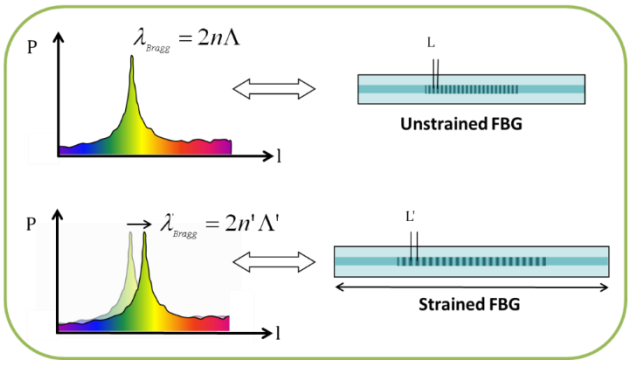

Figure 3.8 fibre Bragg grating of strained and unstrained sensor (FBGS, 2020)

Ultrasonic detects damage by using a transmitter and detector at a certain vibration frequency. As the signal wave reaches the defect area the signal is then disrupted which then bounces back to the detector as seen in Fig. 3.9 (Matrix Inspection and Engineering Services, 2017).

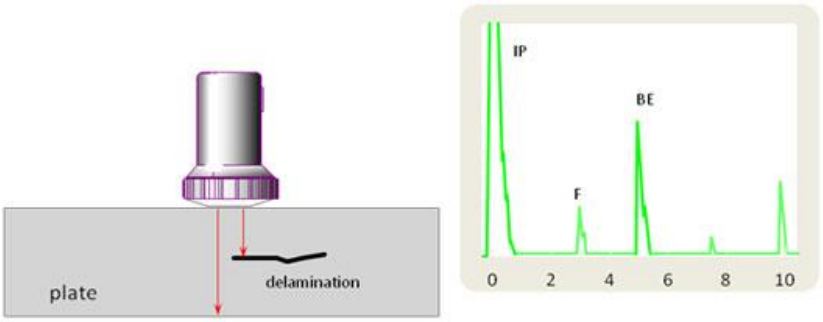

Figure 3.9 Ultrasound sensor (IP- Initial pulse, F- Fracture, BE- Back echo) (Matrix Inspection and Engineering Services, 2017)

Radiography is good for detecting defects via source and detector, for thick or dense parts as X-rays can penetrate the part to reach the defect without loss of signal. Radiography provides good images of defects that cannot be detected by any other methods (Soutis, Fleck and Smith, 1991).

CFRP are electrical conducting materials as discussed in (Amafabia, Daerefa-a Mitsheal Montalvão, David-West and Haritos, 2017), thus when there is a defect in the composite, the electrical resistance of the composite changes. Therefore, the sensitivity can be measured down to individual fibres. For SHM of composites in aircraft this method does not require additional weight to the structure. However, the sensitivity depends on the number and thickness of individual fibres, therefore it is not viable for large structures such as an aircraft wing.

Eddy currents are another non-contact SHM as seen in (Jiao *et al.*, 2016), where changes in magnetic field are detected when conductive material passes through the field as shown in Fig. 3.10 (Gasparin, Santi and Nussbaumer, 2018). This then produces a torque, where the magnetic field is in the opposite direction (secondary field against the primary field), creating a resistance in the coil (back electro-motive force) which can be detected.

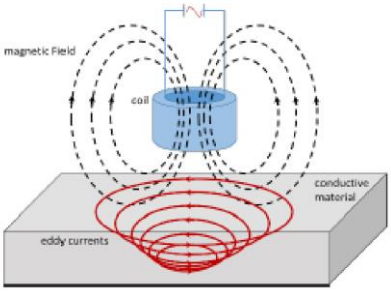

Figure 3.10 Eddy current diagram (Gasparin, Santi and Nussbaumer, 2018)

Magnetic shape memory alloys (MSMA) such as Ni-Mn-Ga can be used as a sensor and actuator (Söderberg *et al.*, 2006) (Hubert *et al.*, 2012). MSMA goes through a phase transition by the movement of twin boundaries when a magnetic field is applied as seen in Fig. 3.11 (Hubert *et al.*, 2012). MSMA changes from martensite to austenite microstructure (magnetic-field-induced strain)(O'Handley, 1999) (Kohl *et al.*, 2014). When stress is applied, the microstructure changes and reduces the volume of the material and generates a magnetic field. The field can be measured through a hall sensor or inductor coil. This is very similar to magnetostrictive materials, however MSMA undergoes a phase change while magnetostrictive material does not, as it is an inherent property and does not depend on twin boundaries.

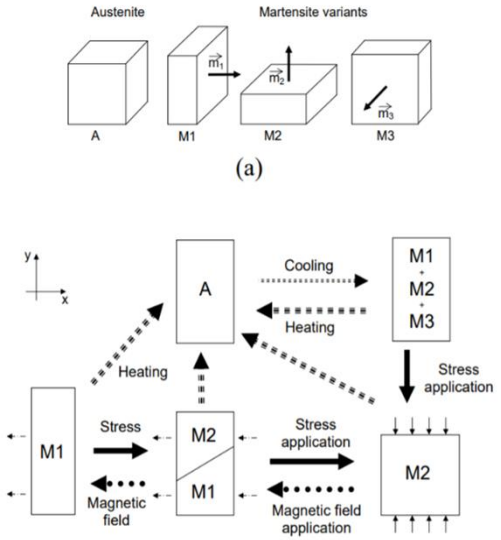

Figure 3.11 Magnetic shape memory alloys behaviour as actuator and sensor in austenite and martensite phase (Hubert *et al.*, 2012)

Table 3.1 shows the different types of SHM sensors and their advantages and limitations (Wilson *et al.*, 2007; Health and Safety Executive, 2015; Drahansky *et al.*, 2016; Jiao *et al.*, 2016; Amafabia, Daerefa-a Mitsheal Montalvão, David-West and Haritos, 2017; Olympus, 2017; Gasparin, Santi and Nussbaumer, 2018; Leong *et al.*, 2018)

Table 3.1 SHM sensor selection, data taken from (Wilson *et al.*, 2007; Health and Safety Executive, 2015; Drahansky *et al.*, 2016; Jiao *et al.*, 2016; Amafabia, Daerefa-a Mitsheal Montalvão, David-West and Haritos, 2017; Olympus, 2017; Gasparin, Santi and Nussbaumer, 2018; Leong *et al.*, 2018)

SHM	**Strain sensitivity (μstrain)**	**Advantage**	**Disadvantages**
Magnetostrictive materials	20 ± 5	-High sensitivity and resolution	-Can be affected by EMI
Piezoelectric	150 ± 5	-Multiple readings -High sensitivity -Widely used in industry	-Vibrations degrade composites -Requires calibration

Electrical resistance in CFRPs	Individual fibers	-No additional sensor or weight -Covers wide area	Sensitivity depends on the composite electrical resistivity (thickness and length). Only senses the fibre breakage or deformation
Optical fibre	2000 ± 1	-Lightweight -Environmentally stable -Immune to EMI and multiplexing capability	-Fragile -High cost to manufacture and install -Low resolution
Ultrasonic testing	25 ± 5	-Fast detection of defects, -Good resolution and flaw detecting capabilities. -Widely used in industry -Good for detecting clean defects.	-Require training and knowledge to use. -Material property is needed to ensure accurate testing. -Requires surface preparation. -Offline detection. -Calibration to filter noise.
X ray radiography	-	-Can detect defect such as porosity in thick structures	-Only used for isotropic materials -Low absorption of low dense materials. -Need extra protection to avoid exposure to users -Care when inserting dye penetrant to CFRP.
Eddy current	1000± 56	-No surface contact or extra preparation	-Needs to be perpendicular to the surface. -Detect surface defects.
Acoustic emission	-	-Quick and effective at locating defects.	-Noise interference

			-Training and experience is needed
Magnetic shape memory	-	-High strain is produced	-Phase change produces large strain which could result in formation of fracture

Table 3.2 Features comparison of PZT, magnetostrictive and MSMA sensors (Grunwald, 2007; Olabi and Grunwald, 2008) (Hubert *et al.*, 2012)

Features	**PZT (Piezoelectric)**	**Terfenol-D (magnetostrictive)**	**Ni-Mn-Ga (MSMA)**
Elongation (%)	0.1	0.2	5
Energy density (kJ/m^3)	2.5	20	1
Bandwidth (kHz)	100	10	0.5
Hysteresis (%)	10	2	30
Cost ($/cm^3)	200	130	200
Strain %	-	0.16	6

Table 3.2 shows a comparison of the sensors such as PZT, magnetostrictive and MSMA sensors (Grunwald, 2007; Olabi and Grunwald, 2008). Magnetostrictive sensors have better features compared to the other sensors such as cost and energy density. However, this is only a rough guide as manufacturing, material selection and installation cost can vary. For example, the cost depends on the material cost and number of sensor that can be installed on aircrafts.

One of the challenges of developing sensor for SHM of CFRP is to install or attach the sensor to the aircraft without interfering and reducing the structural integrity of the aircraft. As defects are locations dependent, in which case the sensor will be placed in selective areas where defects or fracture would occur as seen in Fig. 3.5. In addition to the system developed for all SHM sensor in Fig. 3.7 b, the sensor would need to be connected either by wire or wireless connection to the on board computer. There are two direct ways of placing the sensor, by embedding the sensor in the composite, or adhesion on the

surface. A magnetic field detector would have to be attached to the sensor or close by to detect changes in magnetic field. Each sensor will not be exactly identical, therefore the detection would need to be calibrated to ensure correct readings. In literature (Leong *et al.*, 2019) they have shown that bending and impact damages to the embedded amorphous CoSiB magnetostrictive ribbons in aircraft CFRP, increases magnetic field as defects within the CFRP occurs. In (Komagome *et al.*, 2022) then have embedded magnetostrictive FeCo wires into CFRP composite. The wire drawing increases magnetic permeability for thinner diameter FeCo wires however the Villari effect is reduced due to reduction of magnetic induction. In (Alenia Aeronautica, 2009), they have embedded magnetostrictive wires for smart sensing and repair of CFRP through induction heating. This could be useful in the long term and monitoring repairs. Therefore, the printed magnetostrictive sensor could be either be attached on the surface or embedded using an epoxy that is compatible with the CFRP resin, along with a magnetic field detector close by.

To conclude, SHM for aircraft requires sensors to have high sensitivity of defect with low weight and at low cost without additional disturbance to the aircraft and measurements. Magnetostrictive materials offer high sensitivity and resolution. Magnetostrictive materials do not reduce the life of the composite or the material as magnetostriction is an inherent property. It does not require careful installation like fibre optic or extensive user training and calibration like radiology and ultrasound testing. Magnetostrictive sensor/ actuators can detect further in depth than other SHM techniques such as eddy currents. Therefore, this study will exploit the advantages of magnetostriction property for SHM and improve the sensor by design flexibility through additive manufacturing. As seen in (Alenia Aeronautica, 2009) there is potential to be used to monitor repairing process of CFRP using magnetostrictive materials. This method can be adopted not only for aircrafts SHM but also in other areas of industry where online SHM is needed.

3.3 Magnetostrictive sensor and actuator review

A change of mechanical energy to electromagnetic energy can be measured as shown in (Calkins, Flatau and Dapino, 2007) and Equations 2.14 and 2.15. These equations show that magnetostrictive material can be measured by the change in field under strain or the change in length in an applied field. In (Ekreem *et al.*, 2007) they have shown that there are various ways of direct and indirect methods in measuring the Villari effect and Joule magnetostriction. To measure a change in volume by Joule magnetostriction (under magnetic field), one of the most popular and inexpensive ways is to attach a strain gauge to the surface of the material, which changes resistance as volume is changed. The dilatometry method is where a volume change for magnetostrictive material is measured by recording the movement of the piezoelectric tunnelling tip. The piezoelectric tunnelling tip is in contact with the

cylindrical shaped material and as the volume change the tip moves, thus the change in distance of the tip is recorded. The optical interferometry method uses a laser beam to measure the change in reflection angle of the optical lever attached to the material as it is deformed. The Joule magnetostriction can be measured indirectly for example by observing the shift in ferromagnetic resonance to determine the permeability (under a known stress). The small-angle-magnetisation rotation method involves applying a saturation magnetic field and a small ac field in the opposite direction to rotate the field in the sample (which is detected by another sensing coil). Strain modulated ferromagnetic resonance method measures the intensity of the strain modulated FMR signal by applying a stress caused by a piezoelectric transducer.

Table 3.3 shows the sensitivity in measuring strain by Joule magnetostriction (Ekreem *et al.*, 2007). Strain gauges are inexpensive and flexible compared to the other measurements, however the sensitivity to measure strain is low in comparison. Indirect methods are more accurate than direct methods, which could be due to attachment or position/ contact size of the sensor.

Table 3.3 Sensor type and performance in measuring magnetostriction (Ekreem *et al.*, 2007)

Sensor	**Type of measurement**	**Magnetostriction sensitivity (ε)**
Strain gauge	Direct	10^{-6}
Dilatometry	Direct	10^{-9} to 10^{-5}
Optical interferometry	Direct	10^{-8}
Small-angle-magnetisation rotation	Indirect	10^{-9}
Strain modulated ferromagnetic resonance	Indirect	10^{-9}

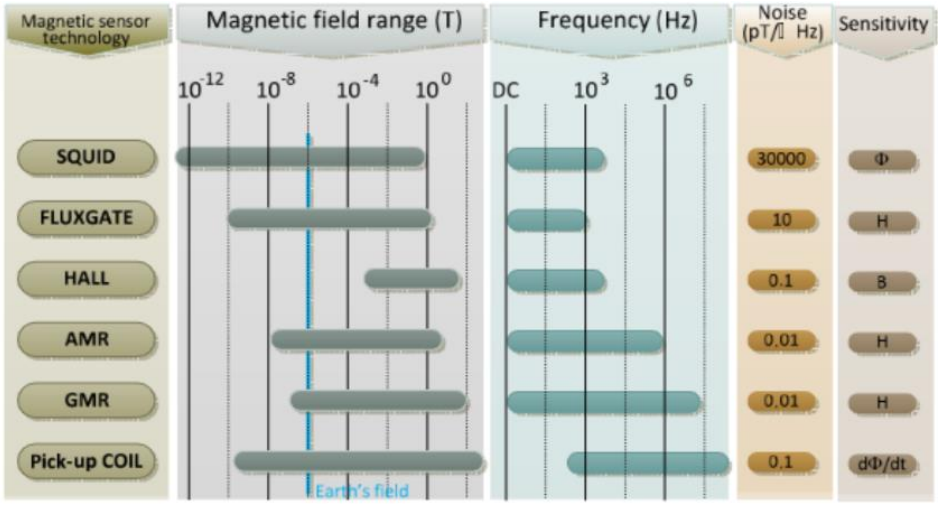

Figure 3.12 Magnetic field sensors (Ramos and Ribeiro, 2014)

The Villari effect can be measured depending on the applied stress/strain to the samples. Nowadays the method in detecting the magnetic field is shown in Fig. 3.12 (Ramos and Ribeiro, 2014). The most common method is by the Hall effect sensor, using a Hall probe or by induction using a pick up coil. As these methods are inexpensive and can pick up small field changes.

The Hall effect is when the magnetic field interacts with the current and generates a voltage proportional to the field, as shown in Equation 3.1 (Honeywell, 2018) and Fig 3.13. Where VH is the Hall voltage, I is the current and B is the magnetic flux density.

Equation 3.1 Hall sensor effect

$$V_H \propto I \times B \quad (3.1)$$

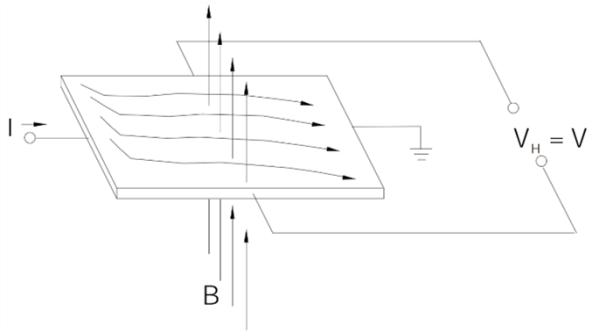

Figure 3.13 Hall sensor effect when magnetic field is applied (Honeywell, 2018)

An induction or pick up coil can measure a field by Faraday-lenz law, which describes the relation between the magnetic field and electrical signal of the coil. This is shown in Equation 3.2 (Dapino, 2004):

Equation 3.2 Faraday-Lenz law of electromagnetic induction (Dapino, 2004)

$$V = -NA\frac{\Delta B}{\Delta t} \quad (3.2)$$

Where V is the induced voltage, N is the number of solenoid turns, B is the magnetic flux and A is the area.

In (Vincent *et al.*, 2020) they explored the use of inductance measurements via LCR meter to measure the change in inductance. As a coil of copper wire produces a small magnetic field (electromagnetic), the forces opposing the field can generate a change in the current direction. This is known as self-inductance where the inductance is influenced by the current flowing in the wire and storing energy around it. The inductance is directly related to the change of magnetic flux as the current flowing in a wire resists the direction of field therefore creating a storage of magnetic flux in the wire. Magnetic flux is directly related to the inductance and current as shown in Equation 3.3. Inductance of a coil can be calculated using Equation 3.4 (TDK Corp, 2020):

Equation 3.3 Magnetic flux derivation from inductance (TDK Corp, 2020)

$$B = LI \quad (3.3)$$

Where I is the current in amperes and L is the inductance in Henries which gives magnetic flux B in Webber.

Equation 3.4 Inductance equation for coil (TDK Corp, 2020)

$$L = \frac{\mu N^2 A_r}{l} \quad (3.4)$$

Where L is inductance in Henries (H), μ is permeability, N is the number of turns of the wire, A is the area of coil and l is the length of wire in meters.

Mutual inductance is where an inductor is influenced by another inductor or magnetic field energy. This induces EMF in the coil which increases the inductance as there is a build-up or reduction of magnetic energy in the coil. There is lag in voltage against the current in the coil which increases the inductance as energy is stored.

3.3.1 Material properties/ selection

All magnetic materials such as ferromagnetic, ferrimagnetic, and antiferromagnetic (Hristoforou and Ktena, 2007) exhibit the magnetostriction property (Söderberg *et al.*, 2006). However, high magnetostriction constants, that are useful for sensor application, are found in ferromagnetic materials such as iron or nickel.

However, the magnetostriction performance is not the same for all magnetic materials as seen in table 2.1 (McHugh, 2011), where magnetostriction depends on magnetic properties such as susceptibility and permeability. The main materials that exhibit good magnetostriction are ferro/ferri magnetic such as from transitional metals like iron, nickel, cobalt and rare earth alloys containing dysprosium and terbium, as shown in table 3.4 (Tholeke, 1993; Dapino, 2004; Yu, 2021). Rare earth containing alloys exhibit high magnetostriction performance around 3000ppm but only at low temperature of 20K (Tholeke, 1993). They are relatively expensive and difficult to manufacture. For example, Terfenol-D (TbDyFe) is brittle at room temperature, therefore unsuitable to be used in applications where they are exposed to stresses. Transitional materials are readily available and tested in manufacturing processes, therefore these are ideal to commercialise and use for SHM by industry. Transition metals have magnetostriction properties because of their electron structure (Zhou, 2015), as the 4s and 3d electron shells overlap creating exchange energy which makes the electrons spin in parallel. Table 3.4 and 3.5 shows that nickel has a higher saturation magnetostriction coefficient than iron and a greater difference in magnetostriction in the [100] and [111] direction.

Table 3.4 Magnetostrictive properties of transitional and rare earth alloys (Tholeke, 1993; Dapino, 2004; Yu, 2021)

Magnetostrictive materials	**Crystal Axis**	**Saturation magnetostriction coefficient λ ($x10^{-6}$) ((m/m)/(A/m))**	**References**
Fe	100	11-20	(Yu, 2021)
		20	(Tholeke, 1993)
		21	(Dapino, 2004)
Fe	111	-(13-20)	(Yu, 2021)
		-41	(Tholeke, 1993)
		-21	(Dapino, 2004)
Fe	Polycrystal	-0.8	(Yu, 2021)
Ni	100	-(50-52)	(Yu, 2021)

		-58.3	(Tholeke, 1993)
		-46	(Dapino, 2004)
Ni	111	-27	(Yu, 2021)
		-24.3	(Tholeke, 1993)
		-24	(Dapino, 2004)
Ni	Polycrystal	-(25-47)	(Yu, 2021)
Co	Polycrystal	-(50-60)	(Yu, 2021)
Terfenol-D	100	90	(Dapino, 2004)
Terfenol-D	111	1600	(Dapino, 2004)

Table 3.5 Magnetic and physical properties of transitional and rare earth alloys (Dapino, 2004) *(O'Handley, 1999)*

Magnetostrictive materials	**Saturation magnetostriction 3/2 λs(x10^{-6})**	**Density (g/cm^3)**	**Saturation induction (T)**	**Curie temperature (^{o}C)**	**Elastic modulus E(GPa)**	**Linear magneto mechanical coupling coefficient (k)**
Fe	-14	7.88	2.15	770	285	-
Ni	-50	8.9	0.61	358	210	0.31
Co	-93	8.9	1.79	1120	210	-
Co/Fe	87	8.25	2.45	500	-	0.35
Ni/Fe	19	-	1	500	-	-
Tb	2630	9.1	1.1	423	-	0.35
TbFe2	3000	8.33	-	-48	55.7	-
Dy	6000	8.56	-	-184	61.4	-

Terfenol-D	1620	9.25	1	380	110	0.77
$Tb_{0.6}$ $Dy_{0.4}$	6000	-	-	-	-	-
Metglas 2605SC	60	7.32	1.65	370	25-200	0.92

In addition to the values found in literature, a database from the Cambridge Engineering Material Selector (Ansys CES Granta) is widely used to select materials based on their properties for engineering applications. A graph can be generated based on their properties and can select a group of material by using a trade off line (depending on the material property of interest). This can be further refined by trade off using another material property.

It is known that for sensing application, low coercive field and low saturation field is suitable. In Fig. 3.14 it shows that for functional magnetic material, Terfenol-D and Galfenol are not ideal for sensor application as they have high magnetostriction saturation, but also have higher coercive field than other materials. Based on stage 1 the materials that are suitable are soft ferrites and nickel doped iron. Fig. 3.15 shows that even though nickel doped iron has good magnetostriction properties in stage 1, it is more expensive than ferrites in stage 2. The price is an important factor when considering manufacturing on a large scale for industry.

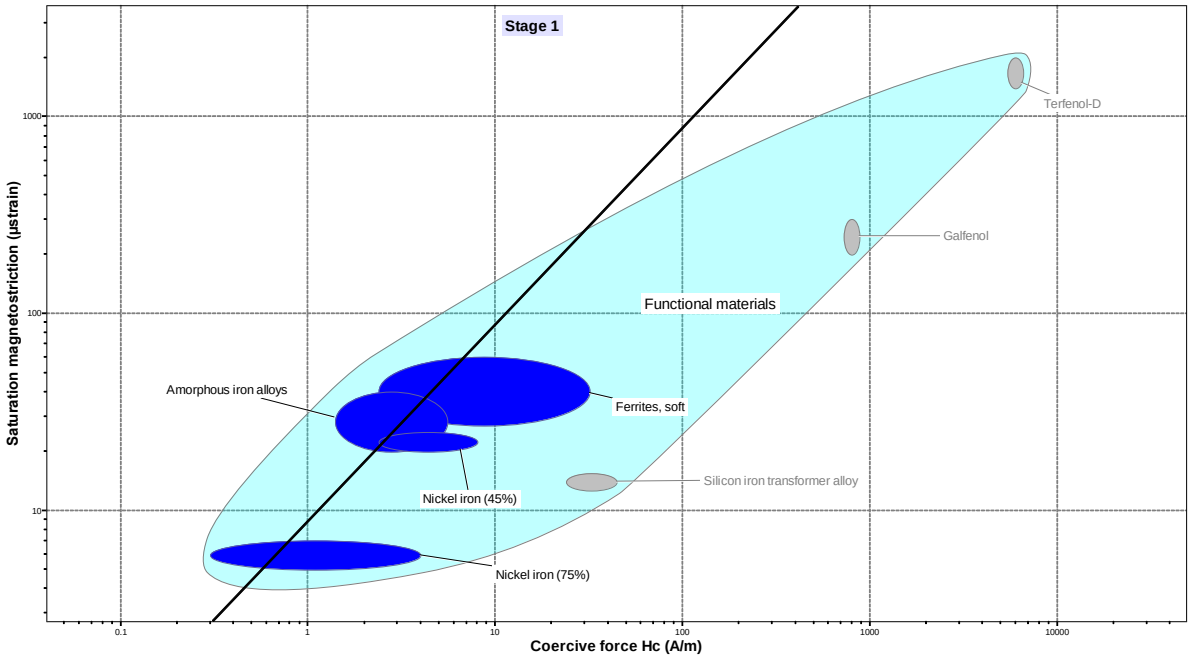

Figure 3.14 Coercive force vs saturation magnetostriction taken from CES granta database

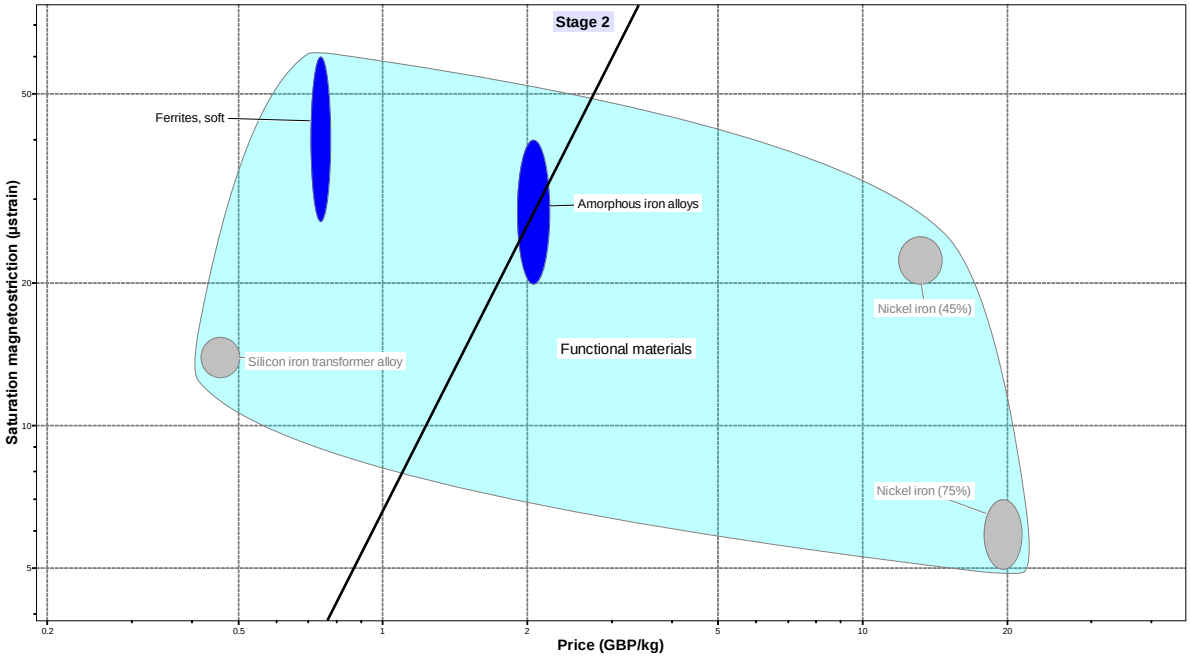

Figure 3.15 Price vs saturation magnetostriction of functional materials, taken from CES granta database

In literature (Herzer, 2013), Fig. 3.16 showed that amorphous and nanocrystalline materials perform better than crystalline materials with low eddy current losses and lower coercivity similar to the database result in Fig. 3.14 and Fig. 3.15. Both database results show that Fe/Ni/Co based amorphous/nanocrystalline materials are suitable for sensing applications. Iron based amorphous materials are shown in both databases to be most attractive for sensing application due to their low cost and low coercivity with high saturation magnetostriction.

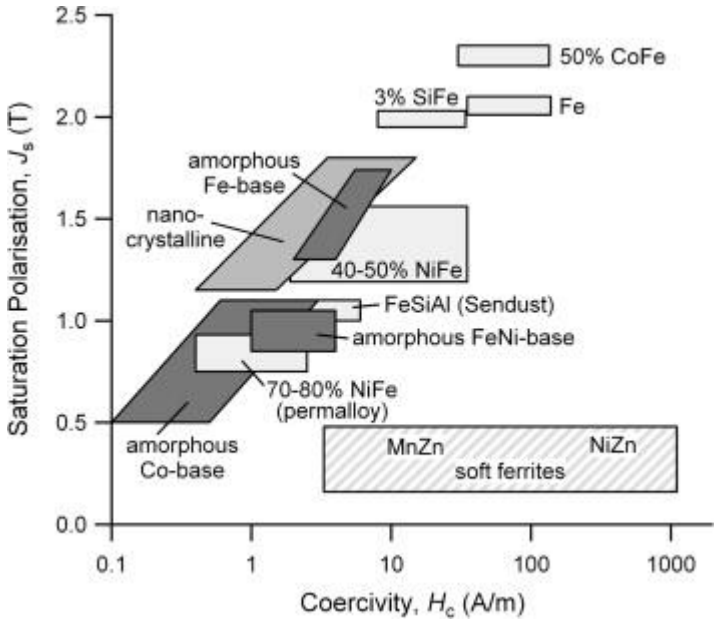

Figure 3.16 Comparison of soft magnetic materials, taken from (Herzer, 2013)

3.3.2 Repairing composite structure

An aircraft will have damage to its structure over its lifetime, due to environmental changes, impact and aerodynamic stresses, therefore if the damage is small, it is more economical to repair the CFRP than replace the structure.

The repair process (scarf repairs) for a composite material is to remove the damaged material and apply extra layers of composite on top, with adhesive/ epoxy (Budhe, Banea and de Barros, 2018). The repair then has to be cured to make sure that the epoxy maintains a strong bond. This restores the structural integrity of the damaged part. It is important to monitor the repaired patch because of changing conditions that could affect the adhesive during operation. Temperature fluctuations can cause the adhesive to become too soft or too brittle at high and low temperature respectively. This can produce further fractures as the adhesive and the composite have different thermal expansion temperature.

Magnetostrictive materials can repair composite structure by using RF heating to cure the CFRP as shown in Fig. 3.17 (Alenia Aeronautica, 2009). As a magnetostrictive actuator is used for damage sensing application, this can be used to monitor the structural integrity before and after repair. This is useful as there is no current method to monitor repaired CFRP in an aircraft.

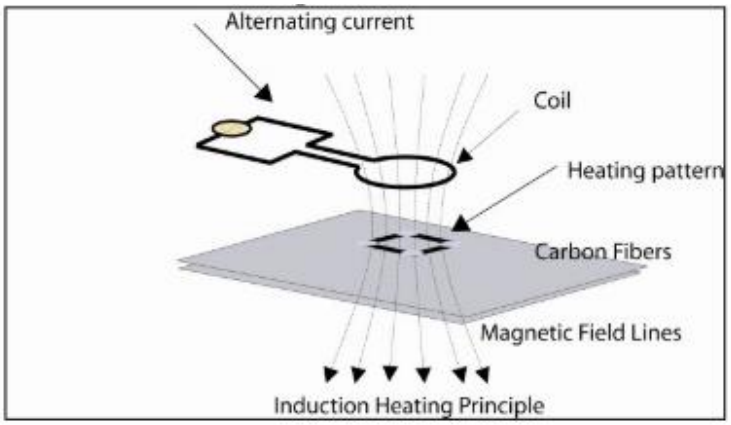

Figure 3.17 Curing CFRP by induction heating (Alenia Aeronautica, 2009)

3.3.3 Design of magnetostrictive sensor

There are various ways in detecting damages to CFRP using magnetostrictive materials, however the design and development of magnetostrictive materials for SHM has been reviewed in literature for various structures. The issues that could affect sensing damages on CFRP is the reliability in manufacturing and installation of magnetostrictive materials. This could be as manufactured (as cast) or in mixture as part of CFRP or polymer. Manufacturing has an effect on the design of the

magnetostrictive material which could affect the field sensitivity to strain. Different types of tests were carried in literature to test the performance of the Joule magnetostriction and Villari effect.

Magnetostrictive sensors manufactured in the form of a wire by glass-coating and melt spinning have been studied by (Christopoulos *et al.*, 2014; Al-Taher *et al.*, 2017). This has been proven successfully as SHM in CFRP structure but in (Christopoulos *et al.*, 2014) concluded that micro cracks formed in the CFRP composite, therefore reducing structural integrity of the CFRP structure. In (Leong *et al.*, 2018), they explored and demonstrated that SHM of CFRP by using FeSiB magnetostrictive ribbons was possible, for example measuring the change in magnetoresistance using an AMR sensor as the CFRP was strained. This proved successful, as the ribbons were able to provide damage detection as CFRP were subjected to strain by impact.

In (Sossou *et al.*, 2019), they have modelled a voxelized geometry of a composite consisting of silicon and magnetostrictive material in a mixture to test actuating performance. They have shown that as the structure was at twist at an angle of 12 degrees, saturation was reached at -5 to -10 λ_s for both magnetostrictive material with low and high young's modulus respectively. This has shown that it is possible to use a polymer/ magnetostrictive material mixture, to exploit magnetostriction property even with a polymer within the mixture. However, the issue arising in mixing two material composition together is that there is a lack of homogeneity, therefore increasing localised defects. In (Quattrone *et al.*, 2000), they have designed a composite consisting of resin and terfenol-D. By performing mechanical testing and applying a force in the axial and transverse direction, they have found that there is a change in field using a Hall probe, therefore there is scope to use it as SHM applications.

Designing a magnetic sensor has been explored in the literature such as in (Mandache, Lapointe and Genest, 2016) where they have discussed the design of magnetostrictive materials. For example, magnetostriction performance of magnetic wires were tested through COMSOL simulation. The best design for achieving higher magnetic field performance, was found to be the spiral coil design, as the spiral coil is tightly packed which improves sensitivity of field when there is a notch compared to the rectangular shaped coil as discussed in (Mandache, Lapointe and Genest, 2016). It was observed that the spiral coil design had an increased demagnetisation field compared to the square coil design. This is due to increased magnetic dipole interaction along the whole spiral coil, rather than localised dipole in the square coil design.

Shape anisotropy plays an important part in designing a sensor or actuator. In (Yoo *et al.*, 2016) they explored and calculated the angular magnetisation and the demagnetising factor of Nickel isotropic magnetostrictive material by performing lamb wave stresses. It was found that a uniaxial comb shape was preferred as it had a larger difference in demagnetising factor in the parallel and perpendicular direction, than the square or circular comb patches, as seen in table 3.6 and Fig. 3.18.

Table 3.6 Demagnetising factor for different designs in parallel and perpendicular angle (Yoo *et al.*, 2016)

Sample	Demagnetization factors	
	N (parallel)	N (perpendicular)
Square patch	0.0296	0.0296
Uniaxial comb patch	0.0179	0.1924
Circular comb patch	0.0179	0.0179

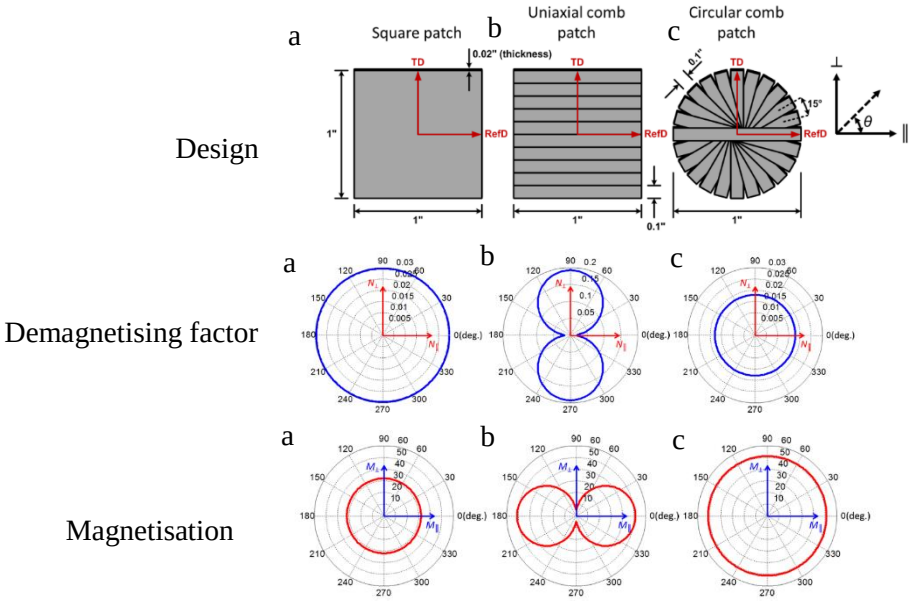

Figure 3.18 Demagnetising and magnetisation angle prediction for (a) square, (b) uniaxial comb and (c) circular comb patch (Yoo *et al.*, 2016)

The paper (Yoo *et al.*, 2016), goes further and develops an experiment to test the Villari effect of the nickel patch when exposed to lamb wave using a PZT transducer on the structure as seen in Fig 3.19. The field was measured by a pancake coil attached on top of the circular magnetostrictive patch. The shape can be redesigned for example in the literature it showed that uniaxial circular patch displayed magnetic anisotropy behaviour on substrate such as aluminium. The circular comb patch design shows greater change in field and anisotropy when exposed to the lamb wave on a thin aluminium structure.

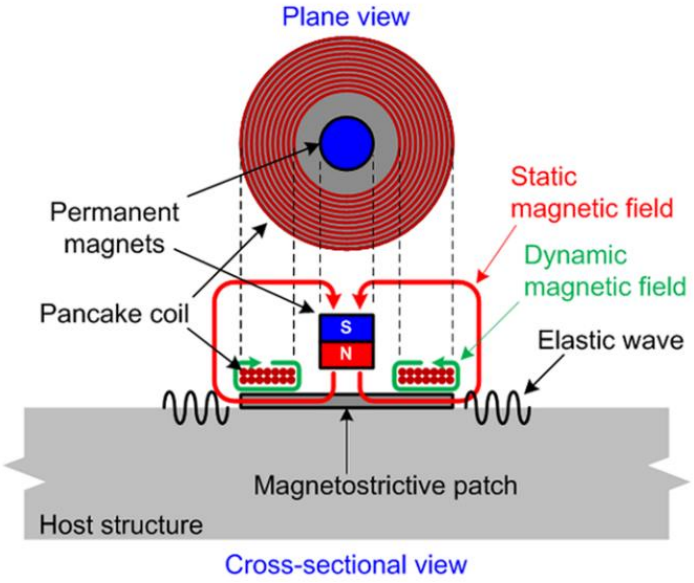

Figure 3.19 Magnetostrictive sensor setup, showing pancake coil, magnet, magnetostrictive patch on top of the structure (Yoo *et al.*, 2016)

3.4 3D printing technologies for magnetic materials

3.4.1 Printing magnetic materials review

3D printing is an additive manufacturing (AM) technique that essentially builds material layer by layer through thermal fusion or chemical binder. Printing has been used to build sensors for a wide range of industries such as temperature, humidity and gas flow sensors(Xu *et al.*, 2017). In the literature (Utela *et al.*, 2008; Sames *et al.*, 2016), there are a number of steps before manufacturing using ALM, these are.

1. Powder/ink formulation
2. Binding method and selection
3. Liquid binder formulation and powder compatibility for printing
4. Printing parameters
5. Post processing procedures

Magnetic materials can be printed by powder bed fusion (PBF). PBF technique is a printing system that uses high power laser or electrons to melt the powder in layers and bind them to form a printed structure. The heat fuses the materials together (below the material melting temperature) and then additional layer is placed over on top to build up the structure in the Z-axis. (such as selective laser melting (SLM), selective laser sintering (SLS) and electron beam melting (EBM)) (Jhong, Huang and Lee, 2016; Chaudhary *et al.*, 2020), direct energy deposition (DED) (Geng *et al.*, 2016; Mikler *et al.*, 2017; Goll *et al.*, 2019) , binder jetting (O'Heir, 2018) , material jetting (Song *et al.*, 2014) and extrusion (Patton *et al.*, 2019).

In (Geng *et al.*, 2016; Mikler *et al.*, 2017), they show a DED printer where the powder is fed through the nozzle and melted as it passes through the laser, therefore reducing the amount of powder material. This consequently builds up to produce a 3D structure. This technique also allows multiple power compositions to be printed for compositional variations during the build such as addition of binders or other additives. Laser engineered net shaping (LENS) has been used to print functional materials, for example in (Mikler *et al.*, 2017) they have used a LENS system to produce magnetic materials (FeNi and permalloy).

Inkjet printing uses metallic ink with a precursor to form a thick film structure, which is then cured either by UV light or sintering. This produces a uniform print and does not require pre-processing of powders. Inkjet printing has been a cost effective way of manufacturing electronic circuit boards and could be used to print magnetic materials.

Extrusion based printing is where a material is extruded using a mechanical actuator on to the printer bed. Polymers have been widely used as a material for extrusion printing. Recent development (Desktop Metal, 2018) has shown that extrusion printing can be used to print metal structures by mixing the metal with a polymer in an injection moulding machine.

Table 3.7 Comparison of ALM printers

Printer	Advantages	Disadvantages
PBF	-High accuracy -wide adaptation of materials	-Surface roughness -Interference from magnetised powders (EBM)
DED	-Near net shaping -homogenous deposit	-Requires high quality smooth powders -Expensive

	-Reduction of layer thermal stress	-Porosity generation
Binder jetting	-No need for support material -Versatile -Lower cost	-Low strength -Post surface treatment
Material jetting	-High accuracy -Low cost	-Limited materials -Difficult to produce 3D structure -Requires post-treatment and evaporation of solvent -Quality depends on viscosity of ink
Extrusion	-Simple using and maintaining -Easily accessible -Multi-material structures -low cost	-Limited materials, -Rough surface -Shrinkage issues -Multiple processing steps

Table 3.7 shows the advantages and disadvantages of the printers for printing magnetic materials, the best type of printer to print magnetostrictive sensors should have low cost and high accuracy. Therefore, extrusion and material jetting are good candidates for printing magnetostrictive materials.

3.4.2 Issues with 3D printing magnetic materials

Additive manufacturing for magnetic metals using these techniques have been studied (Sames *et al.*, 2016) and they found that there is a negative effect on magnetostriction. The main issue with printing magnetic materials is the presence of defect such as pores and cracks, which depends on a number of factors for example, shrinkage/warping, material compatibility, quality of raw material, thermal stress and post treatment. This is because pores can reduce the mobility of magnetic domain walls, therefore degrading the permeability by requiring more energy to move the domains and align with the magnetic

field or demagnetize (Goll *et al.*, 2019)(Vovrosh *et al.*, 2018). In (Shishkovsky and Saphronov, 2016) they have shown that pores can be seen in permalloy printed by SLM, as seen in Fig. 3.20. Pores within the 3D printed magnetic alloy could have an effect on the magnetic anisotropy. As domain wall are restricted, and pores can isolate neighbouring magnetic moments, thus forming a directionality in the structures where it is easy to magnetise in a certain direction depending on the location and number of pores.

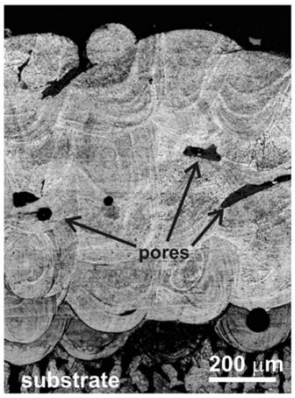

Figure 3.20 Optical microscope of pores in SLM 3d printed permalloy
(Shishkovsky and Saphronov, 2016)

By adjusting the printing parameters as seen in Fig. 3.21 (a), the number and size of pores could be reduced by increasing density. The density of the structure can be altered via the laser power from 200 W to 350 W (-/+), which is controlled during the printing process to as seen in Fig. 3.21 (b) (Yap *et al.*, 2017)(Sames *et al.*, 2016). Therefore, reducing anisotropy and improving isotropic magnetisation in the structure. Laser speed is another parameter that could be tuned to increase the hardness and homogeneity across the nickel microstructure. Such as increasing from 200 mm/s to 500 mm/s as seen in Fig. 3.21 (a). Hatch spacing increase from 0.1 mm to 0.2 mm reduces the overall density as the laser melts less material. The distance from the centre from 20 mm to 40 mm, has little effect on the density. All of the parameter shown in Fig. 3.21 (a) are non-linear for example, increasing laser power beyond 350 W would not mean the density will increase, rather the density will reduce due to the loss of material and increase porosity.

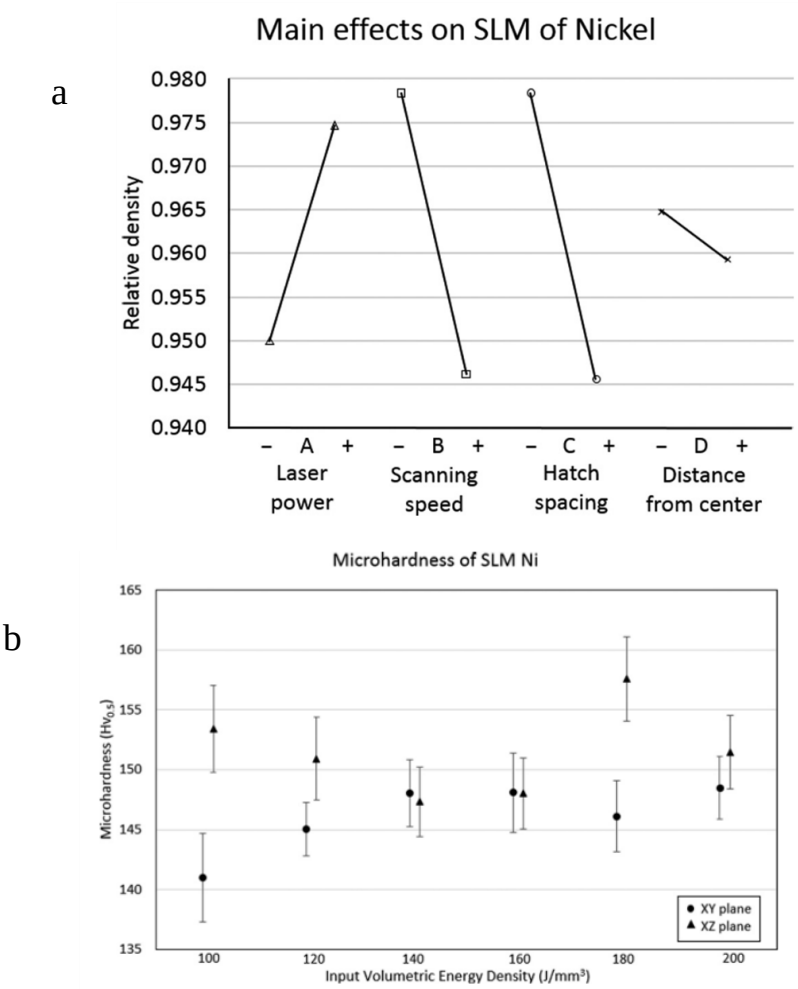

Figure 3.21 (a) Main effects on SLM of Ni (b) Microhardness and VED of SLM processed Ni (Yap *et al.*, 2017)

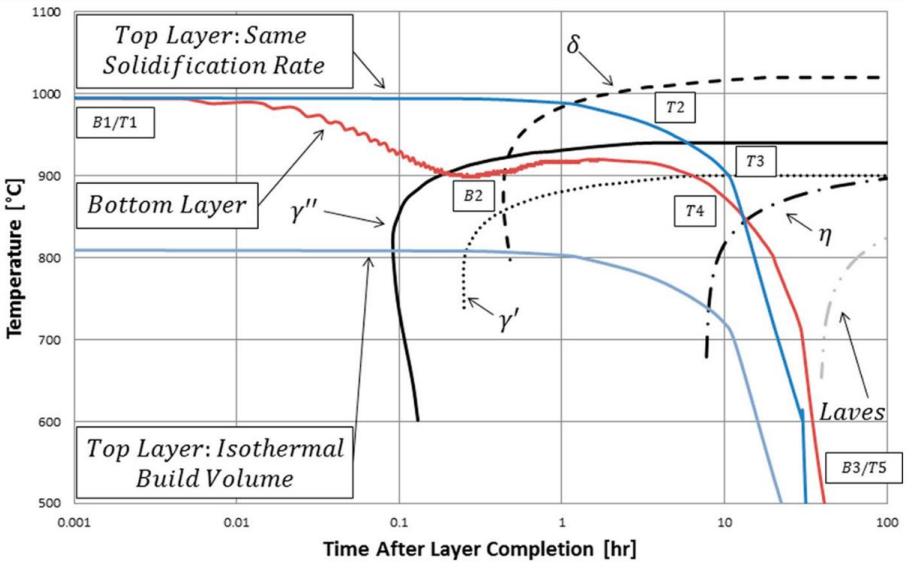

Figure 3.22 Temperature distribution in printed structure by CCT diagrams and phase change(Sames *et al.*, 2016)

However, increasing laser power may produce a heterogeneous microstructure where thermal stress can trigger a defect such as grain boundary cracking and phase change, which could reduce the magnetic properties. The rate of solidification (liquid to solid state) has been discussed in Fig. 3.22 (Sames *et al.*, 2016) which shows temperature difference in the top layer and bottom layer. This produces a difference in the phase change as the material is cooled after melt, which explains residual stress within the structure. Therefore, a balance of scan speed and laser power is needed to reduce thermal stress.

Fig. 3.23 (Elhajjar, Law and Pegoretti, 2018) shows how the shape of the magnetic powders has an effect on the magnetostriction constant. The flake shaped magnetic powders show better magnetostriction constant as they have better packing density than the spherical or granular shaped powders. In (Na, Galuardi and Flatau, 2017), they show how larger the size of a galfenol (FeGa) powder has larger saturation magnetisation compared to the smaller sizes. In contrast, a paper by (Jones *et al.*, 2018) discusses that large grains are good for magnetostriction but highly textured materials are needed to improve mechanical strength. Therefore, there needs to be a balance between the powder size and strength of the material.

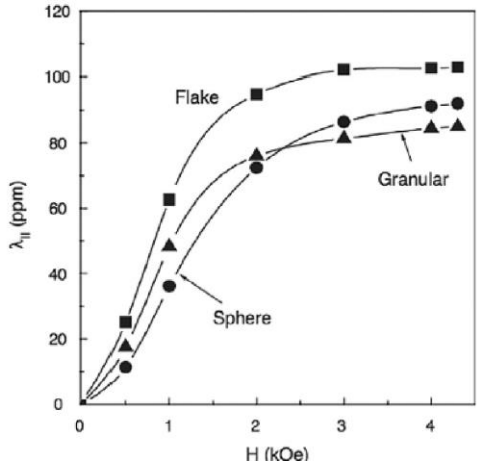

Figure 3.23 Shape of magnetostrictive FeCo powder
(Elhajjar, Law and Pegoretti, 2018)

To reduce the amount of pores within the print, a sintering method is used. Sintering can improve the density of the material as temperature and pressure reduces any air/pores inside and increases the size of the grains by diffusion (mass transport) as seen in Fig. 3.24 (Al-Qudsi *et al.*, 2014). As pores are reduced, the print undergoes shrinkage (Sames *et al.*, 2016). The shrinkage results in 10 to 20% reduction in size (depending on the geometry) (Nandakumar, 2019). As pores are removed, this could produce warping or sagging in non-uniform structures. Therefore, the final result could produce a

structure that is geometrically different to the initial final design. This needs to be taken into account before printing. Therefore, controlling post-processing parameters are important to avoid inaccurate dimensions and damage to the structure after printing.

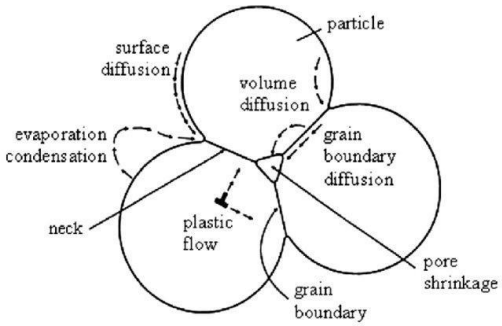

Figure 3.24 Solid state sintering method on powders(Al-Qudsi *et al.*, 2014)

Sintering parameters such as temperature and the environment type can affect the magnetic properties (Mostafaei *et al.*, 2017). Environments such as vacuum instead of argon can change the magnetic properties. In (Páez-Pavón *et al.*, 2017), they show that the effect of the sintering process on magnetic field or hardness depends on the type of atmosphere. The paper shows that hydrogen as an atmosphere in the sintering process produced the best sintered product for FeSi soft magnets. However, this depends on the type of material for example, Fe_6Si sintered best in vacuum conditions because it reduces the existing oxides in the material therefore reducing density. The time and temperature also affects the magnetic properties, which agrees with (Nandakumar, 2019) as shown in Fig. 3.25. Longer times below the melting temperature gives better density.

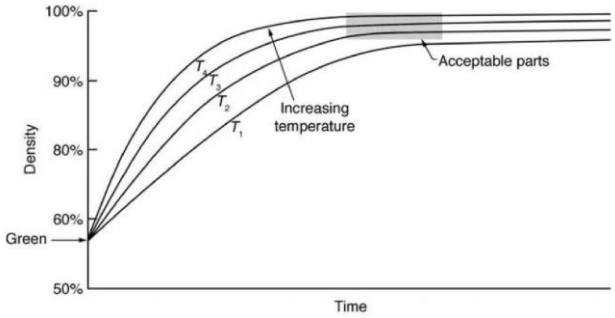

Figure 3.25 effect of time of sintering and density of final material(Nandakumar, 2019)

The material composition can affect the magnetic properties of the material, such as saturation magnetisation and anisotropy in the material. High entropy alloys contain 5 or more elements with one

base element, this is more commonly present in soft magnetic materials. This is because the elements provide stability while maintaining low coercivity, high magnetisation saturation and other properties such as mechanical and structural stability. However, the manufacturing method is important and sometimes need different composition to produce a structure. For example, in metal extrusion printing, a polymer must be used as part of the printing process in order to extrude and print the structure. In (Khatri *et al.*, 2018), they explored the effect of infill percentage of the polymer in stainless steel 17-4ph in metal extrusion. As acrylonitrile butadiene styrene (ABS) was used as a binder to extrude the metal, the effect of increasing the polymer binder on magnetic properties was explored. It was found that an increase of acrylonitrile butadiene styrene (ABS) reduced the saturation magnetisation as seen in Fig. 3.26 (Khatri *et al.*, 2018), this is because the polymer is a diamagnetic.

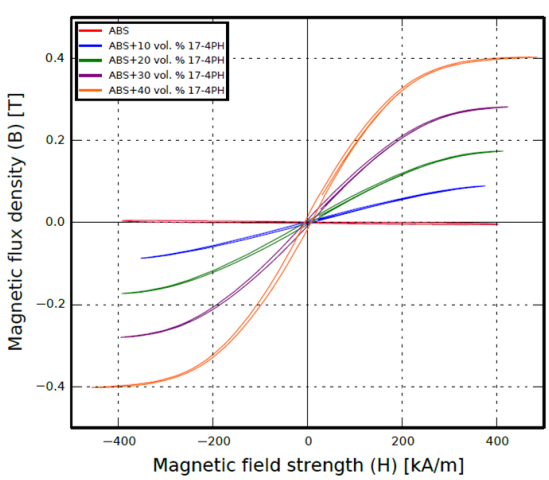

Figure 3.26 Effect of polymer percentage in magnetic properties in extrusion printing (Khatri *et al.*, 2018)

Directional magnetisation (anisotropy) is important for magnetostrictive sensors as strain can be produced in a certain direction as seen in Fig. 3.27 (Périgo *et al.*, 2019). In (Patton *et al.*, 2019), they explore the effect of shape of as-printed design by the extrusion process and the effect it has on magnetisation. It is understood that shape anisotropy has an effect on the direction of magnetisation, depending on the print direction. It is reported for a number of printers (DED, extrusion and material jetting) that printing parameters can affect the anisotropy. For example, in (Song *et al.*, 2014; Mikler *et al.*, 2017; Jones *et al.*, 2018; Zou *et al.*, 2018; Al-Milaji *et al.*, 2019; Patton *et al.*, 2019) have reported parameters that include the vector speed, direction, laser power and nozzle temperature. The vector speed limits the time and duration of raising the temperature or applying the raw material for printing. For example, in laser melting the time spent over a material will risk going above or below the material's T_m point, which would risk structural stability of the print and increasing pores. Direction of printing is important for layering and spacing between the tracks (hatch spacing) to avoid excessive rise in temperature such as the heat affected zone (HAZ). Direction can affect the anisotropy of the structure as the gaps between the tracks can influence the directionality of the material due to shape anisotropy

for each track. Laser power is directly proportional to the laser speed as increasing the speed, higher laser power is needed whereas reducing the speed a reduction in laser power is needed to melt the material in SLM printing. Nozzle temperature applies to extrusion printing, where temperature of the nozzle is needed to sufficiently extrude the polymer/ metal mixture, as it is important not to completely melt the print or clog the material in the nozzle.

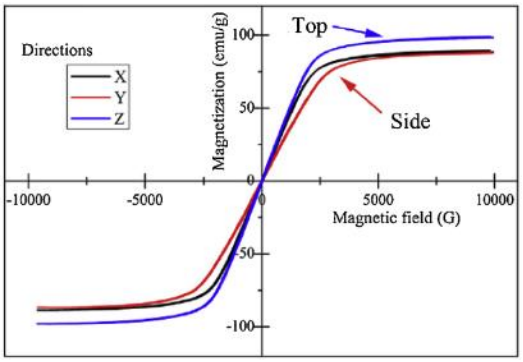

Figure 3.27 Hysteresis loops of Fe-Ni-Si alloy SLM printed structure showing anisotropy in top and side directions (Périgo *et al.*, 2019)

3.5 Inkjet printing

Magnetic materials for inkjet printing is a new area of research which requires careful consideration into the factors for inkjet printing as shown in Fig. 3.28 (Grabham, Beeby and White, 2001; Andò and Marletta, 2016; Raut and Al-Shamery, 2018):

1. Ink precursor
2. Droplet formation
3. Substrate material
4. Printing pattern
5. Post printing treatments

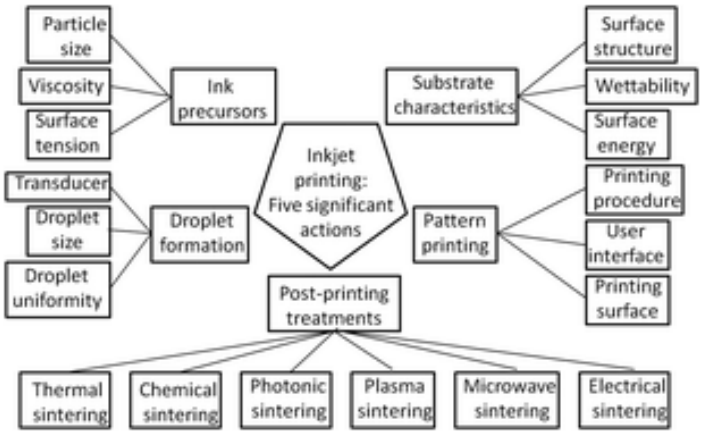

Figure 3.28 Factors for inkjet printing (Raut and Al-Shamery, 2018)

All of these factors affect each other. For example, if an ink precursor needs to be cured at a certain temperature then the post treatment and substrate needs to be chosen carefully. Likewise, if a pattern needs to be a certain size then the droplet size and jetting needs to be aligned to follow the pattern.

3.5.1 Ink precursor

Metallic inks usually consist of mostly solvent with small amounts of pure metal materials. Additives are added such as organic additives to prevent metal particles from touching and to maintain the shape and size of the particles (Tan *et al.*, 2019). The solvents used are typically water or alcohol based. One of the most important properties of the inks for inkjet printing is the viscosity to prevent clogging in the system. Therefore, the solvent and metal composition need to be mixed well to avoid clumps and maintain low viscosity. It is important to filter the inks before printing as the inks could cause aggregation, which can cause clogging in the inkjet printer (Salaoru, Maswoud and Paul, 2019). Equation 3.5 shows the Z number which determines printability of the inks (Zhang *et al.*, 2016; Liu and Derby, 2019) .

Equation 3.5 Printability of inks

$$Z = \frac{\sqrt{\rho d_o \gamma_t}}{\mu_v} \quad (3.5)$$

Where ρ is density, d_o is the orifice diameter, γ_t is the surface tension of the ink and μ_v is the viscosity of the ink. The ink needs a Z number to be between 1 to 10 in order to be printable.

Particle size and shape determines the viscosity and properties of the metal ink. It is desirable to have the smallest metal particles possible to improve viscosity and avoid clogging in the inkjet printing

system. However, the metal particle size negatively affects the melting temperature of the bulk metal as shown in Fig. 3.29 (Raut and Al-Shamery, 2018), as the particle size drops below 5 nm the melting temperature of the bulk metal, in this case gold, drops significantly.

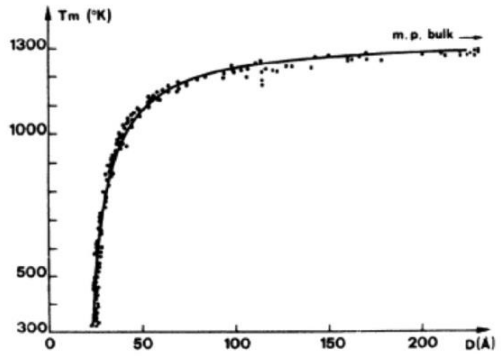

Figure 3.29 Particle size of gold and effects on melting temperature (Raut and Al-Shamery, 2018)

The metal based materials can be in the form of nanoparticles (NP), metal-organic decomposition (MOD), catalyst or reaction inks. Each has differences in printability such as sintering temperature to solvent composition as shown in table 3.8 (Chen *et al.*, 2015).

Table 3.8 Ink type characteristics

Metallic ink types	**Sintering temp (^{0}C)**	**Ink stability (clogging)**	**Solvent composition**	**Thickness control**
Nanoparticle	>150	Poor	Multiple	Deposition layers
MOD	70~130	Good	Binary	Deposition layers
Catalyst	25~100	Excellent	Single	Reaction times
Reaction inkjet	21	Excellent	Single	Reaction concentrations

NP are most commonly used to print metals such as copper or gold as they have high electrical conductivity at lower price compared to other ink types. However, the ink's non-electrical conductive solvent needs to be evaporated at elevated temperature (100 to 200^{0}C), therefore substrate selection is limited. MOD are metal salts dissolved in organic solvent, where the metal salts decompose during curing or heating, leaving conductive metal materials on the substrate. MOD have lower curing and sintering temperature than NP inks however MOD have complicated steps to synthesize the inks in the

first place. The catalyst ink method involves printing catalytic metal particles onto a substrate and then transferring the print to an electroless plating bath to form solid metal. For example, to print copper lines by catalyst method, palladium ions are printed and then copper is electroless plated in a bath to form conductive copper lines. The reaction ink system uses a redox reaction of two inks, one a reduction ink and the other is metal ink which is printed separately on each other. A redox reaction occurs which leaves metal material on the substrate at room temperature. However, there are issues in precision printing and mixing of the two inks.

3.5.2 Jetting via inkjet printer

Once a precursor ink is identified and compatible with the metal NP, then it can be stored in the inkjet printer storage compartment. The ink is then pumped into the nozzle chamber where it is pushed out by an actuator or transducer. There are two types of printer, continuous and drop-on-demand (DOD) inkjet printing as seen in Fig. 3.30 (Raut and Al-Shamery, 2018).

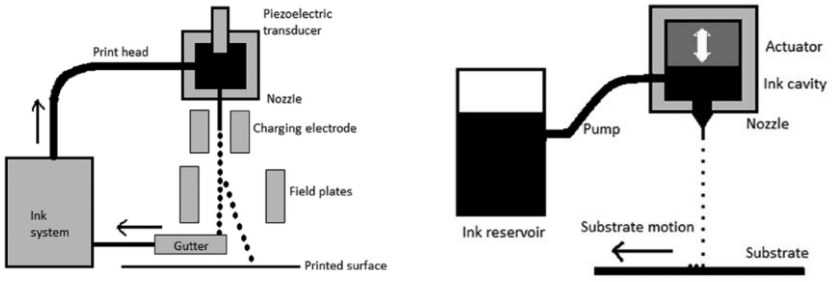

Figure 3.30 Inkjet system continuous and drop on demand (DOD) (left to right) (Raut and Al-Shamery, 2018)

Continuous printing applies a charge to the ink as it leaves the nozzle using electrodes, the inks are then deflected by field plates to the substrate. The inks that are not deflected away are recycled into the ink storage. DOD system does not recycle ink, instead it is printed directly on to the substrate.

However, the ink needs to be compatible for each type of printer, for example, table 3.9 (Liu *et al.*, 2015) shows that for continuous and DOD (thermal and piezoelectric) printer the viscosity and surface tension needs to be within a certain range in order to print and avoid clogging or to obtain high quality print.

Table 3.9 Ink requirement for each printer type (Liu *et al.*, 2015)

Printer type	**Particle size (µm)**	**Viscosity (cP)**	**Surface tension (γ_t)**	**Density (g/cm^3)**
Continuous	<1	1-10	25-70	~1
Thermal	<1	5-30	35-70	~1
Piezoelectric	<1	1-20	35-70	~1

3.5.3 Substrate and droplet formation

Substrate materials available for inkjet printing are polymers (such as kapton, PET and PVC), paper (such as photo paper) and glass (Nayak *et al.*, 2019)(Raut and Al-Shamery, 2018). Printing on metal is also popular, for example, ink can be printed on aluminium, copper or silver. However, this depends on the oxidation, as copper oxidises in air, therefore it needs to be either coated or prepared first before printing. The substrate selection also depends on the compatibility to print for example, adhesion between the ink and substrate is essential. The substrate is important to consider, as the ink cannot be printed unless the substrate material forms good wettability and high surface tension during printing.

The surface tension of the ink depends on 3 phases, gas, liquid and solid as seen in Fig. 3.31 (ramé-hart instrument co., 2019). The angle between the liquid and solid phase is a way of measuring the wettability of the liquid on to the surface. The angle is measured from the surface to the liquid/gas phase. If the angle is above 90 degrees, then there is no wetting involved (hydrophobic) or no surface tension between the liquid/solid phases. Below 90 degrees then there is too much wetting involved (hydrophilic) which would have high surface tension. Equation 3.6 describes the surface energy between the solid and liquid also known as the Young's equation.

Equation 3.6 Wetting angle equation

$$\gamma_{sv} = \gamma_{ls} + \gamma_{lv} \cos \theta_c \qquad (3.6)$$

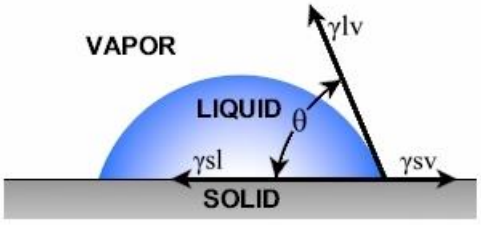

Figure 3.31 Wetting angle diagram (ramé-hart instrument co., 2019)

Where γ_{sv} is the solid/ vapour surface free energy, γ_{ls} is the liquid/ solid surface tension, γ_{lv} is the liquid/ vapour surface tension and θ_c is the contact angle.

Adhesion between the substrate and ink can be further improved as discussed in (Raut and Al-Shamery, 2018) where a layer of adhesive agent such as Ethyl cellulose dissolved in 1-methyl 2-pyrrolidone, was applied to a glass substrate to form copper electrode coating. Another example is the addition of a promoter within the ink. 1 wt% 3-amino propyl trimethoxy silane (APS) was used as an adhesion promoter in the copper ink, therefore forming a hybrid link between substrates such as polyimide.

Fig. 3.32 taken from (Singh *et al.*, 2010) shows droplet formation by solvent evaporation on the substrate. They have shown the dynamics of how evaporation occurs within the droplet on the substrate. Convective flow and Marangoni flow distributes the NP and solvent towards the edges. This allows solvent to be evaporated at the edges and nucleation of the NP, which leaves a gap or pores in the middle of the droplet. This could be an issue when trying to achieve a homogeneous print structure.

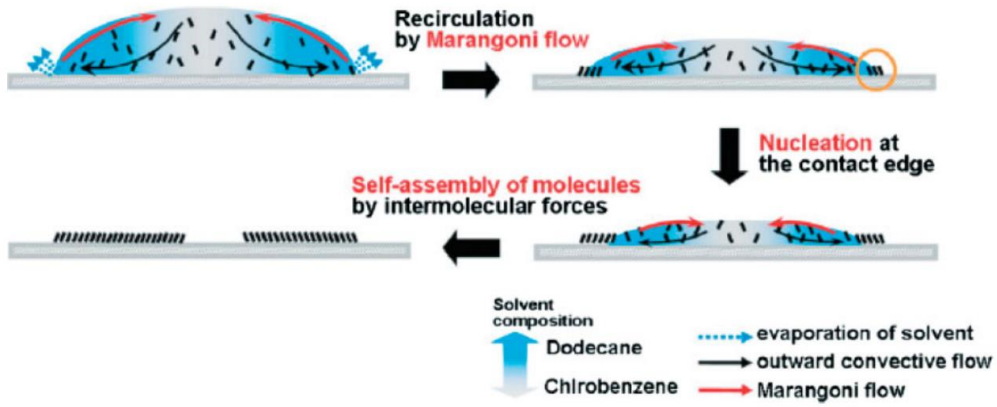

Figure 3.32 Droplet formation on the substrate (Singh *et al.*, 2010)

3.5.4 Additive layering

Additive layering of inks has been a hot topic in the area of inkjet printing. Printing successive ink NP on top of each other to increase thickness and metal NP. For magnetic NP, it may be attractive to print (depending on the material) to increase the magnetisation or anisotropy of the structure. Composite printing has generated a large interest as printing multiple materials over each other can enhance properties as shown in (Pasquarelli, Curtis and Hest, 2008) where they have printed gold NP over nickel NP to improve adhesion and as a diffusion barrier. Another example is by printing copper where it is useful in electronic applications however pure copper is vulnerable to oxidation in air, therefore nickel ink can be printed over the copper to prevent corrosion as passivation layer as shown in (Tan *et al.*,

2019). In (Saleh *et al.*, 2017), they have shown composite printing of magnetic NP on electroactive substrate to form a structure for electromagnetic application.

Further comparisons of 2D and 3D inkjet printing have been made in (Zub, Hoeppener and Schubert, 2022) where they explored the advantage and issues in 3D printing. Issues such as wetting angle of each ink and evaporation of solvent can influence the adhesion for layering composite. Sufficient drying or UV curing of each layer is needed which could be a disadvantage for composites manufacturing using inkjet printing systems (depending on the thickness). Subsequent layering would cause porosity to the layer underneath due to addition of solvent, therefore evaporation would need to be controlled during the printing process. However, issues can be resolved which makes composite inkjet printing attractive in the future.

3.5.5 Post printing treatments

Post printing treatment includes curing and sintering of the inks. After printing the solvent used as part of the inks are no longer desirable therefore the metal density is important. The first step is to evaporate the solvent that is left in the print. Solvent evaporation (thermal) is an essential part of curing the inks to leave the metal base material on the substrate. The temperature and time for the solvent to evaporate is critical as the rate of evaporation depends on this. For example, in Fig. 3.33 (Zhang *et al.*, 2016) shows for N-Methyl-2-pyrrolidone (NMP) the rate of evaporation. At higher temperature such as 200 °C the rate of evaporation increases than a temperature of 140 °C.

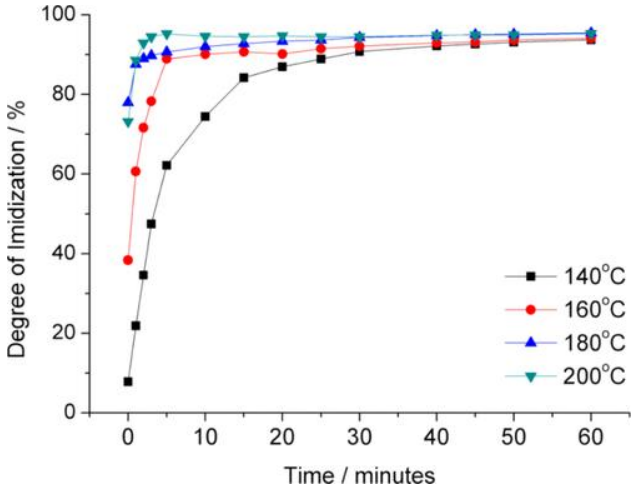

Figure 3.33 NMP evaporation rate (Zhang *et al.*, 2016)

In (Zhang *et al.*, 2016) they show that curing at a lower temperature than the evaporation temperature of the solvent means that the solvent is not fully evaporated. This can affect the desired properties of the metal such as electrical conduction or magnetisation. The print pattern could be affected if the solvent evaporation temperature is low. For example, a drop of ink as discussed in (Chen *et al.*, 2015;

Zhang *et al.*, 2016; Al-Milaji *et al.*, 2019; Nayak *et al.*, 2019) can cause the imbibition of metal particles to the substrate on the edges higher than the centre of the ink, this is known as the coffee ring effect.

In (Wünscher *et al.*, 2014), they explored different ways of curing and sintering inks on flexible polymer substrates other than the traditional oven. These are chemical, electrical, plasma, photonic and microwave sintering. Depending on the solvent, many of the polymers such as PP are not suitable due to their low glass transition and melting temperatures. For example, NMP solvent as discussed previously requires solvent evaporation temperature at around 160 degrees whereas PP would melt at that temperature. They have shown that polyimide (kapton) can withstand higher temperatures while being more flexible than most polymer substrates and providing better electrical conductivity than other materials such as paper. Intense pulsed light (IPL) sintering was found to be more desirable however this depends on the ink and substrate.

3.5.6 Printing magnetic materials

Printing magnetic materials by inkjet printing is achievable however there are certain factors that could influence the base metal which are(Song *et al.*, 2014; Raut and Al-Shamery, 2018):

- Nozzle and droplets
- Alignment of moments
- Magnetic and non-magnetic printing

Magnetic inks can form long liquid bridges from the nozzle which makes the DOD system difficult to print with magnetic inks. The inkjet system uses piezoelectric actuator to push inks from the ink chamber to the nozzle therefore controlling the amount of drops to the substrate. However in (Raut and Al-Shamery, 2018) mentioned that magnetic inks could be pushed by a magnetic field instead of an actuator or any mechanical device. This would mean controlling the magnetic particles further by ensuring each drop contains magnetic metal particles and breaking the bridge with the drop to the nozzle, which could improve densification and further control of the droplets.

Magnetic alignment has also been studied in the literature (Song *et al.*, 2014), which investigates alignment by 3D printing square and circular magnetic material using an inkjet printer as shown in Fig. 3.34 and 3.35. It was shown that hysteresis loss can be decreased when moments are aligned as shown in Fig. 3.35.

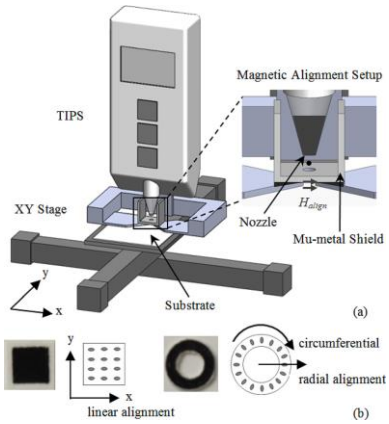

Figure 3.34 Magnetic shielding for inkjet printing(Song *et al.*, 2014)

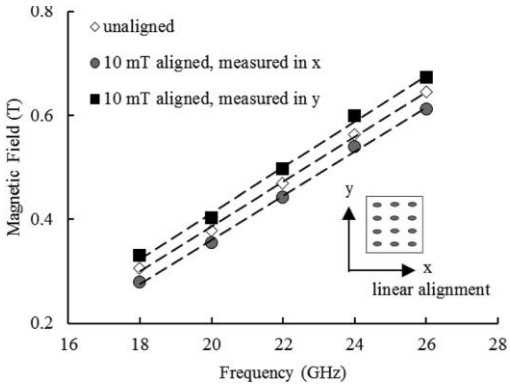

Figure 3.35 Magnetic alignment in inject printed samples(Song *et al.*, 2014)

Magnetic materials have an influence on printing inks with low viscosity. For example, in- the presence of a field, the NP can be orientated and cover more area as shown in Fig. 3.36 (Al-Milaji *et al.*, 2019). The coffee ring effect, which causes materials to form on the edges, can be reduced by applying a field to the base. The coffee ring occurs by the substrate and liquid interface upon solvent evaporation. Therefore, the field disrupts the flow of NP along the edges and increases the NP distribution across the droplet on the substrate.

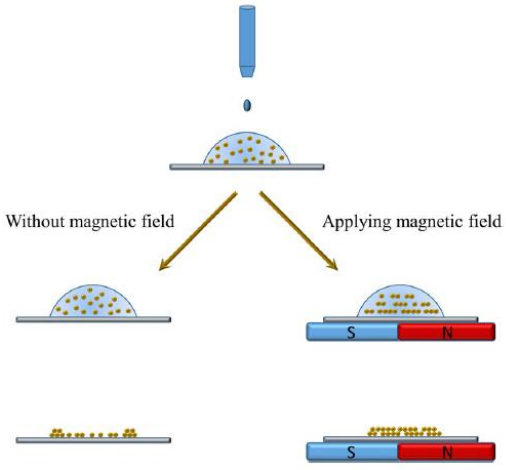

Figure 3.36 Ferromagnetic ink jetting with and without applied magnetic field (Al-Milaji *et al.*, 2019)

Thick film magnetostrictive material has been produced and measured by (Grabham, Beeby and White, 2001). They have produced a paste containing Terfenol-D and glass frit and printed by screen printing.

By measuring magnetostriction as shown in Fig. 3.37, they reported that it has a lower magnetostriction constant than bulk materials due to void formation in the thick film.

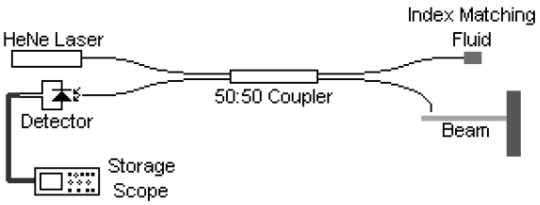

Figure 3.37 Thick film magnetostriction measurement from (Grabham, Beeby and White, 2001)

Nickel and magnetite are soft magnetic materials (Ferromagnetic) that can be used for printing magnetostrictive sensors. In literature, nickel and magnetite NP has been used and successfully printed/ deposited by (Cabrera *et al.*, 2008; Pasquarelli, Curtis and Hest, 2008; Li *et al.*, 2009; Tiberto *et al.*, 2013; Marjanović *et al.*, 2014; Park and Kim, 2014; Altay, 2018; Vaseem *et al.*, 2018; Raut and Al-Shamery, 2018; Kolchanov *et al.*, 2019; Tan *et al.*, 2019). Although nickel and magnetite has been shown to be printable, there has been issues with ink synthesis, droplet formation, substrate and post printing treatment as discussed in sections 3.51, 3.52, 3.53 and 3.54 respectively.

There are various ways to synthesise magnetite and nickel ink such as additives, sol gel and solvents to improve printing and post printing process. The substrate plays a key role in retaining the NP and evaporating the solvent. In (Pasquarelli, Curtis and Hest, 2008) they have shown that nickel can be printed on glass slides using a Dimatix Materials Printer inkjet system for electronics application. The nickel inks printed, were preheated to 140 ℃ on a hotplate and then heated to 180 degrees after printing to avoid wetting and to sufficiently evaporate the solvent. However, glass as a substrate material cannot be used as a magnetostrictive sensor as there needs to be greater flexibility in the substrate. Polymer materials can be used to print nickel ink however there are limitations for example, in (Altay, 2018) they show that the PET substrate material caused shrinkage and blistering problems when curing nickel inks. Kapton film could be used as the melting point for kapton is around 400 °C, well above the curing temperature of nickel. In (Park and Kim, 2014) it has been shown that nickel ink (with ethanol solvent) can be printed on kapton and cured on a hot plate for 150 °C for 20 min and then flash light sintered.

In (Vaseem *et al.*, 2018) they have printed magnetite via inkjet printing on sacrificial paper to produce a turntable actuator and explored the effect of synthesising of magnetite solvent to form a photo curable ink such as oleic acid. Polymeric resin is used to strengthen and form bond between magnetite NP. The magnetic properties at RT were measured for both magnetite in original and with polymeric resin (UV cured). It was shown that the polymeric resin reduced the magnetic properties Ms slightly, which is due to the higher level of non-magnetic material within the print. In (Tiberto *et al.*, 2013) they explored the

effect of printing magnetite on paper by changing the jetting (piezoelectric or thermal), temperature of print and size of magnetite NP. The magnetic properties remain unchanged for both piezoelectric and thermal print heads. In (Marjanović *et al.*, 2014), they produced inkjet-printed magnetite inductor core on paper at RT and polyimide (sintered at 300 degrees) by Jetlab IV by Microfab. Oleic acid was used to cover the ink and was treated with potassium hydroxide. Aggregation in some areas were formed however the print was successful on both paper and polyimide.

4 Methodology

4.1 Introduction

This chapter describes the experimental methods and techniques used for modelling the strain by bending and impact testing, printing using desktop and inkjet systems, manufacturing the CFRP, characterisation of the elements and microstructure using (SEM/EDS and FTIR) and measurement of the magnetoelastic effects for steel, nickel and magnetite soft magnetic materials. Modelling and simulating the magnetoelastic effects is important to verify the experimental work and calculated results, in order to provide meaningful results. COMSOL multiphysics is a well-known software package and was used to design and model the magnetoelastic effects. Extrusion and inkjet printing methods for a range of materials were explored in this project. For extrusion printing the different stages included as-received (AR), as-printed (AP) and sintered steel (SS). For inkjet printing the printing process included pre-processing of raw materials, generating CAD designs, outline the printing parameters used and post processing such as heat treatment and coating. CFRP pre pegged sheets purchased from SHD Ltd, were stacked, layered and cured to perform SHM analysis for detecting damages from bending and impact testing. Physical and chemical characterisation allows broader understanding of the material's behaviour during or after processing. Structural and chemical characterisation techniques were used to determine the morphology and the chemical structure of the material before and after printing. Magnetic properties such as saturation magnetisation, coercive force and remanence were important to identify and quantify the dynamics of the magnetisation in the material. There are various ways in which the magnetostriction could be measured as shown in the literature, however due to the surface and printed structure, two different methods were used: strain gauges for the bulk sample and inductance via coil inductor for the printed samples.

4.2 Simulations

4.2.1 COMSOL modelling

Finite element analysis (FEA) simulations for validating the printed designs were performed in the COMSOL 5.6 software. The COMSOL software contained a pre-packaged magnetostriction module, which was utilised within this research. The AC/DC and structural modules were combined to form a multiphysics model for magnetostriction as seen in Fig. 4.1 (Datta, 2013).

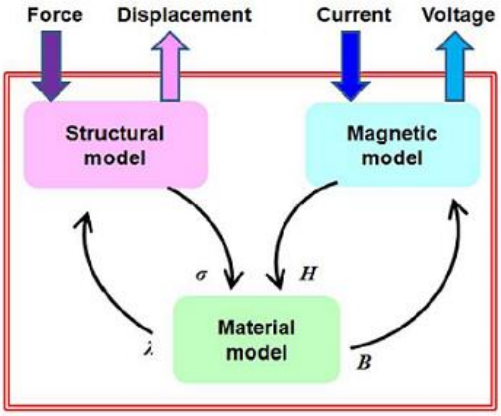

Figure 4.1 COMSOL magnetostriction modelling boundary conditions (Datta, 2013)

The main magnetostrictive calculations used for the magnetic and structural models are shown in the Equation 4.1.1 and 4.1.2. In a simple 1D linear model, magnetostriction can be calculated by the sum of mechanical and magnetic components for magnetic induction and stress/strain as seen in Equation 4.1. From equation 2.3 in the theory chapter 2.1, the permeability (ratio of induction and field) is rearranged to include the relative permeability and piezomagnetic coupling for induction or stiffness matrices and piezomagnetic coupling for strain calculation. This is similar to the Equation 2.14 and 2.15 for Joule and Villari effect in chapter 2.3.1, where the change in temperature can be ignored when at constant room temperature. Equation 4.2 contains the magnetostriction constant for a polycrystalline material and saturation values, replacing the piezomagnetic coupling in the 1D model. The first Equation 4.2.1 is for the isotropic model and the second Equation 4.2.2 is the cubic equation where the magnetostriction for the easy and hard directions are defined. Equation 4.2.3 accounts for the magnetisation vector (M/M_s) where domains are orientated in an applied field H.

Equation 4.1 Linear model in stress (1) and strain (2) relation

$$\begin{aligned} S &= c_H \varepsilon - e_{HS}^T H \\ B &= e_{HS} \varepsilon_{el} + \mu_0 \mu_{rS} H \end{aligned} \qquad (4.1.1)$$

$$\begin{aligned} \varepsilon &= s_H S + d_{HT}^T H \\ B &= d_{HT} S + \mu_0 \mu_{rT} H \end{aligned} \qquad (4.1.2)$$

Equation 4.2 Villari effect model in Isotropic (4.2.1) and cubic crystal (4.2.2) magnetoelastic equation where M is magnetisation shown in (4.2.3) and Langevin function in (4.2.4) and (4.2.5)

$$H_{eff} = H + \frac{3\lambda_S}{\mu_0 M_S^2} S_{ed} M \qquad (4.2.1)$$

$$H_{eff} = H + \frac{3}{\mu_0 M_s^2}\left[\lambda_{100} S_{ed} + (\lambda_{111} - \lambda_{100})\sum_{i \neq j} (S_{ed})_{ij} (e_i \otimes e_j)\right] M \qquad (4.2.2)$$

$$M = M_S L(|H_{eff}|)\frac{H_{eff}}{|H_{eff}|} \qquad (4.2.3)$$

$$\text{Where } L(x) = \coth(x) - \frac{1}{x} \qquad (4.2.4)$$

$$\therefore L = \coth\frac{^3\chi_m |H_{eff}|}{M_s} - \frac{M_s}{^3\chi_m |H_{eff}|} \qquad (4.2.5)$$

Where B is magnetic induction, μ_0 is permeability of free space, μ_r is the relative permeability, M_s is saturation magnetisation, λ_{100}/ λ_{111} are the magnetocrystalline axis, e is the elastic constant, H is the magnetic field, S_{ed} is the devatonic stress/strain relation, e_{HS} d_{HT} is the piezomagnetic coupling, C_H/S_H are the stiffness matrices, λ_s is the saturation magnetostriction, χ_m is the magnetic susceptibility and L is the Langevin function. For modelling linear and non-linear magnetostriction, COMSOL gives 3 ways to model the simulation. One is the linear model where the magnetisation will not reach saturation, the non-linear model are hyperbolic tangent and Langevin function. The Langevin function can be used to model the magnetisation and in high field or high temperature region for paramagnetic materials. The Langevin function forms the anhysteretic magnetization model as seen in Eq 4.2.4. Based on the model the material's saturation and susceptibility function approximates the magnetisation in Eq 4.2.3.

The procedures for creating a model and simulation in COMSOL are listed below.

1. Build a CAD model by using Ansys space claim and import to COMSOL as an STL file
2. Apply material properties to the model
3. Create analysis model (multiphysics model or isotropic)

4. Apply constraints and boundary conditions

5. Generate nodes/ meshing

6. Review/ plot results

By creating the model in COMSOL, there are few differences in the method between the experimental method and the model to perform magneto-mechanical testing. The model is designed to simulate close to the real values however in steps 4 and 5 there are constraints where the simulation is unable to simulate close to the real values.

In Step 4, applying constraints and boundary conditions to the model for example applying or randomising the magnetic field is restricted, COMSOL requires the magnetisation to align in a certain direction when applying strain to the magnetic material. Randomly orientated magnetisations or fields cannot be used in COMSOL as it requires the direction of magnetisation or field to lie in X, Y, Z components. When force is applied in the model, COMSOL requires the model to apply constraints and boundary conditions such as fixed points so that the model does not move to avoid inaccuracies. Whereas bending the material in an experimental method does not require the substrate to be fixed. This could cause an additional stress or strain at the fixed point.

Step 5 is used to generate nodes and meshing, which is an important step to increase accuracy of the model. Each node calculates the equation depending on the node's location in the model. Each element generates an average of 3 or more nodes. Therefore, the higher the number of nodes in the model the more accurate the result will be

4.2.1.1 Desktop print simulation

The simulations performed were to compare designs for magnetic and structural properties i.e. magnetic flux, stress and strain against experiment data. The designs were changed to compare and contrast the effect of the change in strain for each design. A simple grid design as seen in Fig. 4.2, was made to measure the effect of changing track distances from 5 mm to 3 mm, to compare the strain and magnetic field changes. The 1.5 mm track gap model required increased computation and time to solve due to smaller element sizes thus increasing the number of calculations. Therefore, a solid block (30 x 30 x 2 mm) was used to replace the 1.5 mm track design to increase the element size and keep the model simple.

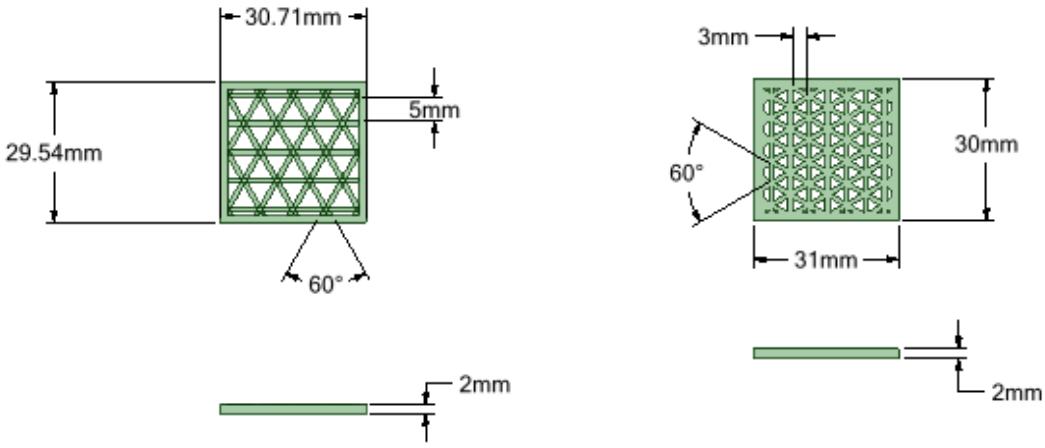

Figure 4.2 Dimensions for 5mm (left) and 3mm (right) track gap CAD model

A mesh was required to form the elements and node for each CAD design. The type of mesh used was tetrahedral with normal physics controlled size. In Fig. 4.3 (a) shows the result of the mesh convergence for the gird model. The predefined element size for maximum and minimum sizes are 5 mm and 0.9 mm respectively.

The desktop printed model was simulated in an air environment with force applied in the Z direction, constraint (cantilever) and field of 10 A/m in the X direction are applied as shown in Fig. 4.3 (b). The model was performed in steady state, when equilibrium is reached.

a

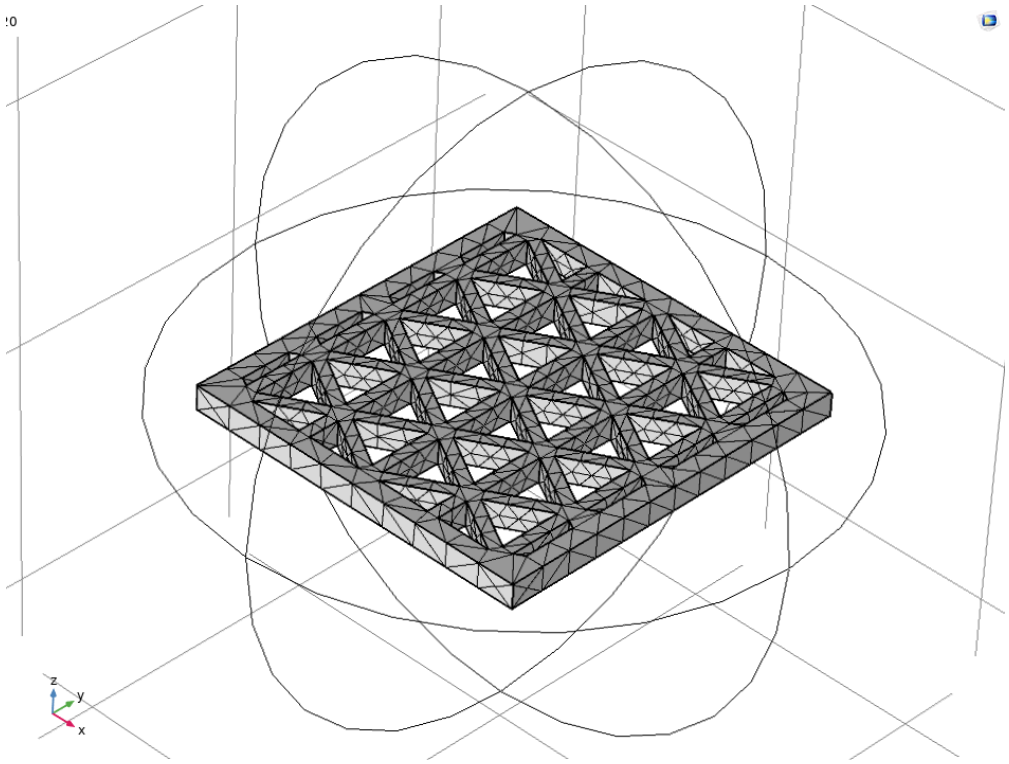

b

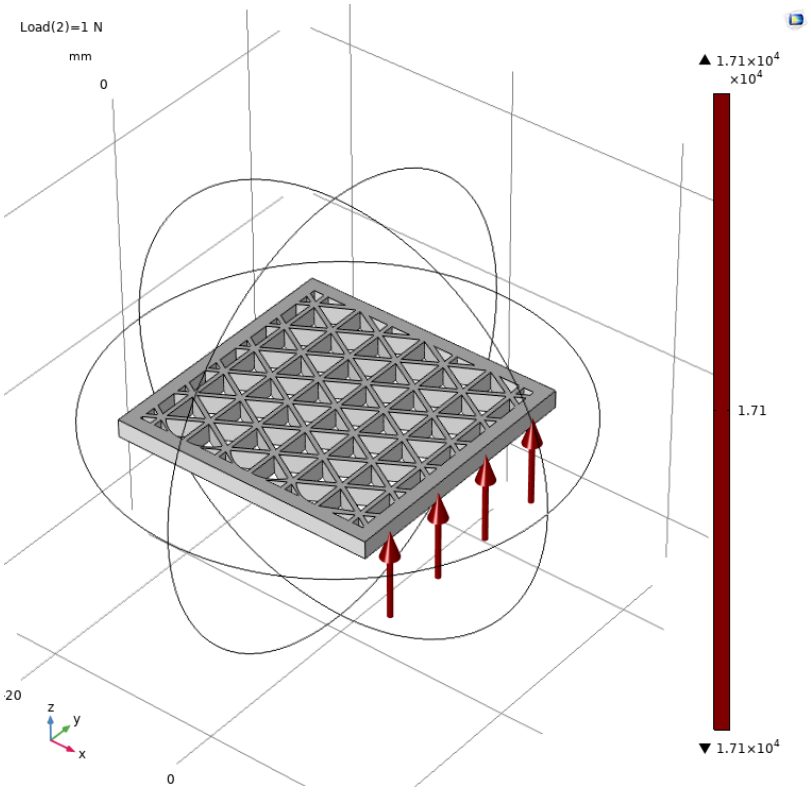

Figure 4.3 COMSOL design model showing (a) tetrahedral meshing convergence and (b)force applied in Z direction of the grid structure in air

The material used was Stainless Steel 405 Annealed and the properties were based on the COMSOL database. The properties were then adjusted for stainless steel 17/4 ph as seen in Table 4.1, where published values of steel were used (Bakker, 2013; Benyelloul and Aourag, 2013) for magnetic and mechanical properties.

Table 4.1 Material properties used for modelling stainless steel 17/4 ph

Material property	**Data**
Young's modulus, Pa	$2x10^{11}$
Saturation magnetostriction, λ_s	$1.5x10^{-5}$
Magnetostriction constant 100, λ	$2.5\ x10^{-5}$
Magnetostriction constant 111, λ	$-2.5\ x10^{-5}$
Saturation magnetisation, A/m	$1.5\ x10^{6}$
Elasticity constants c11, Pa	$200\ x10^{9}$
Elasticity constants c12, Pa	$130\ x10^{9}$
Elasticity constants c44, Pa	$110\ x10^{9}$

4.2.1.2 Inkjet printer simulation

Inkjet printing via drop on demand on a substrate can be simulated in COMSOL. The dimensions of each droplet were measured previously from the experimental data. The droplet size and depth is based on the inkjet-printed magnetite on paper. The diameter of each droplet is around 150 µm and the depth of each droplet is around 100 µm as measured using a Nikon light microscope and Bruker contour elite microscope. To simplify the model, the magnetite droplet is based on single layer print rather than multiple layers on top. This model will look at the effect of droplet gap distance and its effect on magnetisation while bending. To model this and the effect of magnetostriction, the same equation and model was used as seen in equation 4.1 and 4.2. The magnetite data for modelling magnetostriction is shown in table 4.2.

Table 4.2 Material properties used for modelling magnetite

Material property	**Data**
Young's modulus, Pa	$2x10^{11}$
Saturation magnetostriction, λ_s	$3.6x10^{-5}$
Magnetostriction constant 100, λ	$-2x10^{-5}$
Magnetostriction constant 111, λ	$8x10^{-5}$
Saturation magnetisation, A/m	$4.7x10^{5}$
Elasticity constants c11, Pa	$273x10^{9}$
Elasticity constants c12, Pa	$106x10^{9}$
Elasticity constants c44, Pa	$97x10^{9}$

In COMSOL, the 2D droplets are fixed to a silicone substrate (no friction or debonding can take place) which has a size of 25 mm x 0.2 mm. Fig. 4.4a shows the component of air, magnetite, substrate and bend rig which was designed in COMSOL. Fig. 4.4b shows the mesh formed as finer mesh and adaptation is needed to model the droplets. Mesh size range from 0.013 mm to 4 mm with regular refinement. A fixed 10 A/m field was applied during the simulation in the X direction for convergence of the model. The force applied varies for each design until the change in magnetisation reaches equilibrium state. At both sides of the substrate the force is gradually applied until there is sufficient contact between the ends of the substrate and the bend rig. Magnetite droplets were placed in the range of -0.2 mm to 0.2 mm with each other on the substrate. Each droplet dimension was based on the microscope analysis as shown as schematic in Fig. 4.5, ranging from small droplets of 0.15 mm x 0.05 mm to larger droplets of 0.3 mm x 0.1 mm. The distance between two droplets refers to the distance from the end of one droplet to the start of the neighbouring droplet. For example, in Fig. 4.6 the distance

between two droplets is 0 mm as the end of the first droplets and start of the second droplets are touching therefore, there is no gap or overlap between them. The number of droplets varies to maintain and fill the space above the substrate by leaving a gap of 1 mm or less on each size of the substrate. For example, in 0.1 mm droplet distance design, the number of droplets is 230 whereas in 0.2 mm the number of droplets is reduced to 58 to maintain a filled substrate.

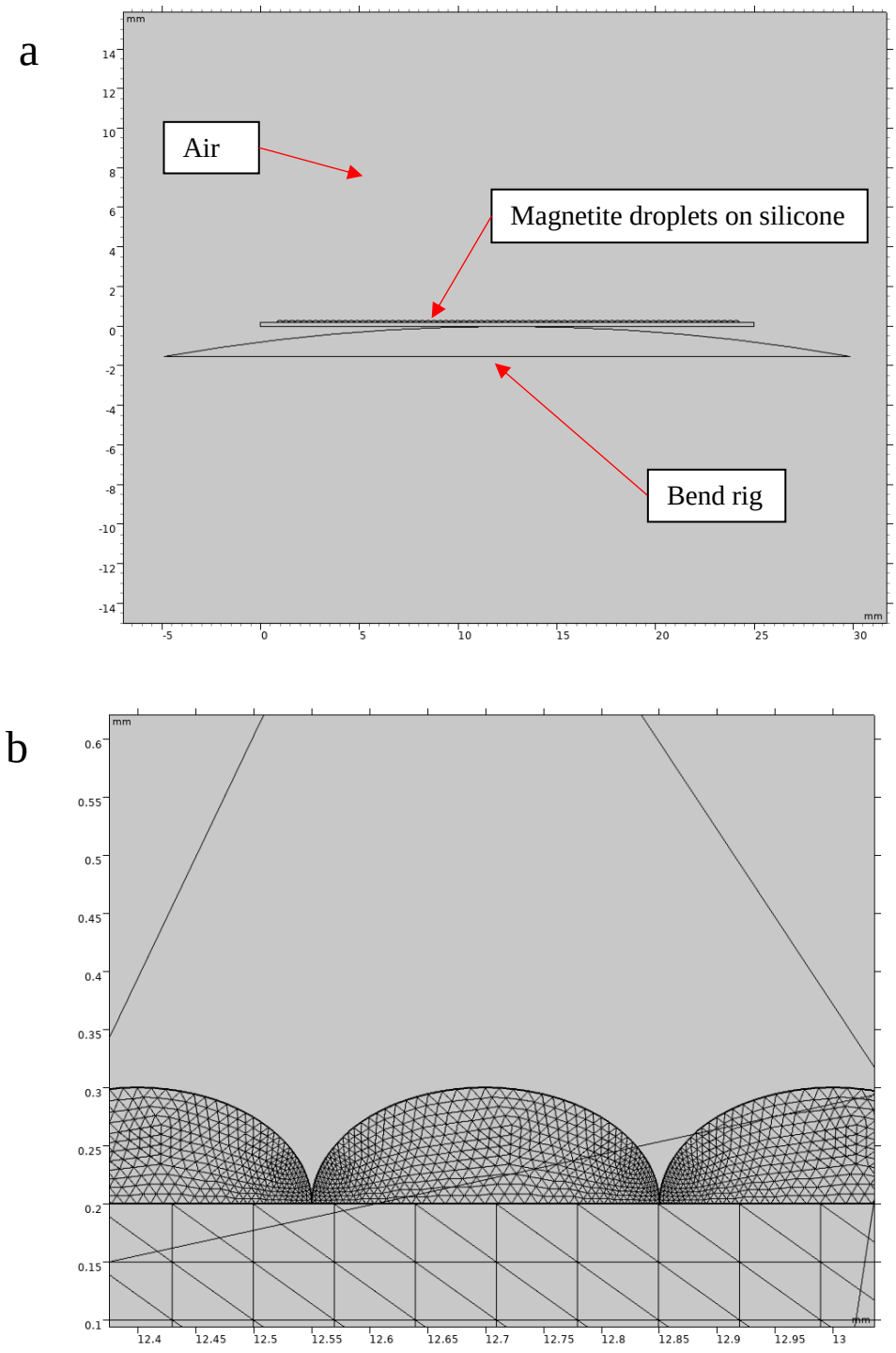

Figure 4.4 (a) COMSOL simulation set up and (b) COMSOL mesh generation

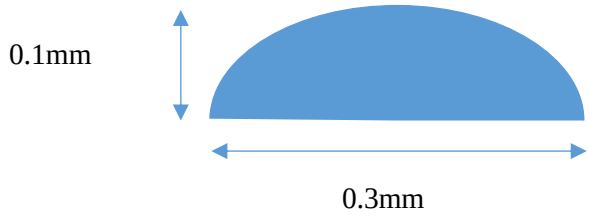

Figure 4.5 Droplet dimensions in COMSOL model based on microscope analysis of magnetite on paper

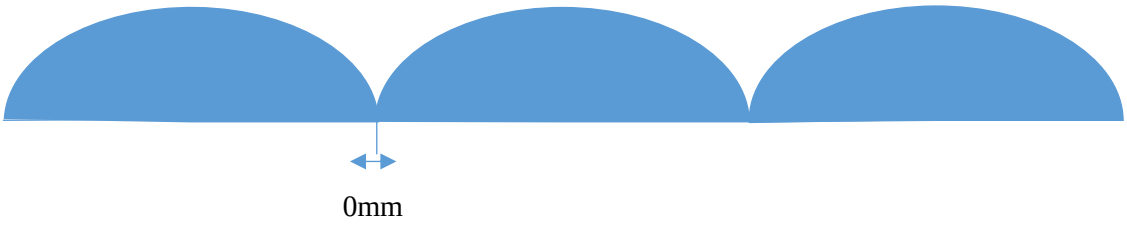

Figure 4.6 Droplet gap distance from 0 mm (touching)

4.2.2 Analytical calculation

The analytical calculation is used alongside COMSOL pre-packaged model and experimental data as a rough estimation, where analytical calculation can be further improved by calculating cubic and anisotropic model, for this project a general value is sufficient to compare whether it fits the COMSOL and experimental data.

Equation 4.3 bending stress in the x direction

$$\sigma_x = \frac{t_s E_{sub}}{2R(1-v_s^2)} \qquad (4.3)$$

Where σ_x is the stress in the X direction, t_s is the thickness of the substrate, E_{sub} is the Young's modulus of the substrate, R is the radius of curvature and v_s is the Poisson ratio of the substrate. A 1D model of a bar was calculated using the linear Equation 4.1. The equation relating to bending used is shown in Equation 4.3. This is a part of the equation used in the COMSOL linear model. The calculations were performed in excel to compare. The strain was previously calculated based on the radius of curvature

for substrate as shown in chapter 4.3 using Equation 4.4. The material properties used in this calculation are the same for the materials used in the COMSOL model. For each bend rig radius of curvature, the maximum strain is calculated and therefore the maximum theoretical magnetic flux density in Tesla was calculated in excel.

4.3 Printing methodology and materials

4.3.1 Desktop metal bound deposition printer

The design to be printed was created within CAD and was converted to an STL file which was then produced by using the desktop metal printer software. A software by Desktop Metal Inc was used to generate a printable model of a 3D block (30 x 30 x 2 mm), based on the CAD in STL file as seen in Fig. 4.7. The software generates the bed and wax supports to prevent failure during printing. The infill tracks are part of the printing process where a solid block in CAD design would have tracks inside the block when printed, to save cost and material. The pre-programmed infill tracks can be adjusted to increase or decrease the density of the block using the software.

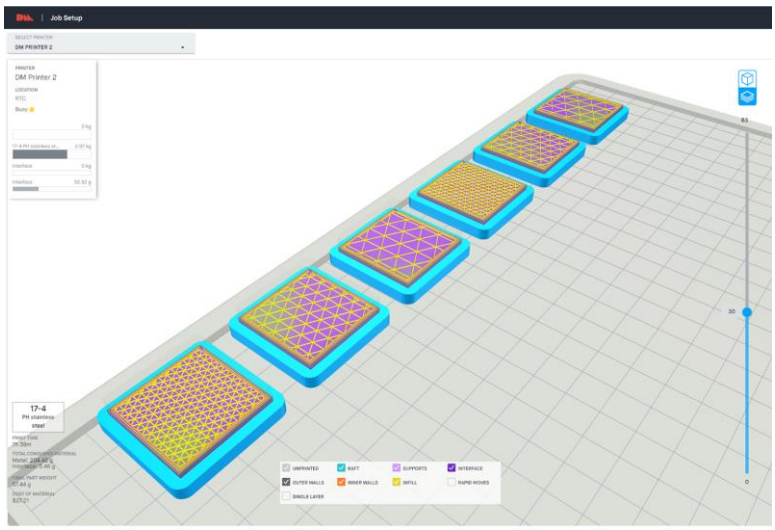

Figure 4.7 Desktop metal design software

Stainless steel 17/4 ph was chosen as a magnetic material to print using the DMBD printer. Both polymer binder and metal element are mixed together by the injection moulding process. The feedstock (as received) is then inserted into the printer (as seen in Fig. 4.8) where it is heated and fed by mechanical extrusion onto the plate. A support was made by extruding wax material which the feedstock binds to it. Once the print is completed the structure is known as the green part (AP), and is sent to the debinding process. The debinding process was done in two stages, the first is the solvent stage (either water acetone or ethanol) and the second is the thermal stage. The print is submerged into the solution

for 24 to 48 hours at a set temperature. Once dried, it is placed in a furnace under an inert atmosphere of argon-2.8% hydrogen. The thermal debinder burns off any remaining polymer and wax, now known as the brown part. This is to remove any impurities left behind such as carbon or oxygen.

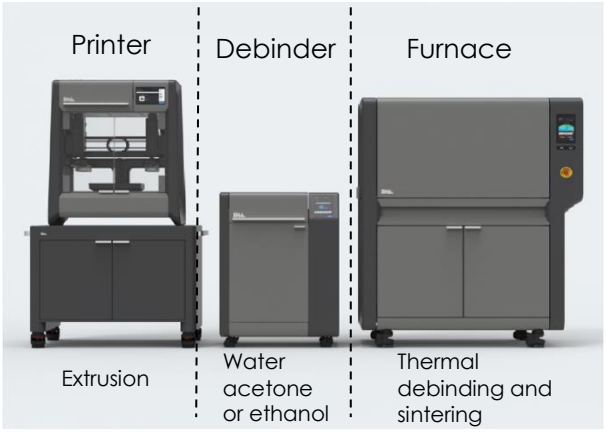

Figure 4.8 DMBD printer, debinder and furnace

The furnace is in an atmosphere (argon) with 2.8% hydrogen to prevent oxidation. The brown part is kept at a temperature close to the melting point (less than 1673 K). After the sintering process is completed, the part is then left to cool to room temperature. Steps for thermal debinding and sintering in the furnace are presented in table 4.3 (Nandakumar, 2019).

Table 4.3 Procedure for heat treatment, sintering and cooling for DMBD printer (Nandakumar, 2019)

Steps	Temperature Range, K	Time, minute	Ramp Rate, K/min
1	323 ➔ 433	Over: 120 Hold: 90	0.91
2	433 ➔533	Over: 300 Hold: 180	0.33
3	533 ➔ 873	Over: 114 Hold: 240	3
4	873 ➔ 1613	Over: 247 Hold: 120	3
5	Cooling	Until room temperature	Max

The first experiment was to explore the effect of printing at different stages on the magnetisation *i.e.* as-received (AR), as-print (AP) and sintered steel (SS) samples as seen in Fig. 4.9.

Figure 4.9 Samples from DMBD from left to right- injection moulded, as-build and post-treated stainless steel 17/4 ph

Larger more complex designs were printed such as a grid structure as shown in Fig. 4.10. The 100 x 100 x 2 mm size structure was successfully printed but failed at the sintering stage as cracks formed and propagated across the structure. This may be due to the warpage and heat stress such as shrinkage and expansion rate during heat cycles. Therefore, smaller grid sizes were printed instead. Hence, the DMBD printer is not suitable to print larger complex structures due to shrinkage and warping, however other sintering techniques such as hot isostatic pressing (HIP) could yield better final structures without excessive warping.

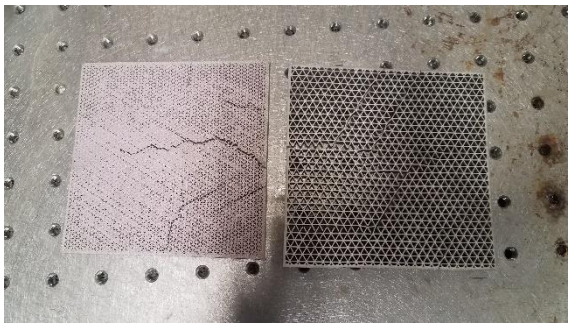

Figure 4.10 100 x 100 mm sintered grid size with fracture visible across the sample

The print size of 30 x 30 x 2 mm with different track gaps of 2 mm, 4 mm and 6 mm with the height of 2 mm was successfully printed and sintered as seen in Fig. 4.11. The sintered grid structures undergo shrinkage with a rate of 16.6 % therefore the final dimensions are track gaps of 1.5 mm, 3 mm and 5 mm as seen in Fig. 4.12.

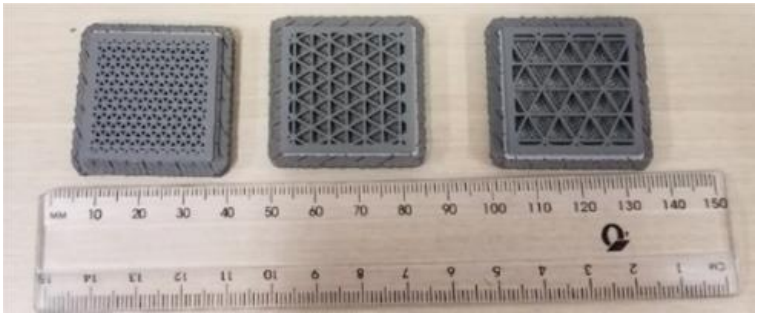

Figure 4.11 As-printed grid structure from DBMD of 2mm, 4mm and 6mm (left to right)

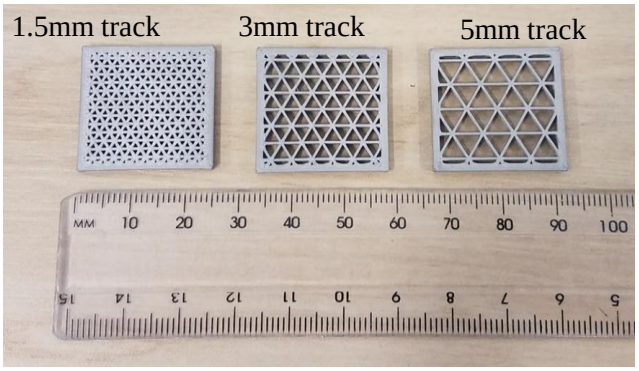

Figure 4.12 Sintered sample showing different track length of 1.5mm, 3mm and 5mm (left to right)

4.3.2 Inkjet printing method

4.3.2.1 Ink properties

The metal dispersion inks that were selected to be studied in this research were 20% Magnetite with Dimethylformamide (DMF) and 2% Nickel with N-Methyl-2-pyrrolidone (NMP) nanoparticles (NPs) inks, manufactured by Nanoshel. Table 4.4 shows the composition and physical properties of the inks. These include the solvent within the ink, the viscosity of the ink, surface tension, particle size and solvent evaporation temperature. The composition and physical properties are vital for printing NPs using an inkjet system to avoid clogging and printability on a substrate. For example, particle size above 100 nm would be prone to clogging depending on the nozzle size. Viscosity was estimated by the manufacturer as the ink composition and particles were readily available and tested by the manufacturer. However, for inkjet printing application, it is critical to know the viscosity of the ink.

A viscometer was used to measure the viscosity of both inks. The viscometer was calibrated by one-point calibration technique with water at room temperature before measuring the inks. Distilled water was measured at a known temperature and then compared to published values as shown in table 10.1 in appendix (James, Mulcahy and Steel, 1984). Magnetite and nickel ink were placed in a polycarbonate container and placed in a sample holder. Two vibrating probes and thermocouple were lowered and aligned to the meniscus.

Table 4.4 Nickel and magnetite ink properties

Metal NP	**Solvent composition**	**Viscosity at 298 K (cP)**	**Density (g/cm^3)**	**Surface tension (mN/m)**	**Particle size (nm)**	**Solvent evaporation temperature (K)**
Ni (2% Wt)	NMP and water	7.5-10	2.07	72.8 (water)	80-100	473 (NMP)
Fe_3O_4 (20% Wt)	Organic Solvent (DMF), IPA Ethanol, Water (ddH2O)	7.5-10	5.17	72.8 (water)	50-80	426 (DMF)

4.3.2.2 Pre-printing process

A range of different substrates were tested and selected for each metal NPs. As the metal NPs are part of ink containing organic solvent such as water and DMF/NMP, the concentration of metal is less than 20% Wt in the ink solution therefore the excess solvent needs to be evaporated once on the substrate. PET, PP, kapton, paper and PTFE substrates were tested by pipetting a drop of ink onto the substrate surface and heating it to the solvent evaporation temperature or until dried on a hotplate.

The experimental procedure for printing the metal NPs in the JetLab IV is to first prepare the ink. An ultrasonic bath was used for 30 minutes before transferring the ink to the ink reservoir. Approximately 3ml of ink was transferred to the ink reservoir. The reservoir was then placed into the JetLab IV printing machine. The jetting parameters were then calibrated. Before printing the substrates were cleaned by air dry to remove any dust or impurities on the substrate.

4.3.2.3 Printing process

The piezoelectric print head bought from Horizon Instruments, has a nozzle size of 60 µm with controllable voltage output. The printing parameters used was a standard wave at rise time of 5 µs, dwell time of 5 µs, fall time of 50 µs, echo time of 6 µs, rise time of 10 µs, idle voltage of 0 V, dwell voltage of 60 V and echo voltage of -60 V as seen in Fig. 4.13. There is slight variation in these parameters depending on the ink mixture. For example, the dwell voltage may change to 65 V or dwell time may change to 3 µs to prevent clogging or satellites in each droplet. For example, Nickel ink has heavier metal particles which were not easily mixed into the solution, therefore creating an additional issue when there is a difference in the density at the nozzle. This created a clogging problem where the

jetting parameters are not calibrated for the heavier particles of the solution. This results in irregular print which cannot be altered during printing.

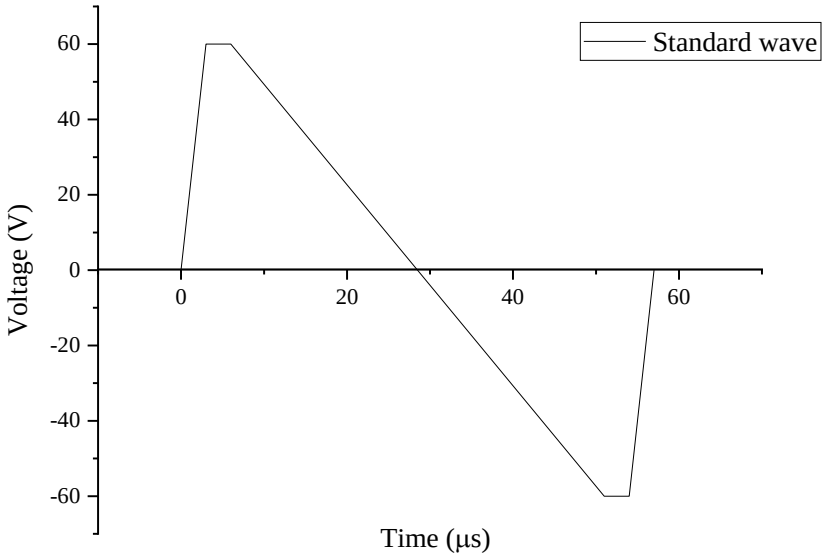

Figure 4.13 Jetlab signal input standard wave for each droplet

Designs for printing were made in Ansys CAD Space Claim and converted into bitmap monochrome files. Examples of the designs printed are seen from Fig. 4.14 to Fig. 4.17, where the white area is the printed design. The resolution of the image depends on the number of pixels in the image. Therefore, the larger the number of pixels there are, the larger the print will be. Printing 25 x 25 mm design required 128 x 128 pixels, which were measured in the paint software.

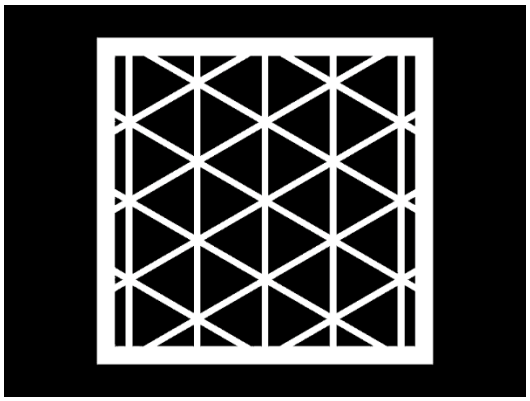

Figure 4.15 Monochrome image of 5 mm grid CAD converted to bitmap for inkjet printing

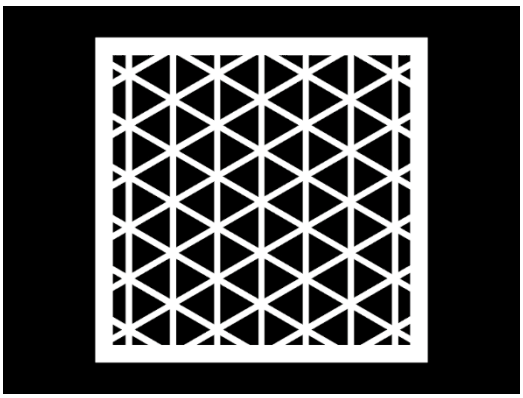

Figure 4.14 Monochrome image of 3 mm grid CAD converted to bitmap for inkjet printing

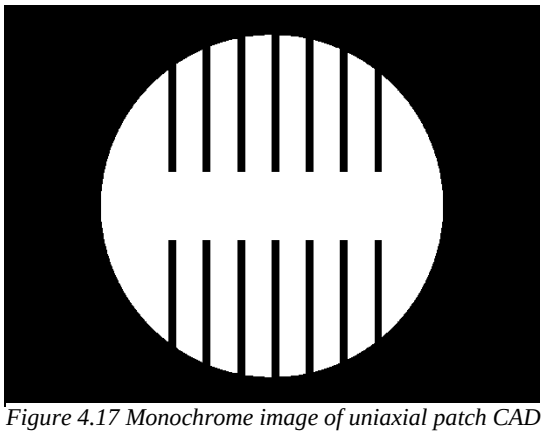

Figure 4.17 Monochrome image of uniaxial patch CAD converted to bitmap for inkjet printing

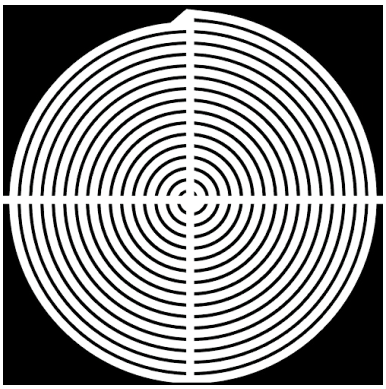

Figure 4.16 Monochrome image of coil CAD converted to bitmap for inkjet printing

4.3.2.4 Post treatment

After the printing process, the printed design is not ready for use, as a sensor, as it requires further treatment to avoid damage to the print. The first stage involves drying the print after the printing process. The print was left at room temperature to allow the ink to settle and then cured under UV light (400 nm) for around 15-20 seconds. The UV light source was placed 10 cm away from the print for exposure with 60% UV emission as shown in Fig. 4.18. This ensured that all the solvent within the printed design had evaporated, leaving the metal NPs on the substrate. This method is more efficient than the traditional hotplate or the oven as the UV light directly heats the ink from the top through to the bottom, ensuring the solvent is evaporated first. A hotplate or oven would take time to heat and evaporate the solvent.

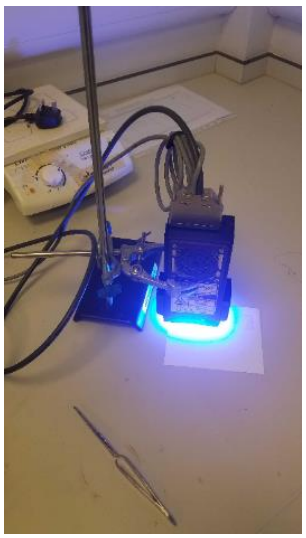

Figure 4.18 UV curing on paper

Coating is another treatment, which serves to protect the inkjet-printed designs from external environments. Two ways of applying a coating were used, which were by applying a layer of silicone via spin coater or spray coating a layer of acrylic polymer. Both coating methods have advantages and disadvantages of applying and protecting the print. Spray coating is the easy way of applying and protecting the print as it needs no additional machines or equipment. However, the spin coater ensures an even coating which is useful without compromising thickness and detection of magnetic field.

An Ossila spin coating machine was used to apply a layer of polydimethylsiloxane (PDMS) to the print under a fume hood as seen in Fig. 4.19. The PDMS (Slygard 184) used was purchased from Sigma Aldrich, which came in pre-packed solutions of resin and hardener. The pack contained both solutions in which the 2 parts were mixed within the pack (kneed) until thoroughly mixed. The photo paper with magnetite print was secured on a plastic petri dish, which was secured on to the chuck by using double sided tape. As the PDMS solution was viscous, the spin coater was set at 3000 RPM for 12 seconds. The setting was selected through trial and error using empty photo paper with various RPM, time and sizes as seen in Fig. 4.20. The coated print was left to dry at room temperature for 24 hours. The print was then taken out of the plastic petri dish and was then placed in an oven at 333 K for 1 hour to cure and then left to cool for another 24 hours. An acrylic conformal coating spray was purchased from RS component. The spray was used under a fume hood and sprayed directly onto the print from 15 cm away.

Figure 4.19 Ossila spin coater machine

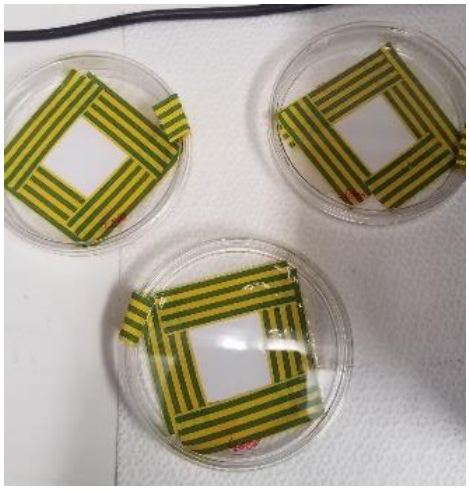

Figure 4.20 Spin coated paper with PDMS at 4000, 3000 and 2000 RPM

4.3.3 Production of carbon fibre composite

CFRP composite was supplied by SHD Composites Ltd. Carbon fibre prepreg 4 ply twill weave (VTC401- C200T-HS-3K-42%RW) was used in this project. They were formed into a composite laminate by using vacuum bagging. The prepreged CFRP were cut to size and layered on top of each other on a glass substrate and sealed in a vacuum bag at -28 Hg. The autoclave was used to apply pressure of 6 bar and heated to 333 K at a rate of 3 K/min and held for 60 minutes. Then the temperature increased to 393 K at a rate of 3 K/min for 60 minutes and then cooled down to room temperature as seen in Fig. 4.21. The cure cycle was recommended for the specific carbon fibre prepreg (VTC-401) from the supplier (SHD, 2022) and as demonstrated in (Vincent *et al.*, 2020).

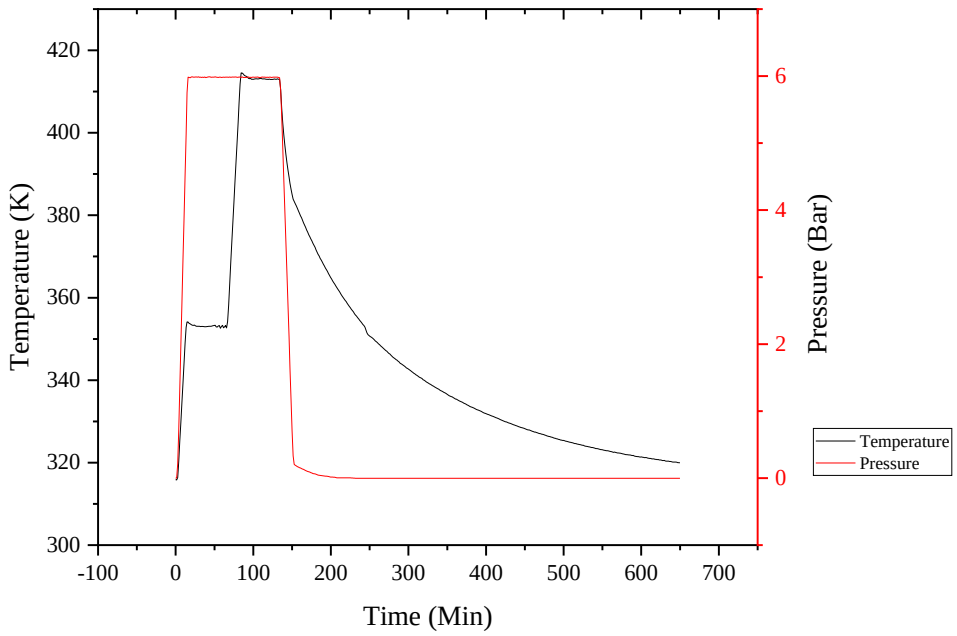

Figure 4.21 Temperature and pressure for curing CFRP in an autoclave

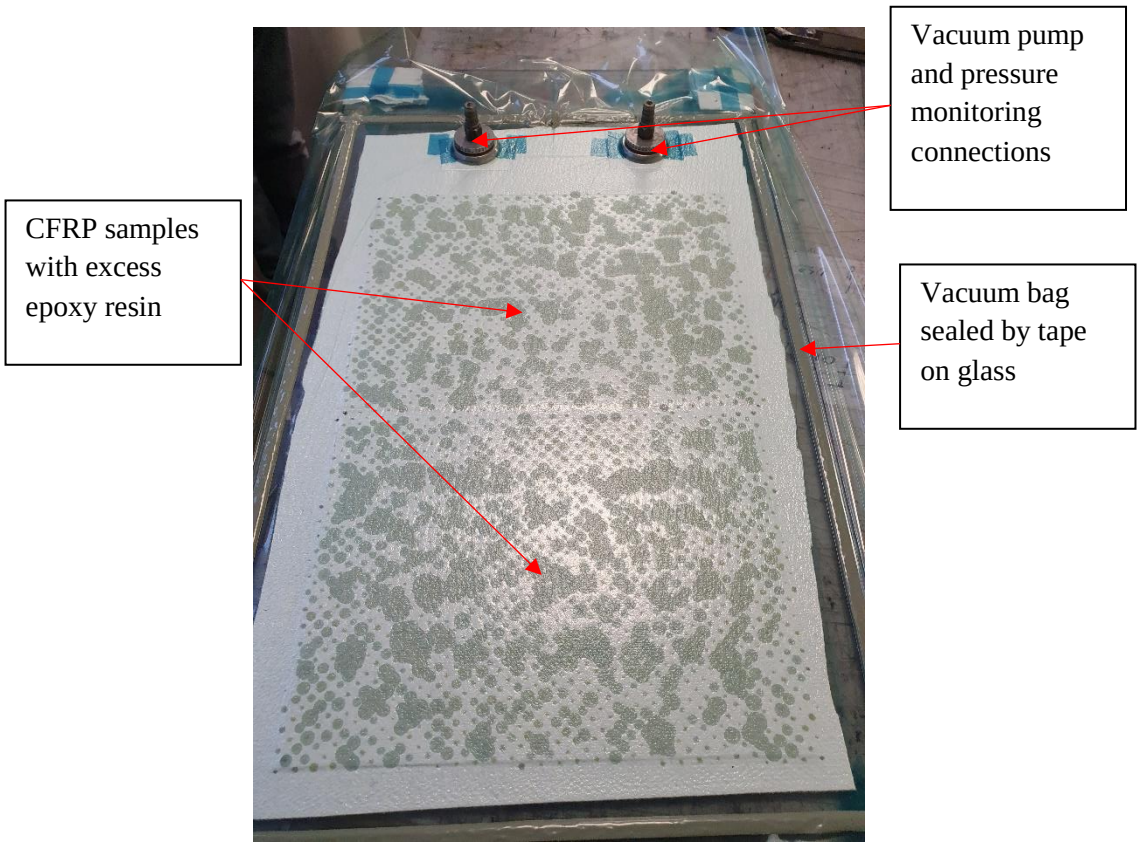

Figure 4.22 Vacuum bagging CFRP samples

A tile cutter was used to cut the CFRP to size. This included a blade submerged in water to prevent excess dust from cutting the CFRP samples. For strain bending test, the laminates were made to size of 25 × 50 × 0.75 mm. For impact testing, the samples were made into 100 x 100 mm size to accommodate the coil and tube for dropping the weight on the cast iron base. For cutting a cross section of the impact, a diamond blade was used in a secotom cutting machine.

4.4 Characterisation

4.4.1 Structural and chemical characterisation

For both the desktop and inkjet printed materials, scanning electron microscopy (SEM) and energy dispersive x-ray spectroscopy (EDS) were performed on a FEI Inspect F50 at 15kV and mapped using AZtec software by Oxford Instruments. The samples were placed into a conductive Bakelite powder and formed into a disk under heat and pressure. For the polymer metal composite samples, the samples were cured in a resin and hardened for a day in a low pressure container. For SEM, silver paint was applied to give a conductive layer to the polymer. The procedure (from Bueluer) used to polish stainless

steel is seen in table 4.5. After each step, the sample was cleaned by applying isopropanol onto the surface and then dried.

Table 4.5 Buehler polishing steps for stainless steel

Step	Paper/cloth	Solution	Size and abrasive	Load, [N]	Speed, rpm	Rotation direction	Time, min
1	Carbimet	Water	320 grit (P400)	6 [27]	300	Clockwise	Until plane
2	Ultra pad	Diamond suspension	9 micron pad	6 [27]	150	Anti-clockwise	5
3	Trident	Diamond suspension	3 micron cloth	6 [27]	150	Clockwise	3
4	Micro cloth	Diamond suspension	0.05 micron cloth	6 [27]	150	Anti-clockwise	2

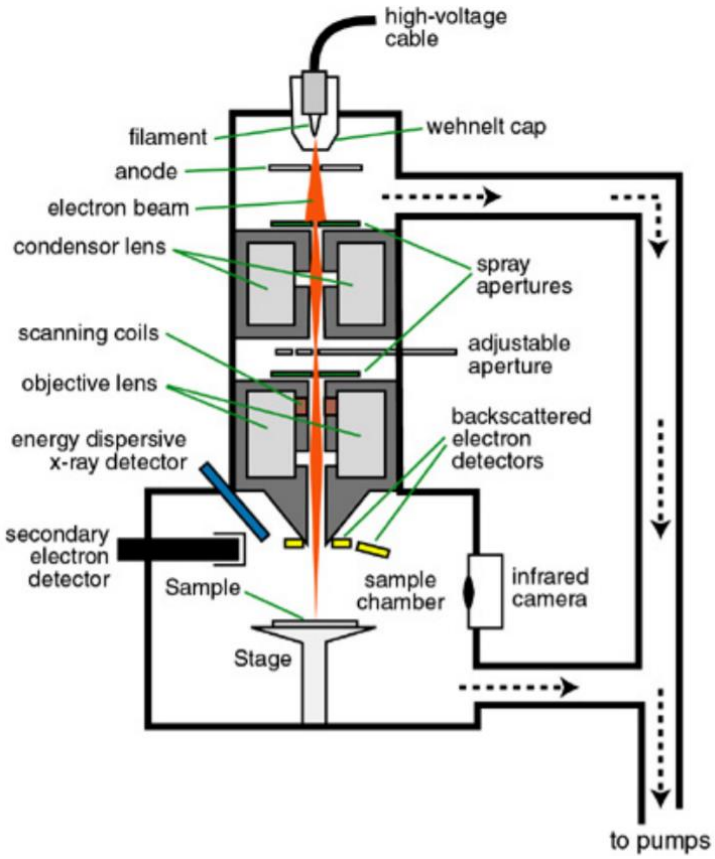

Figure 4.23 SEM diagram (Mabon *et al.*, 2017)

SEM is where charged electrons are released and focused on to the sample positioned on the stage as seen in Fig. 4.23. As the electron beam hits the sample, secondary electrons (SE), backscatter electrons (BE) and X-rays are emitted and detected, which are then used to produce images and provide the element composition. SE are where an electron is ejected from the atom whereas BE is where the primary electron comes back out of the sample. Therefore, both SE and BS have a range of energies which can be detected. X rays are produced when the primary electron knocks off an electron within the shell leaving a vacancy, X ray energy is then produced when an electron from a higher energy shell moves to fill the vacancy. The wavelength of X-ray defines the element whereas the intensity determines the element present in the material.

Fourier transform infrared by attenuated total reflection (FT-IR ATR) was used to identify the types of polymer in the desktop printed samples by identifying functional groups as seen in Fig. 4.24 (Gulmine *et al.*, 2002). Functional groups were then identified through published values (Jung *et al.*, 2018). A sample size of roughly 1 mm length was cut off the print and was placed in the FT IR machine. The sample size was thin and flat to ensure good contact with the diamond tip and light to the machine.

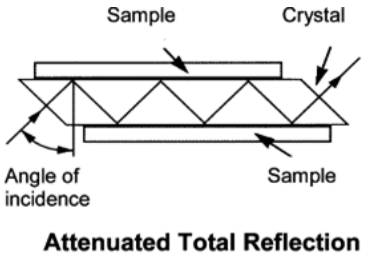

Figure 4.24 FT-IR ATR mechanism for identifying functional group(Gulmine *et al.*, 2002)

A Netzsch DIL402 Expedis was used to perform thermomechanical analysis (TMA) on a desktop track piece (5 x 10 x 2 mm) to measure the coefficient of thermal expansion (CTE) of the SS sample. As the sample expands or contracts, the sample holder, made of Al_2O_3 moves, therefore the change in length is measured. The change in length was measured in each X, Y and Z direction as shown in Fig. 4.25. As the temperature was increased in steps of 100 K from room temperature to 1000 K.

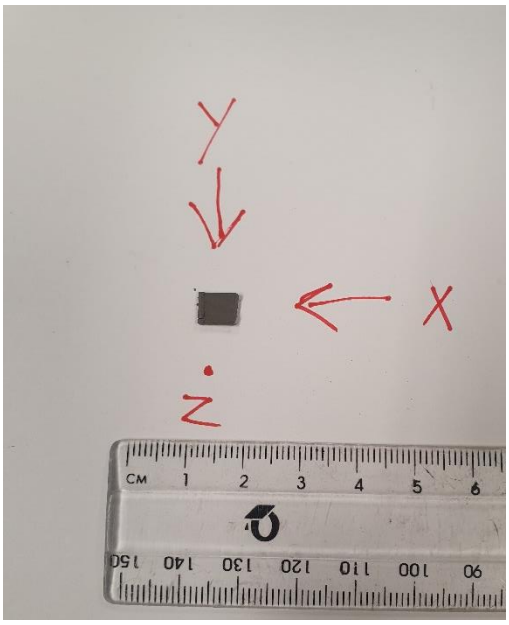

Figure 4.25 Thermomechanical analysis (TMA) on sintered steel in X, Y and Z direction

A Bruker contour elite optical profiler as shown in Fig. 4.26 from (Bruker, 2020) was used to measure the surface roughness and the thickness of the inkjet-printed samples. This was measured by illuminating the sample with a laser (green or white) on to the sample surface to measure the difference between the dark and white areas (fringes) using the VSI mode. The level of fringes was calibrated and adjusted before measurement. This was done by tilting and moving the stage until the number of fringes reaches less than 15 and the thickness is as large as possible. The magnetite print roughness was measured on paper, kapton and glass substrate. The substrate was held down by plasticine or tape to avoid movement during the stitching process. The stitching process involves automated measurement of the singular images over a selected area. This is useful when capturing a large area (square or circular) without having to recalibrate. Vision 64 software is used to analyse the data into 2D and 3D plots. The surface roughness is calculated from the mean centreline as seen in Fig. 4.27. R parameters are used to give the final surface roughness. Post processing of the surface profile included removal of tilt and restoring data for all profiles using the Vision 64 software.

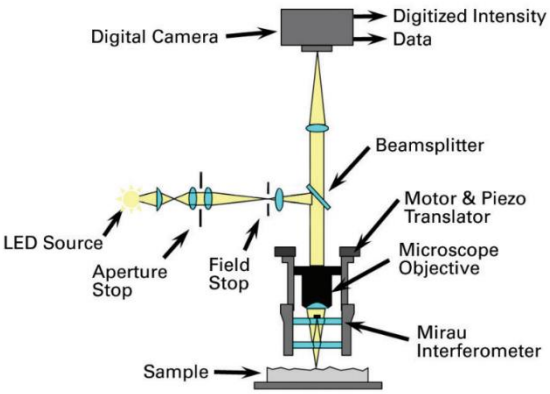

Figure 4.26 White Light Interferometry set up (Bruker, 2020)

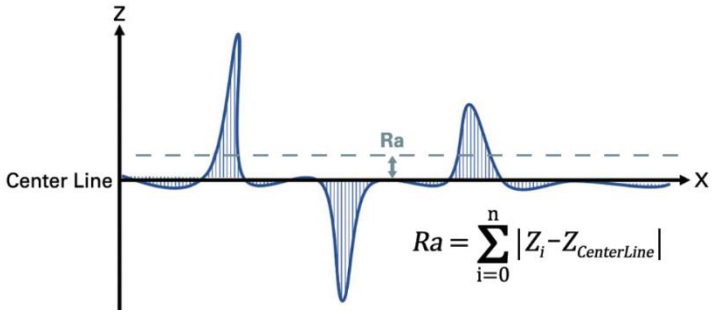

Figure 4.27 Mean roughness calculation (Bruker, 2020)

4.4.2 Magnetic measurements

4.4.2.1 SQUID magnetometer

The magnetic properties were measured using the MPMS-3 SQUID magnetometer by Quantum Design. The SQUID magnetometer measures the magnetic moment of the sample using detection coils, which are placed in cryogenic temperature (helium) as seen in Fig. 4.28. A Josephson junction which consists of two superconductors connected by a weak link such as an insulator, it measures small variation in voltage due to the increased inductance from the detection coil. The Vibrating Sample Magnetometer (VSM) method measures the change in magnetic flux as a function of time of the sample in an applied field. To achieve this, the sample is oscillated between two detection coils. This creates an emf in the detection coils, which is converted to the magnetic moment of the sample using Maxwell equations, once the vibration frequency (amplitude) and applied field is known. This is done by the Quantum design software that runs the magnetometer. For this work, the SQUID magnetometer was calibrated against a known sample (Ni) sample, using the calibration programme from Quantum Design. An empty measurement made sure that there were nothing in the chamber that could affect the background.

Most of the measurements were taken at room temperature (300 K). While for samples such as steel track, the temperature used was from room temperature to 1000 K. The samples were placed in a gelatine capsule and white tape was used to secure the sample in place to prevent movement. Kapton tape was used to keep the capsule closed. The capsule was then inserted into a plastic tube and positioned using the quantum design measurement tool. Magnetic field was applied in steps of 40 kA/m to 1200 kA/m.

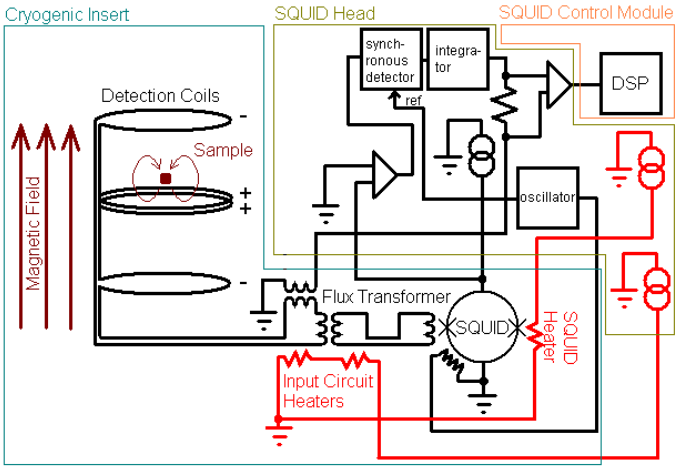

Figure 4.28 SQUID schematic diagram

The rotator tube as seen in Fig. 4.29, which was used to rotate the sample in the plane every 45 degrees for each hysteresis loop measurement. A single desktop track plane (10 x 5 x 2 mm) was placed on the cradle by applying GE varnish to the cradle. The angle of the cradle was calibrated by measuring the initial angle of the cradle before transferring it into the SQUID.

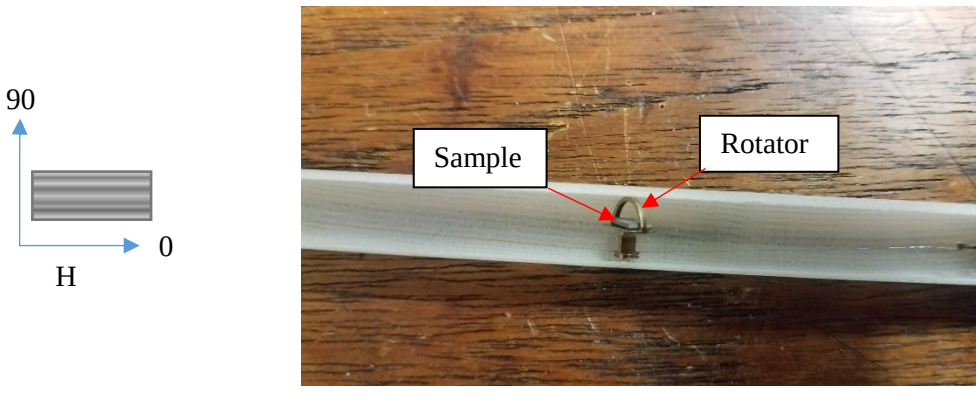

Figure 4.29 SQUID rotator sample holder and angle of applied field

A quartz rod was used to measure the magnetisation while applying a field in a singular direction. Two samples were prepared in the 90 and 0 degree to the track plane and were secured to the quartz rod by GE varnish. A quartz tube was used to measure the field out of plane. The quartz tube was placed in a

brass holder where 2 parts of the quartz tube held the sample (sandwich) in out of plane direction. The brass holder background was subtracted from the hysteresis loop of the sample.

4.4.2.2 Magcam

The demagnetising field of different desktop prints were imaged using a magnetic camera from Magcam. The magnetic camera contains 1000 Hall sensors used to measure magnetic field across the sample. As a result, the Magcam has a resolution of 0.1 mm^2, which is suitable to capture an image of the structure's demagnetisation field. A difference of magnetic field was measured for various track distances as shown in Fig. 4.30 (a). The Magcam device was connected to the computer using a Magscope software as seen in Fig. 4.30 (b). The software allowed data to be averaged over time for 128 frames to obtain clear image of the field.

a

b

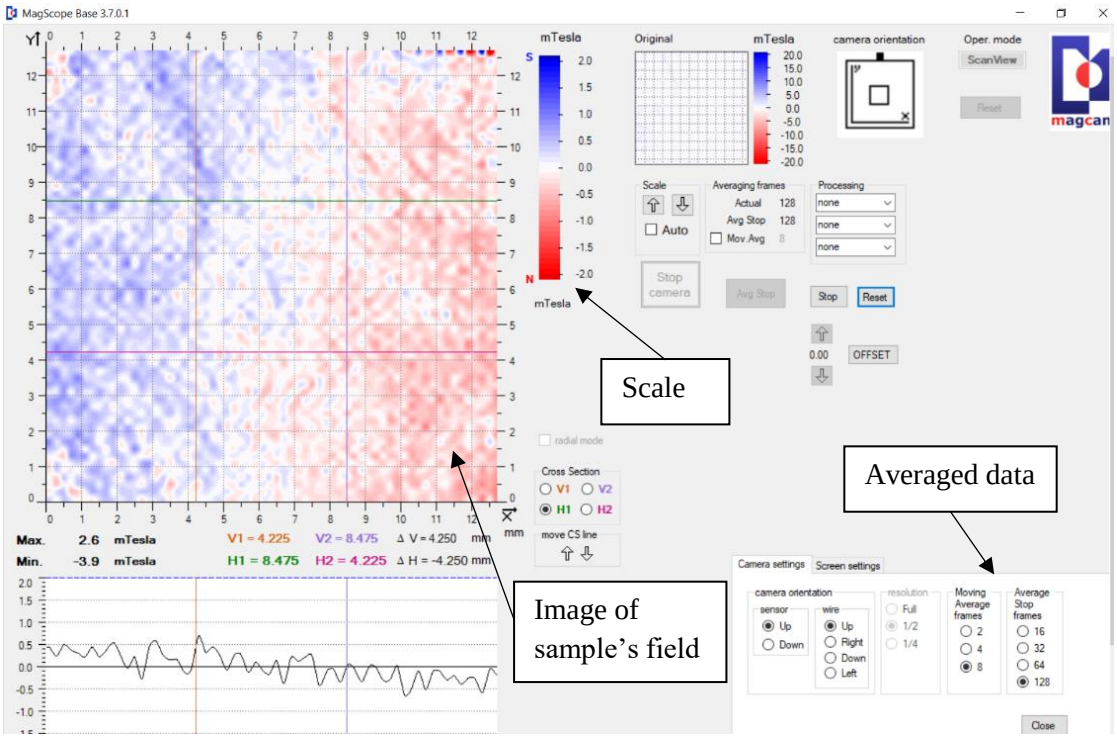

Figure 4.30 (a)Magnetic camera (Magcam) and (b) Magscope software

4.5 Magnetostriction measurements

From the literature chapter 3.3, there are various ways in which magnetostriction (Joule and Villari effect) can be measured but due to the availability and limitations of the equipment, not all methods outlined in the literature could be used. For Joule magnetostriction, the resistance and voltage of a strain gauge attached to the sample under a magnetic field was measured. This method is suitable for bulk magnetic material such as the stainless steel in this work. However, for the inkjet-printed structure, measuring Joule magnetostriction is difficult as the strain gauge will need a greater material contact in order to measure the change in length. Other methods include optical interferometry which needs the sample to have a thickness of more than 2 mm, however the inkjet-printed structures have a thickness of less than 2 mm due to the droplet size and NPs size. The Villari effect was measured by a pick-up coil as seen in (Vincent *et al.*, 2020), where a coil inductor is placed on the sample to detect a change in field. In (Leong *et al.*, 2018) they have used an AMR method to detect field during applied strain, however good contact on the magnetic material is needed, therefore it cannot be used for inkjet-printed samples. The pick-up coil allows flexibility in applying various strain or stress to the sample without the need for specialist equipment.

To quantify and compare the magnetostriction measurement for sensor and actuator performance, the saturation and gradient of the measurement can be recorded. For example, in Fig. 4.31 (Datta, 2013) shows an example of measurement taken for direct (Joule) and inverse (Villari) magnetostriction. The measurement can be positive or negative in both cases depending on the material and stress applied. The change of field changes in a linear trend and then saturates as maximum stress or field is applied. This is the magnetic moments and domains orienting towards the applied field or stress, therefore the overall measurement is non-linear. It can be expressed as shown in Equation 4.4, where it shows the relation between the direct and inverse magnetoelastic effects (Lee, 1955). It shows that the change in stress as a function of field is proportional to the change in field as a function of stress with inverse length. The rate of which the field or strain is increasing, can be analysed by performing a linear fit as shown in Fig. 4.31 where the dash line fits the linear part of the graph for both direct and inverse effects. Therefore, fitting was performed in Origin Lab software using the converted strain values. The gradient of the fit will determine the performance of the print to strain or field, as a higher change in gradient would be ideal for a sensor.

Equation 4.4 Magneto mechanical in direct and inverse effects

$$\frac{1}{l}\left(\frac{dl}{dH_m}\right)_{\sigma} = \left(\frac{dl}{d\sigma}\right)_{H} \quad (4.4)$$

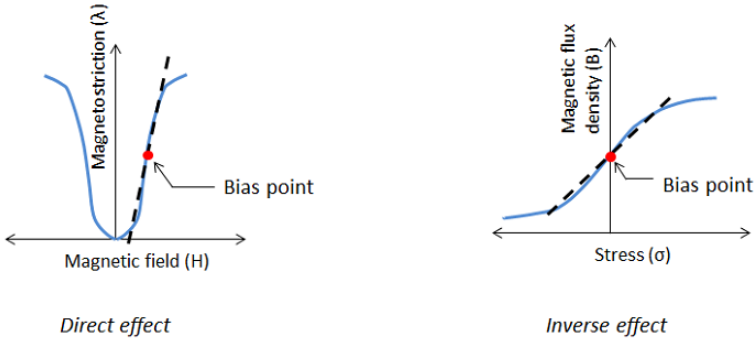

Figure 4.31 COMSOL magnetostriction direct(Joule) and inverse (Villari) effect example (Datta, 2013)

Where H_m is the magnetic field, σ is stress and l is the length of the sample. To measure both effects is ideal however in this work, one is sufficient to validate the magnetostriction effect such as by applying a stress or magnetic field. In (Gullapalli *et al.*, 2021) they have performed linear fitting of the inverse effect by applying a strain to an iron and nickel ribbon over a known curvature up to 300 mm as seen in Fig. 4.32. This made it easy to quantify and select the better sensor for SHM applications. For example, the fitting performed in Fig. 4.32, shows the positive and negative sensor behaviour in blue and red respectively. The overall result from using different techniques had shown that the FeSiB ribbon had the highest gradient, which proved to be accurate as it had the higher magnetostrictive constant (32 ppm) than Fe and Ni nanoparticles (in epoxy). This makes it possible to test and evaluate different types of sensors based on their magnetostriction performance.

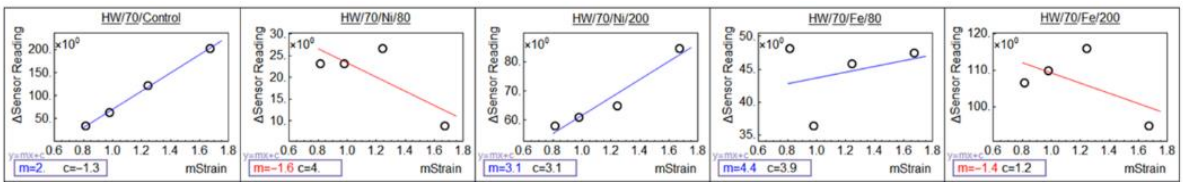

Figure 4.32 Linear fitting analysis of FeSiB ribbon (control), Fe in epoxy and Ni in epoxy field detected using a hand wound coil inductor showing positive and negative gradient of field as a function of strain (Gullapalli *et al.*, 2021)

4.5.1 Joule magnetostriction

Joule magnetostriction was measured by using a strain gauge to detect small changes in length. The change in resistance and voltage of the strain gauge was recorded (gauge factor of 2.1), as shown in Equation 4.5. This can be rearranged to give Equation 4.6 to calculate the strain, and hence the magnetostriction constant, ($\lambda = \varepsilon$), where R is resistance, G is the gauge factor of the strain gauge and L is the length of the sample. An Agilent E4980A from IPCMS was used to record the resistance of the strain gauge while 2 V DC bias was applied at a 100 kHz frequency.

Equation 4.5 Change in resistance and length relation from a strain gauge

$$\frac{\Delta R}{R} = G\frac{\Delta l}{l} \qquad (4.5)$$

Equation 4.6 Strain equation from change in resistance of a strain gauge

$$\varepsilon = \frac{\Delta R}{RG} \qquad (4.6)$$

A strain gauge (smaller in size than the sample) was fixed on to the sample by using cyanoacrylate glue. The connecting wires from the strain gauge were then soldered onto a copper wire. A magnetic field was applied by placing the sample in an electromagnet, therefore the field could be controlled by changing the voltage as shown in Fig. 4.33. The field was changed manually by gradually increasing or decreasing the voltage. A Hall probe was placed near the sample to measure the field during the measurement. The Wheatstone bridge is used to measure an unknown resistance in a circuit (in this case the strain gauge on the samples is the unknown). The setup of the Wheatstone bridge is shown left in Fig. 4.34 where a quarter bridge is used. This consists of two 120 Ohms resistance strain gauges where one is placed on the sample to measure length changes and the other is placed near the sample (on a non-magnetic surface). The two strain gauges compensate for the change in noise in the measurement such as temperature or pressure changes which could affect the resistance and voltage changes, this is shown right in Fig. 4.34. One 120 Ohms fixed resistor and one variable resistor are used to balance the resistance across the circuit.

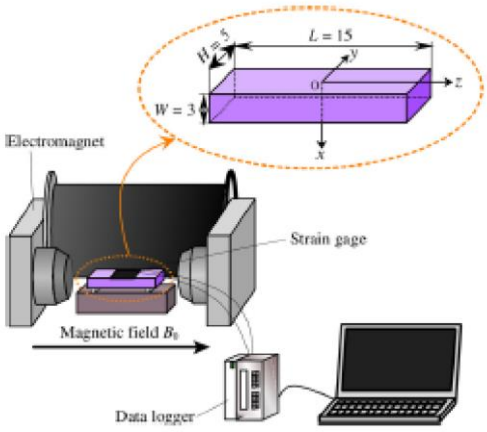

Figure 4.33 Strain measurement in an electromagnet set up

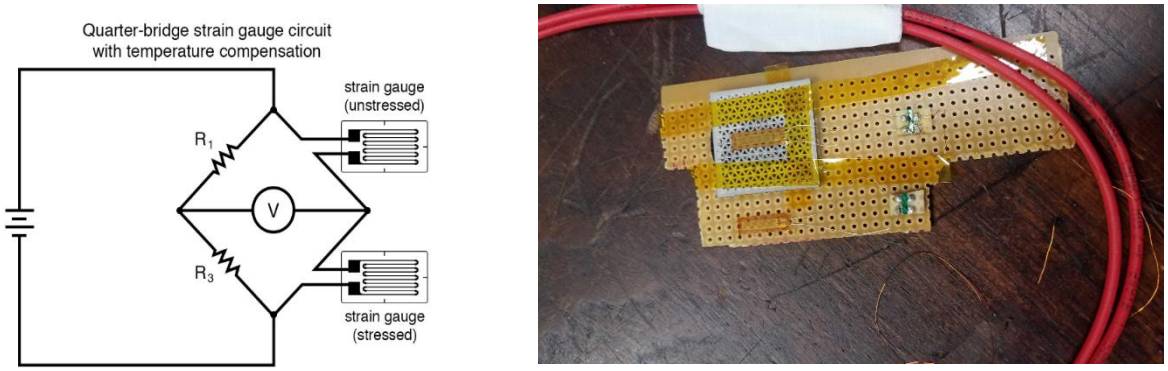

Figure 4.34 Quarter-bridge wheatstone schematic diagram (left) and strain gauge place on stainless steel structure (right)

Fig. 4.35 shows the experimental set up for measuring Joule magnetostriction in parallel and perpendicular direction. The strain gauge was mounted on the side for all printed stainless steel. Field direction in parallel and perpendicular to the sample by adjusting the electromagnet position.

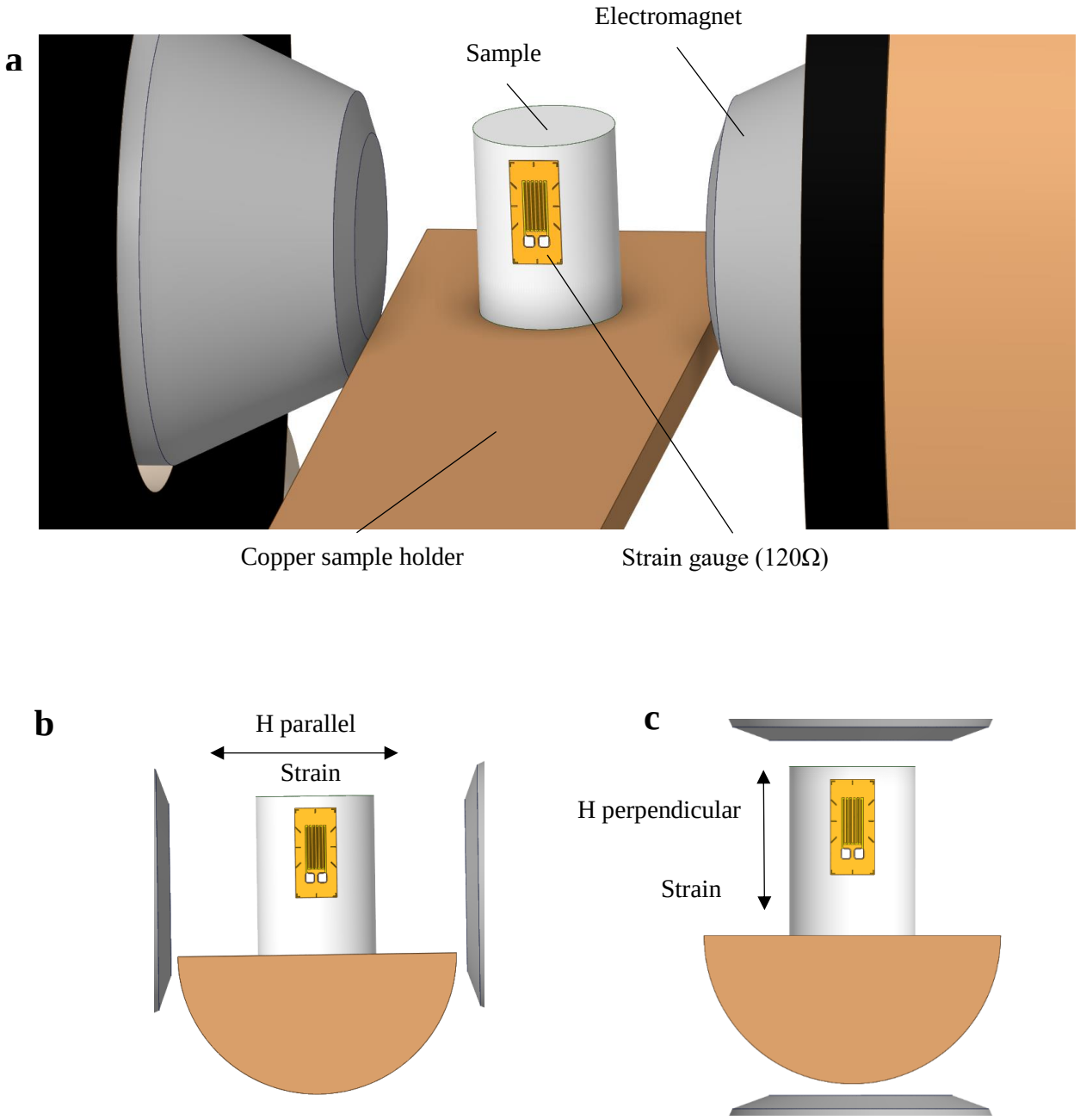

Figure 4.35 (a) Magnetostriction measurement schematic showing (b) parallel and (c) perpendicular configuration of the experiment with respect to magnetic field (H) and strain (not to scale)

4.5.2 Villari effect magnetostriction

4.5.2.1 Strain bending test

Both a Hall probe and an inductance measurement were used to measure the magnetoelastic performance of the soft magnetic material designs when strained. These methods were selected from literature as they have proven to detect magnetic fields as seen in chapter 3.3. The magnetic prints were

strained by placing them on a bending rig to apply a bending force. The bending test setup shown in Fig. 4.36, shows the force applied on two ends which forces the sample around a known curvature radius. The dimensions of the bend rig and radius of curvature was measured and produced in Ansys CAD design package. The CAD design was converted to an STL file for printing. A resin photo-polymer printer was used to print 3D bend rigs as shown in Fig. 4.37. As the print is at the top of the paper, the bend will produce a tensile force and reorientate the magnetic moments, therefore producing a change in the magnetic dipole and field.

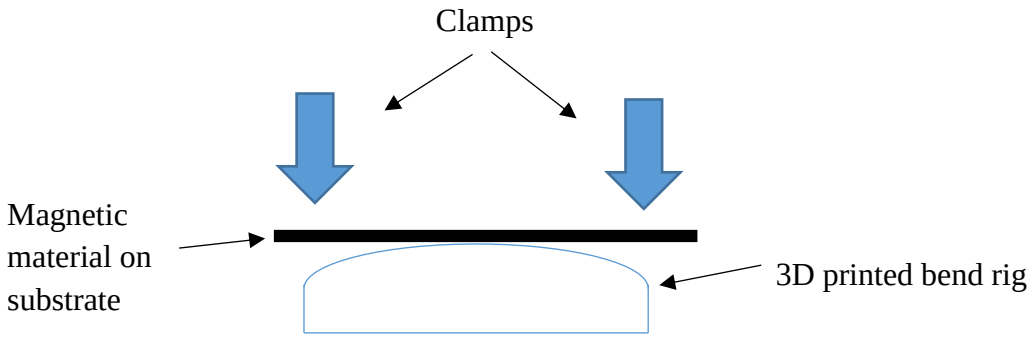

Figure 4.36 Bending test on known radius of curvature

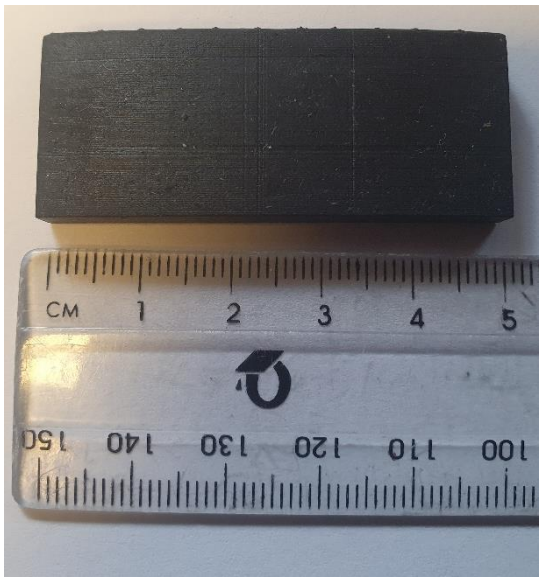

Figure 4.37 3D printed bend rig

The radius of curvature is converted to strain by using Equation 4.7. Where ε is strain, y is distance from the neutral axis and R is the radius of curvature. By converting the radius of curvature of R1000, R900, R800, R700, R600, R500, R400, R300, R200 and R100 to strain values of 0.13, 0.14, 0.16, 0.19, 0.22, 0.26, 0.33, 0.43, 0.65 and 1.3 με respectively (where R1000 = 1000 mm radius) for paper substrate. The strain depends on the distance of curvature from the neutral axis therefore calculated values for

paper, kapton and CFRP are presented in the appendix in Fig.10.1. The 3D printed bending rig dimensions were measured again after printing for recalculation of the strain.

Equation 4.7 Bending rig strain calculation

$$\varepsilon = \frac{y}{R} \qquad (4.7)$$

The Hirst gaussmeter GM08 Hall probe was used for measuring the magnetic field from the print design in millitesla (mT). A transverse Hall probe was placed directly above the print as shown in Fig. 4.38. This is because printed structure will have a demagnetising field that will be detected if the Hall sensor is close and normal to the print. In chapter 3.3, the introduction of the Hall effect is explained where in Equation 3.13 shows that the change in voltage is proportional to the field. Therefore, the equation can be rearranged to calculate an electromagnetic force EMF on the sensor, thus measuring the field of the print. Equation 4.8 shows that the change in induction with constant electrical charge, changes the overall electrical field, which allows the magnetic field to be measured. Where F is the electromagnetic force, q is the charge, E_f is the electrical field, v is velocity and B is the magnetic induction (O'Handley, 1999; Nave, 2000b).

Equation 4.8 Lorentz force equation (Nave, 2000b)

$$F = q(E_f + v \times B) \quad (4.8)$$

Figure 4.38 Hall probe measurement setup

Measuring a change in inductance is another direct way of measuring the change in field of a material. For example, a coil was made to measure the change in inductance as strain was applied to the print. The inductance as shown in chapter 3.3 is proportional to magnetic flux as shown in Equation 3.3 therefore magnetic flux can be derived from the inductance at a constant current in the coil (TDK Corp, 2020). This allows flexible measurement to adjust the sensitivity of the inductance. Equation 3.4 shows that in a coil the number of turns increases the inductance greatly, therefore increasing the area and storage. However, increasing the inductance would affect the signal to noise ratio (SNR) of detecting small changes in magnetic field during measurement. This is because the resistance is increased as the length of the copper coil is increased. An SNR test was performed by measuring inductance of coils wound with 70, 100, 150, 200 and 250 turns as shown in Fig. 4.39 (a). The coil holder was made by 3D printing using a resin printer, cured with UV light at 35 degrees for 120 minutes. The dimensions of the coil holder are shown in Fig. 4.39 (b) where the diameter of the inner air core is 5 mm and diameter of the coil holder is 16 mm. The inductor was made from, copper wire of thickness 0.1 mm and air core size radius of 1.5 mm.

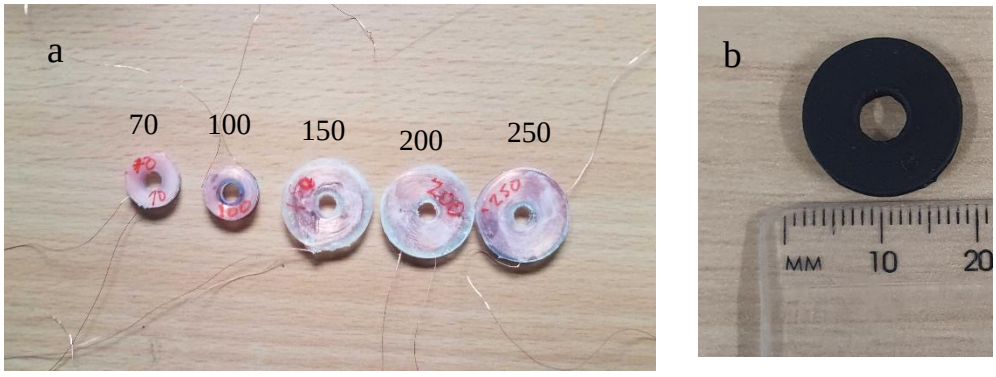

Figure 4.39 (a) Set of copper coil, 0.1 thickness in 3D printed resin for inductance measurement (70, 100,150, 200 and 250 turns) used for SNR and (b) showing the dimension of the coil used for inductance measurements

The experimental setup to measure the inductance included an 880 handheld LCR and an 891 bench top LCR meter from BK precision connected to a coil inductor as seen in Fig. 4.40. The LCR meter was connected to a computer via USB to capture the data points during measurements. A current was applied at a frequency of 1 kHz with voltage of 0.6 V for the 880 handled LCR meter and 1 vrms for the 891 LCR meter. The inkjet-printed design was then placed on the 3D printed bend rig with radius of curvature of 1000 mm to 100 mm. An inductor was then placed directly on top of the cured ink, as it was used to measure small changes in inductance from the printed structure. A clamp with polymer grips were used on both sides of the photo paper on the bend rig, to ensure the paper was strained onto the bend rig.

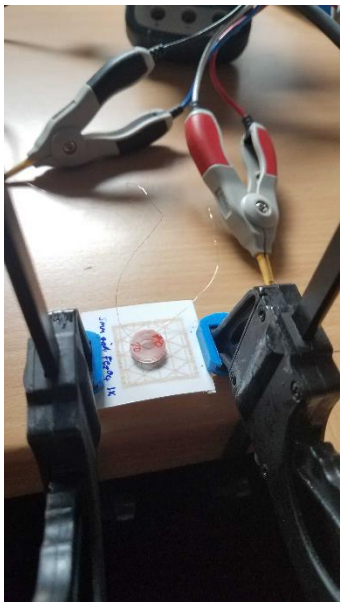

Figure 4.40 Inductance measurement with coil and clamp on 3d printed bend rig

In addition to the strain bending test performed on the inkjet-printed sample, the DMBD printed steel grids were strained but without using a known radius of curvature bend rig. To measure the magnetic flux of the grid samples, to compare the results with the COMSOL cantilever model, a simple experimental setup was used. This consisted of clamping the metal grid at one end with a known weight attached to the other end of the grid as seen in Fig. 4.41. A set weights of 0.1 kg were added and a Hall probe used to measure the field at one point.

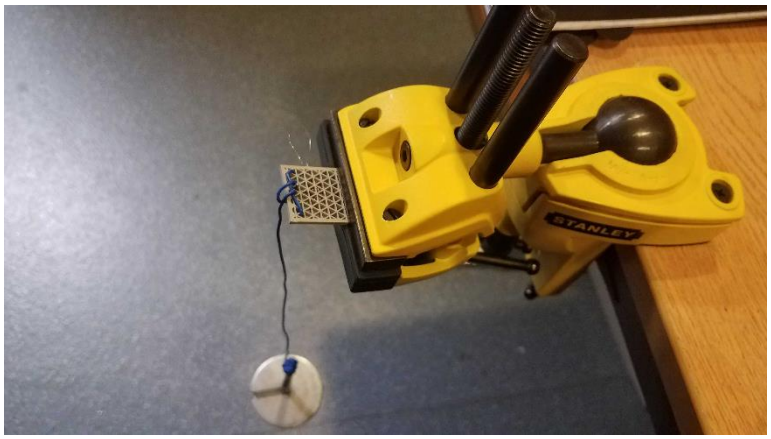

Figure 4.41 Experimental setup of weight attached to the grid structure

4.5.2.2 Impact testing CFRP

To determine whether the ink-jet printed sensors worked on CFRP, they had to be attached to the CFRP surface, which can be done in three ways. One way is by hot press them on, which can only be done by using a kapton substrate, as the heat will form a bond between the kapton and the CFRP resin. Only certain types of kapton substrate can be used such as modified kapton with lower surface energy than the resin or treating the surface with corona/ozone that will put a reactive group on the surface and help stick to the CFRP resin. Another way was by applying an adhesive or epoxy onto the surface of CFRP and to the substrate of the magnetic print, forming a bond between them. The epoxy was then left to cure at room temperature for a few days. Thirdly, they can be directly printed onto the surface of CFRP to ensure greater contact between the sensor and the CFRP without any substrate or interface between the CFRP and the sensor.

For the impact testing, a weight up to 1 kg steel cone-shaped object, was dropped at a set height of 1 m onto the CFRP laminate to simulate low velocity impact. The gravitational potential energy before impact was calculated by using Equation 4.9 where the size of the impact is 0.03 m and kinetic energy calculated in Equation 4.10. The impact will force a damage on the CFRP to induce cracking or delamination to replicate damages such as debris impact on runway or hailstones on aircraft structures in challenging environments (Artero-Guerrero *et al.*, 2014). The tensile strength of VTC-401 for 2 mm thick CFRP is measured to be around 700 MPa as seen in Fig. 4.41 (provided by SHD composite). Therefore, the impact test will be calculated to cause stress less than the manufacturer's limit of stress to fracture.

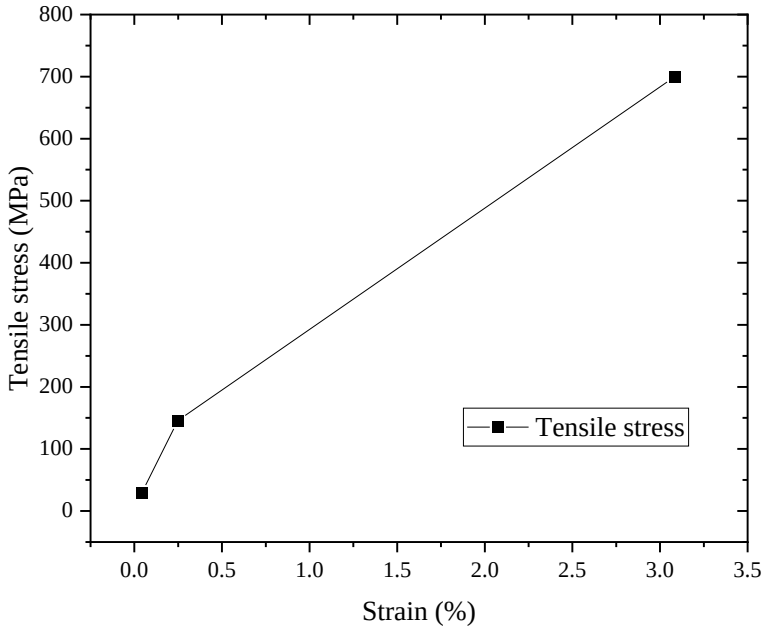

Figure 4.42 Tensile test of CFRP with 2.07mm thickness provided by SHD composites Ltd

Equation 4.9 Impact force

$$F_i = mgh/d \qquad (4.9)$$

Where m is mass of the object dropped, g is the gravitational constant, h is the height of the object dropped (1.1 m) and d is the contact diameter of impact measured to 0.00322 mm.

Equation 4.10 Kinetic energy

$$KE = \frac{1}{2}mv^2 \qquad (4.10)$$

Where m is mass in kg and v is velocity in m/s which was calculated to be 4.64 m/s (see table 10.2 in appendix for full calculations). Before the measurement took place, the inductor coil connected to the 891 BK precision LCR meter was placed on the magnetostrictive sensor until the signal was stable i.e. there was zero drift in inductance. The LCR meter was changed for better data reading by LabView 2020. The impact site can be seen in Fig. 4.43 where an inductor coil is placed near the impact site on a transparent polycarbonate sheet (left) and sensor placed on the PC sheet attached by epoxy. Fig. 4.44 shows impact on 10 cm x 10 cm CFRP sheet where a defect can be seen on the surface. The magnetostrictive sensor was placed and fixed to the CFRP with an inductor attached, the weights were held and dropped from a fixed height using a tube as shown in Fig. 4.45. The tube diameter was 7.1 cm in width while the cast iron base had a diameter of 11 cm. The maximum height of the tube to drop the weight is at 1.1 m. The location of the impact was between 4.5 cm to 5 cm from the sensor. The impact

was done both at the front and the back of the sensor on the CFRP sheet. This was to test the effect of damage to the CFRP and the position of the sensor.

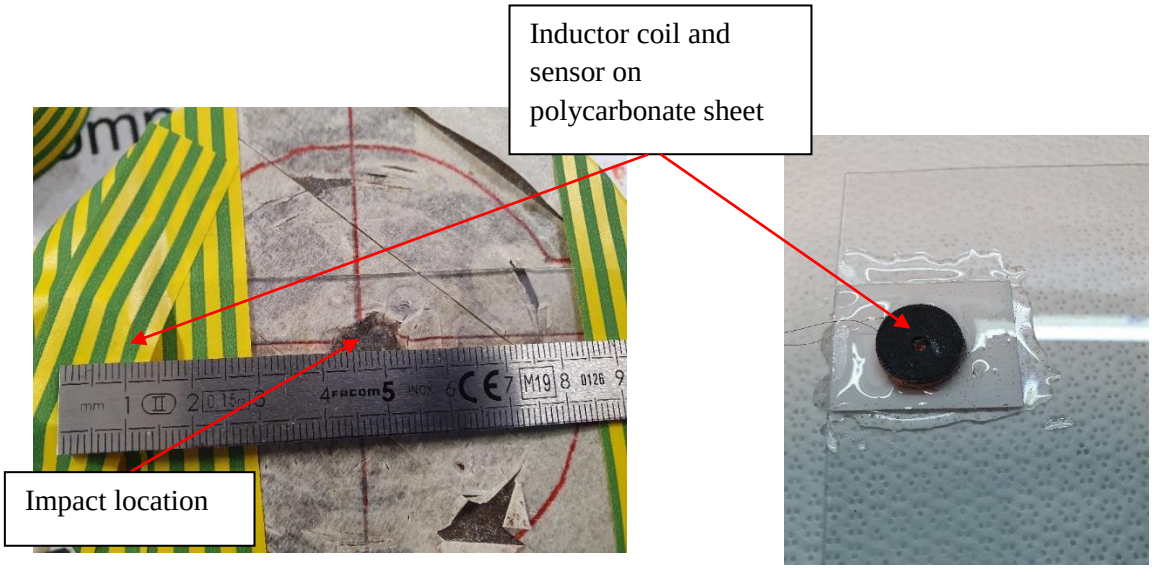

Figure 4.43 Impact site with inductor close to the impact (left) and magnetostrictive sensor on polycarbonate sheet with coil attached by epoxy (right)

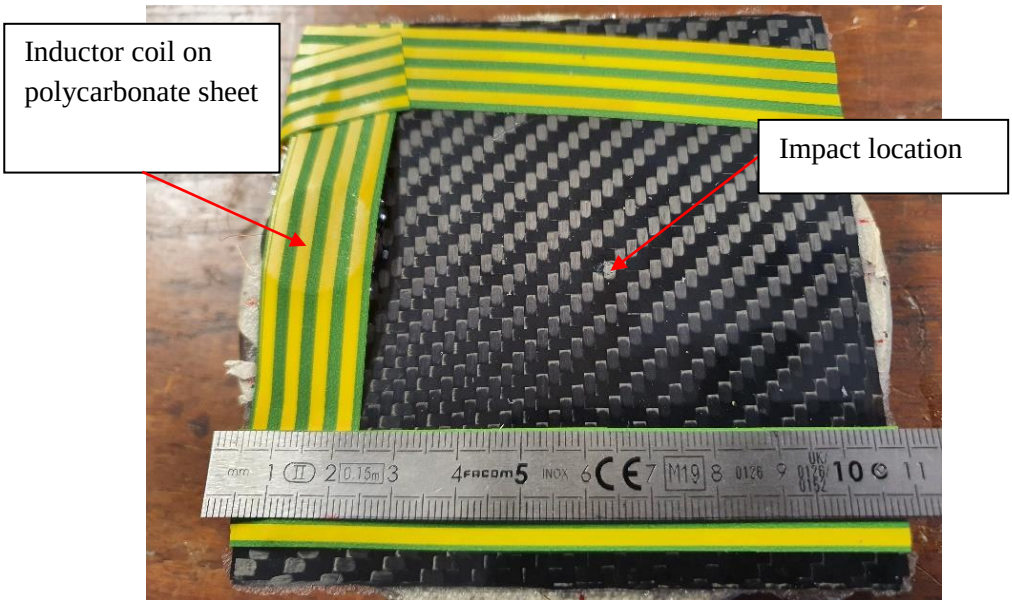

Figure 4.44 CFRP sheet secured on impact base

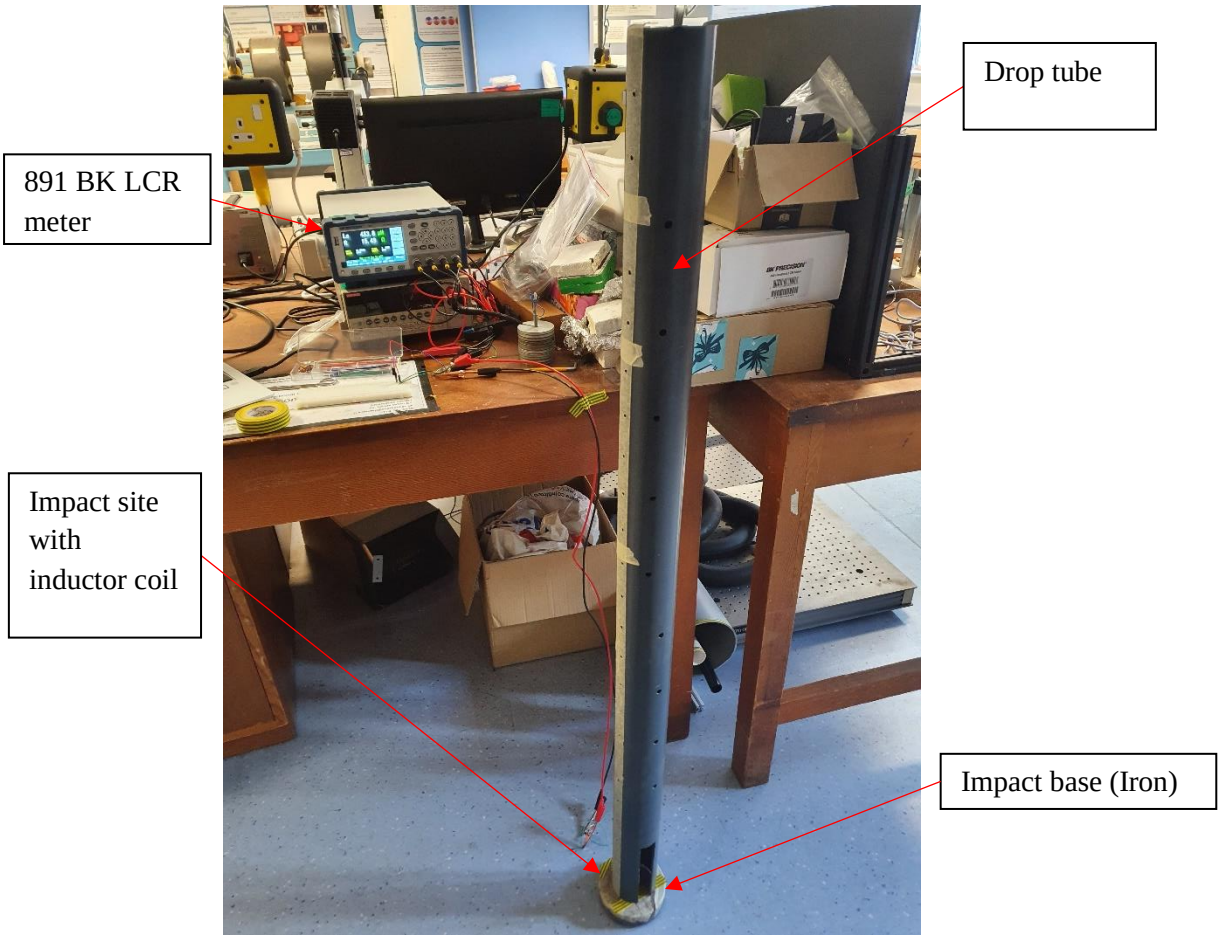

Figure 4.45 Impact testing setup

Chapter 5

Desktop printer results and discussion

5 Desktop printer results and discussion

5.1 Abstract

This chapter investigates whether a desktop metal bound printer can be used to 3D print magnetostrictive materials for structural health monitoring (SHM) and repair of aircraft carbon fibre reinforced polymer (CFRP). As the desktop metal bound deposition printer (DMBD) shows potential to print cost effective sensors. Therefore, this chapter focuses on evaluating the DMBD printer for magnetic and structural properties such as magnetisation/ anisotropy, morphology and characterisation of each sample at different stages in printing. The material selected was stainless steel 17/4 ph as a soft magnetic material to test magnetostriction and sensor performance. The stages in printing selected were as-received (AR), as-printed (AP) and sintered steel (SS) samples. A basic rectangular grid design was printed to evaluate the magnetic and structural properties before designing complex structures. The magnetisation for a track sample was measured using the superconducting quantum interference device (SQUID) to create B-H hysteresis loops with maximum field reaching to 1.5 T. A hysteresis loop was created at each stage of the printing process. The sintered sample had better magnetic properties than the AP sample. It was found that the AP structure had better directional magnetisation than the sintered track, when the sample was rotated within the field plane. Structural analysis of the printed structures included Scanning Electron Microscopy (SEM), Energy Dispersive X-ray spectroscopy (EDX) and Fourier-Transform Infrared Spectroscopy (FT-IR). Structural analysis identified polypropylene and stainless steel 17/4 ph elements within the printed structure and sintered structure. Magnetostriction was simulated using COMSOL and compared with the experimental work. This involved applying a force on one end of the structure while the opposite end was fixed, this was to simulate a bending force. The magnetic field for both simulation and experimental work were very similar in comparison.

5.2 Introduction

The desktop bound metal deposition printer (DMBD) is a printer that is more cost effective than other printing techniques such as selective laser melting and electron beam melting. The printer uses

feedstock, which is a metal embedded into a polymer, made by an injection moulding process. Therefore, it could be economically viable for industry to print via DMBD and improve SHM in their CFRP structures. See chapter 3.4 for in depth comparison of each printer.

The experiments that have been carried out were to perform structural and magnetic characterisation of the printed designs, along with measure the magnetostriction performance of the printed structure (Ahmed *et al.*, 2023). The DMBD printer used to print the designs in based at the Royce Translation Centre at the University of Sheffield. To test the DMBD printer, stainless steel 17/4 ph was selected. A range of designs were printed to test the effectiveness and sensitivity of the magnetisation and magnetostriction. For example, prints with different size gaps and thickness could give a change in magnetostriction sensitivity. Modelling using COMSOL was performed to test the magnetostriction performance in relation to the track distance and block thickness. The DMBD printing process consists of different stages including: as-received (AR), as-printed (AP) and sintered steel (SS), see chapter 4.2 for further detail on the method for printing at each stage. Therefore, each stage was evaluated against magnetic and structural performance.

5.3 Results and discussion

5.3.1 Physical and structural characterisation

5.3.1.1 Microstructure and material characterisation

The polymer used within the DMBD feedstock was identified to be polypropylene (PP) in the AP structure, by using the FT-IR ATR as shown in Fig. 5.1. The black data shows the spectra for AR stainless steel 17/4 ph with a polymer binder and the red data shows the AP desktop printed stainless steel 17/4 ph with a polymer binder. The spectra for the AR and AP look almost identical except for the percentage transmittance. This is due to the sample absorption of infrared light therefore in the AP sample there are more bonds due to layering and extrusion by heat. For both injection mould and as-build samples, there are absorption peaks at 2950 cm^{-1}, 2915 cm^{-1} and 2847.91 cm^{-1}, which suggest that the sample has a C-H_n functional group, similar to the polypropylene published values (Jung *et al.*, 2018) as seen in appendix in Fig. 10.1. The peak at 1738 cm^{-1} is not from the polypropylene spectra, which suggest that this may be a mixture of polymers as the peak is from a C=O stretch which from the literature suggests that the functional group C=O, closely resembles PETE. However, PETE does not contain C-H_n group therefore the FT-IR spectra matches the spectra for PP. The transmittance decreases as the wavelength (cm^{-1}) decreases, which is because of reflection from the sample and may be due to the stainless steel as it has high reflectivity.

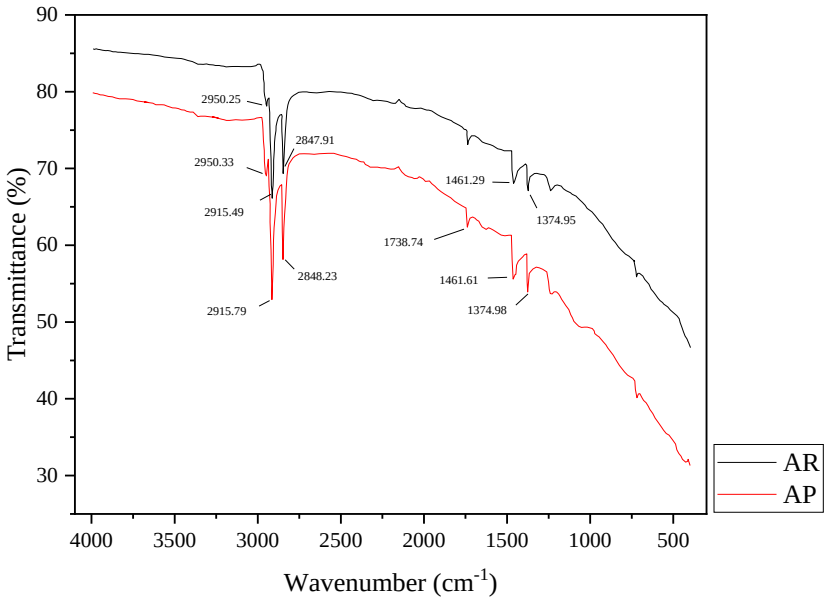

Figure 5.1 FT-IR spectrum transmittance and wavelength of AR (black) and AP (red) samples

Fig. 5.2 shows the metal particles in the AR sample it, can be seen that the sample contains large spherical-shaped particles with a diameter of 25 µm and below. The polymer binder can be seen as a non-spherical shape due to the fibrous nature of the binder. Therefore, the polymer binder holds the metal together by adhesion and restricting the movement of the metal particles therefore, loosely holding the structure together.

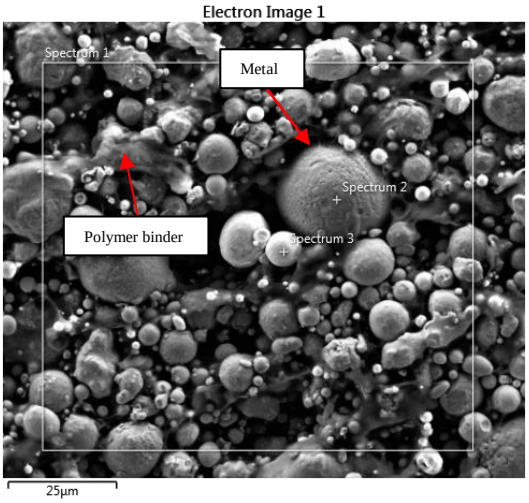

Figure 5.2 As-printed SEM image showing polymer binder and metal sites

Fig. 5.3 shows the SEM backscattered image, element map and composition of the AR, AP and SS samples in (a), (b), (c), (d), (e) and (f), with the weight percent shown in (g) for AR (h) for AP and (i) for SS and given as average (3 data sets) in Table 5.1. The EDS in (b) shows iron and chromium elements loosely bonded with impurities of oxygen. The EDS mapping in (g) shows the elements iron and chromium are present in the AP steel, whereas oxygen and silicon are either impurities or air gaps within the structure. This matches the supplier's element composition for stainless steel 17/4 ph (Desktop Metal, 2018). For the SS sample, the EDS map shows that there is a notable increase in iron as the iron is homogeneous across the sample. In (e), the SEM image shows the boundaries are homogenous and crystallised as the air is removed. In the AR and AP EDS maps, the iron is localised in the metal/polymer mixture. This could mean that the magnetisation would be higher in the SS sample but with an isotropic magnetisation direction.

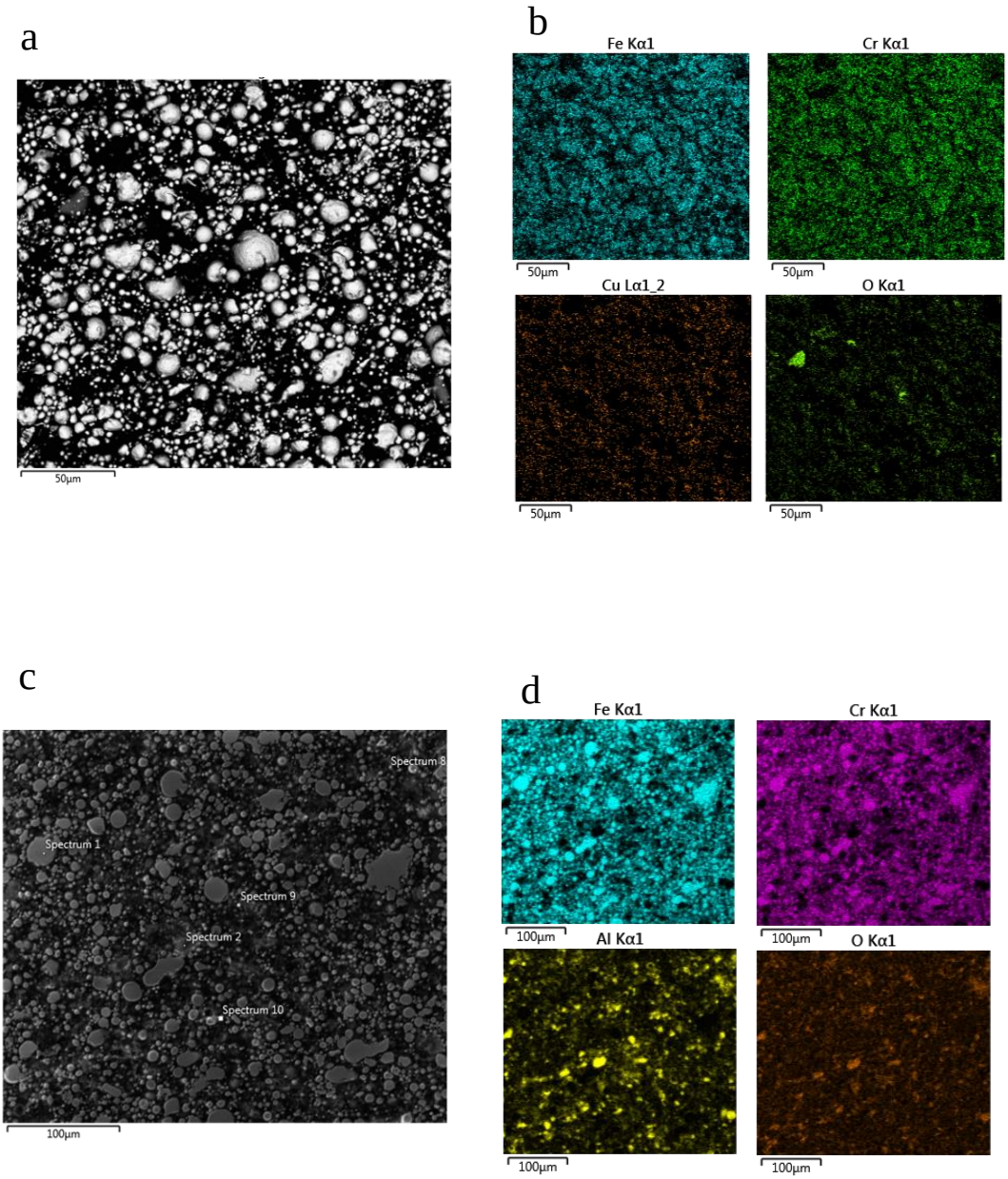

e

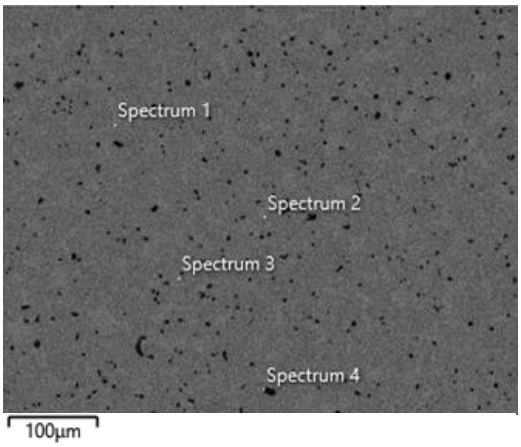
Spectrum 1
Spectrum 2
Spectrum 3
Spectrum 4
100µm

f

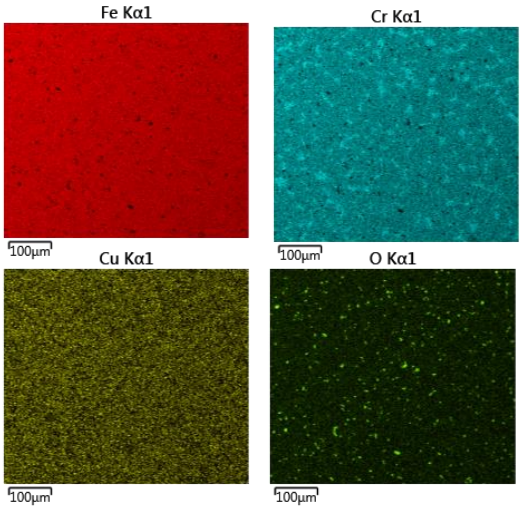
Fe Kα1
Cr Kα1
Cu Kα1
O Kα1
100µm

g

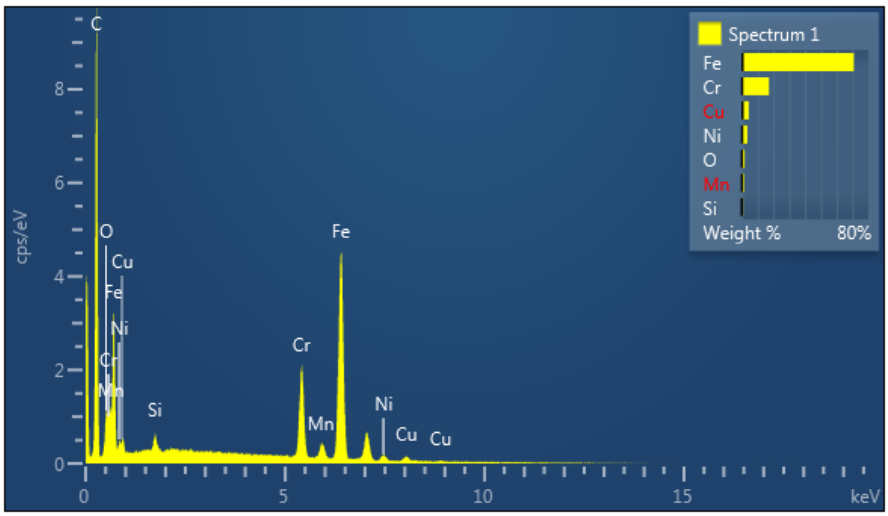
Spectrum 1
Fe
Cr
Cu
Ni
O
Mn
Si
Weight %
80%
cps/eV
C
O
Cu
Fe
Ni
Cr
Mn
Si
Fe
Ni
Cu
Cu
keV

h

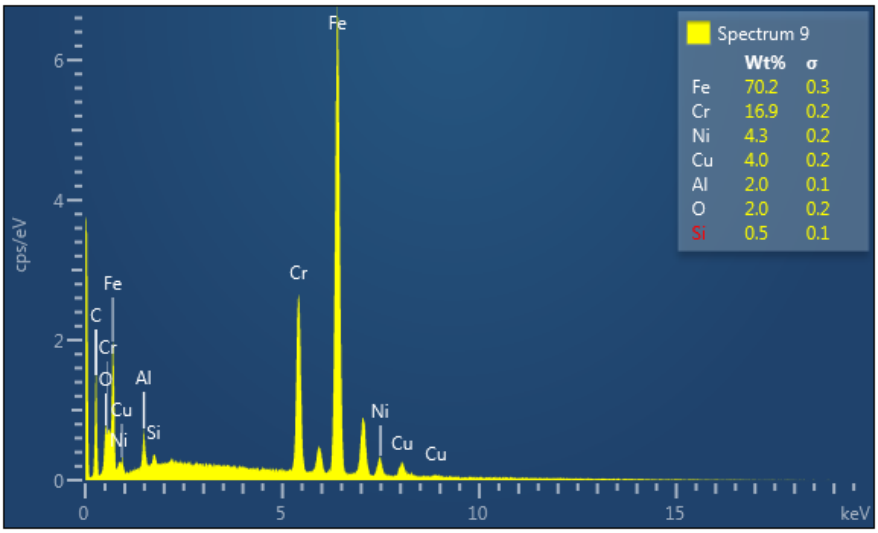
Spectrum 9
Wt%
σ
Fe 70.2 0.3
Cr 16.9 0.2
Ni 4.3 0.2
Cu 4.0 0.2
Al 2.0 0.1
O 2.0 0.2
Si 0.5 0.1
cps/eV
Fe
C
Cr
O
Al
Cu
Ni
Si
Cr
Fe
Ni
Cu
Cu
keV

i

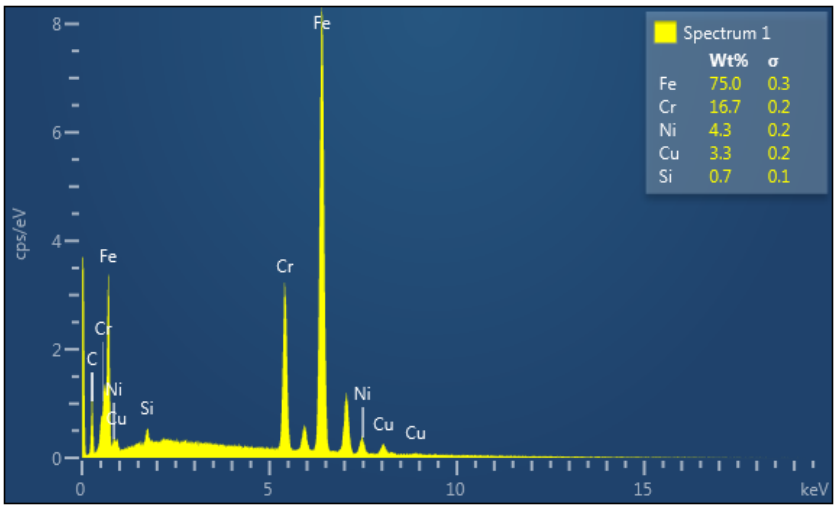

Figure 5.3 AR structure (a) SEM and (b) EDS map, AP structure (c) SEM and (d) EDS map and SS structure (e) SEM and (f) EDS map (g) Weight percent of AR (h) Weight percent of AP and (i) Weight percent of SS

Table 5.1 Average weight percentage of elements from the EDS spectrum of AR, AP and SS samples

Elements	AR	AP	SS
Fe	70.6	63.8	73.8
Cr	17.1	15.5	16.7
C	<1	<1	<1
Cu	4.4	2.6	2.9
Si	1	1	1.1
O	1.9	1.1	<1
Al	<1	10	<1
Ni	1.9	1.4	1.6

However, pores (size of 10 µm) from the honeycomb structure can still be seen in the sintered print as seen in Fig. 5.3 (e) and Fig. 5.4. Although the pores are very small and would have little effect on the mechanical or magnetic performance, if a large number of pores are present, then this can be further improved by using Hot Isostatic Pressing (HIP). HIP applies pressure on all sides of the sample, removing any trapped air by force while at a sintering temperature. Therefore, this would allow grain growth and reduction of air at the same time.

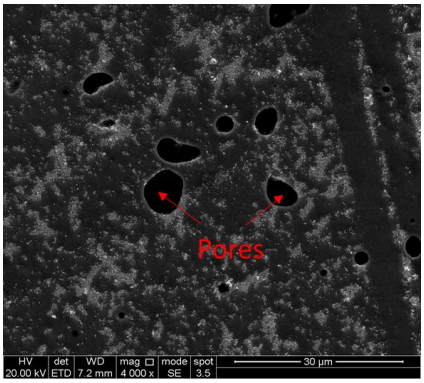

Figure 5.4 SEM image of post-treated stainless steel, showing visible spherical pores of size of 10um

5.3.1.2 *Thermal properties*

Environmental changes in applications such as in the aircraft can occur rapidly during operation and extreme temperature changes in 3D printing can cause the material to deform. It is known that magnetostriction property (both Joule and Villari effect) can be affected by changes in temperature in numerous ways, as shown in (Ludwig and Quandt, 2000; Clark *et al.*, 2005). For example, as seen in theory chapter 2.3, increasing the temperature past the Curie temperature (T_c), removes the magnetic dipole moment from the domain, therefore reducing the magnetostriction property. Galfenol and Terfenol-D were shown to have reduced magnetic properties as the temperature was increased.

Mechanically, as the temperature increases the thermal expansion of the steel also increases, which can change the response of magnetoelastic rate in certain directions such as in plane and out of plane. Printing long and thin structure such as the grid design printed using the DMBD printer, is anisotropic due to the shape anisotropy, therefore would affect the structural and magnetic performance in the X, Y and Z direction. Thermomechanical analysis (TMA) of in plane and out of plane directions was performed to test the mechanical performance as the temperature was increased.

The results from the TMA measurement of the steel track sample (as seen in section 4.4, Fig. 4.25), shows that as temperature was increased, the steel track undergoes shrinkage from room temperature to around 450 K in (a) X, Y and (b) Z directions as shown in Fig. 5.5. However, only one heating run was carried out therefore could not confirm if the rate of shrinkage would be repeated. Above 450 K, the steel expands to 1200K however, the coefficient of thermal expansion (CTE) value is different for the X, Y and Z directions. If the sensor is being used at a temperature higher than 373 K, then this would shrink or contract the steel in the Z and Y direction which could affect the magnetostriction measurement by reducing the mechanical properties of the steel. In the initial temperature increase from 400 K the Y direction shows a higher contraction strain than in X or Z direction. Although it is reported in literature that antiferromagnetic materials undergo negative thermal expansion (Kobayashi and Mochizuki, 2019), this stainless steel is a known ferromagnetic, therefore magnetic ordering is not the main reason for the initial negative thermal expansion. The negative expansion could be due to the

effect from the 3D printed material where flattening of the print layers occurs before the initial expansion. From 500 K to 1200 K both X and Y directions show similar results in (a) as in the X direction the CTE is 16.7 K^{-1} whereas for the Y direction the CTE is 19.2 K^{-1}, however in the Z direction the CTE is much higher at 49.5 K^{-1}. This could be due to the relaxation of the print layers which could increase the length. There will be a large deviation in the Z direction as the thickness of the track is thin. The change in expansion at 1000 K to 1050 K in all X, Y and Z direction is due to the phase change occurring. This can be seen in literature (Hsiao, Chiou and Yang, 2002; Sabau and Porter, 2008) where around 1000 K a phase change occurs from martensite to austenite as the dimension of the sample shrinks and then expands. None of the literature has shown a change in dimension occurring at around 450 K, therefore in Fig. 5.5, the shrinkage seen at 450 K could be due to porosity. Another important test that could have been carried out here is the effect of cooling rate as the sample is heated to 1200 K, as seen in literature is that the cooling has an increased shrinkage rate after the phase transition occurred. As during cooling the change is dimension is present at 450 K in literature, this is reported as a phase change back into martensite.

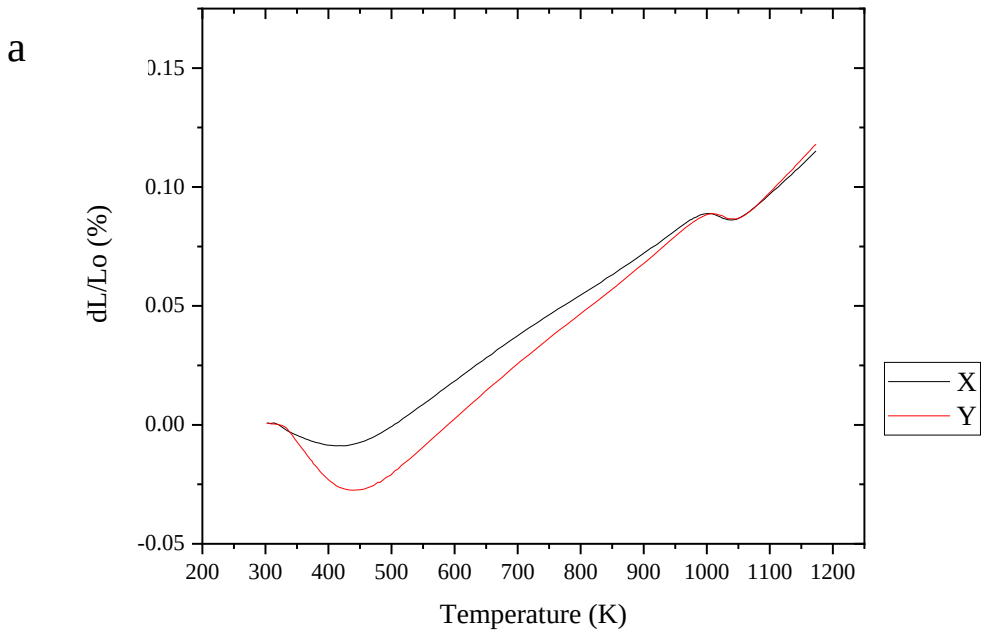

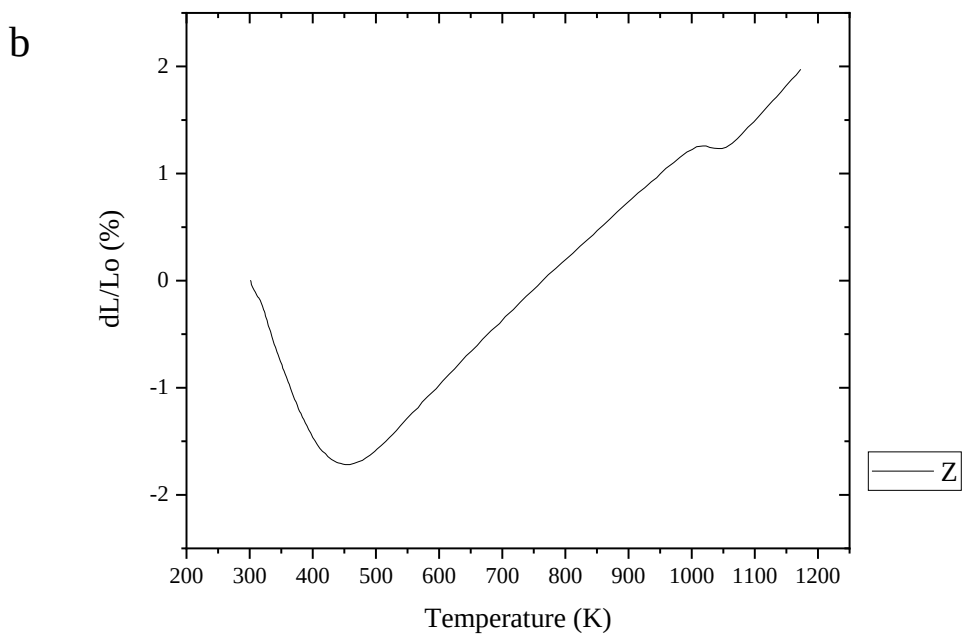

Figure 5.5 TMA thermal expansion of SS track in (a) X and Y direction (b) Z direction

5.3.2 Magnetisation

5.3.2.1 Hysteresis loop

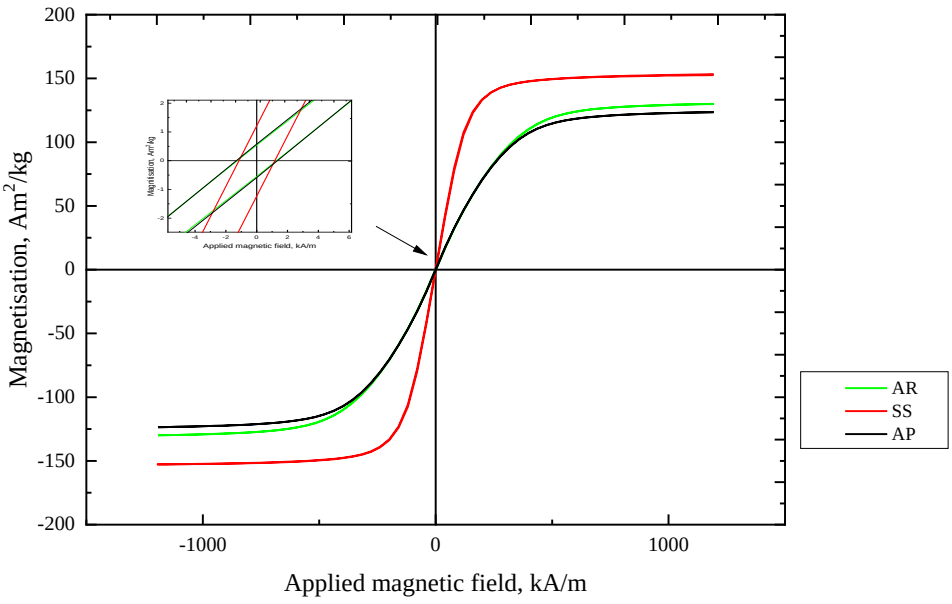

Figure 5.6 SQUID hysteresis loop of AR, AP and SS samples where coercivity, remanence and saturation magnetisation was observed

Fig. 5.6 shows the hysteresis loops for the AR, AP and SS samples. The magnetic field was applied in steps of 40 kA/m to 1200 kA/m for all samples. While the magnetic field step is acceptable for measuring saturation, smaller steps for the coercive force and remanence field was needed as larger steps would have increased error. Therefore, the calculated coercive force and remanence is only an estimate and not a true value. While the applied magnetic field data can be set at 0 A/m, the large jump in field to 40 kA/m would only estimate the remanence, therefore smaller step is needed when magnetic field is near 0 kA/m. Both the AP and AR samples have similar magnetic properties, i.e. the saturation magnetisation, remanence magnetisation and coercivity are within 5 % of each other. It was thought that the AP sample would have a higher saturation magnetisation than the AR sample due to the compaction of the polymer and steel by extrusion. As this measurement is measured by weight of the sample (0.03 g) then this could mean that the composition of the polymer and steel remains unchanged from AR sample to the AP sample. The AR, AP and SS samples saturation magnetisations were measured to be 130, 123 and 150 Am^2/kg respectively. While the remanence magnetisation for the AR, AP and SS samples were 0.560 ± 0.005, 0.590 ± 0.010 and 1.2 ± 0.010 Am^2/kg respectively and the coercivity for AR, AP and SS print were 1.27 ± 0.010, 1.33 ± 0.010 and 1.16 ± 0.010 kA/m respectively. The hysteresis loop of the SS sample showed an increase in the saturation magnetisation of 20 %, and remanence of 50 %, while a reduction in the coercive field of 13 % compared to the AP sample, due to the reduction in the porosity and removal of the polymer. This is expected, as there was less non-magnetic material in the sample, therefore better domain wall motion, which decreases the coercivity. From literature (Khatri *et al.*, 2018) it was shown that applying high temperatures (673 to 873 K), increases the magnetisation by burning off the polymer. For each 10% volume of stainless steel 17/4 ph gained, there is an increase of remanence of about a factor of two. Therefore, both experimental results and literature agree that the effect of removing polymer from the AP sample increases remanence, saturation magnetisation and reduces coercivity.

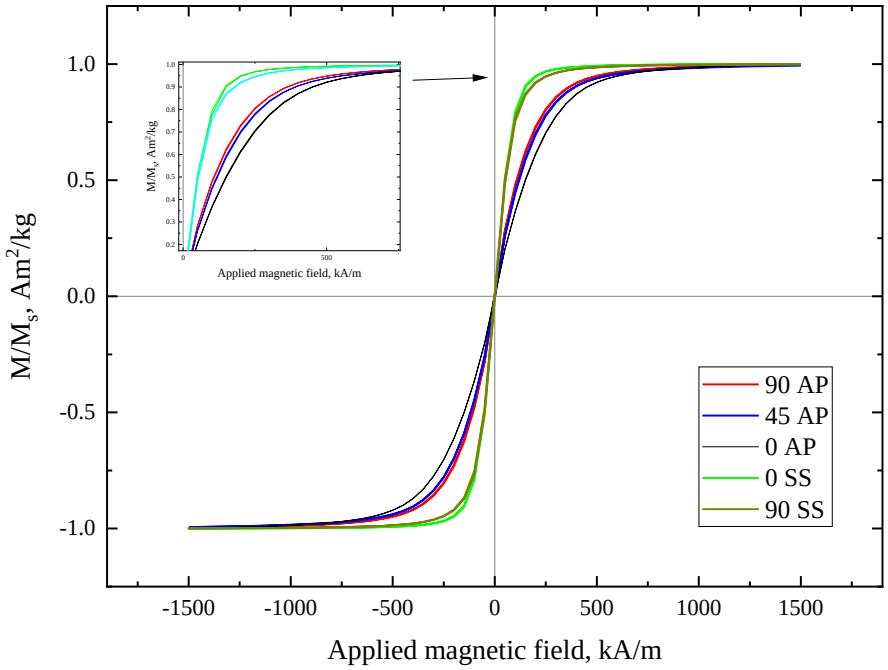

Figure 5.7 Hysteresis loop measured and anisotropy is observed in 0, 45 and 90 degrees angle for AP and SS track samples

Fig. 5.7 shows the hysteresis loops for the AP and SS samples for the magnetic field parallel (0 degrees) and perpendicular (90 degrees) to the base. Anisotropy is observed in the samples, as there are easy and hard axis loops. For the AP track sample at 90, 45 and 0 degrees the saturation magnetisation was 114.340 114.150 and 114.520 Am^2/kg respectively. For the SS track samples, the saturation magnetisation at 0 and 90 degrees was 147.830 and 147.830 Am^2/kg respectively. The remanence magnetisation for the AP track sample at 90, 45 and 0 degrees was 0.970 ± 0.010, 0.960 ± 0.020 and 0.750 ± 0.020 Am^2/kg, while for the SS track sample at 0 and 90 degrees, it was 1.36 ± 0.070 and 1.85 ± 0.080 Am^2/kg respectively. The magnetic coercivity for the AP track sample at 90, 45 and 0 degrees was 1.16 ± 0.020, 1.24 ± 0.040 and 1.25 ± 0.030 kA/m respectively and for the SS track sample at 0 and 90 degrees was 0.760 ± 0.040 and 1.03 ± 0.050 kA/m respectively.

The results for the AP track shows that there was an increase in coercivity and remanence magnetisation at 90 degrees compared to 0 degrees, hence the easy axis lies in the perpendicular direction to the plane. The magnetic anisotropy may be due to the printing stage where the direction of extrusion is directly perpendicular to the track plane. The change in anisotropy field (H_k), is greater from the 0 degrees to 45 degrees than from 45 degrees to the 90 degrees direction. In the paper by (Watson and von Lockette, 2020), they showed that controlling the direction of deposition can influence the anisotropy within the printed sample. Therefore, as the print direction is parallel to the layers, the demagnetisation effect increases, which increases sensitivity perpendicular to the track plane. In (Patton *et al.*, 2019), the paper contradicts these results as they showed the infill orientation is sensitive in the parallel direction.

However, the print location is different from the result shown, as in literature, the print location direction is on top (one continuous print) whereas for this result, the print is done one track direction at a time, reducing the stress and increasing binding between layers. The anisotropy therefore could be due to porosity, as seen in SEM image (Fig. 5.3c) as there is less thermal stress and binding involved, hence more porosity parallel to the print.

The SS track sample shows greater isotropic magnetisation in the in-track plane, as both 90 and 0 degrees hysteresis loops have similar slope and magnetic properties. The difference in the change in coercive field and remanence magnetisation for the SS sample is larger than the AP track sample. However, as the remanence magnetisation is larger at 90 degrees for the SS track sample, there is an increase in coercive field by 26 %, which is unusual and suggest that the easy direction has switched from 90 degrees in the AP track to 0 degrees (in plane) for the SS track. This may be due to the reduction of pores and increase in grain growth in the track direction as sintering causes relief of the internal stresses. This therefore forms a homogeneous structure with greater directional magnetisation than the AP track. The paper by (Stashkov *et al.*, 2019) suggests that the uniform magnetic properties arise due to the γ(fcc)-α(bcc) transformation that may have occurred after the heat treatment. Although the AP structure has anisotropic magnetisation, the effect of heat treatment and sintering has caused the post-treated structure to have isotropic magnetisation. Therefore, further research is needed for post treatment such as hot isostatic pressing or magnetic field induced sintering to obtain anisotropic magnetisation within the printed sample.

The change in temperature can directly affect the magnetic and magnetostriction properties. The magnetisation can be reduced as temperature is increased to the T_c as magnetic dipole are out of alignment. The T_c of stainless steel 17/4 ph is around 900 K as shown in Fig. 5.8, which shows the hysteresis loop of SS track from room temperature to 1000 K in steps of 100 K. From this, it is clear that the temperature increase of steel reduces the overall magnetisation when heated to 1000 K. As seen in chapter 5.3.1.2, the expansion of steel track increases as temperature is increased. Therefore, the mechanical properties are reduced due to thermal expansion and the magnetic properties are reduced due to the temperature going past the T_c. Both affect the magnetostriction performance mechanically and magnetically.

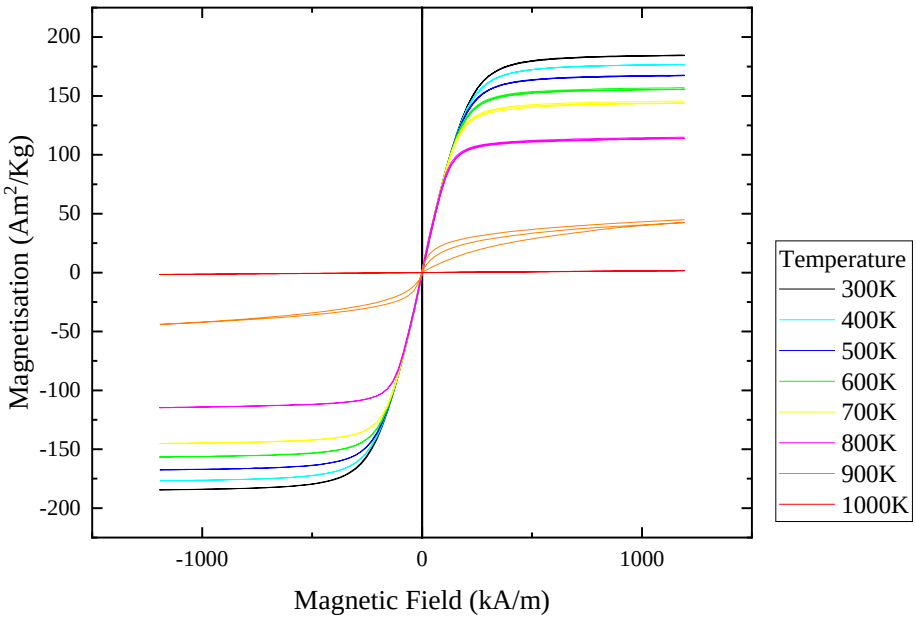

Figure 5.8 Hysteresis loop of stainless steel 17/4 ph SS from 300K to 1000K to observe the Curie point

To measure the directionality of the steel print in easy and hard direction, an H_k is calculated. The difference of H_k in the parallel and perpendicular to the print direction will quantify the directionality of the sensor. This is due to the easy and hard direction of the material where the angle at which it is easy to magnetise, will have an increased gradient whereas the hard direction will have a lower gradient from the coercive force to saturation. Therefore, a low H_k makes it easy to magnetise to saturation magnetisation. The greater difference in parallel and perpendicular H_k would mean the effect of printing has induced directionality and could be used to improve the sensor. Fig. 5.9 shows an example of estimating H_k from the hysteresis loop. Part of the hysteresis loop and the slope from the coercivity is shown. The area of saturation magnetisation and the slope from the coercive field from each AP field direction is shown. Fig. 5.9b shows the estimated H_k of stainless steel 17/4 ph derived from the slope from coercivity and saturation magnetisation in Fig 5.9a. It shows that the AP sample anisotropy at 90 degrees field direction, has 33.2 % less H_k compared to the field direction in 0 degrees. In comparison with the SS sample, the H_k for field direction at 90 degrees has 4.7 % less H_k than at 0 degrees. Although the AP sample has anisotropic magnetisation, the effect of heat treatment and sintering has caused the SS sample to have isotropic magnetisation. Therefore, further research is needed in post treatment such as hot isostatic pressing or magnetic field induced sintering to obtain anisotropic magnetisation within the track.

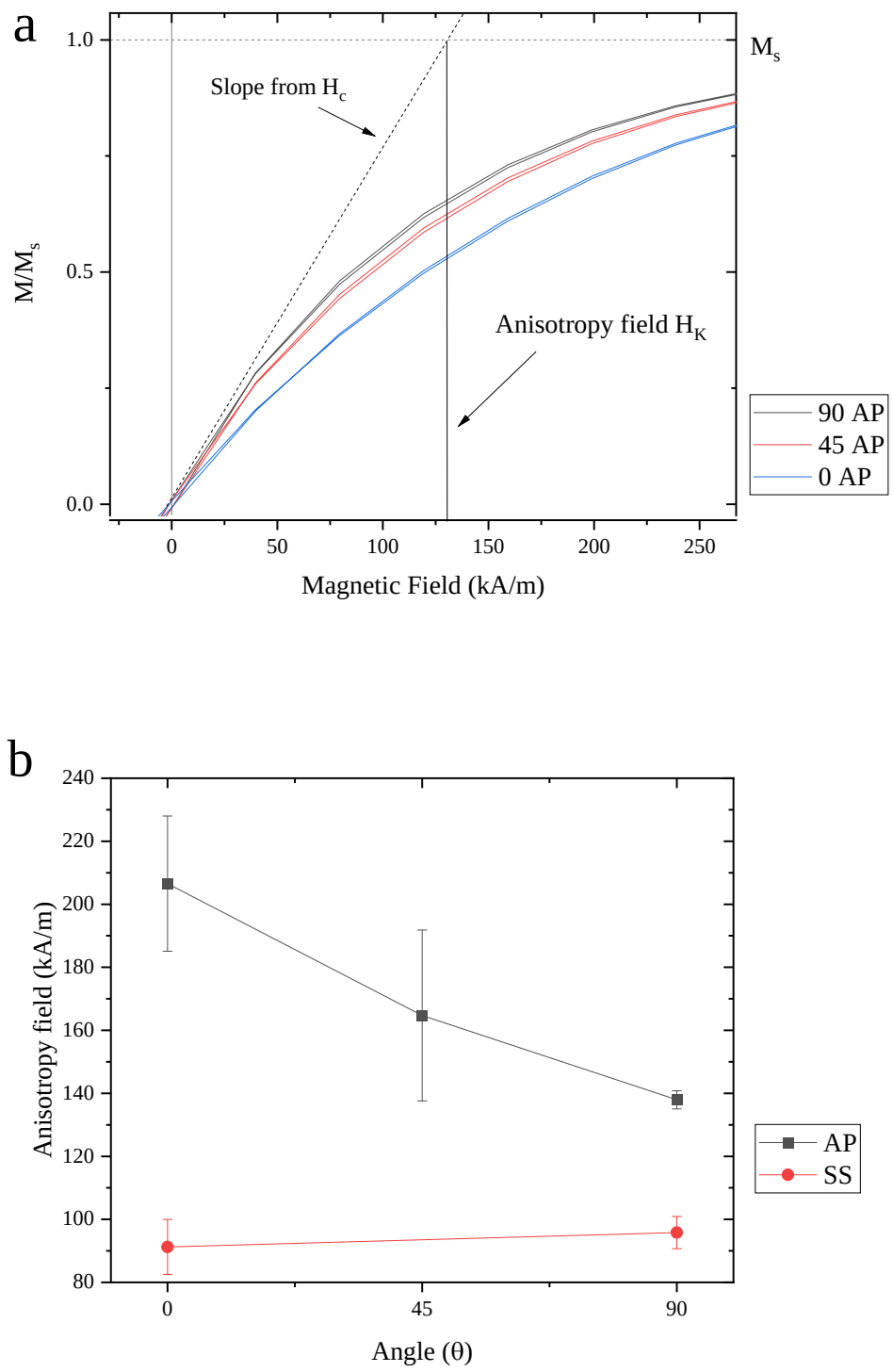

Figure 5.9 (a) Estimated anisotropy field calculation from hysteresis loop and (b) Anisotropy field H_k of as-printed (AP) and sintered steel (SS) in 0, 45, 90 field direction

5.3.2.2 Magnetic camera

The demagnetising field of the SS sample measured on the Magcam shows that there is an interesting demagnetisation arrangement of negative and positive fields out of plane magnetic field as shown in Fig. 5.11. This could be due to the warping of the grid structure during heat treatment. From chapter 5.3.1.2 the thermal expansion in the Y direction is larger than the X direction. Since this is after the sintering stage, the magnetic ordering could occur when cooling after the sintering process below melting temperature (T_m) therefore the domain size and orientation is affected when the steel is warped. In (a), the 1.5 mm track distance SS shows small differences in positive and negative fields. The difference in positive and negative field increases as the track increases to 3 mm shown in (b) and 5 mm shown in (c). Each track can be seen to have its distinct demagnetising field in (c) as the track gap is increased. In (c) it appears to have a higher definition and strength in positive and negative fields than (a). This suggests that the design of the 3D printed grid design plays an important role in domain orientation by warping during heat treatment and sintering.

a

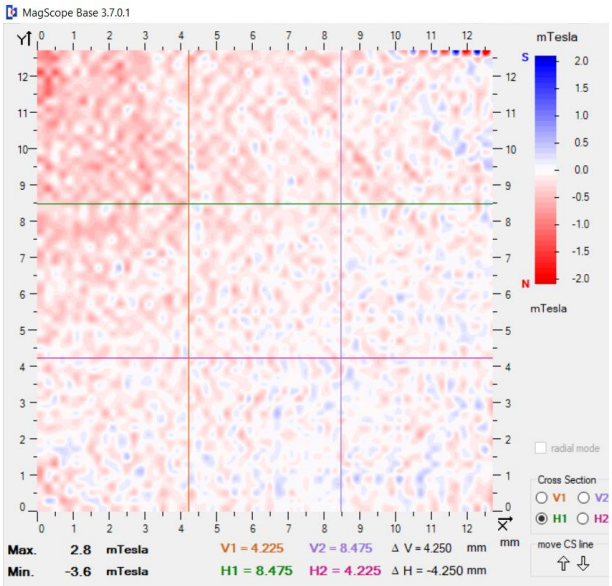

b

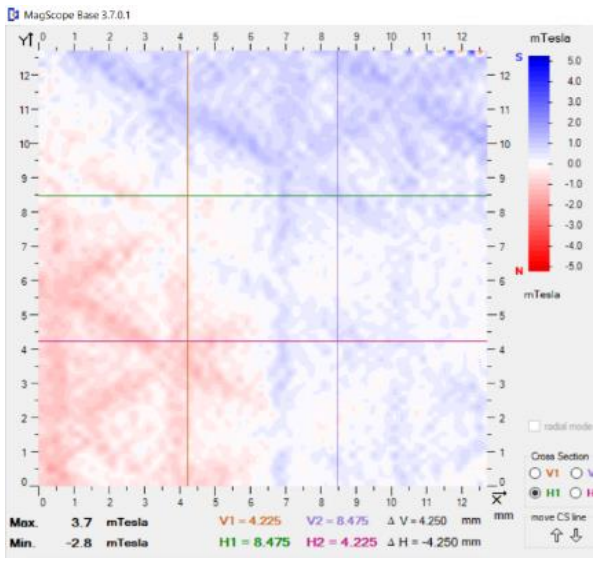

c

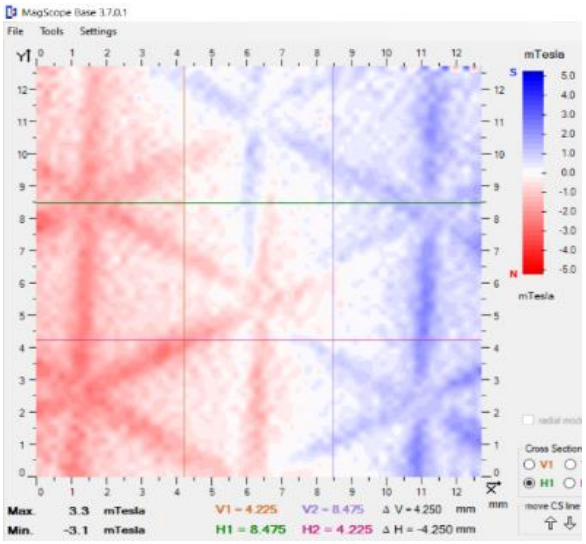

Figure 5.11 Magnetic camera image of (a) 1.5 mm, (b) 3 mm and (c) 5 mm track

a

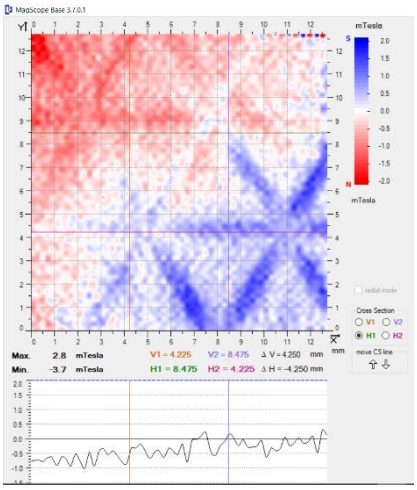

b

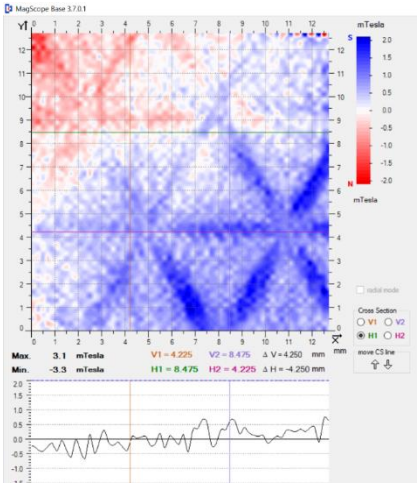

Figure 5.12 Magnetic camera image of the SS sample with (a) 5mm track distance with no stress applied and (b) 5mm track distance with stress applied in the y direction

As demagnetisation was observed in Fig. 5.12, as stress is applied, it would be ideal to show the change is field visually as this further investigates the change in magnetisation in the grid sample. Fig. 5.12 shows the stress applied to the 5 mm grid sample where (a) is an image taken with no stress and (b) is where an image is taken during an applied stress with a vice in the Y direction (in plane). For visibility, the field range was reduced to 2 mT. In comparison, the positive magnetic field has increased out of plane as stress is applied. This therefore shows the dynamics of Villari effect visually when applying stress to the grid structure. Much smaller stress effect on the magnetic camera image was observed for AP sample in agreement with its smaller magnetostriction.

5.3.3 Magnetostriction

5.3.3.1 Villari effect

To test the Villari effect of the 3D printed steel grid designs, an experimental setup was designed as seen in Fig. 4.41 in chapter 4.5.2, was used to apply a force to the SS grid sample and record the change in field. A COMSOL simulation was used to verify the results while using the same parameters as seen in methods chapter 4.2.1 where the model is seen in Fig. 4.3. It is expected that the field will increase as stress and strain applied by the weights, will force a tension and compression force on the grid sample. Therefore, the magnetic moments will align towards the strain direction causing a change in field across the sample. However, the strain applied in one direction on the grid design will not be the same on all tracks as they have an angle of around 60 degrees to each other. This will create a non-uniform strain propagation therefore a field difference across the grid sample.

Fig. 5.13 (a) and (b) shows the result of the COMSOL modelling with different track distances. They show that the highest flux changes are in the middle of the design. There are small differences in magnetic flux density between the (a) 5 mm and (b) 3 mm grid design as both show the flux is higher towards the middle. However, as the 5mm grid design has less structural integrity than 3mm grid design, therefore there is greater change in flux density as strain is higher in the 5mm grid design. An error of 0.001% has been achieved as shown in the convergence result as seen in Fig. 5.13(c)

a

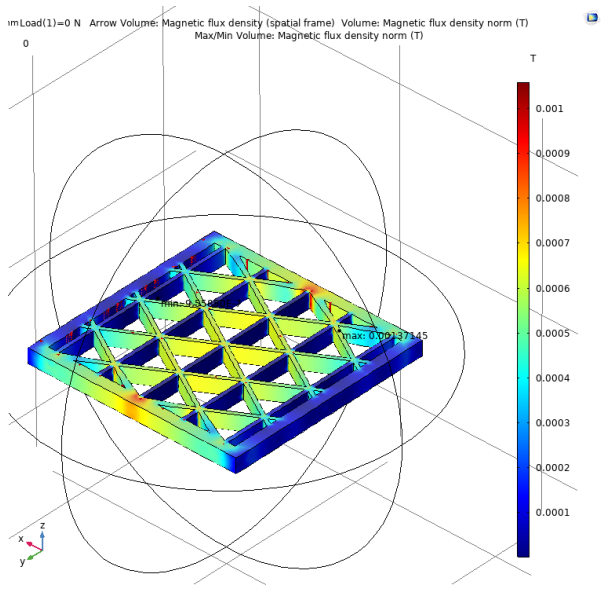

b

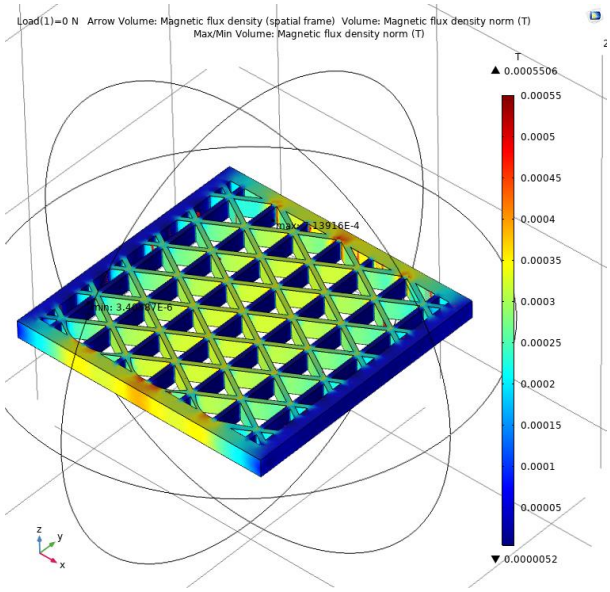

C

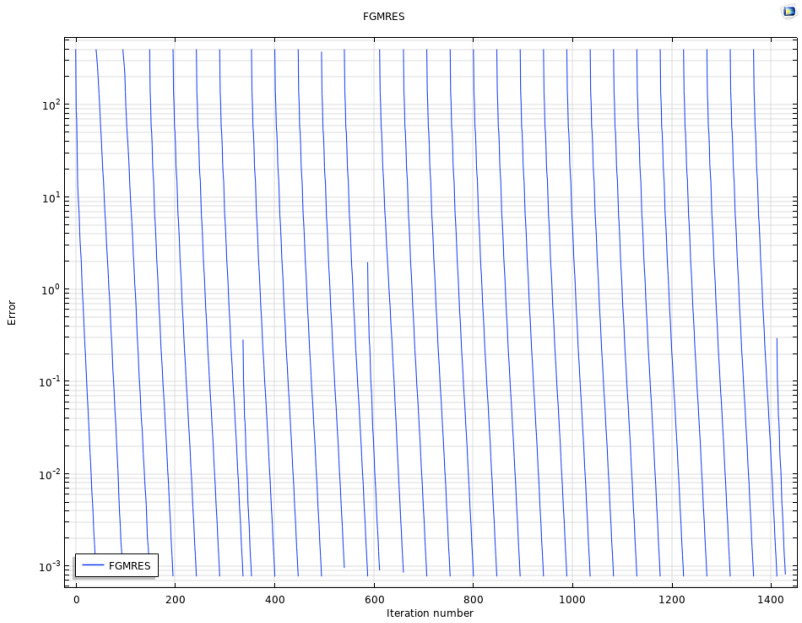

Figure 5.13 (a) 5mm, (b) 3mm track gap COMSOL simulation result and (c) Mesh convergence result

In comparison with the experimental result, there is good agreement between the experimental and simulated values as seen in Fig. 5.14. The results show similar change in gradient in magnetic flux density as weight is added to the structure. The model has an error of ± 2.70 x 10^{-4} T to the experimental data. The simulated data is slightly higher than the experimental result, which may be due to the addition of 10 A/m field in the model. Analytical calculation of the block design shows similar magnetic flux values but shows a larger change in magnetic flux as weight is added. As the analytical calculation gives a rough idea (using simple COMSOL equations) of where the magnetic flux would be as stress is applied, it is not as accurate as the COMSOL model, which is expected. Overall, the experimental result does not show a satisfactory change in field as a function of stress as all the SS prints show a relatively flat gradient, which is not useful for SHM applications. However, this could be due to the higher error and location of placing the Hall probe on to the SS grid sample. The magnetic flux values from Magcam shows that there is a higher flux/stress gradient from measuring the maximum value than using the Hall sensor, which shows a value at a single point. Therefore, measuring the magnetic flux from a single point would be eliminating the change in flux across the sample as seen in the Hall probe experimental values. From simulation results seen in Fig. 5.13 (a) and (b), the highest flux lies around the midpoint of the steel structure. However, tracks that are perpendicular to the stress, show a reduction of magnetic flux compared to other tracks in the structure. The overall change in field is better measured using a Magcam that has a larger area of measurement rather than at one single point.

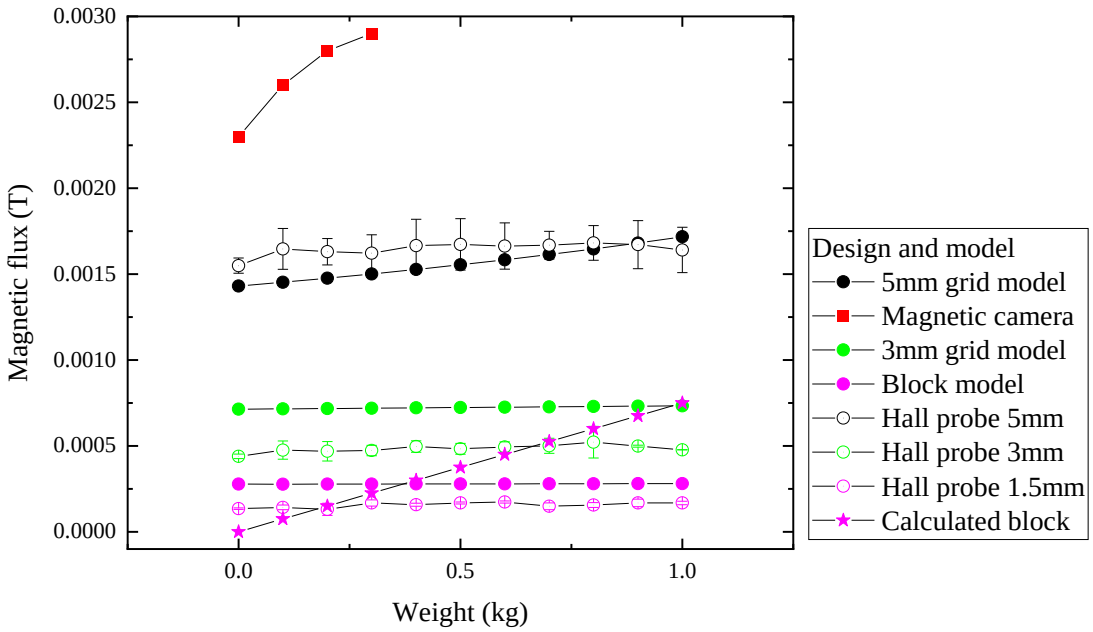

Figure 5.14 Experimental and simulation comparison for stainless steel grid structure

In literature (Ara *et al.*, 1986; Ara, 1989) they have reported the inverse magnetostriction values of various stainless steel (SUS 403) by compression and tension of a steel rod as shown in Fig. 5.15. The values are higher than the experimental results of around 2.0 x 10^{-2} T, this is due to better magnetic properties such as lower coercive force (6 to 15 Oe). However, some grade of steel were peaking in the range of 5 x 10^{-3} T. The experiment conducted in this work was limited and used a weight of 1 kg whereas in literature, the weights applied to the steel was greater and applied a higher stress to the steel using a weight of 4 kg/mm^2. Therefore, the steel used in this work, even though lower weight and stress was used, is comparable to steel in literature work. However, the design and structure of the 3D printed steel in this work has not been tested for Villari effect for sensor applications. It is important to test other designs that could show a good level of the change in flux as a function of stress where a steel rod may not be suitable for SHM due to design limitations. Another factor to consider is the temperature, as in (Ara, 1989) and Fig. 5.15, they have shown that a heat treatment temperature rises from room temperature to 573 K improved the Villari effect slightly. The T_c of the steel tested were between 983 K to 1000 K so well below the T_c in the literature. They have shown that further heat treatments to the steel can improve the magnetostriction effect.

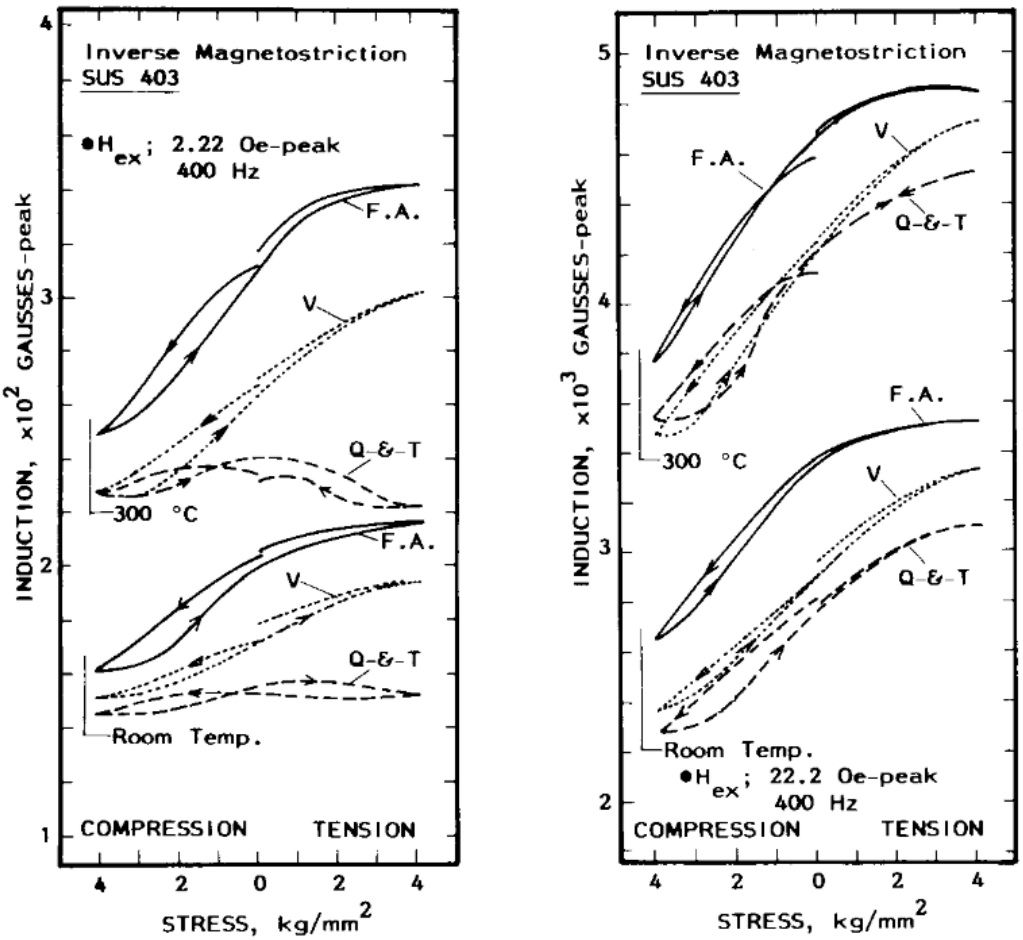

Figure 5.15 Inverse magnetostriction of SUS 403 and its changes with heat treatment and temperature; measured at an excitation of 2.22 Oe (peak)/400 Hz (left) and 2.22 Oe (peak)/400 Hz (right) (Ara, 1989)

5.3.3.2 *Joule effect*

The Joule effect of the DMBD stainless steel 17/4 ph was measured using a strain gauge as shown in chapter 4.4.2.2 which shows the methodology of using the strain gauge to measure magnetostriction. The strain gauge was attached to the 1.5 mm track gap steel structure, the results are comparable with literature values from (Bakker, 1989) as shown in Fig. 5.16, with saturation magnetostriction around 26 ± 5.8 ppm for printed steel. In literature the results are varied for duplex stainless steel as it states for anisotropic material that the saturation values are 15.5 ± 3.3 ppm and for steel that are isotropic the saturation values reduce to 5.7 ± 2.2 ppm. The preliminary magnetostriction constant for 1 mm SS 17/4 ph was measured to be around 26 ppm in the positive field direction (Fig. 5.16). The martensite steel showed equiaxed grain structure in the SS part. Compared to literature, the highest magnetostriction constant for duplex steel achieved was around 18 ppm (Bakker, 1989). Interestingly the published value shows a sharp increase in strain and saturates around 48 kA/m whereas the 3D printed SS sample saturated around 300 kA/m. This is due to the structure of the sample, as in the literature they have used a cylinder shape where the easy axis is along the cylinder axis whereas this result has a rectangular type

shape, therefore reaches saturation later due to the shape and size of the sample. However, the results do appear to be similar to the published values as most duplex steel lies between 5 ppm to 18 ppm depending on their composition and microstructure.

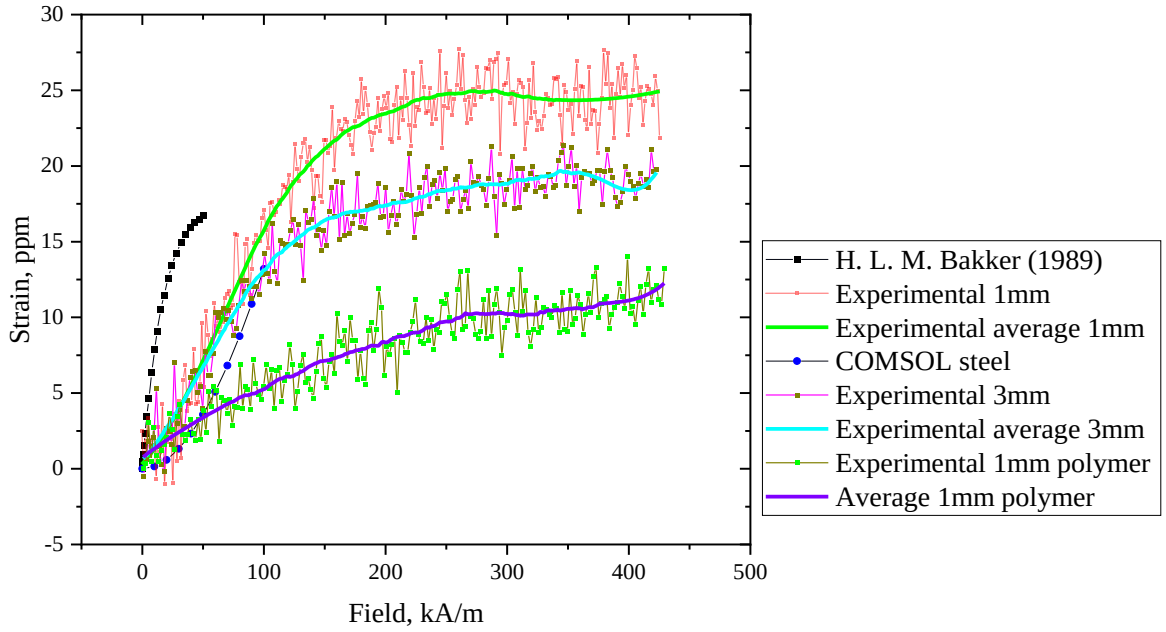

Figure 5.16 Comparison of duplex steel and stainless steel 17/4 ph in the parallel direction

The magnetostriction constant for the printed grid designs was measured for the AP sample and the SS sample parallel and perpendicular to the magnetic field as seen in Fig. 5.17. The SS sample shows a maximum magnetostriction constant of 26 ppm whereas compared to the AP sample of 12 ppm, parallel to the magnetic field. There is also an effect due to design, as the 3 mm SS magnetostriction is slightly lower than the 1 mm SS grid design magnetostriction. When the field is applied perpendicular to the designs, the magnetostriction constant reduces near to zero magnetostriction.

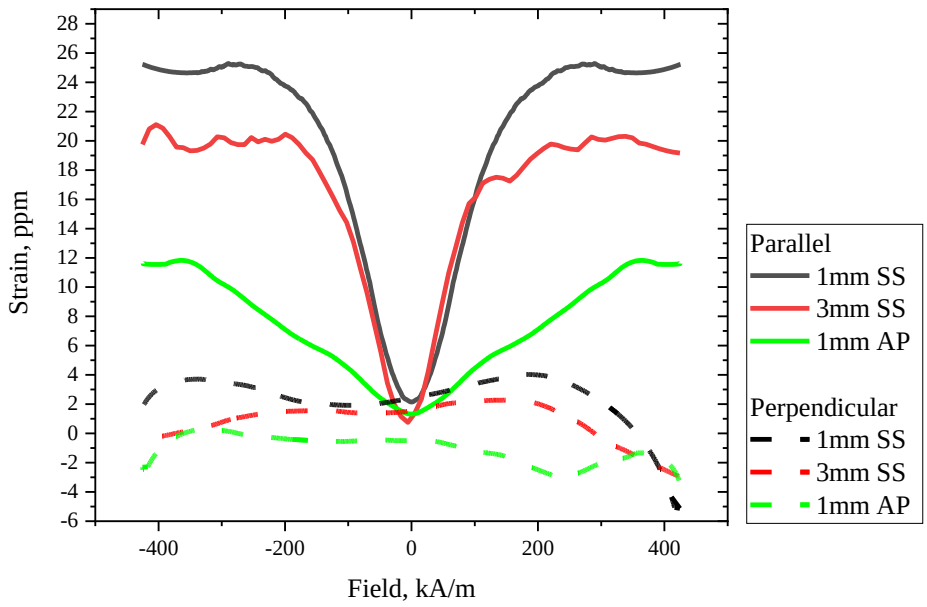

Figure 5.17 SS (black and red line) and AP (green line) magnetostriction parallel (solid line) and perpendicular (dash line) to field

The magnetostrictive result shown in Fig. 5.17 shows that the AP sample had a smaller magnetostriction constant compared to the SS sample. This is due to the presence of non-magnetic components such as polypropylene in the AP sample, that will affect the magnetostriction constant by restricting the steel domains in the parallel direction to the field. Further for the two SS samples with 1 mm and 3 mm gap, the field at which the magnetostriction becomes saturated is reduced by 50 % compared to the 1 mm AP. This is due to the magnetic domains being more free to orientate towards the field direction than the 1 mm AP sample. Furthermore, the field at which saturation magnetostriction occurs for the AP sample is at 400 kA/m which forms a broader strain/field rate. The broadening of the rate is due to the polymer binder that restricts orientation of the metal particles to align towards the field. Interestingly the polymer could be used to manipulate magnetostriction either by tailoring the sintering process e.g. hot isostatic pressing or designing porous structures in the future. For the negative field, the 1 mm SS sample has a higher magnetostriction constant than the 3 mm SS sample, due to the track distance of the print, as the 1 mm track SS print reaches around 26 ppm. For the positive field, the strain for both samples reaches around 22 ppm. This may be due to the positioning of the sample print in the electromagnet as the saturation magnetostriction at a field is not the same for both sides. For example, the saturation magnetostriction is at -318 kA/m whereas the saturation at the positive field is at 400 kA/m, therefore the positive field may have not fully saturated.

Air gaps or porosity in the printing process can affect the mechanical properties such as toughness and modulus however the same is not said with magnetic properties. In (Mohaideen and Joy, 2014), they explore the effects of sintering cycles and magnetostriction on cobalt ferrite nanopowders. The increase

in density due to the sintering cycles was found not to be proportional to magnetostriction. However, intergranular pores had an effect on magnetostriction.

When the magnetic field is applied in the perpendicular direction to the strain gauge as seen in Fig. 5.17, the saturation magnetostriction remains the same for both the AP and SS samples, as they are both near to zero magnetostriction. However, after plateauing the strain reduces to a negative value for both positive and negative fields at around 239 to 318 kA/m. This is more prominent in the 1 mm SS sample, where the rate of negative magnetostriction is the highest of around -8 ppm. This may be due to the design rather than the microstructure of stainless steel 17/4 ph as the change in design from 3 mm SS sample to 1 mm SS sample increased the negative effect.

5.4 Summary

A magnetic sensor of a size of 25 x 25 x 2 mm grid was successfully printed using the DMBD printer. This work explores the structural and magnetic properties of each stage in printing. Structural analysis by FTIR and SEM of the AP structure shows that there are polypropylene and stainless steel 17/4 ph elements. Further analysis using EDS and element mapping showed the composition of polymer and steel in the AR, AP and SS structure. Magnetisation and anisotropy measurements showed that there is an increase in magnetisation after the sintering stage. The track in-plane shows the stronger uniaxial magnetisation direction than out of plane track direction. It was shown that the steel sample has a Curie temperature around 900 K, which makes the steel useful for sensing in extreme temperature environments. SS showed a reduced anisotropy than the AP structure. This is due to the removal of polymer within the structure reducing non-magnetic particles and inducing isotropic behaviour.

The magnetic camera was used to image the demagnetising field of the SS grid structure. The 5 mm track distance showed greater difference in the positive and negative demagnetising field than the 1 mm track distance, which may be due to warpage and expansion during heat treatment. Experimental data, COMSOL modelling and analytical calculation of the Villari effect, shows similar magnetic flux values however the gradient of flux as a function of stress remains flat in the experimental result when measuring at a single point. The magnetic camera shows a larger gradient in magnetic flux density as a function of stress than measuring on a single point. The Joule effect was measured using a strain gauge and change in magnetic field using an electromagnet. Stainless steel structure shows a similar trend with literature values of steel. The stainless steel tested in literature for magnetostriction varied in values with highest of 23.3 ppm. The saturation magnetostriction measured in literature is lower than this work however it reached saturation at a higher rate, which may be due to the shape and size of the sample.

It was concluded that additive manufacturing of magnetostrictive materials by extrusion is a viable option as shown in results. However, to print large thin samples with a sample size of 100 x 100 x 2 mm, extraction based printing is not suitable as the percentage of shrinkage and warping in heat treatment can damage complex shapes as shown. This is due to the difference in thermal fluctuation in certain areas of the samples which will lead to fracture. Another aspect of printing magnetostrictive materials is the ability to produce a sample with anisotropic magnetisation. AP samples do show an anisotropic behaviour however the structural and mechanical properties are not suitable for use in service. Material jetting or inkjet printing could be a way of printing anisotropic structure by selecting materials or designs. Types of anisotropy which can be made are natural anisotropy (material dependent) and forced anisotropy (field dependent). Manipulating anisotropy during printing would otherwise be difficult in extrusion or PBF printing.

Chapter 6

Inkjet printer results and discussion

6 Inkjet printer results and discussion

6.1 Abstract

For inkjet printing in the work, magnetite and nickel nanoparticle (NP) dispersions were used with a Jetlab IV drop on demand (DOD) printing system. These soft magnetic NP allow for design flexibility such as printing thin sensors with an advantage over the additive manufacturing into 3D structures. The NPs were simulated under bending using the COMSOL multiphysics software. It was found that there was a significant effect on the change in field as a function of strain when the gap between each droplet changed on the substrate. The ideal gap distance was found to be between 0 mm (touching) and 0.1 mm as the field was highest in the Y direction at a radius of curvature of 100 mm. For experiments, different substrates were used to test the printability and wetting angle of the inks which were glass, paper and kapton. It was found that paper was ideal to print on as the wetting angle was increased by higher solvent absorption and roughness. However, kapton and glass were printable when they were pre-heated to around 373 K, which increased solvent evaporation and prevented a low wetting angle. Hysteresis loops for magnetite and nickel NP were measured using the SQUID magnetometer. It was found that magnetite NP had a larger saturation magnetisation and lower coercivity than the nickel NP, therefore the magnetite NP is ideal as a softer magnetic material for SHM than the nickel NP. Viscosity for each ink was measured to determine the printability in using the inkjet printing system. Both inks were suitable for inkjet printing as the viscosity was below 20 cP. Jetting the NPs by using the JetLab 4 system (with a piezoelectric print head and 60 µm orifice size nozzle), the droplets were not as consistent due to the NP size and solvent mixture. Jetting consisted of satellite droplets and clogging which interrupted the printing process, this was due to amalgamation of the NPs. SEM showed that larger NP were deposited and were not homogeneous in each droplet. EDS confirmed that elements of iron and nickel were present in magnetite and nickel respectively. An optical profiler measured the roughness of magnetite print where it showed that paper and kapton had 0.5 µm roughness value whereas glass showed a lower roughness value of around 0.3 µm, which was as expected. Both a Hall

probe and an inductor coil measured the magneto mechanical sensitivity for each print. The sensitivity was found to be too small to be detected by a Hall probe while the inductor coil was able to detect the inductance when the print was strained. The different designs that were printed to be tested for sensitivity to strain were coil, uniaxial patch, grid and rectangular block. The best print design that had the best field/strain change was the coil print. It was found that the signal to noise was increased by changing the placement of the inductor coil, adding more NP ink layers and adding a capacitor. A coating applied by spin coating or spray coating helped to protect the print from external damages.

6.2 Introduction

Printing sensors via inkjet printing has been around for decades, for example printing copper conductive lines (Park *et al.*, 2007) and various sensors on PCB board for electronic applications. More recently, magnetostrictive actuator embedded in a polymer matrix has been developed by (Gullapalli *et al.*, 2021) which have shown that the magnetic field changes as a function of strain. Printing magnetostrictive sensors could prove to be an advantage by saving cost, manufacturing and improve monitoring of CFRP.

The JetLab 4 inkjet printer manufactured by Microfab technologies inc, works by drop on demand technique, where the piezoelectric print head can be programmed to specify each drop. Jetlab has been used to successfully print silver ink for electronic application in literature by (Hamad, Archacki and Mian, 2020), therefore could be used to print metal and magnetic NP inks. However, the downside is that the inks are expensive to purchase, as the nanoparticles need to be less than 100 nm in diameter to avoid clogging (depending on the size of the print head). This is due to the ink formation of metal NP and depends on the solvent for ink stability. As the metal NPs tend to form together, the solvent prevents amalgamation of NPs. Reduction of amalgamation is desirable as the viscosity increases when particles clump together. Another disadvantage of inkjet printing is that each print will contain a small amount of magnetic material due the solvent in each droplet (for stability), this could be rectified by printing multiple layers but this can be time consuming. This leaves a gap between inkjet printing (thin structures) and PBF (bulk printing). Printing thick magnetostrictive materials has been achieved and studied in literature by (Grabham, White and Beeby, 2000; Grabham, Beeby and White, 2001). Screen printing was used and developed to print Terfenol-D. However, the result showed that the print contained significant air gaps within the print, which could influence the sensor performance. Therefore, inkjet printing is a viable manufacturing process, which can print ferromagnetic materials with controllable jetting of each droplet, resulting in improved sensor performance. The inkjet-printed structures were subjected to a force where a change in magnetic field is detected (Villari effect). The change in magnetic field, could be affected by direction of printing, design, material choice and additive

layering. Therefore, this chapter will explore the effect of printing and testing whether the design or printing factors affect the sensor sensitivity. This will allow better designs to be printed in the future for SHM application. Magnetite and nickel ink were purchased from Nanoshell Ltd. The inks contained Dimethylformamide (DMF), isopropanol (IPA) and water for magnetite ink whereas nickel ink contained and N-Methyl-2-pyrrolidone (NMP) and water.

Simulations were performed to show the effect of gap distance and size of each droplet for the change of field as a function of strain. This was to see whether the jetting parameters used in JetLab IV printing system which can be tuned to vary the size and gap between each droplet, affect the magnetic field measured as a function of strain. COMSOL multiphysics was used to model the droplets gap field changes as it has proven to model (using the in-built magnetostriction package) the change in field as stress was applied to the desktop printed samples in chapter 5.

For the experimental result, strain was applied similar to the experiment procedure in chapter 4.3 where the inkjet-printed magnetic material was strained over a bend rig with known curvature of radii. To evaluate the magnetite prints as a sensor, an inductance or Hall probe was used while the print is strained over a known bending rig radii. A range of bending rigs were used from 1000 mm to 100 mm radii in this project. The purpose is to strain the design during the bending test to replicate a force applied to the CFRP structure such as a wing of an aircraft, which undergoes a continuous strain during flight. The sensitivity is determined by the gradient change of strain to field.

6.3 COMSOL Simulations

To simulate the inkjet-printed magnetostrictive material, a bend test model was created as seen in method chapter 4.2.1.2. This was to simulate the bending test method performed in the experiment seen in chapter 4.3. Since the magnetic NPs were printed via DOD, the simulation created is designed to test the changes in field of an array of droplets on a silicone substrate. The simulation was performed by simulating cured magnetite in solid form, this is because the solvent in the ink would have been evaporated by UV light and left with just magnetite on the surface. Therefore, COMSOL simulates magnetite as a single solid object. In section 4.2.1.2, the material and magnetic properties used are shown in Table 4.2. Non-linear model was performed in COMSOL using equation 4.2 non-linear isotopic model. Unlike simulations performed previously where nodes are connected to each other such as in the extrusion printed steel sample, the inkjet printed NP are confined to individual droplets where the magnetic moments and dipoles interaction are measured for each droplets. Therefore, magnetostriction is treated differently for each droplets as applied stress is not transferred, only the magnetic field and dipole plays a role field interference in neighbouring droplets. Fig. 6.1 (a) shows the

schematic of the droplet created in COMSOL for simulating bending of each droplet on silicone substrate. The mesh convergence shows an error of 0.001 % as shown in Fig. 6.1 (b).

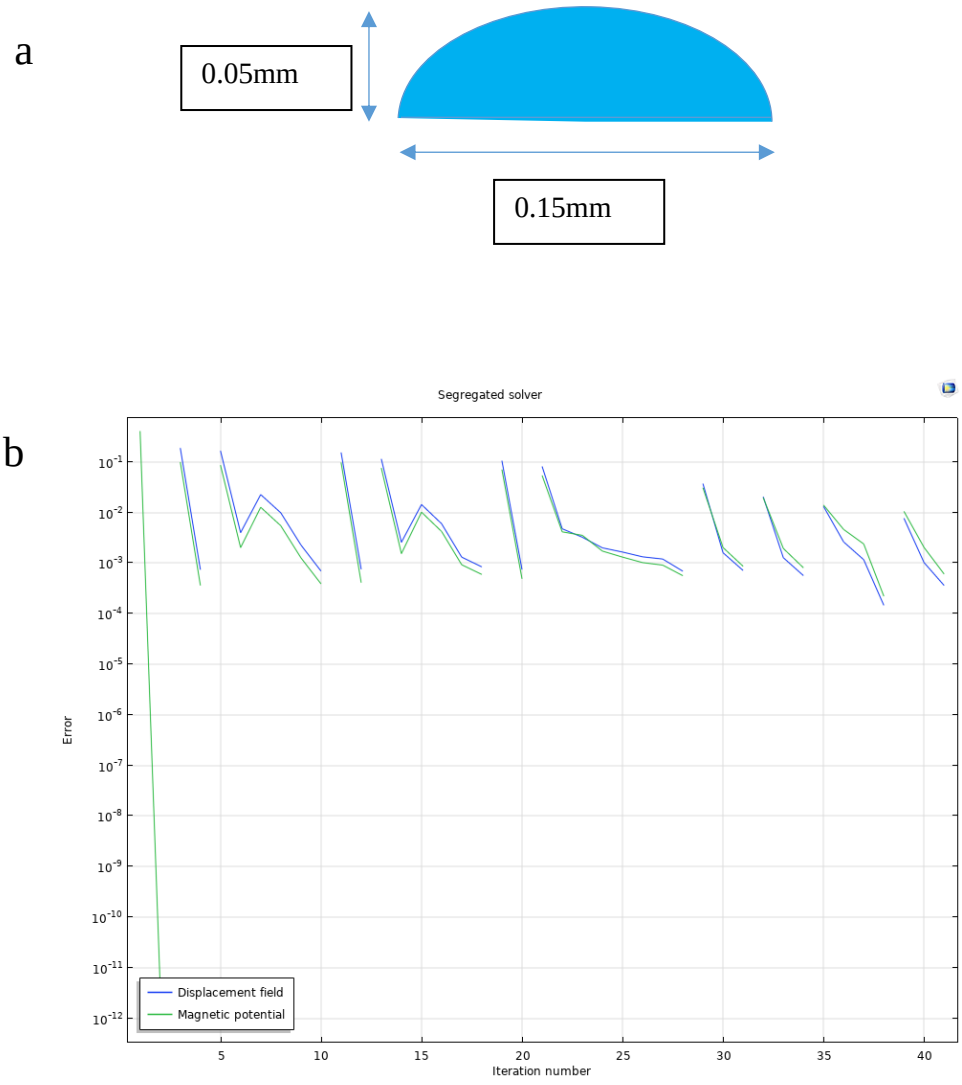

Figure 6.1 (a) Droplet size schematic in COMSOL model and (b) mesh convergence study with displacement and magnetic field solver

The method for simulating the inkjet-printed droplets are shown in methods chapter 4.2.1.2. The droplets were strained on a silicone substrate over a bend rig with a known curvature radius. The distance between each droplet is changed. Therefore, the interaction of droplets will be explored, including when the droplets are in close proximity or overlapping each other during bending. It is known that a bar undergoes tension and compression during bending forces however, for bending droplets, the effect is reduced to the individual droplets. Therefore, the sensitivity depends on the interaction of neighbouring droplets and their magnetic dipole.

The results from the COMSOL simulation shows the direction of the magnetic field vector for each node as seen in Fig. 6.2. The field intensity can be seen in the elements and contour where the colour is mapped against the field strength for example, red is highest and blue is the lowest field calculated. It can be seen in Fig. 6.2 for gap distances of (a) -0.1 mm and (b) -0.05 mm, the direction of magnetic field is cancelled out due to overlapping of the magnetite droplets. This makes it difficult for the field to change to normal to the plane. The field needs to be rotated to the normal of the plane due to sensor detection in the experimental set up. The inductor used to detect the field, detects the change of inductance from the top of the print, therefore the droplet gap with the best change in field with strain in the y direction is desirable for SHM. As the droplet gap is increased to (c) 0 mm, i.e. when they are touching, the change in fields are isolated towards the point in between each droplet. There is an interaction between the field of neighbouring droplets magnetic dipole, as seen in (c), which appears to show an increase in the change in field with strain. The field magnitude peaks at 0.05 mm gap distance where there is strong directional change in the Y direction as the interaction between droplets is reduced seen in (d). As the gap is increased the change in magnetic field is reduced as there is less interaction between droplet's magnetic dipole and reduction in array of droplets across the substrate as seen in (e) with a gap of 0.1 mm.

a

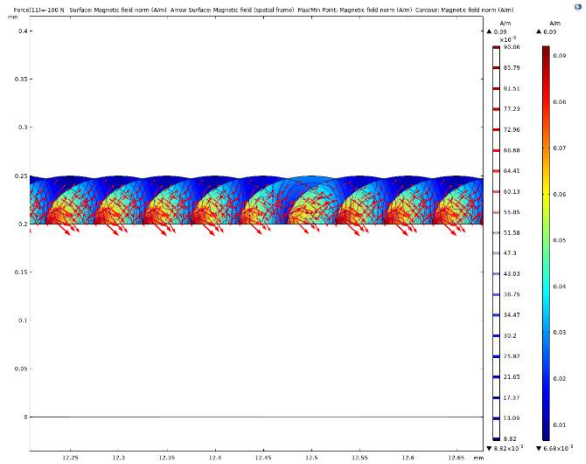

b

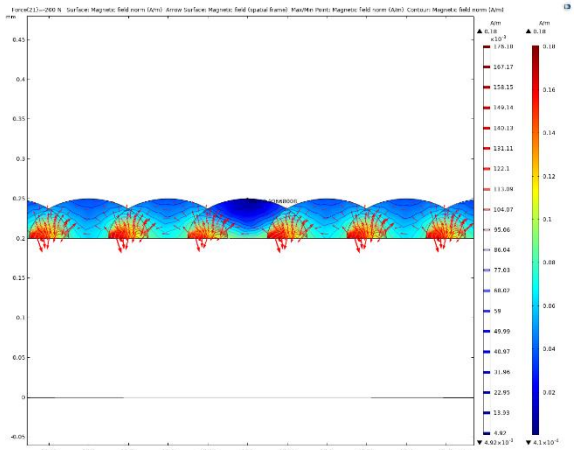

c

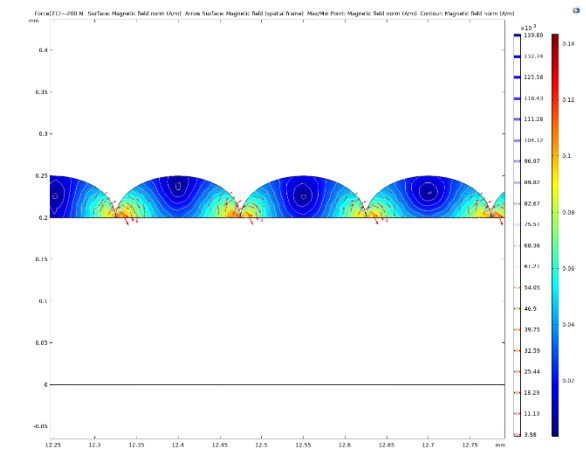

d

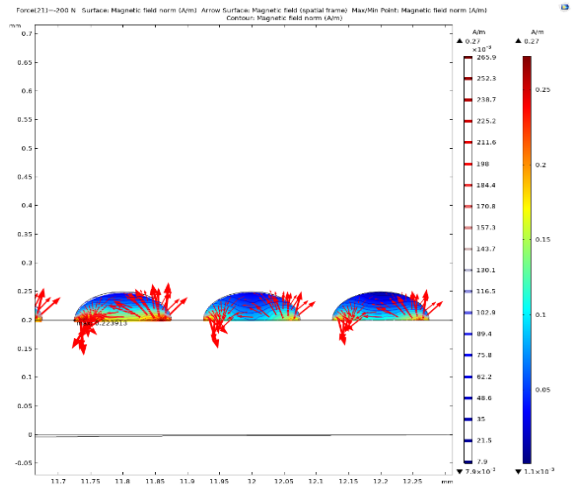

e

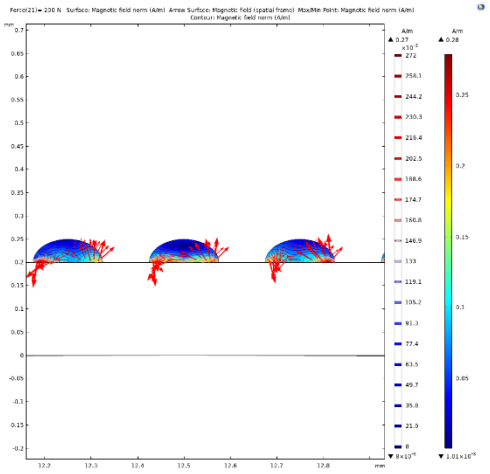

Figure 6.2 Magnetic field of magnetite droplet gap (a) -0.1,mm (b) -0.05mm, (c) 0mm, (d) 0.05mm, (e) 0.1mm

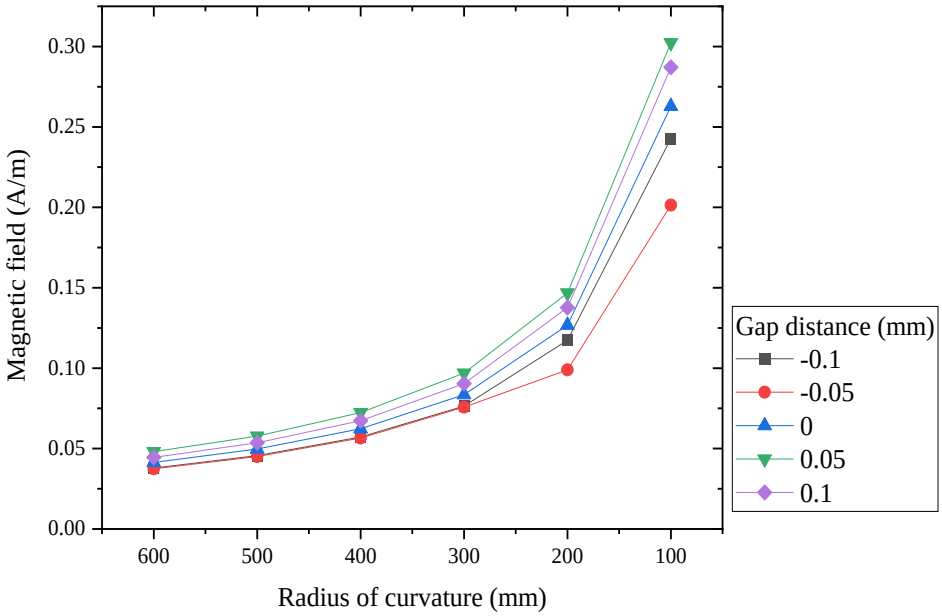

Figure 6.3 Change in gap and magnetic field of magnetite droplets (0.15 x 0.05 mm) while bending over a known radius of curvature

The maximum magnetic field was recorded for each radius of curvature once the displacement of the substrate reached zero, this would mean the substrate is fully in contact with the bend rig therefore the field at that point was recorded. Fig. 6.3 shows an increase in magnetic field as the strain is increased, demonstrating the Villari effect in the droplets. Where the magnetic field changes determines the dynamics of magnetic moment in the material, therefore it is related to how well the material performs under strain. Most importantly the gap between the droplets does affect the sensitivity of the print, when strained. As a result, the gap distance that has an increased change in field is between 0.1 mm to 0.05

mm. As expected the greatest change in field can be seen in the 100 mm radius. The distance between the droplets is largely due to the magnetostatic energy interaction between two neighbouring droplets. As seen in the COMSOL images in Fig. 6.2, the magnetic poles are confined to the edges of the droplets (free to move) whereas the droplets that are touching or overlapping require greater energy to move similar to the addition of domains in magnetostatic energy where increasing domains reduces demagnetising field, which is similar to a bar of magnetite where the poles are confined to the edges of the single bar. However, as the distance is increased there will be less magnetic material on the surface and less interaction, as a result the field drops.

By increasing the size of the droplets by twice the length and height (0.3 x 0.1 mm), theoretically the field would be higher than the smaller droplet size due to the increased volume, therefore it is interesting to see how sensitive the larger droplets would be against smaller droplets. The images from COMSOL simulation shown in Fig. 6.4 shows that from -0.2 mm and -0.1 mm the direction of magnetic moments is cancelled out (or opposing each other) due to overlapping of the magnetite droplets during bending. For 0 mm droplet distance the field is increased due to the neighbouring droplets, which result in a uniform field across individual droplets. For 0.1 mm, the change in field is increased but confined to the bottom edges of the droplets, which results in reduction of the overall change as the interactions from each droplet are reduced.

a

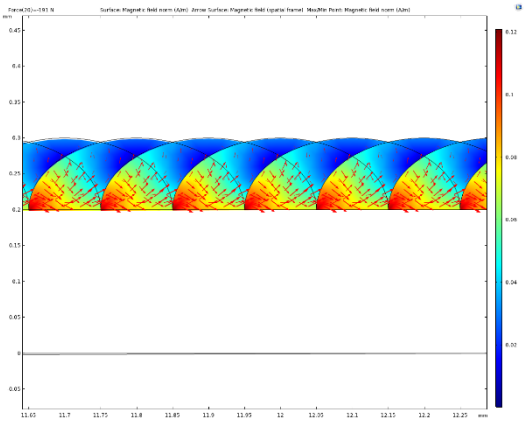

b

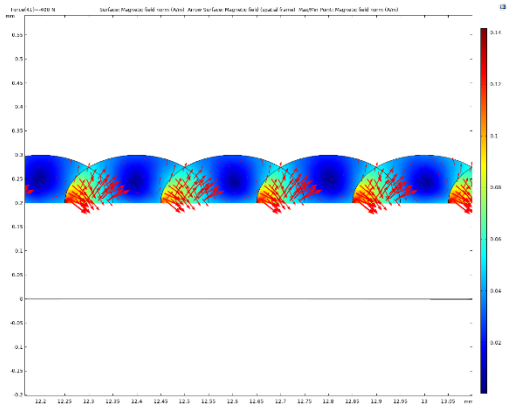

c

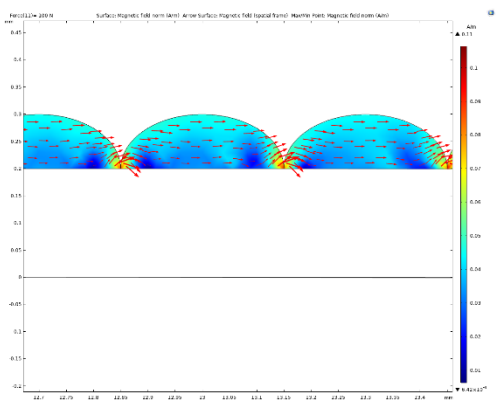

d

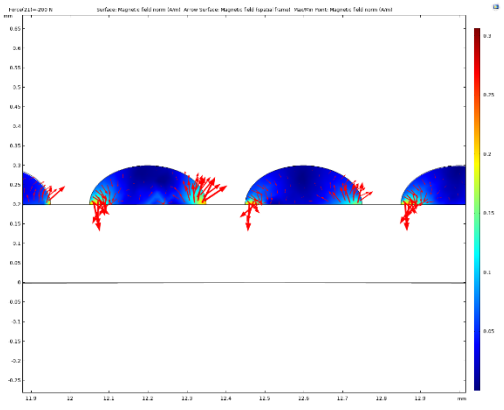

e

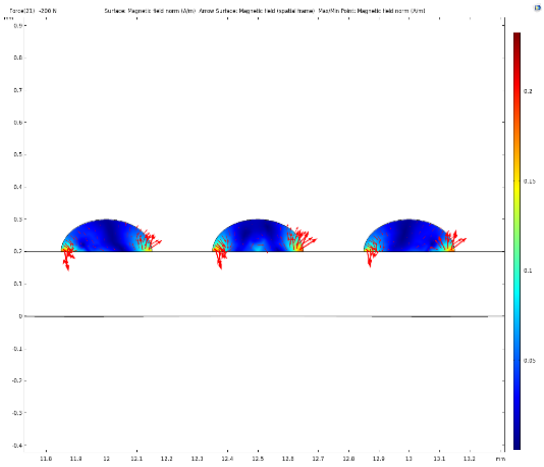

f

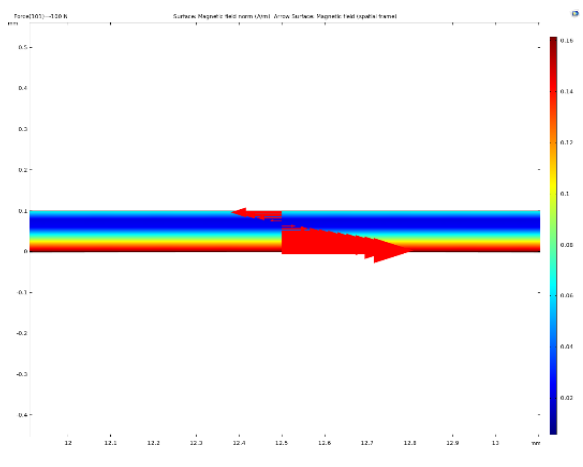

Figure 6.4 COMSOL simulation magnetic field image result of droplets (0.3 x 0.1 mm) with gap distance of (a) -0.2 mm, (b) -0.1 mm, (c) 0 mm, (d) 0.1 mm, (e) 0.2 mm and (f) bar

Fig. 6.5 shows the result from the COMSOL simulation of the larger droplets size of 0.3 x 0.1 mm. It shows that the distance between individual droplets does make a difference on the field in the Y direction (perpendicular to the applied field of 10 A/m) as the radius of curvature is reduced from 600 mm to 100 mm. As the magnetite droplets are placed 0 mm or 0.1 mm apart as shown in Fig. 6.5 (c) and (d) then the magnetic field is increases compared to droplets that are overlapped or placed further apart to each other as seen in Fig. 6.5 (a) and (e). However, the main difference between the larger droplets and smaller droplets sizes is that the sensitivity of larger droplets is sensitive towards 0 mm gap or just touching whereas the smaller droplet size is sensitive when there is a slight gap of 0.05 mm. In other words, the smaller droplets have the biggest effect when the gap is increased from 0 mm to 0.1 mm. This may be due to the amount of droplets on the silicone surface as the smaller droplet sizes will have greater interaction between the neighbouring droplets however, there is also a greater amount of area of air gaps when the droplets are moved further away. As the gap increases, the interaction of magnetic moment for neighbouring droplet reduces as density decreases.

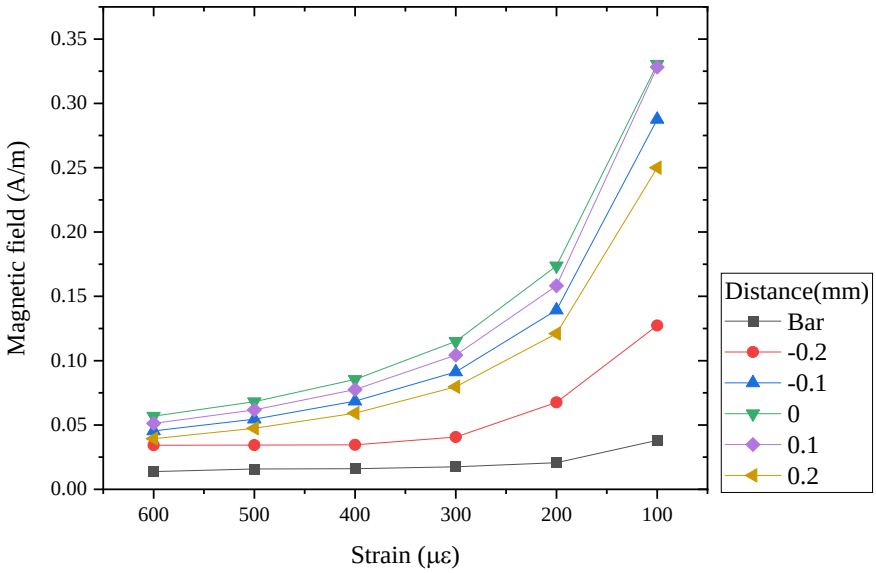

Figure 6.5 Change in gap and magnetisation of magnetite droplets (0.3x0.1mm) while bending

In comparison, by showing only the 100 mm radii, Fig. 6.6 shows that the larger droplet size is more sensitive to field and strain due to the additional material added. However, the smaller droplet has a greater change/ variation as the gap is increased or reduced. For example, from -0.05 mm to 0.05 mm the small droplet the change in field increases significantly which does not follow the change in field as seen in the larger droplet size. Larger droplet size shows a border and stable change in magnetic field. Therefore, care must be taken when printing smaller droplets as the gap can play a big role in producing sensor for SHM application.

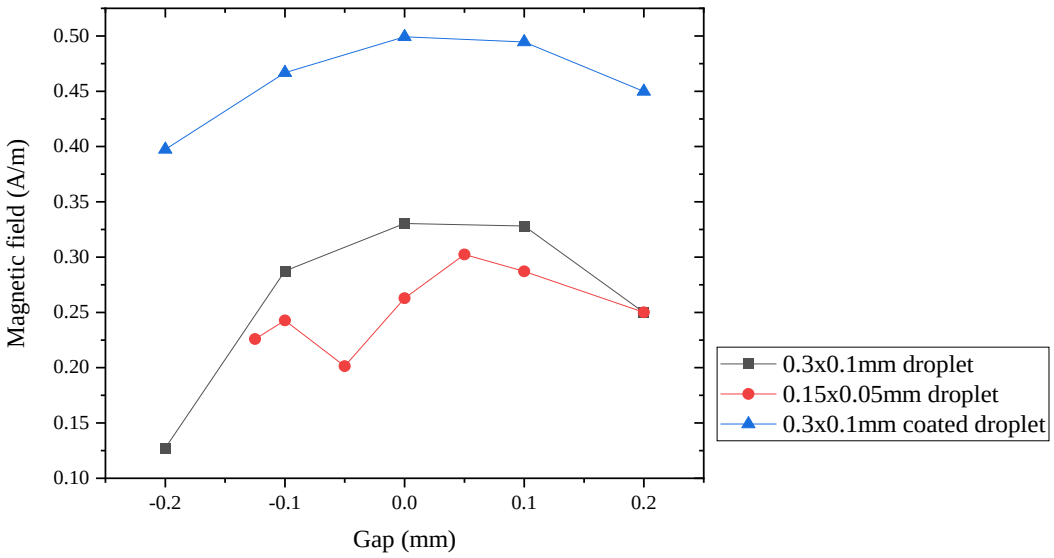

Figure 6.6 Comparison of different size of droplets and coating showing the field as a function of gap distance over 100mm radius of curvature

a

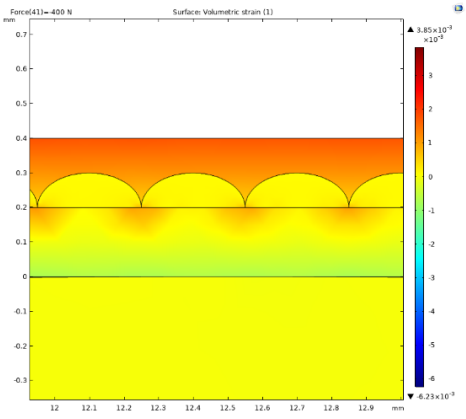

b

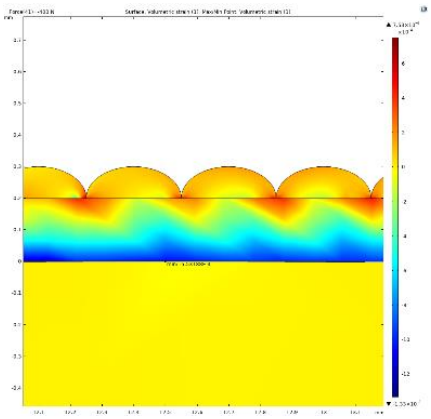

Figure 6.7 Simulation of coated magnetite with PDMS (a) and uncoated magnetite NP(b) field as a function of strain

In the real world the magnetite droplets would be coated to protect them from environmental damage, therefore to COMSOL simulation was used to see the performance of the magnetite droplets with a polymer coating under bending strain. A model was created using the same boundary conditions in methods chapter 4.2.1.2, with 0.2 mm silicone coating layer added on top of the ink droplets seen in Fig. 6.7 (a). The effect of (a) coating and (b) uncoated droplets were simulated to show the difference. The difference between the gap distance of coated and uncoated magnetite is that there is a larger directional field present in the coated magnetite droplets. As the field goes against the initial field of 10 A/m and towards the ends of the droplets. Stress applied as shown in Fig. 6.7, shows that the stress is greater on the top of the coated droplets (a) whereas the uncoated droplets (b), the stress is unequally applied on the substrate. This is due to the silicone coating applying pressure from the top of the magnetite coating. Therefore, the coated droplet is seen to have greater field measured as seen in Fig. 6.6. However, the change in field is reduced which may be due to the amount of stress that is needed to apply to reach equilibrium in displacement.

To conclude, this work has used COMSOL modelling to simulate the effect of gaps and overlaps of magnetite droplets on the change in magnetisation during bending over a known radius of curvature. The results show that the change in magnetisation has a greater change in magnetisation when the droplets are touching or 0.1 mm apart. This could be due to the magnetostatic interaction between each droplet where magnetisation from each individual droplet affect neighbouring droplets. However, as the droplets are moved further apart or overlapping each other, the interaction effect is reduced. Increasing the size of the droplets does make a difference to the change in magnetisation, for example the larger droplet size has an increased magnetic field between 0 mm to 0.1 mm gap size when compared to the smaller droplets.

6.4 Substrate selection

As shown in chapter 4.2.2, the factors that affect the printability of the inks depends on the ink's composition such as the particle size and solvent compatibility to prevent amalgamation and clogging. The NPs were stable from the manufacturer with solvent high concentration in the ink. Both magnetite and nickel ink solutions contained more than 80 % of the solvent. Therefore, it was essential to remove the excess solvent after printing, to obtain high quality print and density of metal NPs. This is done through drying via thermal evaporation or by UV light to reach the flashing point of N-Methyl-2-pyrrolidone (NMP) solvent and organic solvent such as Dimethylformamide (DMF), Isopropyl Alcohol (IPA) and water. Therefore, selecting the correct substrate for printability and evaporation of the solvent is essential. Table 6.1 shows different substrates (Kapton, PET, PTFE and paper) that were tested before printing. A drop of magnetite and nickel ink was pipetted onto the surface of the substrate to test the wettability and surface adhesion after solvent evaporation and curing of metal NPs. The temperature was monitored using a non-contact infrared thermometer.

Table 6.1 Solvent evaporation test to select substrate for printing

Substrate material	Curing method	Magnetite	Nickel
Kapton	373 K for 1 hour	Ring formed, did not fully form, solvent was not fully evaporated	Ring formed as temperature is lower than the solvent evaporation temperature
	433 K for 30 min	Slight covering of droplet on substrate	Similar adhesion but better covering to substrate
PET	433 K for 30 min	PET polymer deformed but good adhesion with magnetite	Good adhesion but PET substrate softened and deformed
	373 K for 30 min	Pet polymer deformed slightly but no adhesion with magnetite	Lower than the solvent evaporation temperature
PTFE	433 K for 30 min	No adhesion	Good adhesion

Paper	Hot plate until dry	Good adhesion	Higher solvent absorption through the paper, no evaporation

Two curing methods were used, one below and one above the evaporation temperature of the solvent. For substrates such as paper or PET, there were limitations on the curing temperature due to the deformation of the substrate occurring at high temperature. For example, paper will burn or degrade at 373 K and PET as seen in Table 6.1, deformed when the temperature increased from 290 K to 373 K. A polymer that can withstand high temperature is PTFE, therefore this substrate would not deform upon heating to 433 K. When heated to 433 K, the nickel performed well as there were good adhesion between the nickel NPs and PTFE substrate, whereas magnetite ink did not sufficiently adhere to the substrate.

Both inks placed on the kapton did not form well as the ink cured and formed powder flakes that were not sufficiently stuck onto the substrate. This could be due to the amount of material deposited on the kapton where in inkjet printing the amount of metal NPs would adhere to the substrate. The nickel ink had better adhesion on the kapton film than the magnetite ink. Thus issues could arise when printing the inks in layers as more material is deposited on the substrate, which would make it difficult to evaporate the solvent and cure the NPs. When heating the kapton substrate to 373 K with the ink pipetted, the pattern formed shares a similar resemblance of a coffee ring effect as seen in Fig. 6.8. which is where the nanoparticles form along the edges of the droplet once solvent is evaporated as mentioned in literature (Al-Milaji *et al.*, 2019; Nayak *et al.*, 2019). The nanoparticles migrate towards the substrate by capillary flow and surface tension therefore the lack of evaporation and substrate adhesion (increased wetting) causes coffee ring effect. Therefore, in Fig. 6.8 is where the temperature did not reach the evaporation temperature of NMP allowing the NPs migrate towards the sides of the droplet. As shown in (Zhang *et al.*, 2016) the curing temperature at 373 K formed a coffee ring effect whereas temperature at 433 K improved densification of the metal composition. A few drops more of both nickel and magnetite ink resulted in uneven spread of powders as shown in Fig. 6.9. For nickel, it showed a similar trend as there were empty areas in the centre of the cured ink, however the result is better than curing at 373 K. Whereas magnetite formed a larger clump of powders but did not adhere to the kapton substrate. Therefore, Kapton substrates would need to be either heated before or during printing in the inkjet printing system.

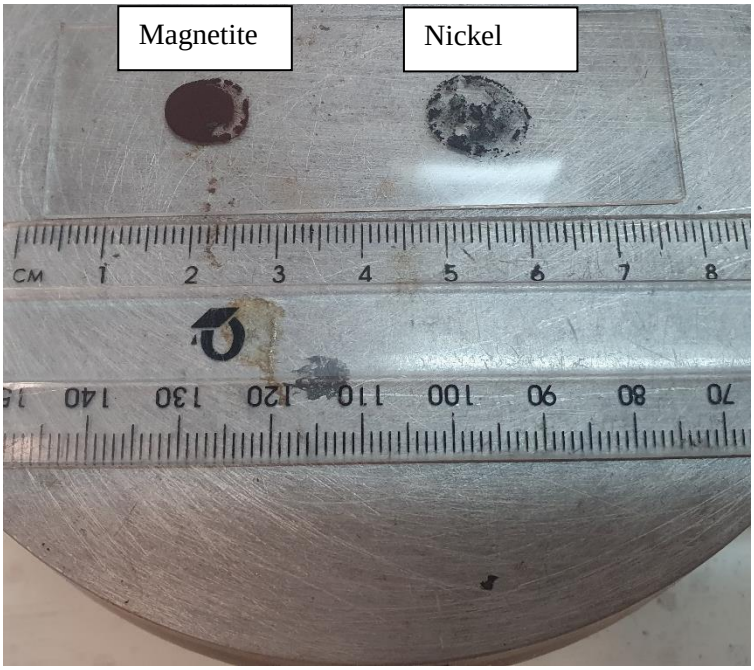

Figure 6.8 Magnetite and nickel (left to right) on glass substrate dried using a hotplate

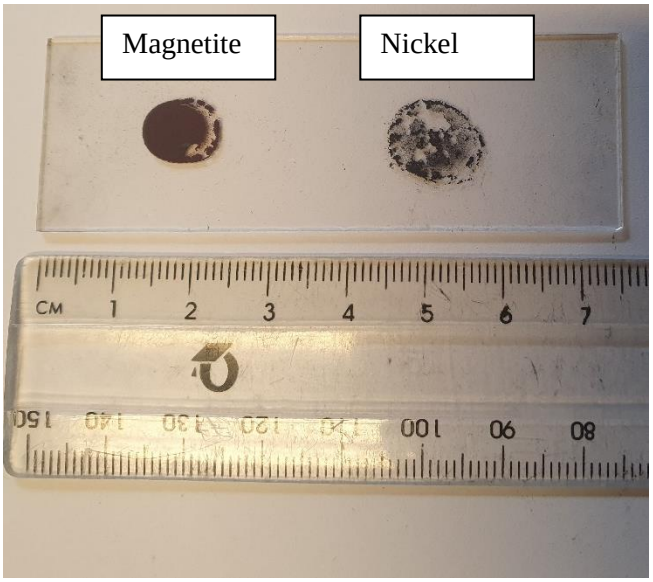

Figure 6.9 Cured magnetite and nickel (left to right) on glass substrate

Overall photo paper was found to be the best for ink adhesion, although the solvent would not evaporate but be absorbed through the paper at lower temperatures, which could cause issues to the mechanical properties of the paper. UV light could be used to evaporate the solvent without degrading the paper after printing.

6.5 Magnetic properties

The magnetic properties were measured by measuring the hysteresis loop using the SQUID shown in Fig. 6.10 and Table 6.2. From the hysteresis loops, it was observed that the magnetite has more than double the saturation magnetisation (M_s) than the nickel powder. The magnetite had a lower coercivity (H_c) and remanence (M_r) than nickel, which is preferable for sensing application. However, it is worth pointing out that magnetite had not reached saturation as the magnetisation is still slightly increasing after 1200 kA/m field.

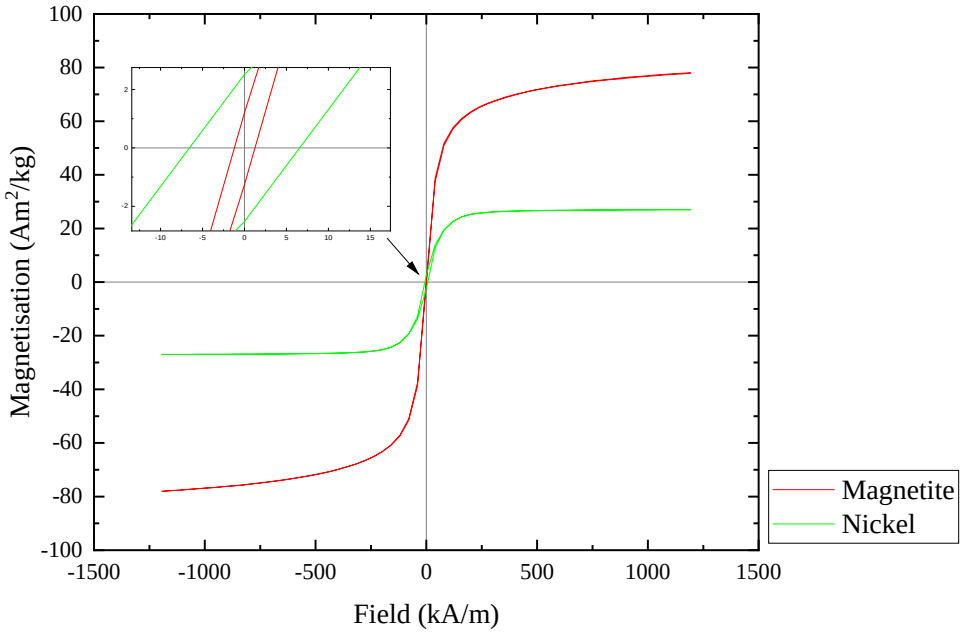

Figure 6.10 Hysteresis loop of magnetite and nickel NP from -1200 to 1200 kA/m field

Table 6.2 Magnetite and nickel saturation magnetisation, remanence and coercivity calculated from the hysteresis loop

Material	M_s (Am^2/kg)	M_r (Am^2/kg)	H_c (kA/m)
Magnetite	76	1.25±0.02	1.22± 0.02
Nickel	27	2.53±0.01	6.56± 0.1

Fig. 6.11 and Fig. 6.13 show the hysteresis loops of both magnetite and nickel ink from the current work and from the literature. They show that the M_s of magnetite is 76 Am^2/kg, which is close to published values at. The bar chart in Fig. 6.12 showing the magnetic properties of magnetite, shows that there are similarities in magnetic properties for all except for one published paper in (Cabrera *et al.*, 2008). Where H_c and M_r shows 10 kA/m and 10 Am^2/kg difference respectively from current work and other published papers. This may be because of the technique used, as (Cabrera *et al.*, 2008) used electrode bath (electrolysis) to form magnetite, which may have reduced particle size which increased the H_c and M_r values considerably. It is reported that bulk magnetite has M_s at 92 Am^2/kg as reported in (Cabrera *et al.*, 2008) which is similar to the measured magnetite M_s, as the difference is due to surface effects such as spin canting.

Whereas the published values and current work for nickel NP seen in Fig. 6.13 and Fig. 6.14 shows that there is considerable variation of magnetic properties. For example, in (Mahajan *et al.*, 2019) the data is closest to this work where the M_s is around 30 Am^2/kg (Mahajan *et al.*, 2019), however in (Zhang *et al.*, 2006) the M_s is around 55 Am^2/kg which was higher than all published and current work. The gap of 20 Am^2/kg is significant, more than the published values for magnetite. The size and composition of NPs of magnetite does affect the M_s value which could explain the high variation between the published values. For example, a particle size of 20 nm has a single domain whereas above this they are multi domain. For example, in (Zhang *et al.*, 2006), they reported the hysteresis loop for Nickel NPs with a diameter of 22 nm has a similar Ms value of around 30 Am^2/kg from the hysteresis loop. However, this work has a particle diameter of 80 nm, far larger than in (Zhang *et al.*, 2006). This may be down to their process in obtaining nickel NP, where thermal fluctuation, solvent and technique could affect their magnetic properties.

The difference in heating the ink from 290 K to 433 K is evident from the result shown for both magnetite and nickel hysteresis loops. While there is not much of a change in the M_s for magnetite, for nickel there is a large difference in M_s which can be seen in Fig 6.13 and Fig. 6.14. As the concentration of nickel is 2%, the difference in M_s could be due to the weighing of nickel and transferring it into the gelatine capsule. Slight inaccuracy in the weight of the nickel content can lead to a large difference in M_s. Overall the differences in magnetic properties of all the published values and current work has been mainly down to the manufacturing and synthesis method in obtaining pure magnetite and nickel NPs. In this work, magnetite has shown to have good agreement for M_s, M_r and H_c values to the published papers. However, the ink used in this work has not been altered or changed from the manufacturer. Due to aging, magnetite could form into maghemite, changing the phase into (γ Fe_2O_3) however magnetic properties are similar as maghemite is still a ferrimagnetic material (Khan *et al.*, 2017; Shokrollahi, 2017).

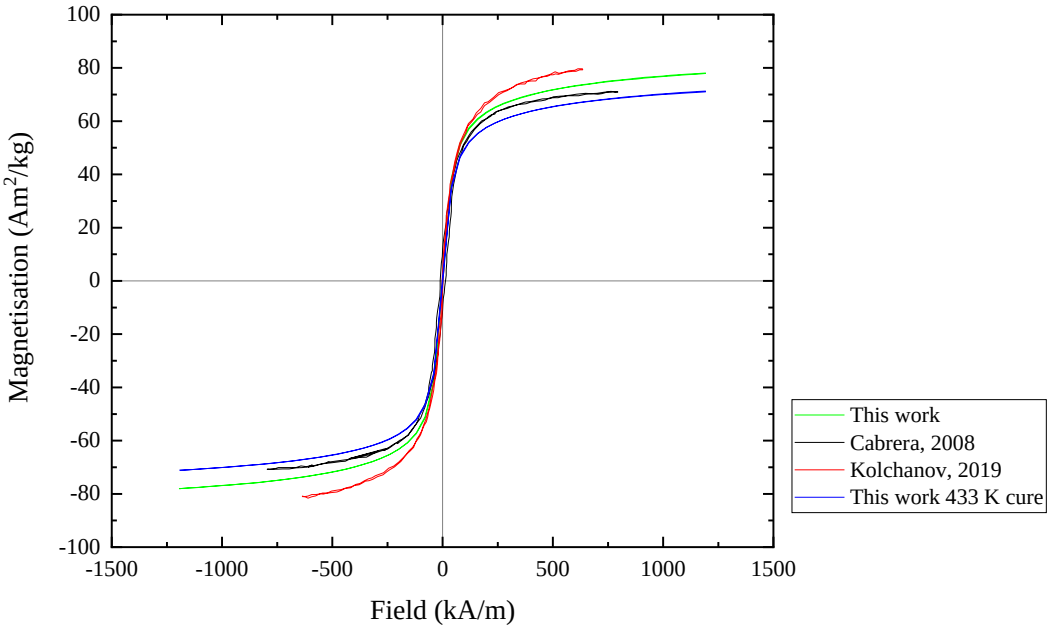

Figure 6.11 Hysteresis loop of magnetite NP in comparison with published data

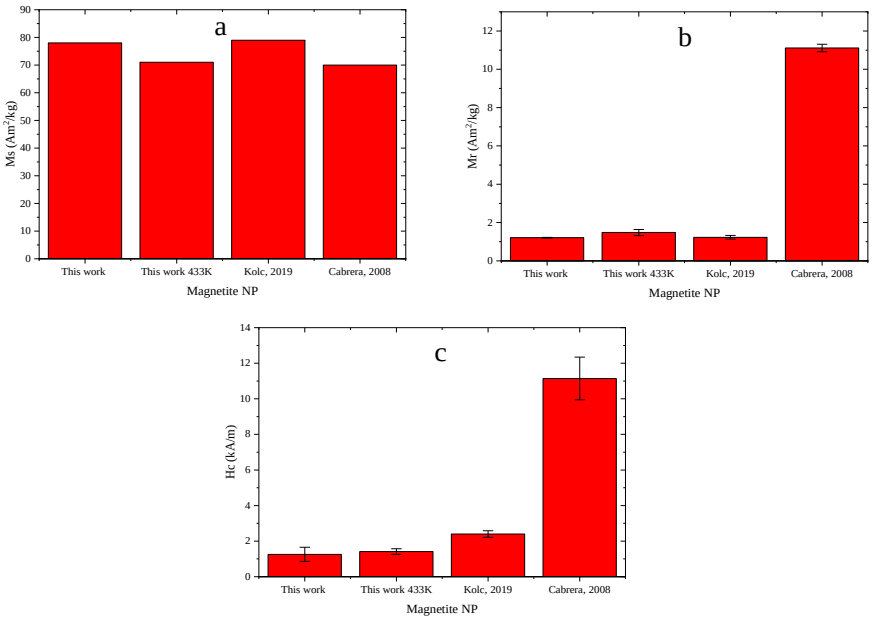

Figure 6.12 Bar charts showing (a) saturation magnetisation, (b) remanence and (c) coercivity of magnetite NPs of published values in comparison with current work at RT and 433 K temperature

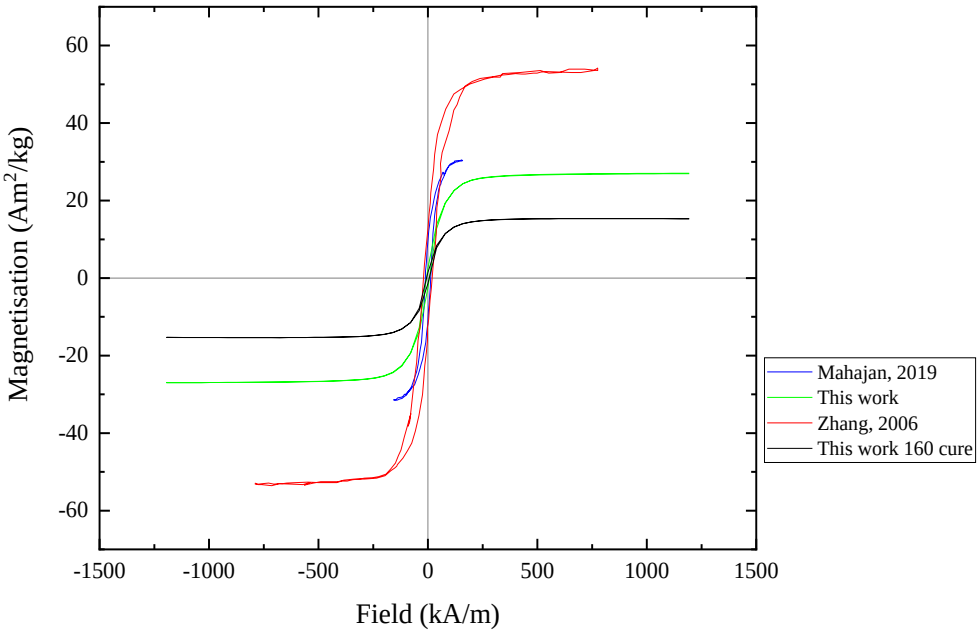

Figure 6.13 Hysteresis loop of Nickel NPs in comparison with published data

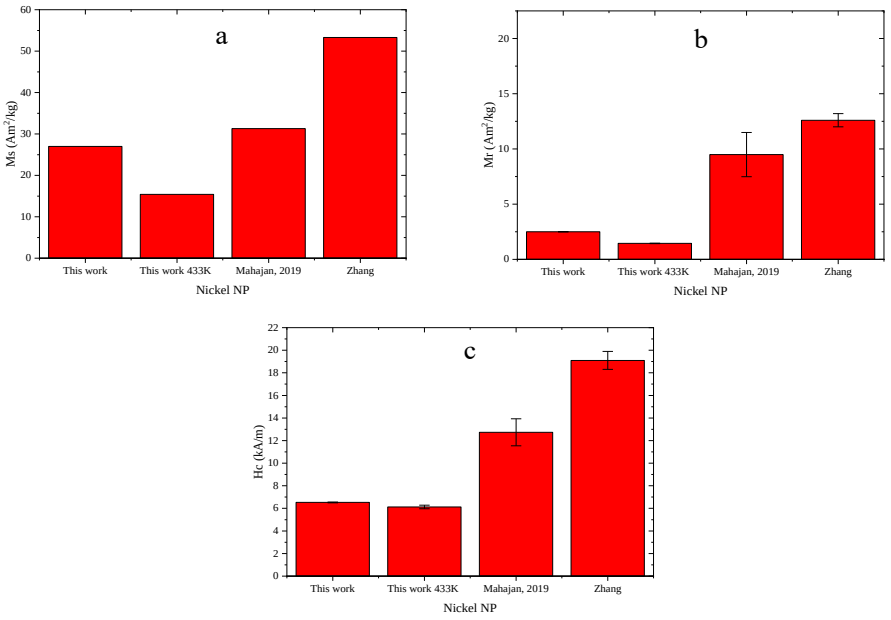

Figure 6.14 Bar charts showing (a) saturation magnetisation, (b) remanence and (c) coercivity of Nickel NP of published values in comparison with current work at RT and 433 K temperature

6.6 Viscosity measurement

Table 6.3 shows the result of 3ml magnetite and nickel viscosity at room temperature measured using a viscometer (SV–1 A, A&D Company Ltd.). This shows that both inks are suitable for inkjet printing as the value is below 20 cP and above 1 cP. However, the measurement was taken at the meniscus

where there is more solvent than heavy NPs. As the heavy NPs tend to drop to the bottom of the polycarbonate container. This creates an issue when measuring, as the measured value is not the true viscosity of the ink, rather it is more of the viscosity of the solvent. Therefore, the process of setting up the measurement was done quickly to prevent the heavy NP dropping to the bottom before the viscosity measurement. The true viscosity is likely to be higher but less than the critical value of 10 cP. What is surprising is that the viscosity for nickel is slightly higher than magnetite ink even though magnetite contains 20 Wt % NPs and Nickel has 2 Wt % NPs in the ink. The higher viscosity could be due to the density of the solvent as NMP in Nickel ink have a higher density than DMF in magnetite ink.

Table 6.3 Viscosity measurement for Magnetite and Nickel NP

Metal NP	Solvent	Temperature (K)	Viscosity (cP)
Magnetite	DMF, IPA and water	294	1.92
Nickel	NMP and water	293.6	2.06

The Z number shown in Equation 3.5, as seen in chapter 3.5.1, was calculated to be around 6-8 cP for nickel and 9.7-12.9 cP for magnetite. Therefore, this makes it suitable for inkjet printing as the Z number is below 20. In published paper (Deepak Dixit and Pattamatta, 2019) the magnetite dispersion from the same company has shown to have a viscosity value of around 1.6-1.7 cP at 297 K. Although the test was not performed at around 297 K, the viscosity in the published values would be slightly lower than this work. Nevertheless, the inks have shown a good level of viscosity for inkjet printing using JetLab 4 printing system.

6.7 Print analysis

Printing was carried out using the jetting parameters and processes described in chapter 4.2.2.3. In Fig. 6.15, it shows the print nozzle in continuous jetting of metal NP where (a) is when the ink is jetted from the nozzle, (b) is where a single droplet is jetted, (c) is where the jetting forms satellite droplet, (d) is where the nozzle is clogged due to amalgamation of NPs. The droplets jetted from the 60 µm orifice nozzle can form a homogeneous print when the conditions or parameters are suitable. In normal conditions, (a) and (b) are ideal as they form a single droplet in a jetting cycle. However, as the ink within the reservoir settles to the bottom and forms amalgamation of NP, this leads to nozzle clogging or excessive NPs in an area on the substrate. This is shown in (c) where satellite droplets are multiple

droplets in one cycle, caused by the jetting parameter or clumps of NPs. In (d) shows the clogging of the nozzle where the NP is unable to pass the orifice, therefore no ink is jetted.

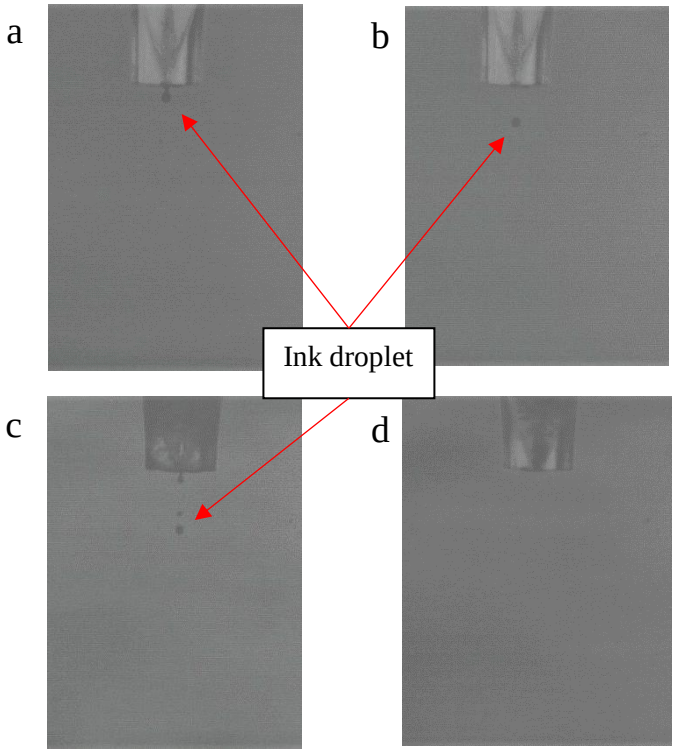

Figure 6.15 Print head nozzle during jetting metal NP when jetting from nozzle (a), single droplet (b), satellite (c) and clogged (d)

Fig. 6.16 and Fig. 6.17 shows magnetite and nickel designs on photo paper printed by Jetlab IV with 60 µm print head orifice. The designs printed were (a) Coil, (b) 5 mm track grid, (c) 3 mm track grid, (d) Uniaxial patch, (e) Grid, (f) Ink drop, (g) Perpendicular print (to strain) and (h) Parallel print (to strain). However, complications occurred during printing for both magnetite and nickel ink, as the heavy metal NP in the ink, made it difficult to ensure even mixture in the ink solution. This led to clogging and calibration issues as seen in Fig. 6.15. There are areas where the concentration of metal NP are high and areas where it is low, for example in Fig. 6.16 (g), the top half has a greater amount of magnetite NP than the bottom half. Clogging is the main issue as it disrupts jetting during printing, as seen in Fig. 6.16 (2c) where the 3 mm grid print stops mid-way. A syringe filter of 0.45 µm was used but this led to the bulk of the magnetite and nickel NPs being easily removed, leaving just the solvent. Therefore, an ultrasound bath was used to disseminate the metal NPs throughout the ink solution to avoid large clumps of NPs and enable filtering using a filter of 0.45 µm. Diluting the ink with deionised water and sonication was useful in separating the larger particles into smaller particles. However, the

concentration was reduced which meant printing over the design to achieve the required density of metal NPs on paper.

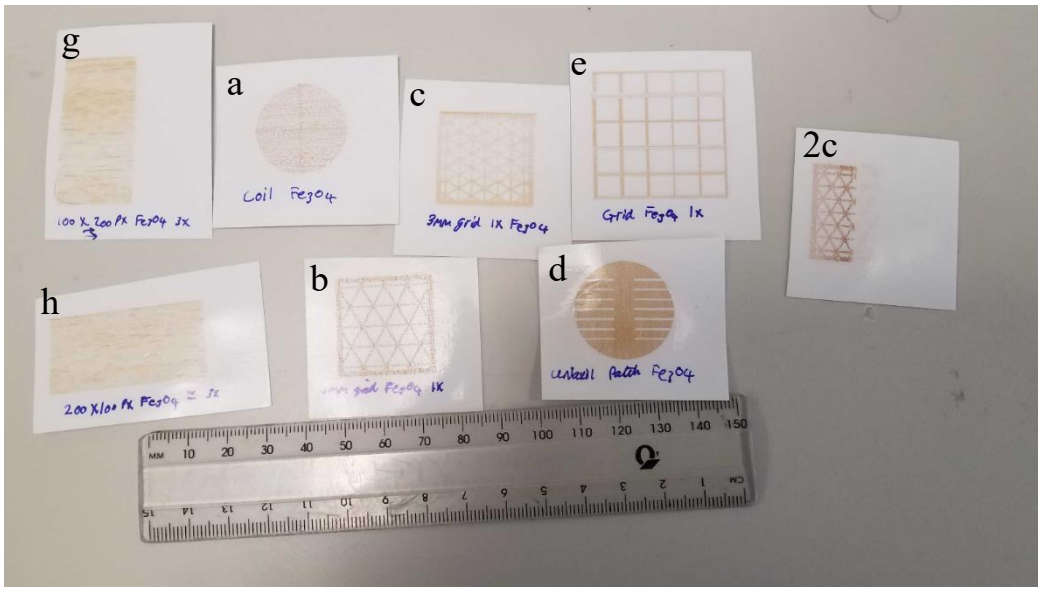

Figure 6.16 Magnetite print on paper

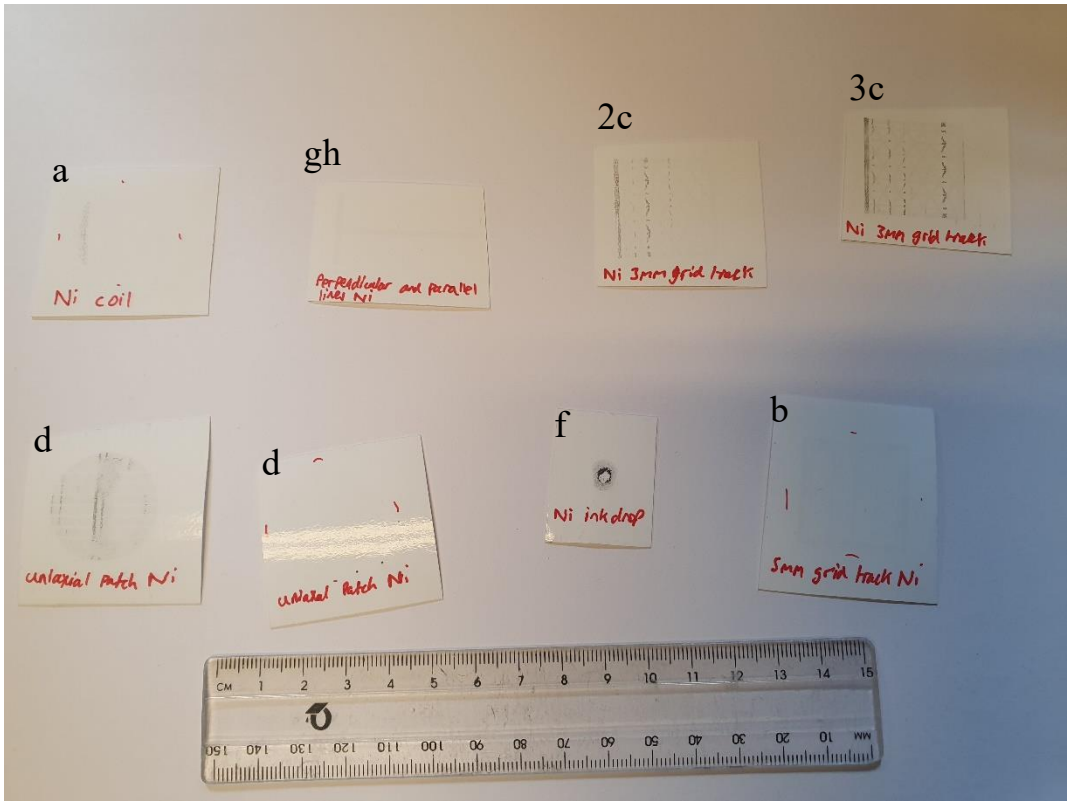

Figure 6.17 Nickel print on paper

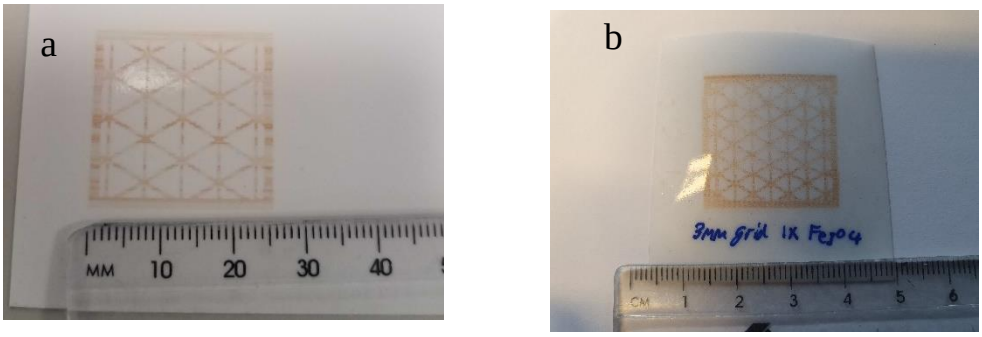

Figure 6.18 magnetite (a) 5mm grid and (b) 3mm grid 200px design

Fig. 6.18 shows (a) 5 mm track and (b) 3 mm track grid designs of magnetite printed on paper. The size of the design is 128 x 128 pixels, which prints a size of 25 x 25 mm. The grid designs have been based on the desktop print designs to see the difference in the magnetoelastic behaviour between both printers. However, the coil and uniaxial patch design were also created and printed to compare designs and to evaluate them as seen in Fig. 6.19. The coil designs were printed in single and 10 layers to see the difference between the magneto mechanical sensitivity by layering the design as seen in (b) as single layers and 10 layers in (c). The multiple layers of uniaxial patch were also successfully printed on paper as seen in (a). This design was inspired from literature as seen in (Yoo *et al.*, 2016) where they found that the uniaxial patch gave an anisotropic direction for sensing application due to the gaps present in the design. This is because the induced gaps cause a reduction in demagnetising factor in plane therefore the field aligned along the gaps are easy to magnetise while the magnetisation perpendicular to the gaps is harder to magnetise. This may be useful as a sensor when strain is applied to measure the Villari effect.

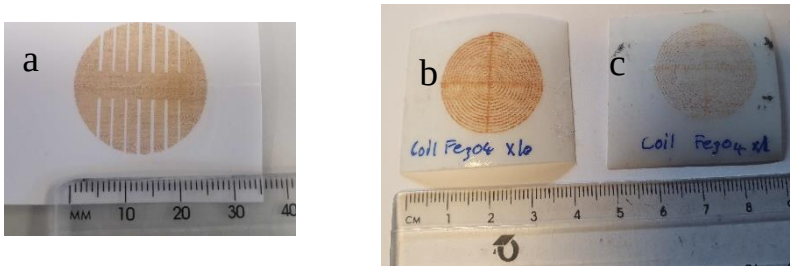

Figure 6.19 Magnetite (a) uniaxial patch design and coil design with (b) multiple and (c) single layer

The microscope image of magnetite print on photo paper shown in Fig. 6.20 shows that each droplet has non-spherical shape but there is good adhesion between the magnetite nanoparticle on paper. Most of the magnetite droplets on paper are non-spherical and changes when the print direction is changed. For example, the print direction from top to bottom and bottom to top are slightly out of position, which results in elongated spherical shape. Some droplets as seen in Fig. 6.20 have joined which may have been due to the droplets being too close together during printing process, this could be improved by adjusting the alignment of jetting such as fixed substrate or reducing satellite droplets by calibration as seen in Fig. 6.15. The radius of droplets (R1, R2 and R3) are all similar to each other with a mean of 78.20 ± 2.5µm, while the diameter (D1, D2 and D3) have a mean of 159.45 ± 5.3µm which is due to the misalignment of droplets. Although the droplets shown to have a slight variation in diameter and radius, the size of the droplets are relatively good considering excess satellite droplets present and clogging issues. The droplets therefore would not induce magnetic direction in the design due to them being isotropic in plane. The design shape and size would play a key role in changing the direction of magnetisation under strain. However, the spacing between each droplet is inconsistent where some are touching and others are around 10 µm apart. This can have an effect on the magnetic field from each droplet as shown in section 6.3, where it can change drastically when they are overlapped or at a distance where the magnetostatic interaction of each droplet does not have an effect. It was shown in the modelling that the best change in field as a function of strain is when the droplets are touching or have a small gap between them. However, in reality it is difficult to control the spacing when printing magnetite NPs.

The nickel coil printed as seen in Fig. 6.21, which shows the microscope image of nickel ink on photo paper. The microscope image shows that the nickel drops are erratic and do not show a good cohesion of the droplets onto the paper. Compared to magnetite, where multiple prints show a relatively good accuracy (print direction on top of each drop), nickel does not print over well as each drop does not overlap each other in multiple prints. There are areas where the print is inconsistent as clogging may have disrupted the printing process. The size of the droplets shown in Fig. 6.21 have a mean diameter of 141.6 ± 2.3 µm (D1, D2 and D3) and spherical mean radius of 70.7 ± 1.5 µm (R1, R2 and R3). In comparison, the nickel drop measured shows that the drops are about 20 µm smaller than magnetite droplets, which is due to the lower concentration of nickel in each droplet and prone to forming voids and non-uniform NPs due to excess solvent in each drop.

The magnetite print has a resolution of around 132 dots per inch (DPI) whereas in literature (Voit *et al.*, 2003), the resolution is much higher at 185 DPI (360 DPI can be achieved by adjusting the printer). There are slight differences in substrate selection and ink synthesis but a similar inkjet printing method was used such as using a piezoelectric print head. However, the size of a single dot on glass was measured at 80 µm, this is significantly smaller than this work, at around 150-160 µm as seen in Fig. 6.20. In literature, they have used a fast drying process during printing, where the substrate was pre-

heated to 373 K, which evaporates the solvent and reduces migration of NPs to the edge. They have mentioned that using paper or polymer substrates would increase dot size due to wetting. In the case of measuring magnetostriction effect, flexible substrates must be used which limits the substrates to paper or polymer. This would also have a limitation on the fast drying process as heating to 373 K cannot be achieved using these substrates including paper.

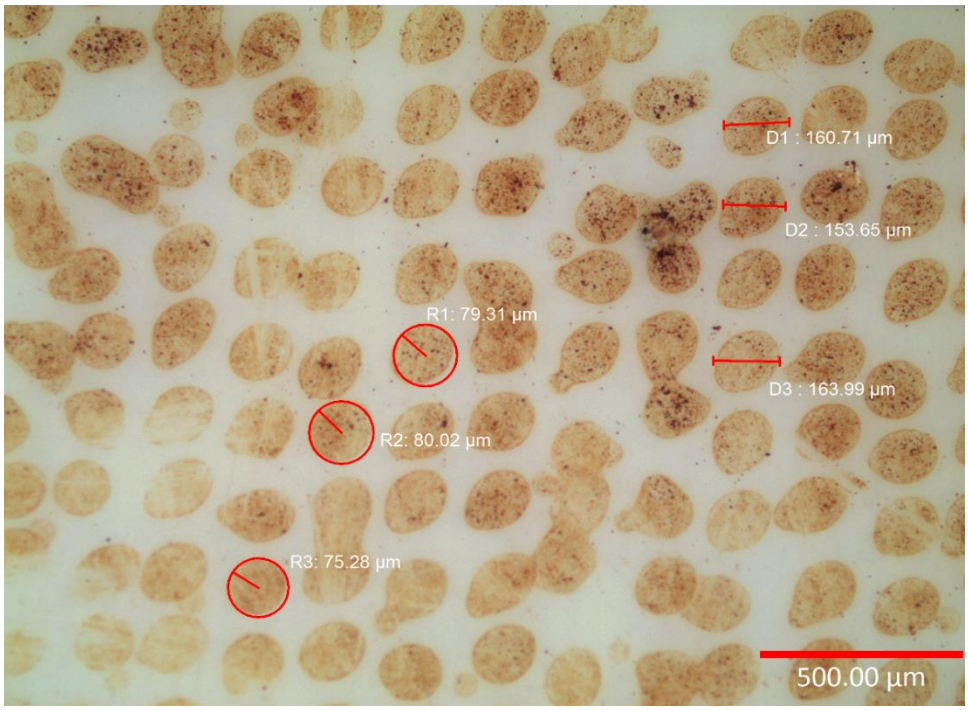

Figure 6.20 Optical microscope of magnetite uniaxial patch design on paper

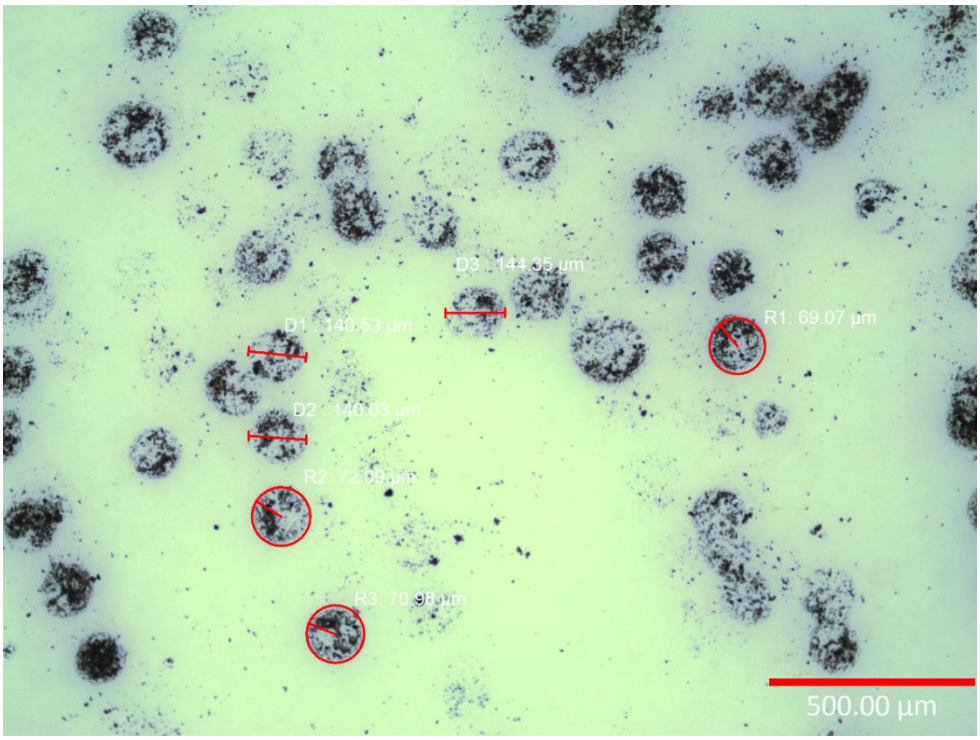

Figure 6.21 Optical microscope of nickel coil design on paper

6.7.1 SEM and EDS analysis

Magnetite and nickel NPs were further analysed by SEM and EDS. Fig. 6.22 shows the SEM and EDS analysis of magnetite print on paper where (a) shows the magnetite droplet on paper substrate. The distribution of magnetite NPs is not homogeneous across the droplet as larger amalgamated NPs can be seen clearly in the SEM image. This will affect the roughness and height of the droplet. Achieving homogeneous droplets is essential to reduce porosity and controlable anisotropy. Instead the droplet will have random alignment if the porosity increases. The EDS image in (b) shows elements of iron, carbon and oxygen present in the droplet. Iron elements in magnetite droplets can be clearly seen, as the iron elements (in red) depicts a similar shape to the droplet seen in the SEM image. Carbon and oxygen can be seen all over the substrate and the droplet, which makes sense as oxygen is an element present in magnetite and paper. Carbon is present in paper however not in magnetite, which could be due to impurities. (d) and (e) shows an EDS spectrum of magnetite NPs in (c), where iron and oxygen elements are in abundance in spectrum 2 and 3. The difference between spectrum 2 and 3 in (d) and (e) shows that spectrum 2 has visible impurities whereas spectrum 3 shows a magnetite amalgamated NPs. Further analysis using the spectrum in (b) shows that both have high oxygen and iron composition,

however the spectrum 2 shows less iron but more silicon which could be an impurity on the surface such as excess paper.

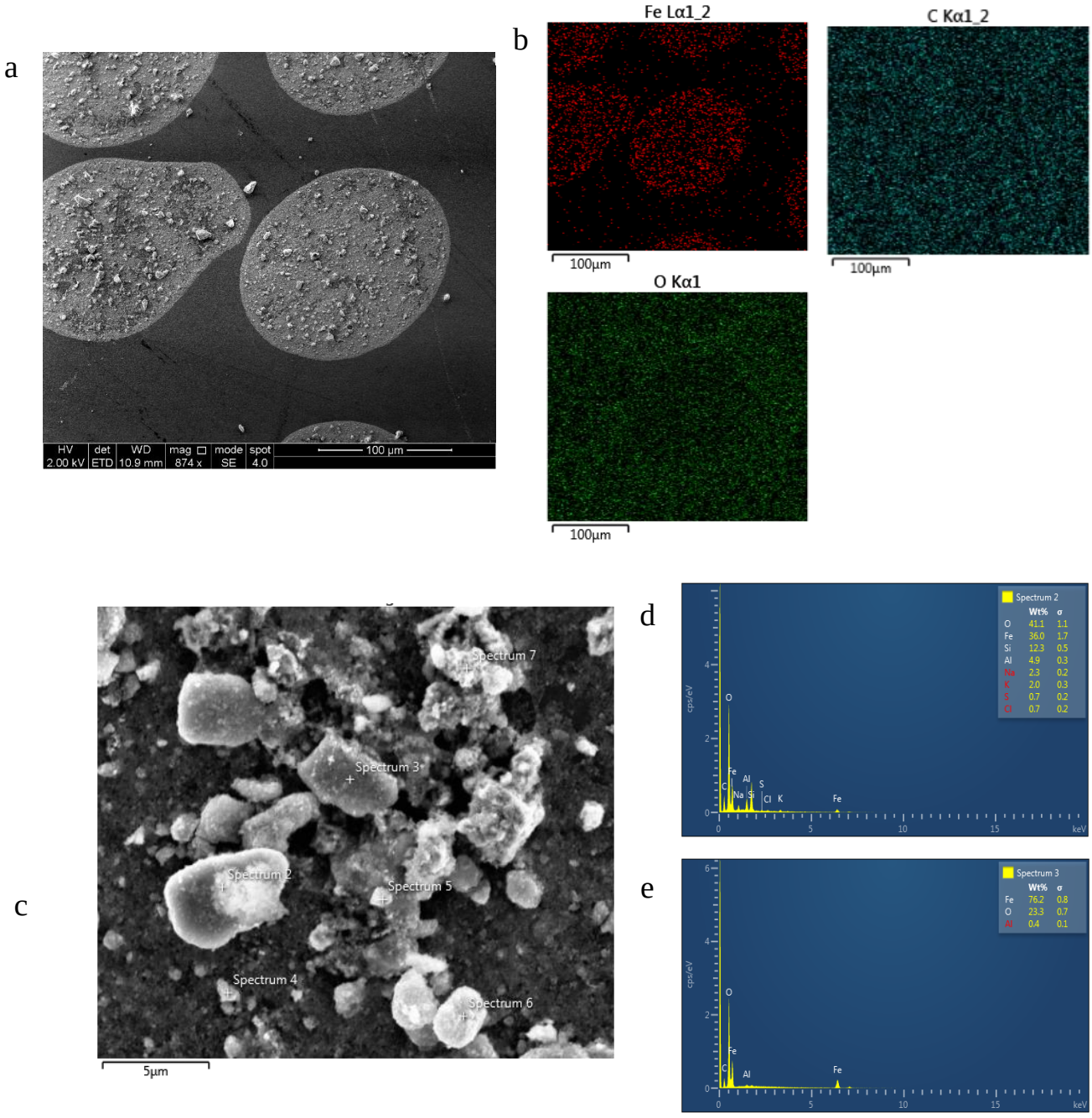

Figure 6.22 a) Magnetite on paper SEM (2kV), b) EDS element mapping (10kV), c) SEM spectrum label (2kV), d) EDS spectrum 2 and e) 3 (10kV)

Nickel droplets SEM and EDS mapping/ spectrum on paper can be seen in Fig. 6.23. Compared to magnetite, nickel NPs on paper contain higher levels of porosity, which can be clearly seen in the SEM layered image in (a). This is due to the higher level of solvent than magnetite which is prone to porosity when it is evaporated or absorbed into the paper. The EDS mapping in (b) shows elements of nickel, oxygen, silicon and carbon present. The droplet shows a clear presence of nickel and carbon elements whereas silicon and oxygen is present in the paper. This is as expected as the nickel NP contains only nickel element and paper showing oxygen element. Spectrum 11 (c) and 12 (d) shows that the SEM image in (a) contained a majority of nickel and oxygen.

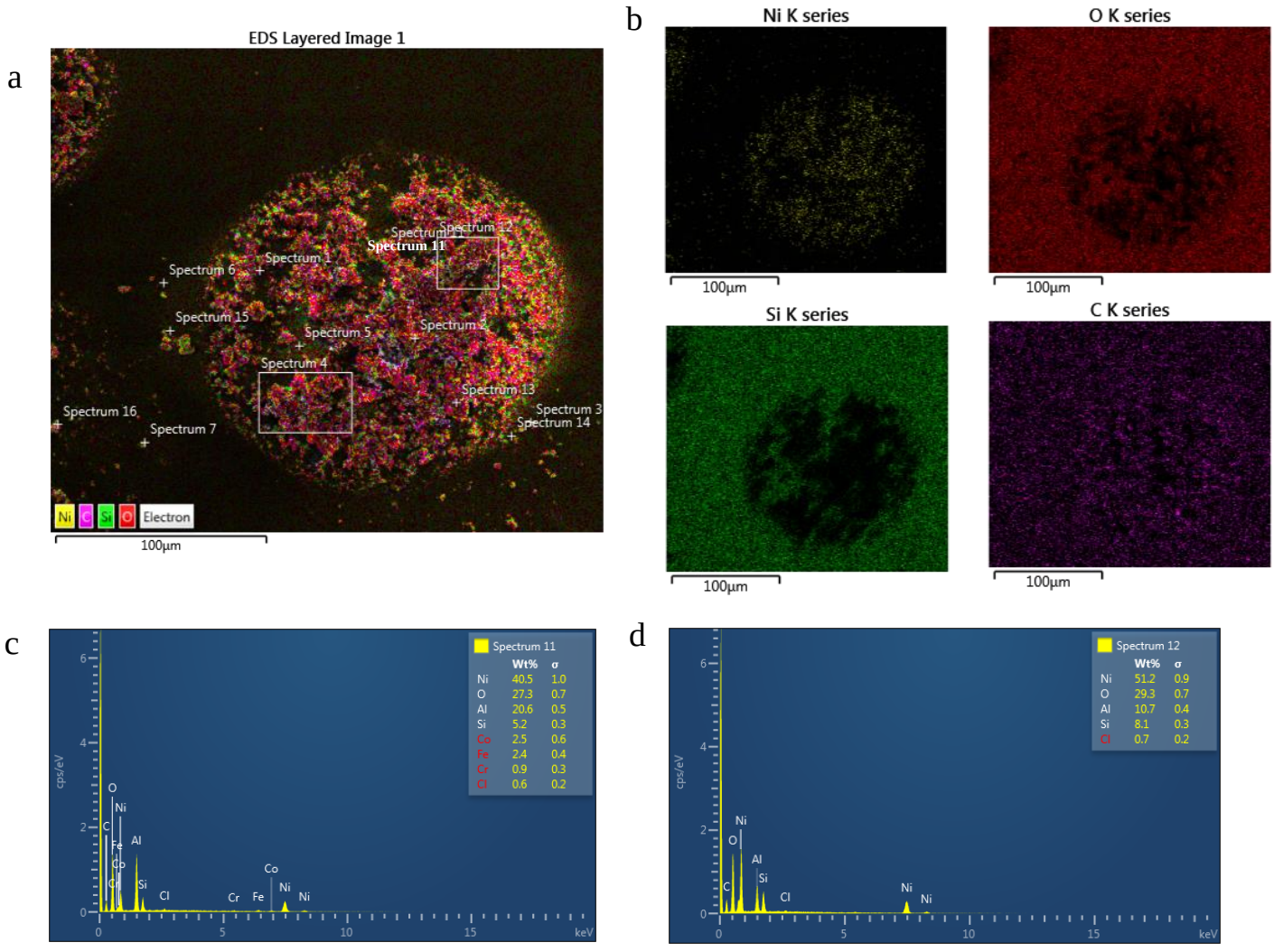

Figure 6.23 a) Nickel droplet on paper SEM (2kV), b) EDS (10kV) layered mapping, c) Nickel EDS spectrum 11 and d) Nickel EDS spectrum 12

6.7.2 Optical profiler

The contour elite optical profiler was used to measure the surface profile of the magnetite ink on various substrates. Surface profile includes measuring the surface roughness and thickness of the print as described in chapter 4.4.1. Fig. 6.24 shows the surface profile of 10 layers of magnetite on glass. The

profile shows a heterogeneous distribution of magnetite (168 x 224 µm) where each droplet shifts and overlaps each other as seen in (a). In (b) the peaks can be seen where the red peaks show a large deposit of magnetite only in a specific location, which leads to higher roughness value, whereas the green peak shows a covering of magnetite with lower roughness value. The red areas with higher level of surface roughness may be due to the amalgamation of magnetite NPs after jetting. There are unsuccessful droplets where the concentration of solvent has increased in the jetting process which leaves empty droplets on the surface, as seen in (a). This can affect the magnetite layer by shifting the NPs and reducing the wetting angle during additive layering and thus increasing the surface roughness. Heat or UV light could be applied to evaporate the solvent during printing to avoid excess solvent build up.

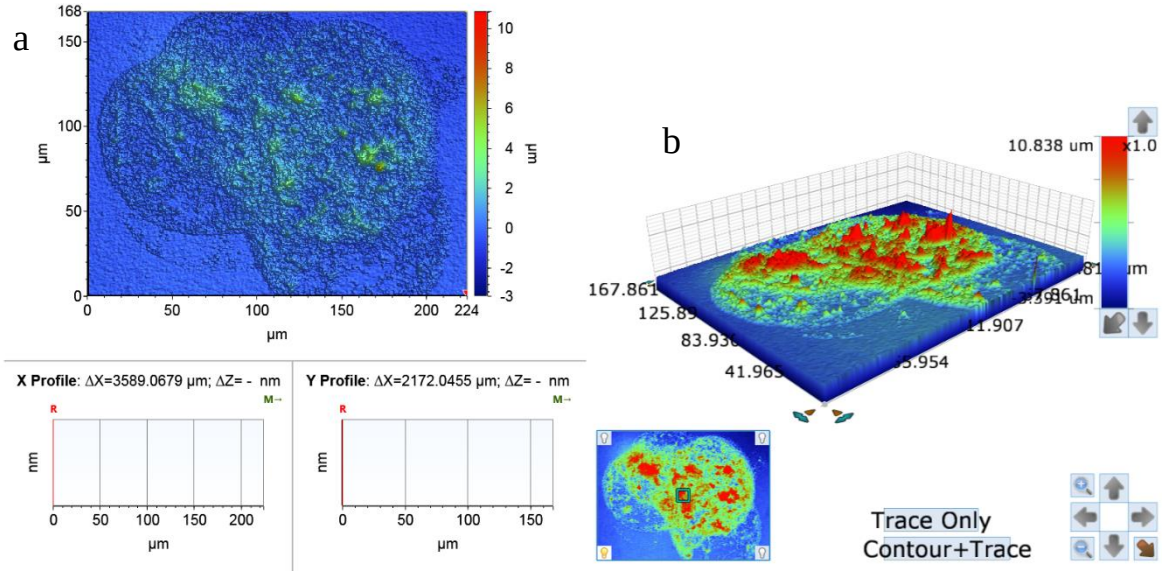

Figure 6.24 Surface profile of 10 layers of magnetite on paper (a) and 3D surface roughness/ peaks (b)

In comparison to literature (Saha *et al.*, 2018) they have explored the effect of layering silver NPs on photo paper substrate had on surface roughness, using an optical profiler. They found that the average surface roughness increased as the number of layers increased (single, double and triple) as seen in Fig. 6.25. The roughness is lowest in double layered silver NPs (b) as the average peaks and troughs are uniform. The single layer silver NPs (a) has uneven edges as the droplet is effectively a dome-shaped structure, as the surface height reduces on the edges. In the triple layer (c) the peaks and troughs are uneven as there is inhomogeneous roughness across the print line. They stated that this could be due to the cracking and pinhole issues. Subsequent layers form and evaporate the solvent at different rate. This would induce cracking due to the contraction of each droplet under the layer and on the interface and additional solvent separating the metal NP to form pinholes and cracking. Therefore, the roughness of each droplet will increase as more layers are formed. The rate of the roughness is not proportional to the addition of layers as stated in (Saha *et al.*, 2018). Although the roughness has increased due to the

cracking and pin hole defects, additional layering reduces the dome shape structure therefore the roughness has slightly reduced.

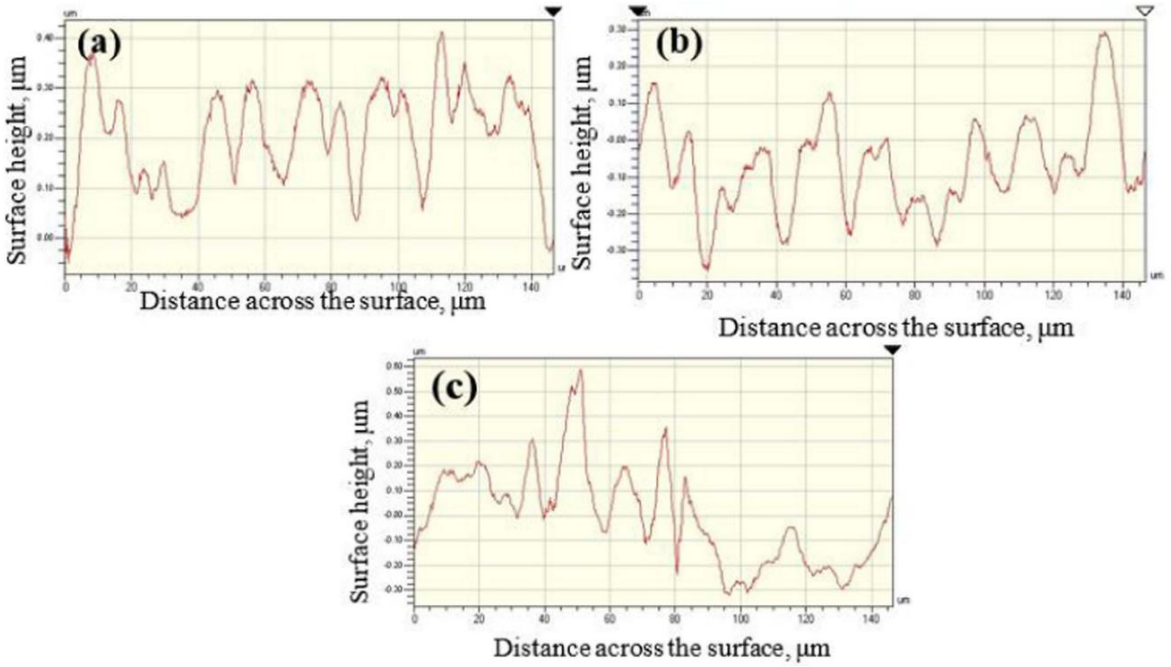

Figure 6.25 Average roughness of 3 different silver NP printed layers on photo paper with a) single layer, b) double and c) triple (Saha *et al.*, 2018)

Although the print lines had spacing and droplet size smaller than this work, the roughness for the magnetite printed particles is not comparable to the published work of around 0.5 µm roughness average as shown in Fig. 6.26. This is due to the larger print droplet size that can increase the roughness of the print and lower the amount of metal NPs, therefore increasing the risk of cracking and pores due to the solvent.

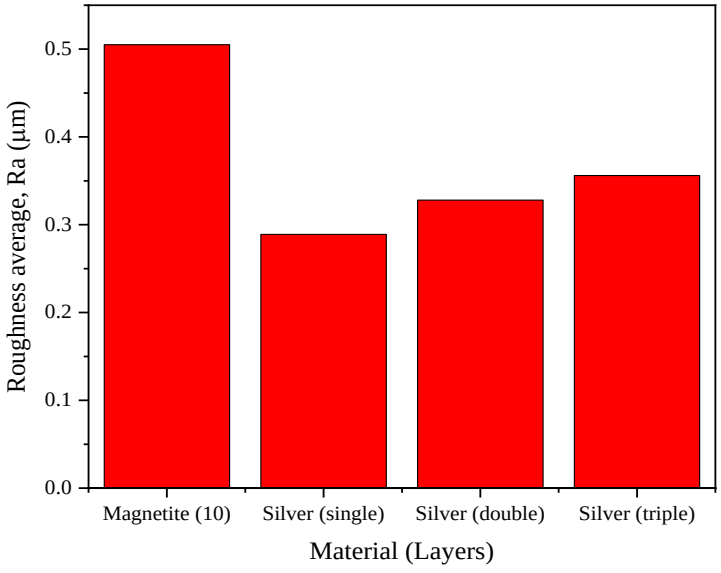

Figure 6.26 Roughness (Ra) of magnetite and silver NP on photo paper (Saha *et al.*, 2018)

Additional roughness measurements were studied to see the effect of roughness and substrate. Paper, kapton and glass were used as substrates to print magnetite NPs. Fig. 6.28 shows the surface profile and line scan for each substrate shown in Fig. 6.27. A 2nd order polynomial fitting was performed on the line scan for each substrate and in X and Y directions. Generally, the droplet form a dome shape structure therefore a 2nd order polynomial is best suited for fitting the line scan, thus both fitting and roughness profile can be compared. The parameters are Ra (roughness average), Rp (maximum peak height), Rq (root mean squared roughness from mean line), Rt (range of collected roughness in data) and Rv (valley depth below the mean line). Fig. 6.28 (d) shows that there is a difference in roughness due to the surface tension and wetting angle. The Ra, Rp, Rq, Rt and Rv value is highest in paper substrate. According to the roughness parameters, the paper is rough in comparison to kapton and glass. Whereas glass substrate show a reduction of roughness in Ra, Rp, Rq, Rt and Rv compared to paper and kapton. As the wetting angle is reduced, for paper and kapton, the surface tension is high therefore the dome shaped structure is more prevalent hence roughness is increased as seen in Fig. 6.27 (b) and (d). However, the range and peak of kapton (Rp and Rt) of the dome shape is lower than the paper as seen in Fig. 6.27 (b) and (d). This is due to lower surface tensions and lower wetting angles on glass and kapton substrate, therefore creating a uniform droplet.

In comparison, the polynomial fitting for line scan in Fig. 6.28 shows the (a) intercept, (b) B1 and (c) B2 fit. It shows for kapton the dome shape can be seen clearly, whereas the paper and glass substrate, the droplet is more flat and uneven. Paper has the largest change in B1 and B2 parameter fitting in X and Y direction than kapton and glass, which is why the Rp and Rt is high for paper in roughness profile. Therefore, the substrate that shown to be rough is paper due to its uneven structure in comparison with X and Y directions.

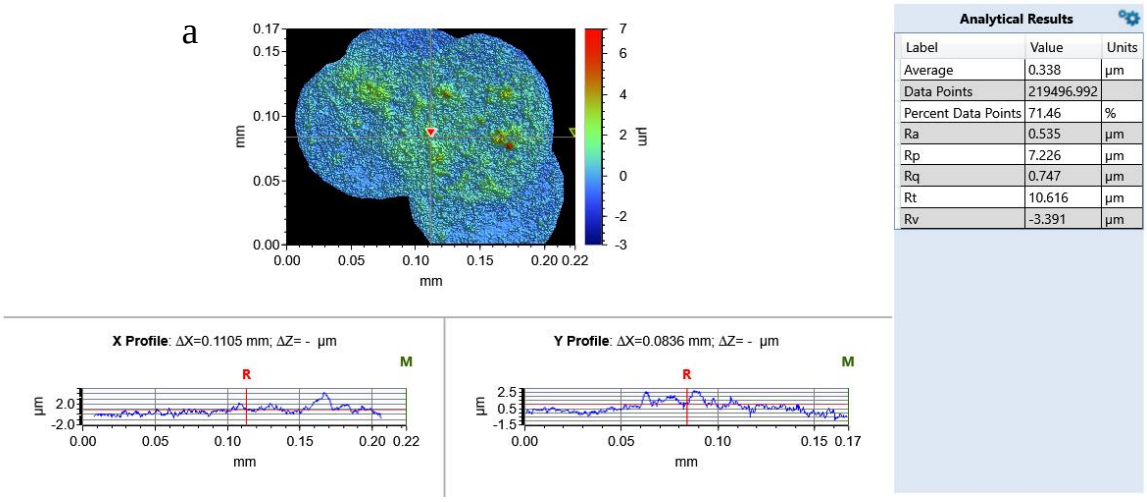

b

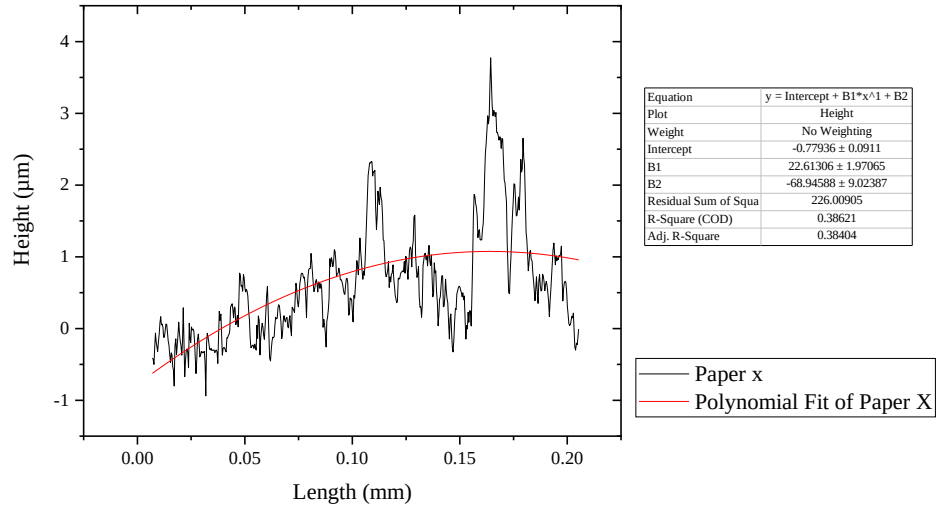

Equation	y = Intercept + B1*x^1 + B2
Plot	Height
Weight	No Weighting
Intercept	-0.77936 ± 0.0911
B1	22.61306 ± 1.97065
B2	-68.94588 ± 9.02387
Residual Sum of Squa	226.00905
R-Square (COD)	0.38621
Adj. R-Square	0.38404

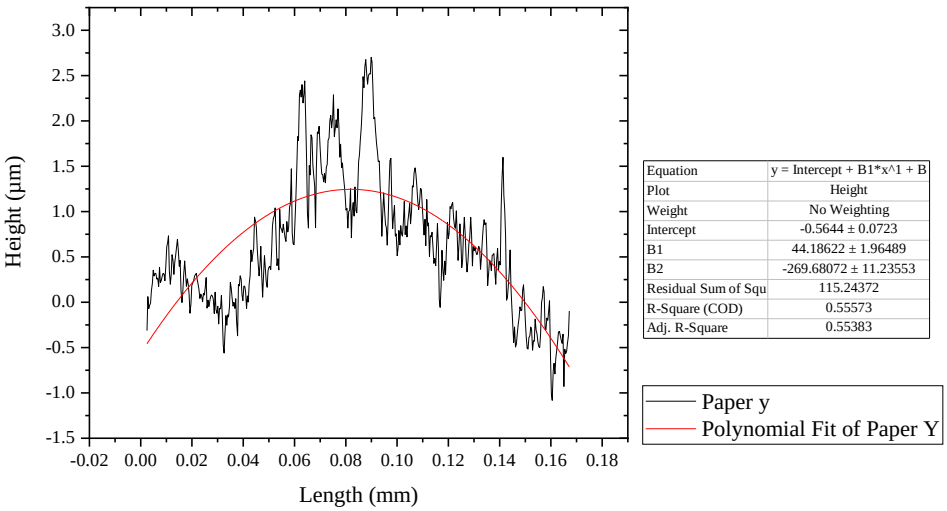

Equation	y = Intercept + B1*x^1 + B
Plot	Height
Weight	No Weighting
Intercept	-0.5644 ± 0.0723
B1	44.18622 ± 1.96489
B2	-269.68072 ± 11.23553
Residual Sum of Squ	115.24372
R-Square (COD)	0.55573
Adj. R-Square	0.55383

c

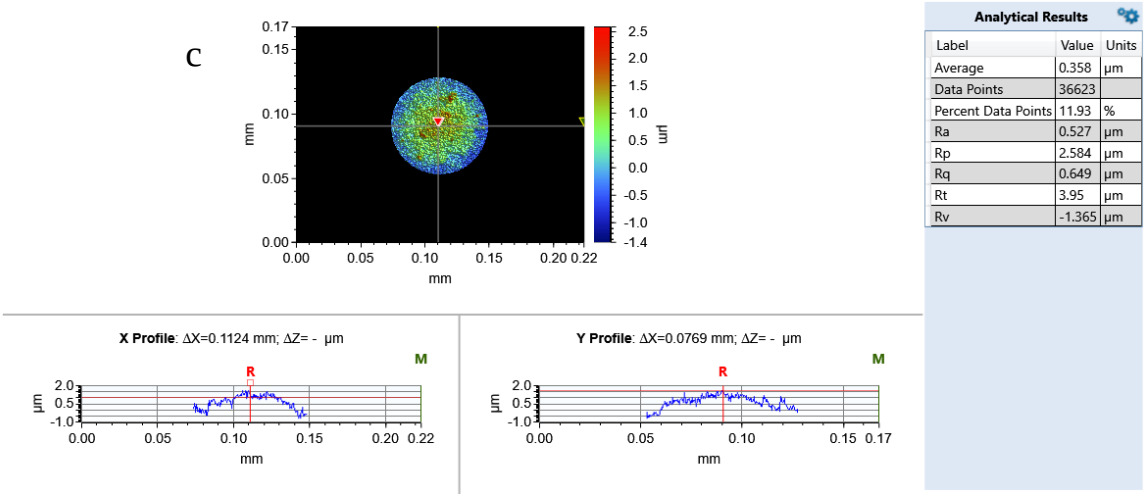

Analytical Results

Label	Value	Units
Average	0.358	µm
Data Points	36623	
Percent Data Points	11.93	%
Ra	0.527	µm
Rp	2.584	µm
Rq	0.649	µm
Rt	3.95	µm
Rv	-1.365	µm

d

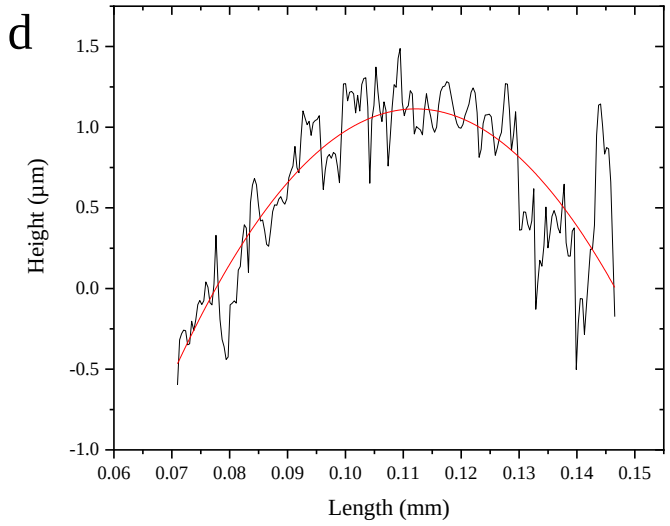

Equation	y = Intercept + B1*x^1 + B
Plot	Height
Weight	No Weighting
Intercept	-10.62717 ± 0.50304
B1	209.43984 ± 9.50785
B2	-934.04414 ± 43.53412
Residual Sum of Sq	16.21373
R-Square (COD)	0.70617
Adj. R-Square	0.70343

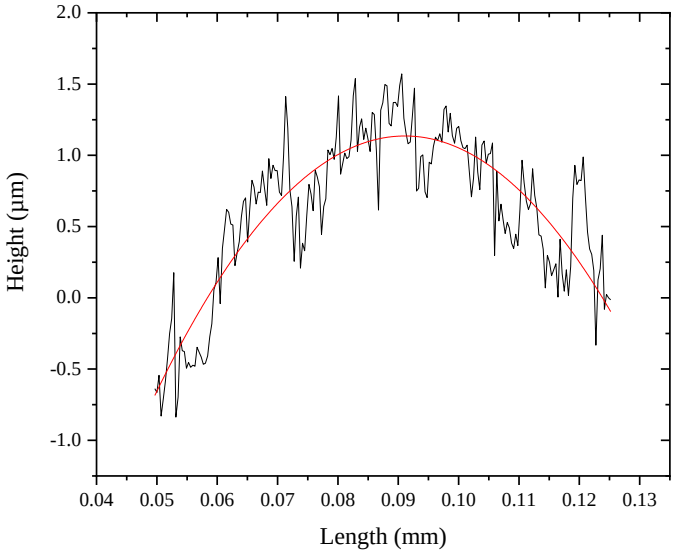

Equation	y = Intercept + B1*x^1 + B2
Plot	Height
Weight	No Weighting
Intercept	-7.6646 ± 0.31737
B1	193.19234 ± 7.56838
B2	-1060.28607 ± 43.01461
Residual Sum of Squa	15.82907
R-Square (COD)	0.7641
Adj. R-Square	0.7619

e

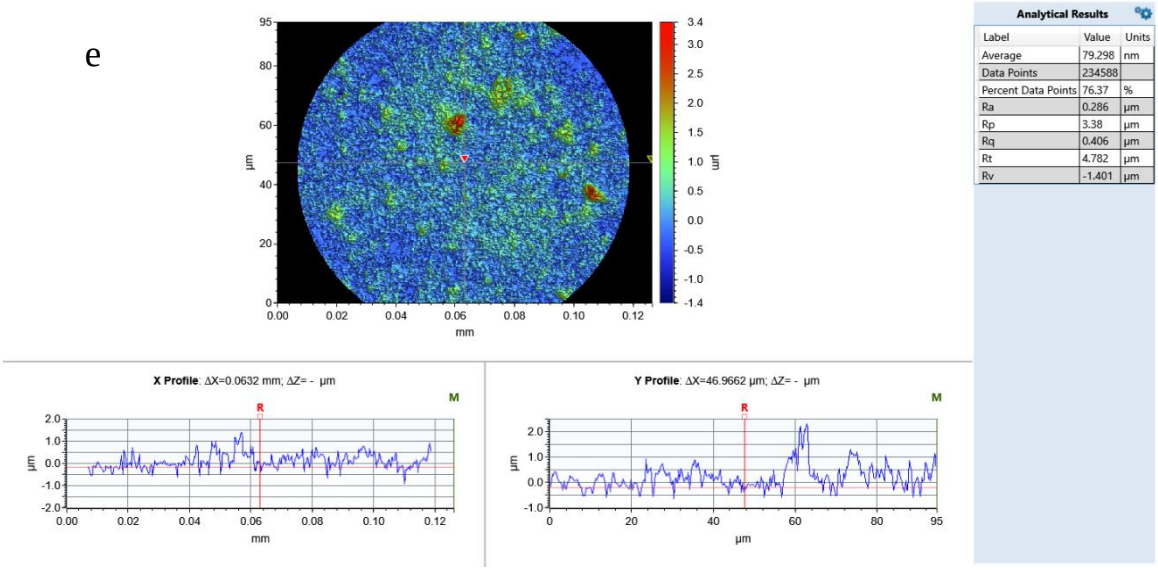

Analytical Results

Label	Value	Units
Average	79.298	nm
Data Points	234588	
Percent Data Points	76.37	%
Ra	0.286	µm
Rp	3.38	µm
Rq	0.406	µm
Rt	4.782	µm
Rv	-1.401	µm

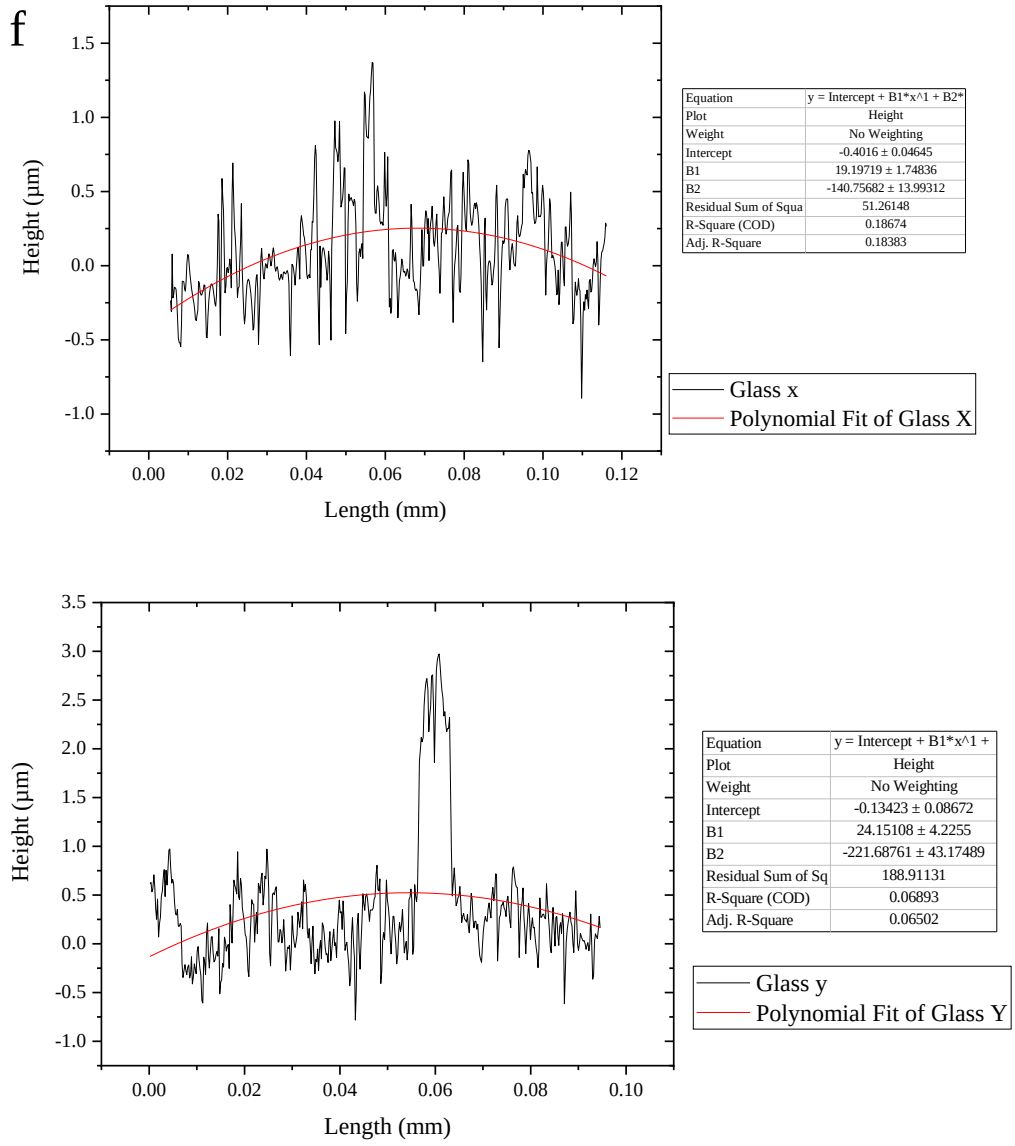

Figure 6.27 Surface profile of magnetite print on a) paper, c) kapton and e) glass. Surface line scan and fitting in the X and Y direction on b) Paper, d) Kapton and f) Glass

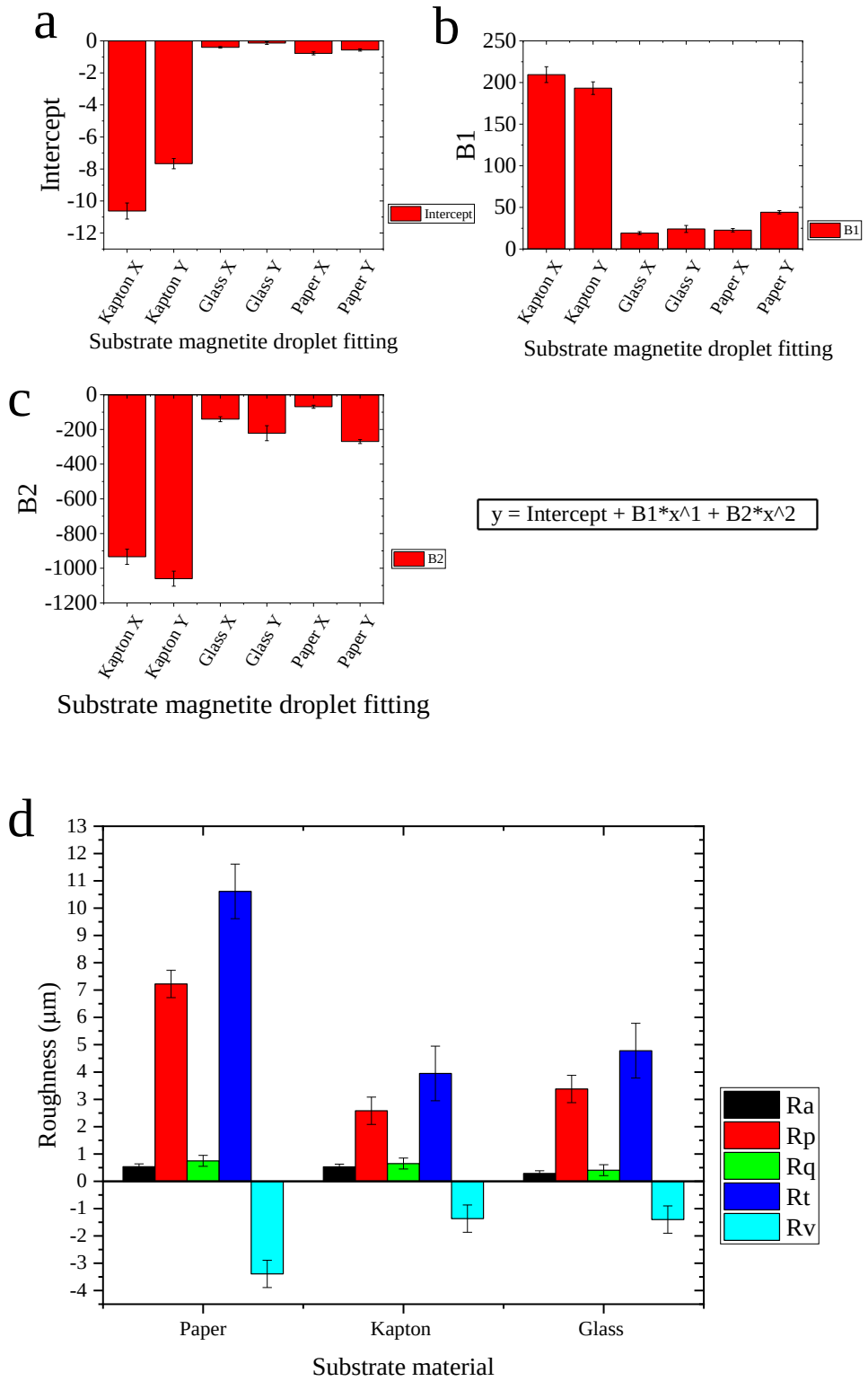

Figure 6.28 Polynomial fitting of line scan (a) Intercept (b) B1 (c) B2 and (d) Roughness values of magnetite on photo paper, kapton and glass

The droplet height is measured in 2D image as seen in Fig. 6.29 for paper (a), kapton (c) and glass (e) substrates. This is because the 2D image measures the height from the lens focusing on the surface, not measuring the surface profile/roughness. Therefore, the line scan of the magnetite droplet on (b) paper, (d) kapton and (f) glass shows an average thickness of droplets to be around 112 µm, 61 µm and 60 µm respectively. Cracking and pores for paper substrate can be seen in the line scan in (b), where beyond 0.15 mm, the peaks and troughs are erratic. This could be due to layers that are not aligned and non-uniform composition in the ink during printing, which resulted in excess solvent deposited. The metal NPs tend to settle, which is normal however, steps could be taken to reduce this such as time taken to print or manual mixing of the reservoir after printing a few layers. The droplet height and size on the kapton and glass substrate is smaller than on paper which is expected. The smaller size is due to heating the glass substrate to 373 K, which helped to evaporate the solvent and prevent migration of magnetite NPs to the edges. Otherwise, printing on glass at room temperature would result in loss of printing resolution. The height has reduced due to the lower wetting angle of the droplet to the substrate.

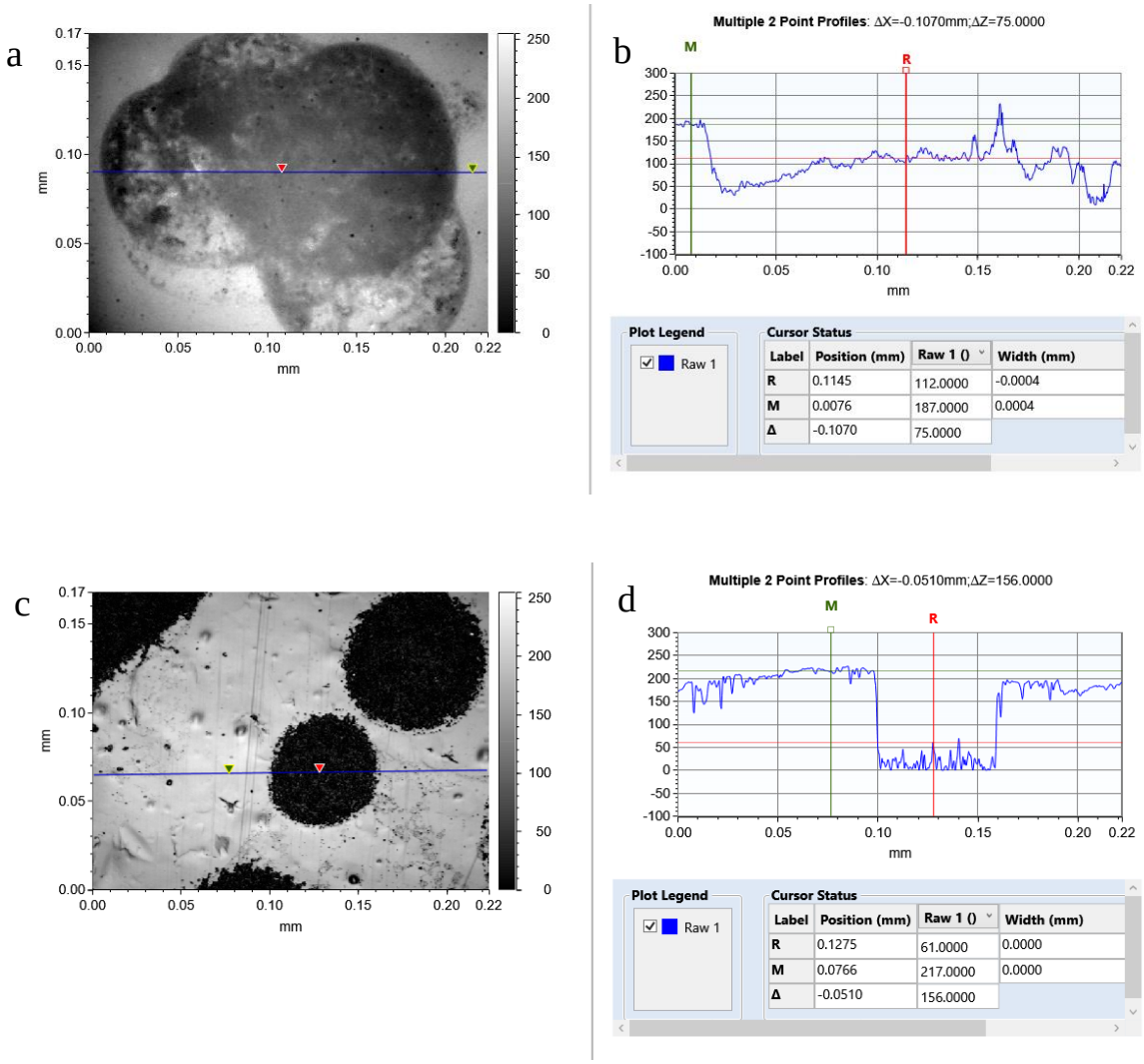

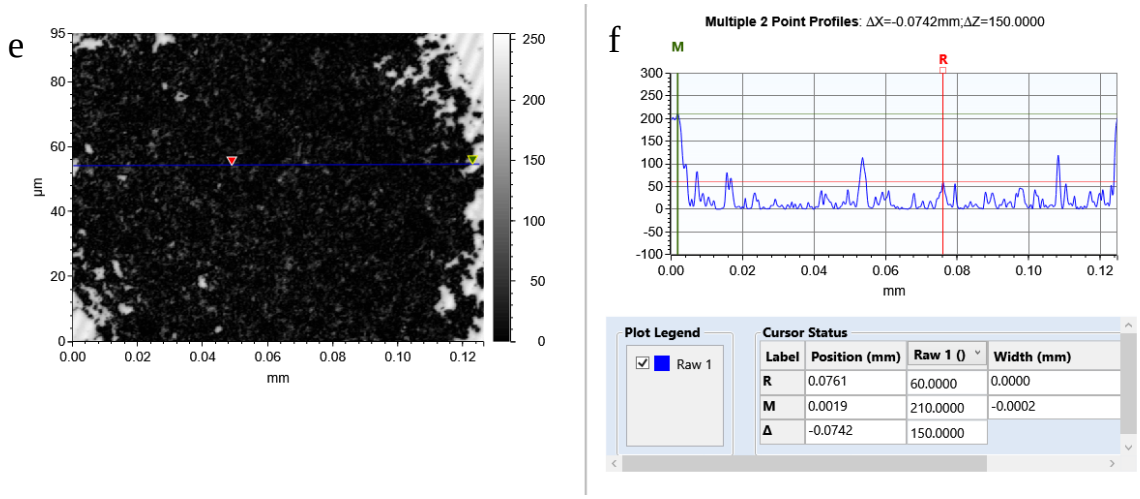

Figure 6.29 2D surface image of magnetite print on a) Paper, c) Kapton and e) Glass. Graph showing line scan and thickness of magnetite print on b) Paper, d) Kapton and f) Glass

6.8 Inkjet printing sensor measurement

6.8.1 Hall probe measurement

Strain bending of the inkjet-printed sensors as shown in methods chapter 4.5.2.1 was carried out to measure the change in magnetic field as a function of strain. The printed sensors were strained over a known radius of curvature bend rig. To measure the magnetic field of the printed sensor when strained, a Hall probe was used, as it is a common method used for measuring magnetic field. The result can be seen in Fig. 6.30 and Fig. 6.31 for both magnetite and nickel print on photo paper respectively. The Hall probe measurements for both magnetite grid prints and nickel print lines show a similar trend and as the strain is increased, the magnetic field changes. However, the results shown here are misleading, while it does show that as the magnetic field increases, the lower limit of the Hirst gaussmeter was reached. This is due to either the background field or the sensitivity of the Hall probe being unable to measure accurately below 0.01 mT. As seen in Fig. 3.12, the Hall probe has a range of measuring down to 1 mT where are other methods can measure field far lower than this. The magnetic field from the print was expected to be small as the thickness of the layer is in microns and would not have a high demagnetising field or stray field to be detected by the Hall probe. Therefore, the field would depend on the amount of material deposited on the substrate.

To quantify the data, a linear fitting was used as shown in methods chapter 4.5 and in (Flatau, 2019) as the gradient/slope of the field as a function of strain determines the sensitivity of the sensor. In (Flatau, 2019), they have demonstrated that for the Villari effect, the linear part of the data (from zero stress to positive saturation or zero stress to negative saturation) could be used to determine and select the sensor for SHM of CFRP. Therefore, using this method, Fig. 6.32 and Fig. 6.33 shows the linear fitting and R-

square respectively for magnetite and nickel print based on the Hall probe measurement of magnetic field as a function of strain. They show that for both nickel and magnetite designs, the change in field with strain are not the same. For example, the 3 mm grid and coil design show a good response to strain in magnetite and nickel respectively. However, there is a large deviation in results, for example in the magnetite uniaxial patch print, the change in field is similar to 3 mm grid design however the deviation in the data is misleading as there is a good level of linear change as seen directly from the data in Fig. 6.32. Fig. 6.33 shows the calculated R square value of the linear fitting. It shows that the fitting for 3 mm grid design is good (above 0.5) as the data is almost linear. However, for other designs, the R squared value is lower than 0.5 which means the fitting is not good from the data. The nickel R-squared value shows a different picture where coil and uniaxial designs are a good fit as they show a good level of change.

Overall the Hall probe measurement of the change in field with strain shows mixed results for both magnetite and nickel inkjet-printed designs. The change in field with strain either increases or decreases as there is no definitive level of change, which could be due to the way magnetite and nickel is printed onto the photo paper. The level of error found in the data and fitting for both magnetite and nickel print shows that the Hall probe is not sensitive to pick up small changes in field. Therefore, a better measurement method is needed to be able to assess the sensors for SHM.

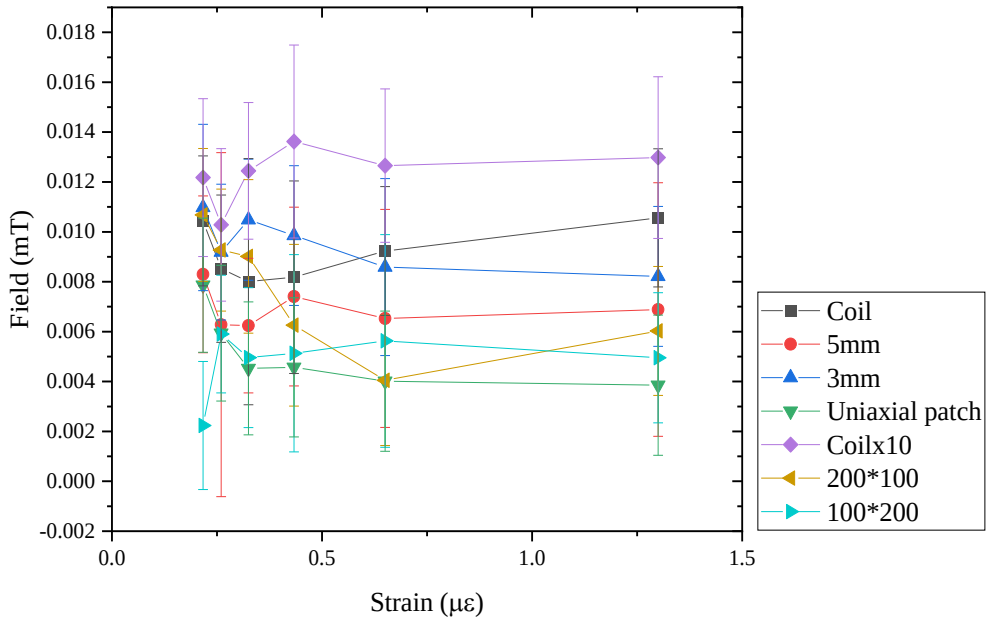

Figure 6.30 Inkjet-printed magnetite designs on photo paper field (mT) measurement via hall probe as a function of strain (με) by bending over a known radius of curvature

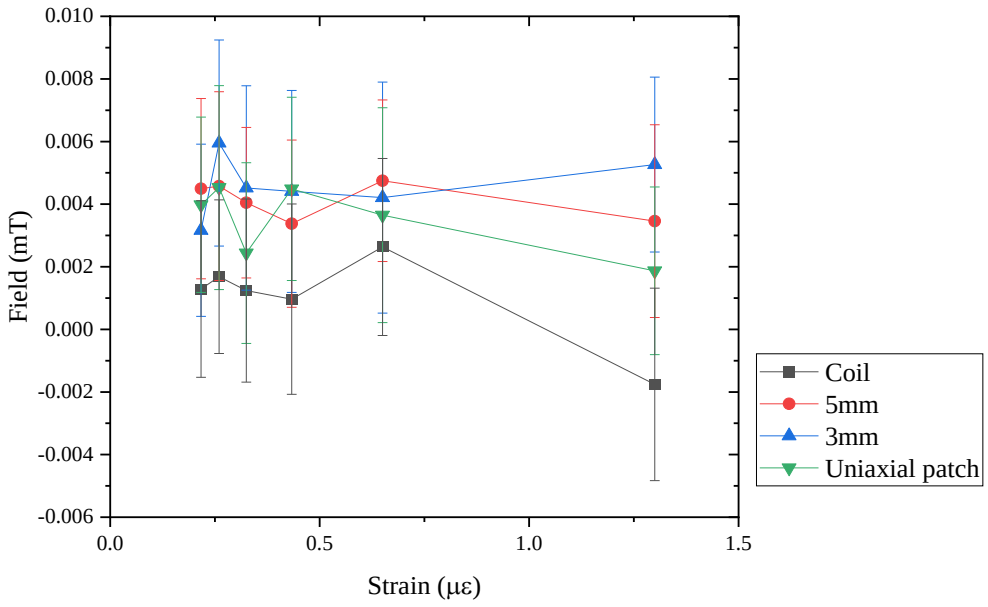

Figure 6.31 Inkjet-printed Nickel designs on photo paper field (mT) measurement via hall probe as a function of strain (με) by bending over a known radius of curvature

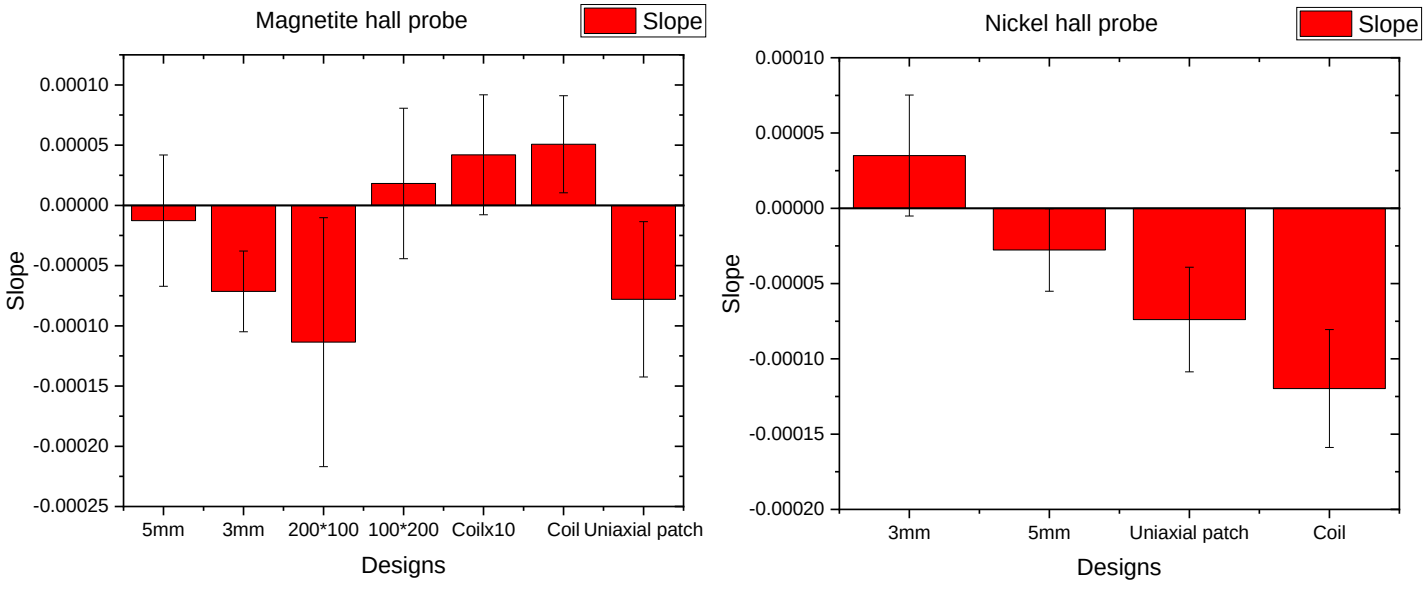

Figure 6.32 Linear fitting of magnetite (left) and nickel (right) designs hall probe measurement

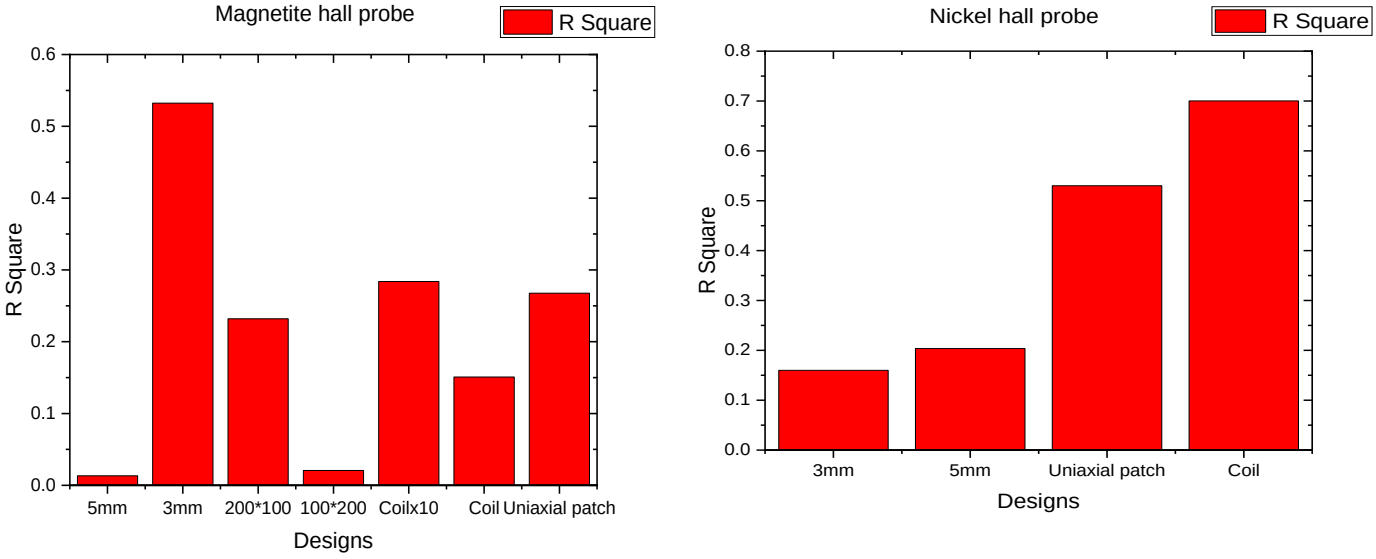

Figure 6.33 R-Square value for magnetite (left) and nickel (right) designs hall probe measurement

6.8.2 Inductance measurement

The inductance measurement method consists of a coil inductor where a current flowing through, changes due to the stored energy from the magnetic field, this creates a voltage lag as it opposes the current. The inductance increases as the wire is wound into a coil, as the storage of energy increases. However, to test how many turns are needed to detect the field from the print, a set of inductor coils were made as shown in methods chapter 4.5.2.1. Fig. 6.34 shows the result of the change in inductance as a function of strain for the different coil turns. The results were taken on bending a well-known magnetostrictive material (metglas), from 600 mm to 100 mm which corresponds to micro stains of 0.22, 0.26, 0.33, 0.43, 0.65, 1.3 respectively. The graph shows that the 250 turns inductor coil appears to have a greater slope than the other coil inductors. However, there are significant changes at lower strain value as the number of turns in the coil increases.

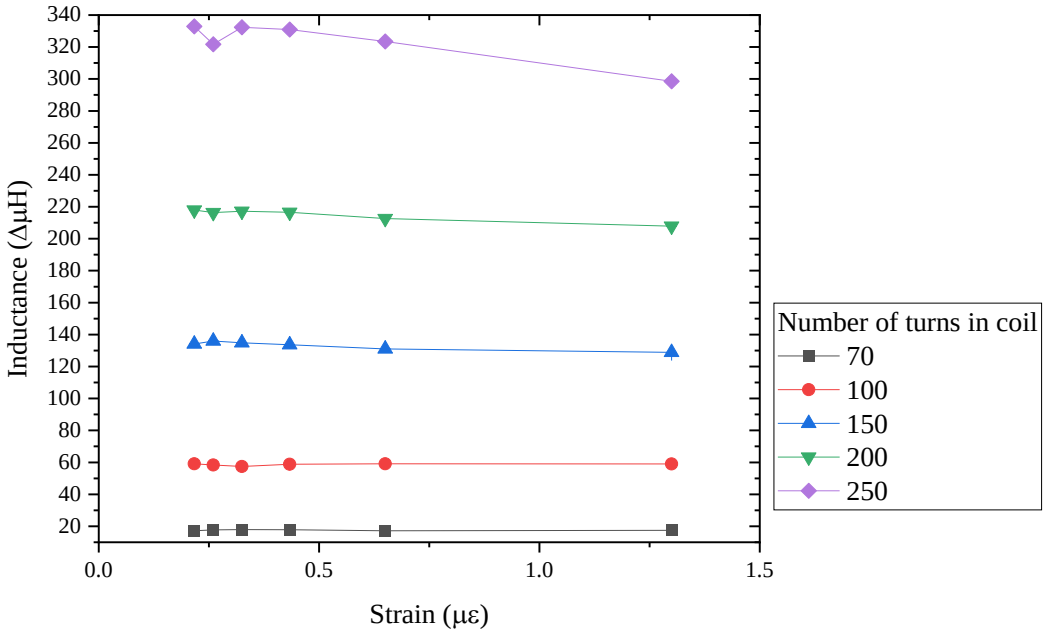

Figure 6.34 Metglas inductance as a function of strain for coil turns of 250, 200, 150, 100 and 70

Fig. 6.35 shows the slope (linear fitting) of the inductance as a function of strain for different coil with 250, 200, 150, 100 and 70 turns. As the number of turns increases, the gradient the of inductance as a function of strain increases. However, it is not simply the case of increasing the number of wire turns in a coil to increase the slope or gradient. It was found that as the number of turns increases the level or error in the inductance measurement increases. This would produce a false reading as the energy stored overpowers the change in field as a function of strain. Therefore, the results show that an inductor can overpower or under power the change in inductance. Therefore, further analysis is needed to quantify and select the correct inductor.

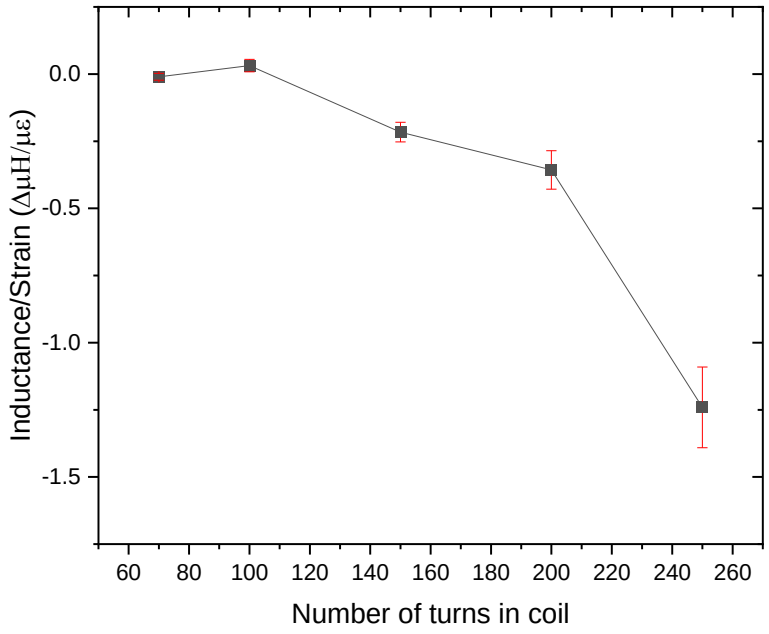

Figure 6.35 Inductance to strain gradient sensitivity of metglas for wire turns of 70, 100, 150, 200 and 250 coil

Fig. 6.36 shows the signal to noise ratio (SNR) of the different coils tested for the change in inductance as a function of strain. The analysis takes into account of the deviation and the change in inductance for each strain value. Interestingly, the SNR for all the coils, fluctuate at lower strain level, then the noise reduces when the strain is increased. This suggests that at lower strain level the signal is low and the SNR is only the measure of the coil inductance, rather than the metglas changing field to strain. There is a slight increase in SNR as the strain is increased for most coil turns, which is due to the change in field as metglas is strained. The analysis shows that the 200 turns has the highest SNR (3.1) in comparison with other inductor coils. However, as discussed the change in SNR is important rather than the highest SNR value, as the SNR should increase at higher strain level. 100 turns show the best improvement in SNR from lower strain level to higher strain level. What is surprising is that the SNR is not proportional to the number of turns in the coil, for example the 250 turns inductor has the lowest SNR value of around 2.5, even though it has shown the highest inductance to strain slope in Fig. 6.35.

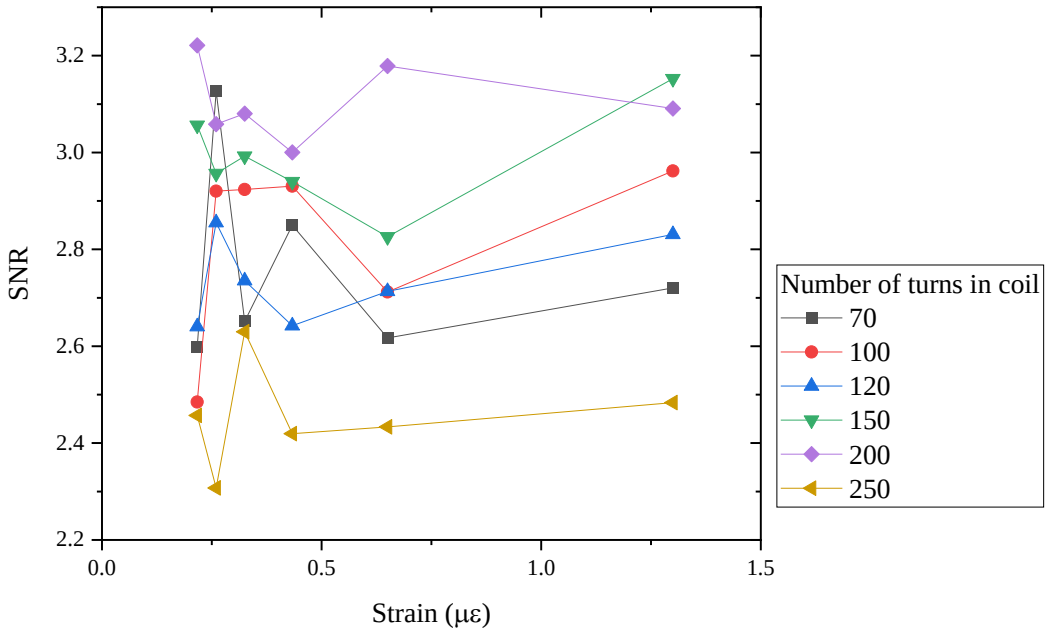

Figure 6.36 Metglas signal to noise ratio as a fuction of strain for different inductor coild turns

To test the inductance of magnetite and nickel NPs, a drop of ink pipetted onto photo paper was first measured to see the effect of magneto mechanical performance without printing any designs. Fig. 6.37 shows a positive trend for magnetite inductance-strain sensitivity, as the radius of curvature was reduced. As the drop of magnetite and nickel is far bigger than inkjet-printed NPs, the order of magnetic moments are different in both processes. A drop from a pipette would have more randomly orientated moment as the amount of magnetite will form cracking and pores, which can increase the orientation of the moments, therefore the sensitivity to strain will be different. Nevertheless, this test proves that the magnetic field of the NPs on photo paper is sensitive as a function of strain and has potential to be used in SHM applications. However, as a sensor and manufacturing difficulty of producing nickel NPs, Magnetite looks to be a better sensor for SHM application. From Fig. 6.37 the Nickel NPs do not perform well to strain and is relativity flat compared to magnetite NPs.

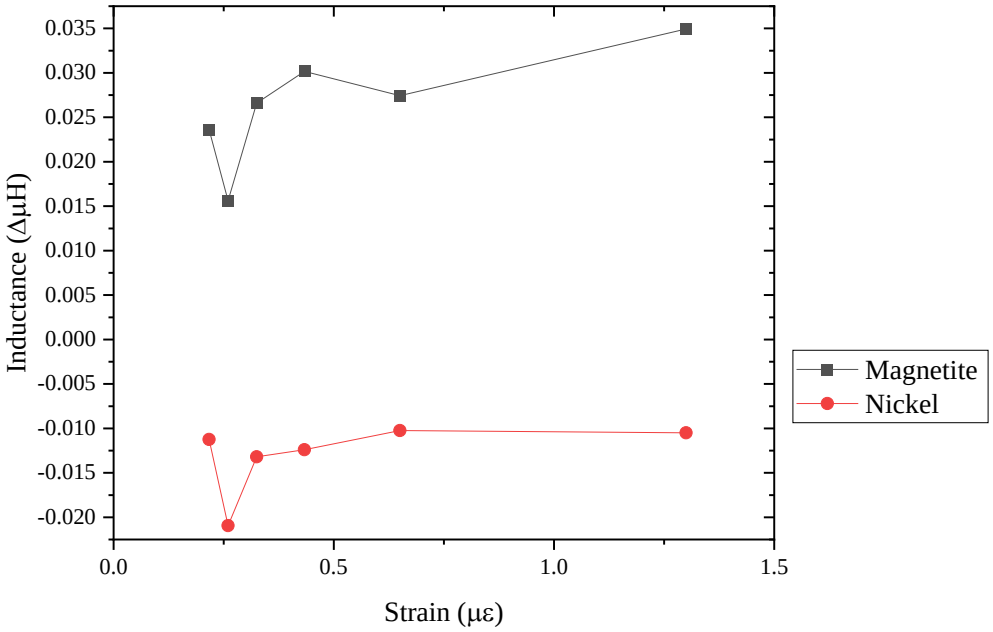

Figure 6.37 Magnetite and nickel drop inductance as a function of strain

The different designs including uniaxial patch, coil, grid and print directions were printed using JetLab 4 inkjet printing system as seen in chapter 6.7. The designs were measured using the bend rigs with a known radius from 600 mm to 100 mm (R600 to R100). The graph in Fig. 6.38 shows the mean value of inductance measured on each bend rig with deviation of +/- 0.005 μH. Most of the results shown in Fig. 6.38 appears to show a negative inductance as the radius of curvature is reduced. As the radius is reduced, the distance between the coil and magnetite print is increased and tension caused by the bend rig would align the moments toward the stress direction, which would naturally assume a negative trend. However, the moment could align towards the inductor under compression, therefore could increase the error. Error in the measurement may increase by changing the bend rig and lifting the inductor. Considering how small the change in inductance is and the magnitude of field measured by the Hall probe, the magnetite print has a relatively weak field response to strain and would make it difficult to measure the magneto mechanical performance. The measured magnetic field may be improved by increasing the density of the print.

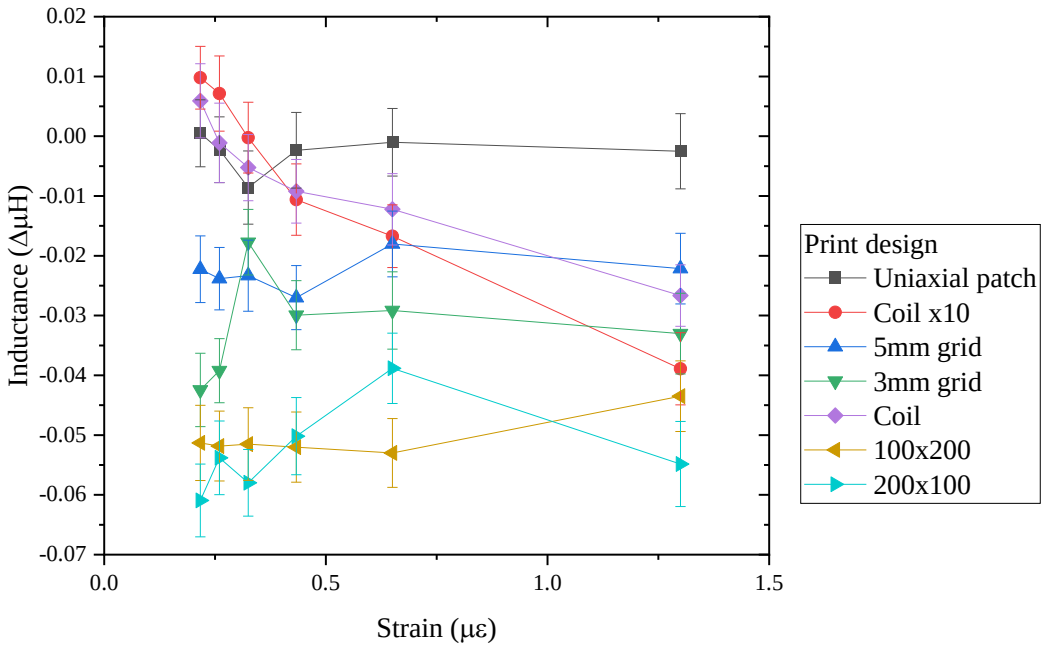

Figure 6.38 Magnetite print designs inductance as a function of strain

By converting the radius of curvature to strain values (0.22, 0.26, 0.33, 0.43, 0.65 and 1.3 με), a linear fit was performed using OriginLab software, as shown in appendix. Fig 6.39 shows the calculated linear fitting of the magnetite print where the graph (a) intercept, (b) slope and (c) R squared values. The slope/ gradient is the rate of field as a function of strain applied, therefore the grater the change means the sensor design performs well as a function to strain. The intercept shows the initial inductance value where no strain is applied, which may be significant to compare with other designs such as increased layers, would mean higher intercept. R squared value shows how well the data fits the linear fitting and if increasing strain changes the magnetic field, for example, if the data is erratic then the R squared value is low. A good R squared value is needed, as it is ideal to have a sensor that is less erratic and follows the fitting slope.

The design that is shown to be most sensitive to inductance as a function of strain is the coil design as shown in (b). However, the gradient of the coil design is lower than other designs, which may be due to the design itself. The R square value (COD) as seen in (c) shows that 80% of the data is due to the applied strain. Whereas, the R value for 5 mm grid, 3 mm grid and uniaxial patch are close to 0, which suggest that the change in strain does not affect the change in inductance. Data could be improved by gradually reducing the radius of curvature while measuring the inductance. For example, the intercept shown in (a) should be showing a positive value due to the demagnetising field of the printed NPs. The negative intercept could be due to the initial applied strain, in other words the starting strain could be too high, resulting in negative reduction in inductance.

The parameters that were used to improve the change in field to strain has been explored such as change in design, number of layers and print directions. The effect of changing design from 5 mm to 3 mm and uniaxial patch do not show a significant change. There is a slight increase in gradient and R squared value for the 5mm grid. However, there is a larger deviation in the 3mm grid than 5mm grid design, which may benefit from additional data points as mentioned before, the same can be said with the uniaxial patch. In comparison with the desktop printing grid design, the change in field to strain (cantilever) did show a difference between 5 mm and 3 mm track gap design. This is due to the larger stress applied to the steel with no substrate material. Nevertheless, the 5 mm grid for both printing methods do show that it is better than the 3 mm grid design. Printing multiple layers does make a difference to the magnetoelastic performance. A coil with 10 layers shows an increased slope in the field as a function of strain compared to the single layered coil, which is as expected due to a greater amount of material deposited on the substrate. Even though the gradient for both single and multiple coil layers show a negative tread, the addition of multiple layering causes an increased gradient to the magnetoelastic performance.

The print that is perpendicular to the strain direction shows the greatest sensitivity to inductance as a function of strain as seen in Fig. 6.39. The 100 x 200 px rectangular print (perpendicular to strain) has a higher inductance to strain sensitivity than 200 x 100 px rectangle (parallel to strain) print. The intercept in (a) is shown to be almost the same for both print in parallel and perpendicular lines. As strain is applied, the perpendicular print produces a positive gradient whereas the parallel print remains at zero as seen in (b). However, looking at the bar chart is misleading and does not represent the full picture. It is true that the perpendicular gives a higher gradient but at lower to higher strain value e.g from 200 mm to 100 mm radius. The parallel print is more sensitive to field as a function of strain at lower strain value than the perpendicular direction. This may be due to the shape anisotropy effect where the alignment of print direction in the parallel, the easy direction is along the axis, which is why the inductance peaked much earlier than perpendicular direction. The perpendicular direction peaked at 100 mm radius, which is due to the hard direction (as the alignment is already aligned towards the perpendicular direction). In Fig. 6.20, the microscope image of the printed magnetite on photo paper shows that individual drops of the magnetite ink are spherical shaped, which suggest that the shape anisotropy is down to the direction of print and not due to the shape of individual droplets.

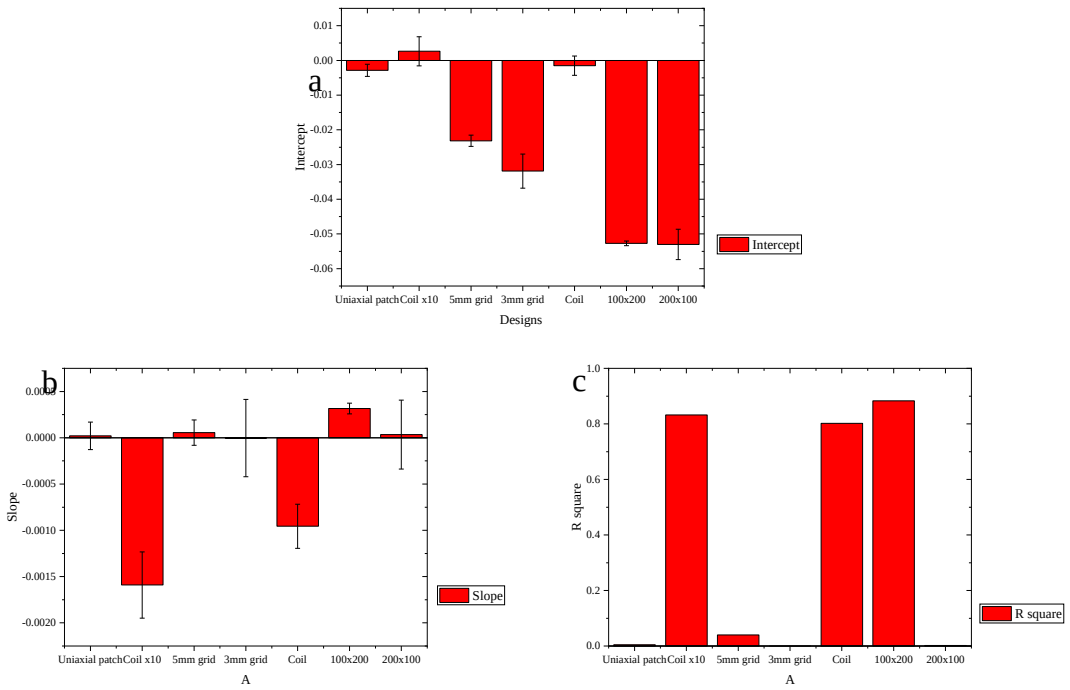

Figure 6.39 Magnetite design linear fitting (inductance/strain) graph showing a) Intercept, b) Gradient, and c) R squared value

In comparison, nickel has shown a higher inductance than magnetite, for example the coil design in nickel at 600 mm is at 0.025ΔμH compared to 0.01ΔμH for magnetite as shown in Fig. 6.40. Considering there's only 2% of nickel in the ink, it was expected to be less than magnetite, however nickel has a higher remanence as shown in table 6.2. This is a direct contradiction to the nickel and magnetite pipette drop inductance as a function of strain in Fig. 6.37, where it is clear that magnetite has higher inductance value than nickel. Therefore, the moment could be aligned initially in plane rather than towards the inductor. The nickel print had to be printed multiple times to be able to see the design itself which could be the reason why excess nickel NPs produced higher inductance. The graph in Fig. 6.41 shows the fitting for nickel with parameters of (a) intercept, (b) gradient/slope and (c) R squared value. In (a) it shows that even though the intercept is higher, all the designs have smaller gradients in comparison to magnetite print as shown in (b). For example, nickel 5mm grid and coil designs gave a good response to inductance as a function of strain. However, they have lower gradient than magnetite coil and 5mm grid design. Although the gradient is very small for all designs, it was expected that the coil design would be more sensitive in nickel ink based on the design change rather than the material change. Again the fitting data is slightly misleading where from Fig.6.40 the coil design shows a much steadier and gradual slope than the 5 mm grid, similar to magnetite coil. For example, in the 5mm grid design, from 600 mm to 400 mm radius, there is a small positive change in inductance but when the radius is reduced to 200 mm radius there is a steep reduction in inductance. Whereas the coil design shows a reduction of inductance from radius of 600 mm to 200 mm. Therefore, the coil design has a

better range of sensing for small and larger strain. The R square values in (c) in both Fig. 6.39 and Fig. 6.41 shows that for both magnetite and nickel, the uniaxial patch is the worst design, as the data is not influenced by the strain size. This could be due to the print direction (perpendicular to strain) and gaps within the design, which could reduce the change in field.

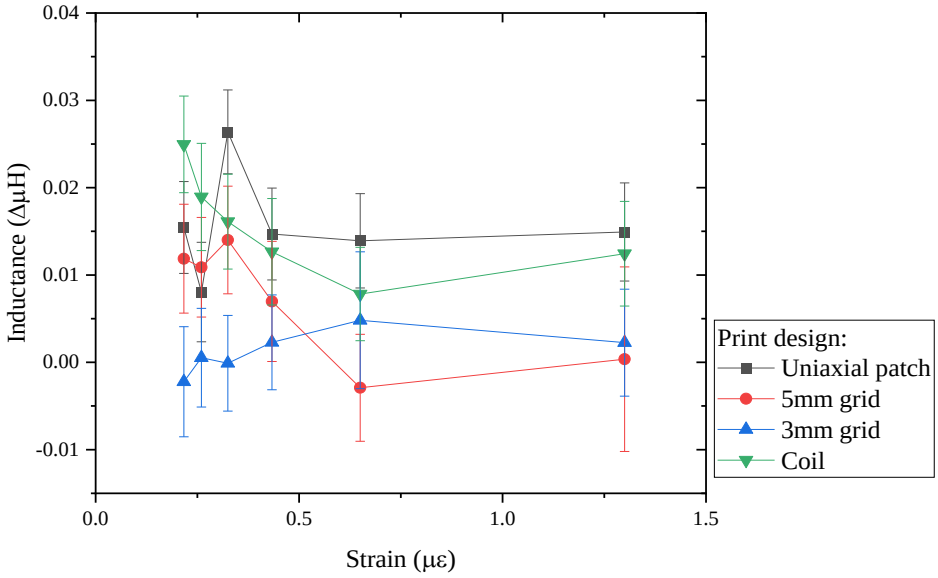

Figure 6.40 Nickel design inductance as a function of strain from 0.22με to 1.3με

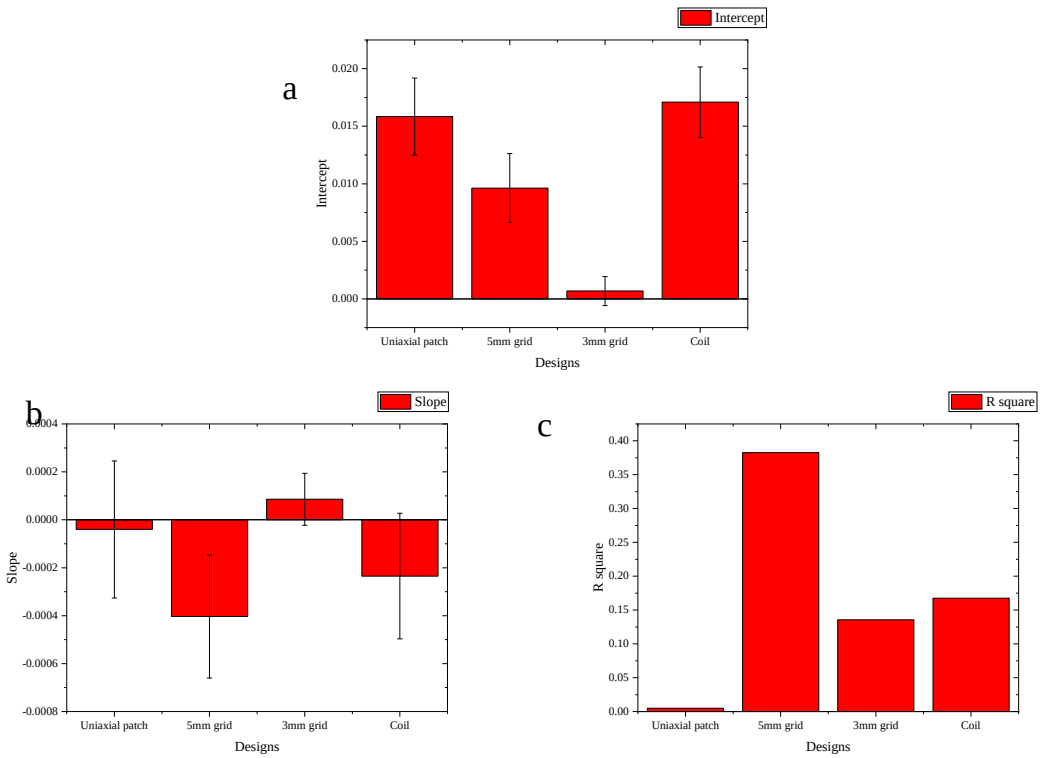

Figure 6.41 Nickel design linear fitting (inductance/strain) graph showing a) Intercept, b) Gradient and c) R squared value

Overall the design that gives the best magnetoelastic response is the coil design. While it does show a negative inductance gradient in both nickel and magnetite material, both do show a good trend of change in inductance to strain. The trend shows a gradual change whereas other designs give a sharp and unpredictable change, which can distort the results. Therefore, this makes it ideal to select it as a sensor in future work. The rate of change in field as a function of strain is higher in magnetite than nickel, even though nickel has a higher intercept (demagnetising field) than magnetite print. Therefore, the material of choice in this work is magnetite. In comparison with literature, in (Vincent *et al.*, 2020) they have reported a 0.01 µH sensitivity to field as a function of strain, whereas this work at best has a sensitivity of 0.007 µH from 600 mm to 500 mm radius as seen in Fig. 6.38 for the 10 layered coil design. Although in literature the inductor used was a shielded pick up coil, this work had used just an air-core coil inductor.

6.8.2.1 Enhancing sensor performance

There are various of ways that could potentially enhance the techniques to measure the magnetoelastic performance of the inkjet-printed designs. Whether it is to change the location of the coil or modify the printing methods, in order to increase the signal to noise ratio and reliability. This would not only apply to the magnetite print, but to any magnetic NPs print by inkjet-printing. For example, coating the print would not only protect the surface but will also strain the top part of the print, ensuring an even applied strain as seen in chapter 6.3. However, coating a material would need to be compatible with the substrate for adhesion and to be thin enough to avoid insulating the small changes in magnetic field. The position of the coil can be moved to measure the field in different parts of the print. For example, the bottom side of the print could be more sensitive than the top as the moment could be aligned towards the bottom when the magnetite ink is deposited. As reported in chapter 6.8.2, applying smaller strain may be needed to see the initial alignment of the magnetic moment. The current radius of curvature is from 600 mm to 100 mm therefore, a smaller radius of 1000 mm is needed to see the full picture. Even if the moments are not aligned or are randomly orientated, the NPs can be forced to align in a specific direction as shown in literature. A NdFeB magnet could be used to align the NPs during printing, by placing the magnet near the substrate or nozzle. Another enhancement is additive layering, which has been shown to improve sensitivity in magnetite coil print. This test will expand and see whether the trend continues beyond layering 10 times. A capacitor could be added to reduce and dampen the noise in the circuit. The signal to noise ratio has been erratic depending on the type of coil used to measure the inductance. Therefore, a capacitor could be used to improve the signal to noise ratio and see an accurate inductance reading for all print designs.

6.8.2.1.1 Coating

The inkjet-printed designs could be further processed to enhance sensitivity to strain. As the magnetite is printed onto the photo paper, strain is greater on the surface but not throughout the droplet. To overcome this issue, a layer of polydimethylsiloxane (PDMS) can be used to coat the top of the print to maintain strain throughout the droplet and print. This would ensure magnetic moments are orientated as the strain is applied. The simulations shown in chapter 6.3, have demonstrated that coated droplets increase the magnetic field at 100 mm radius and the effect of change in magnetic field and gap distance between neighbouring droplets is reduced, as shown in Fig. 6.6.

A coating of PDMS was applied to the magnetite print as shown in Fig. 6.42 by spin coating at 2000 RPM as shown in methods chapter 4.2.2.4. In comparison, the inductance measurement for coated and uncoated magnetite coils on paper, are shown in Fig. 6.43. They show that applying a PDMS coating onto the magnetite print does not have much effect on sensitivity to strain as the data are within error. The magnetite coil with PDMS shows an inductance that is saturated much earlier at lower strain than without a coating. At around 0.2 με and 0.3 με, the gradient of the coated magnetite coil is greater than the uncoated magnetite coil. This suggests that the coating helps slightly to strain the magnetic layer (top and bottom) more uniformly and reaches saturation at lower strain than the uncoated print. In an uncoated magnetic layer, the bottom half is simply strained against the bending rig. Therefore, this leaves the alignment of the magnetic moments, only when a higher strain is applied, the top half is fully aligned towards the strain direction. However, as the strain increases beyond 0.4 με, the coated magnetite print is saturated and the field does not change when strain is increased. The uncoated magnetite print reduces gradually as strain is increased beyond 0.4 με. This suggests that the top half of the magnetite droplet is orientated towards the strain direction. Overall, the same magnetite print shows different sensitivity and dynamics when they are coated or uncoated with PDMS, however no strong claims can be said as the change is very small. In SHM, both of these methods could be used depending on the strain rate and threshold of the CFRP such as an aircraft wing where CFRP are designed to be flexible or near any joints where they are designed not to be flexible. Coated magnetite can be used where low strain is detrimental to the CFRP or uncoated design where higher strains can be an issue for the aircraft to operate or function. Nevertheless, the main function of the coated layer is to provide protection and does not affect the sensitivity of field to strain negatively or positively.

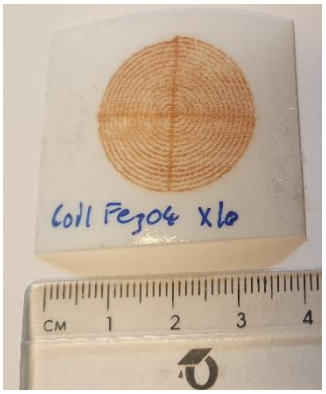

Figure 6.42 Spin coated magnetite coil with PDMS

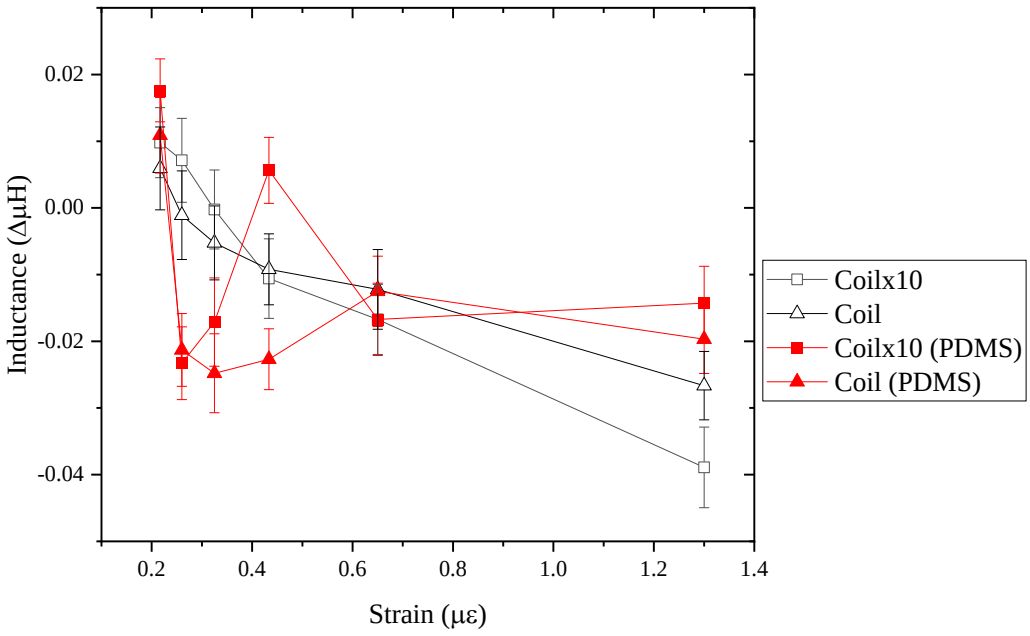

Figure 6.43 The change in Inductance of coated and uncoated magnetite coil with PDMS as a function of strain

6.8.2.1.2 Controlling magnetic anisotropy

The inductor coil has been placed on the top of the print, however from the simulation the magnetic moments are orientated depending on the background field. As the magnetic moments are not fully aligned towards a direction, therefore they are randomly orientated. During jetting there was no applied

field when the droplets are on the substrate surface, thus they are randomly orientated in the background field or in plane. This means when placing an inductor coil on top of the print (as printed on the surface of the substrate) the direction may or may not be sensitive at different locations such as the bottom of the print (the side with no printed magnetite on the surface). Moving the inductor coil inductor from the top to the bottom of the print, can give a better picture of where it is sensitive and alignment of magnetic moments on the substrate. Therefore, further measurements were conducted by measuring the top and bottom of the magnetite coil print.

The graph in Fig. 6.44 shows that there is a very small change in field as a function of strain at the top of the print than the bottom. For example, from 0.2 to 0.7 με, the change in inductance is greater from the top than the bottom of the print. Although they are similar (magnetic moments aligned in the positive direction), which suggest that the moment may lie in plane as the inductance for both sides are within error therefore it cannot be said that one side has greater change in field as a function of strain. The top side does perform better as the magnetite material is closer to the inductor than the bottom. However, the bottom side appears to have a greater demagnetising field than the top side. This could be due to the ink absorption through the paper and alignment of the magnetic moments to the bottom, even though the paper is separating the print on the bottom. Whereas the top side, the coil is in contact but showing less magnetic field than the bottom. However, the magnetic moments are aligned in plane when strained because they are within error and both side show an increase in inductance at the same gradient as seen in Fig. 6.45.

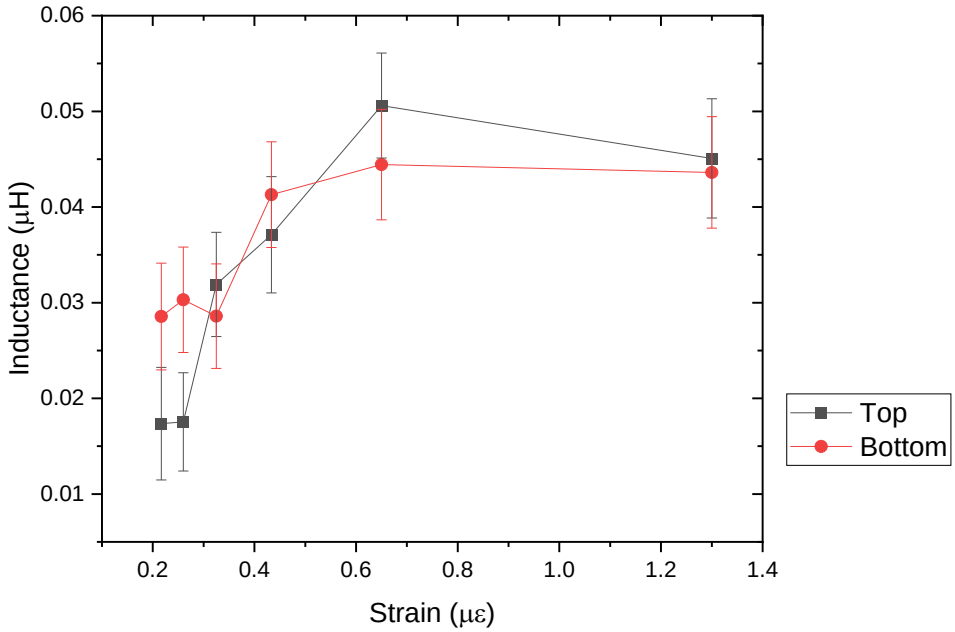

Figure 6.44 Magnetite inductance as a function of strain measured from the top and bottom of the print

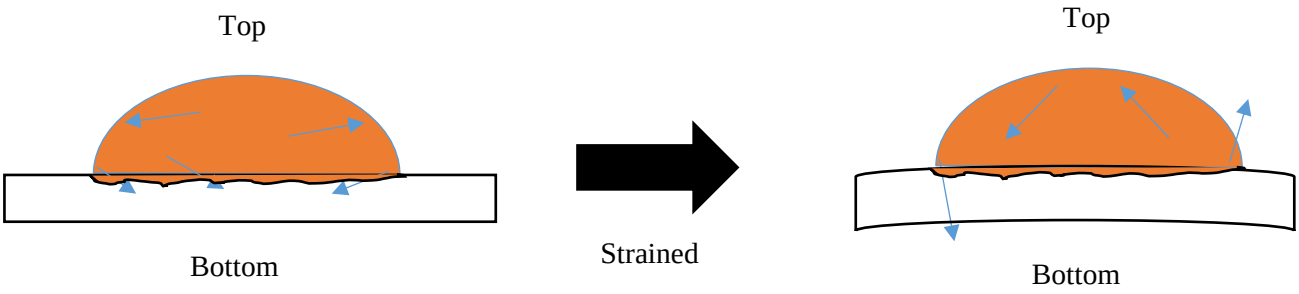

Figure 6.45 Magnetite print droplet with arrow showing magnetic moment direction when strained and unstrained

Using a different inductor coil (200 coil turns) and coil print design, the same trend occurs as seen in Fig. 6.46 when straining and placing the coil on top and bottom of the print. The radius of curvature of the bend rig has been reduced to 1000 mm to see the mobility of magnetic moments as smaller strains are applied. From the result, by applying a smaller strain of 0.13με, the mobility of the magnetic moment can still be seen. It could be said that the gradient of a field as a function of strain is larger when a small strain is applied. Therefore, in comparison with the 100 turns coil inductor as seen in Fig. 6.44, both results confirms that the field lies slightly towards the bottom and when strained the sensitivity is greater from the top of the print.

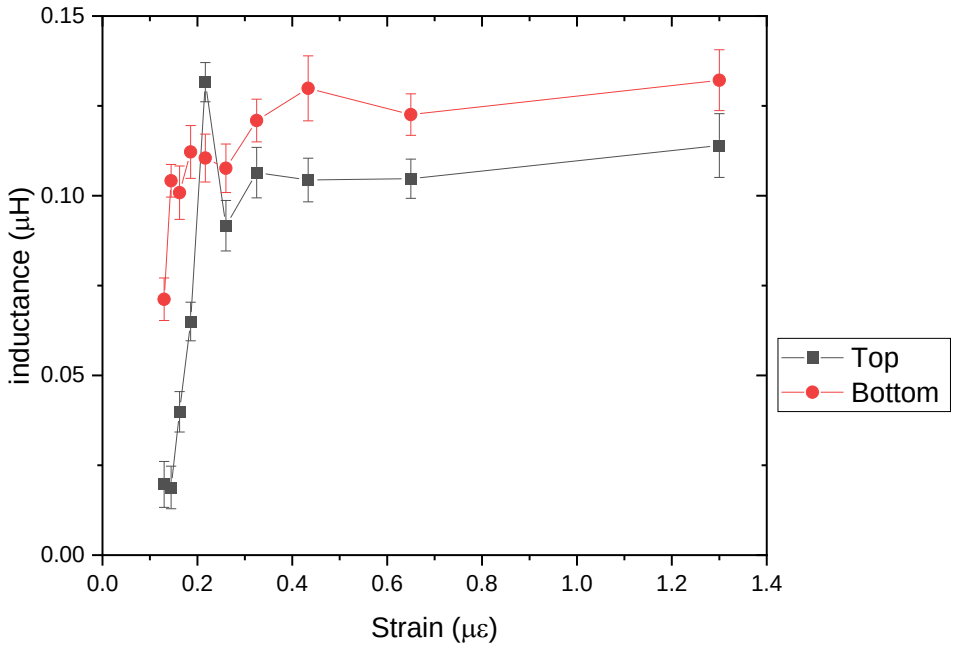

Figure 6.46 Magnetite inductance as a function of strain from top and bottom using 200 coil turns

Following on from changing the position of the copper coil, the sensitivity of the print could be enhanced by controlling the moments during printing. Alignment of magnetic moments was explored

to orientate NPs by an external magnetic field. In theory, re-ordering the moments of magnetic nanoparticles as shown in (Al-Milaji *et al.*, 2019), could improve sensitivity of magnetic field to strain using this method. Another method is shown in (Voit *et al.*, 2003) where it shows that self-alignment of nanoparticles can be achieved by printing in straight lines. However, this depends on the droplet spacing and magnetisation of each droplet. Magnetic moment alignment in the droplets could further improve in addition to self-alignment.

From above, it was found that the magnetic moments are slightly more aligned towards the substrate, the moments could be orientated in plane so that both sides of the print are sensitive to the strain at the same rate. In addition, randomly orientated NPs would cause inconsistent field changes to strain as the moments could change depending on external factors such as background field or neighbouring droplet. Aligned NPs could improve protecting the magnetic print by installing the sensor on the CFRP and measuring the field when the coil is placed on the bottom of the substrate.

Fig. 6.47 shows magnetite nanoparticles (a) without and (b) with magnetic field under optical microscope at x40 magnification. It is shown that without a field, the coffee ring effect is visible and the nanoparticles are unaligned towards the centre of the droplets. In (Al-Milaji *et al.*, 2019) they showed that in unaligned printing (without external field), the droplets formed coffee ring effect, whereas aligned NPs do not form the coffee ring effect. This is due to the three-phase contact line such that slow evaporation rate leads to the nanoparticle transport to the liquid/air interface, therefore leading to the ring formation. By applying a field of 60 mT, the image in (b) shows that the coffee ring effect has been reduced in comparison with (a) as the concentration of magnetite at the edges and centre is more distinct in (a) than (b). The effect of applied field and magnetite nanoparticle mobility can be slightly in (b) as streak line can be seen vaguely along the field direction. However, the print definition and resolution has been reduced for example, the coil print with applied magnetic field of 60 mT reduced the quality of printing, therefore making the printing process ineffective to print designs.

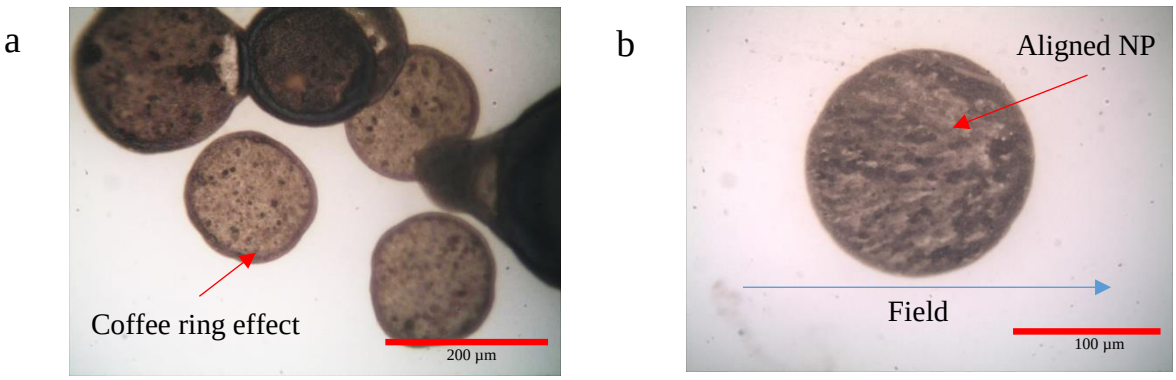

Figure 6.47 Magnetite droplet on photo paper without field (a) and with external field (b) during printing

6.8.2.1.3 Additive layering

Printing magnetite in layers has shown to improve the NPs change in field as a function of strain. However, this was done with one design (coil) and compared with layering a single and 10 times magnetite print coil on photo paper. By printing a simple design such as a square shape (5 x 5 mm), makes it easier to print in layers of 10, 20 and 30. In (Vaithilingam *et al.*, 2018) they showed how to print 3D inkjet-printed silver nanoparticles by layering a square structure (3 x 3 mm) over 1000 times. However, they found that porosity and voids can occur when printing due to the coffee ring effect, effectively forming a trench structure. Building 3D structures can be built with minimal porosity by optimising the printing parameters to build a dense structure. By comparing 600 and 750 DPI prints the higher resolution print were ideal for layering.

Fig. 6.48 shows the magnetite square design (5 x 5 mm) in (a) 30, (b) 20 and (c) 10 layers. Significant differences can be seen in each layering print. For example, the 10 layers show clear print direction across the square design, whereas the 30 layers show erratic print direction thus reducing the printing accuracy. This may be due to the excess satellites and clogging forming during printing, where the excess droplets can be seen on the edges of the square design. Therefore, printing beyond 30 layers, the jetting parameters may need to be recalibrated in order to prevent satellites or excess droplets. The 20-layered print was shown to have good definition and density to form an accurate square patch on the photo paper substrate.

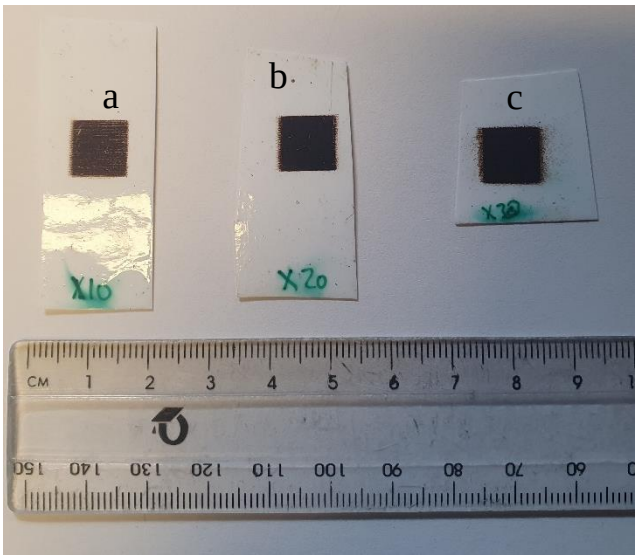

Figure 6.48 Magnetite print in (a) 10, (b) 20, (c) 30 layered square design

Fig. 6.49 shows the bending test performed for each layered magnetite sample in Fig. 6.48. The radius of curvature was reduced from 600 mm to 1000 mm, this is to see the effect of applying smaller strain to the magnetite designs and whether there is any change in inductance, as seen in Fig. 6.46. From all three square designs with layers from 10 to 30, the inductance increased from a strain of 0.13 με to 0.2-0.25 με, then the inductance reduced beyond a strain of 0.25 με. This pattern was present in all print layers, which suggest that the print is sensitive to strain even at 0.13 με. It is clear that the higher number of magnetite layers showed an increase in inductance which is expected but beyond 20 layers the inductance remains constant and does not increase (in 0.13 με). However, all three have shown different levels of noise and sensitivity to strain. In the 30-layered magnetite print, the sensitivity is largest however, by using the same inductor coil, the level of signal to noise ratio for 30 layers is very large compared to other layers. For example, the error/noise in 30-layered print is around ± 4.2 μH whereas the error/ noise in 20-layered print is around ± 2.2 μH. This could be due to the excess porosity and voids present in the print, which restricts magnetic moment orientation. In the 20-layered square design, the sensitivity is greatest beyond 0.2 με and saturates at 0.4 με. The level of error in 20 layers is the best compared to other layered designs. The 10-layered square design shows the least sensitivity to strain and lowest measured magnetic field. This was expected, as there is less magnetite material on the surface hence it will have a lower field, and reduced sensitivity. The level of error is quite large, which is surprising as it would contain less porosity than the other designs such as the 20-layered magnetite. There is a difference in maximum inductance saturation as the more material is layered on top. For the 10 and 20 layers the inductance is saturated at around 0.2 με, whereas for 30 layered magnetite has an inductance maximum at around 0.225 με. This is due to the amount of material on top, as more strain is needed to orientate the moments to reach maximum strain when the coil is placed on top. Coating a thin layer of PDMS or acrylic polymer on the 30-layered magnetite could help with reaching the maximum inductance as seen earlier in chapter 6.8.2.1.1.

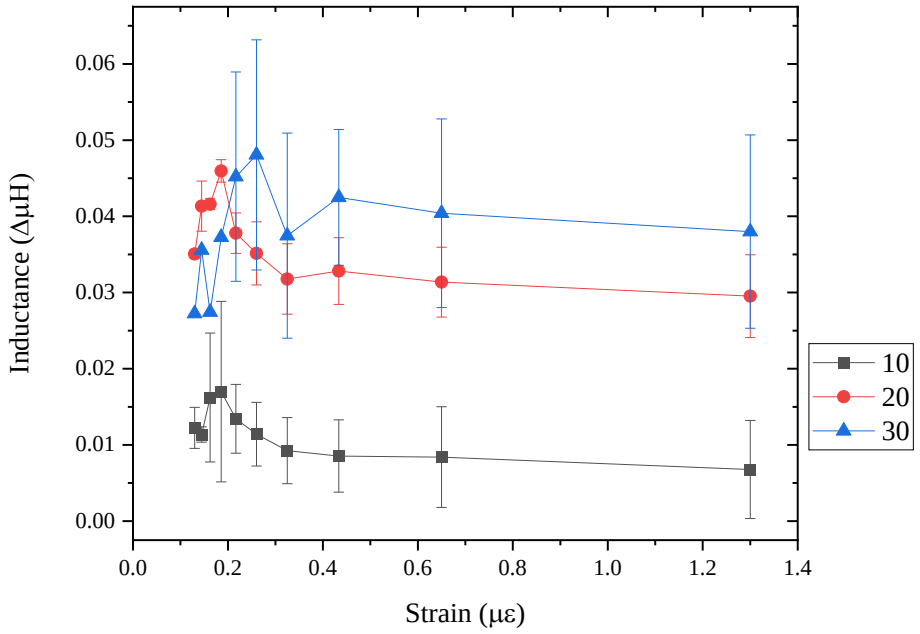

Figure 6.49 Bending test of magnetite square designs of 10, 20 and 30 layers measuring the inductance as a function of strain

6.8.2.1.4 Improving inductance signal

The signal from the inductance measurement of the magnetite print is not ideal for SHM applications as the level of noise is greater than the magnetite print signal. Therefore, from (Vincent *et al.*, 2020) where they describe a RLC (resistance, inductance and capacitance) circuit to form a damped harmonic oscillator, which aims to reduce noise and improve the signal of the inductance generated. From the RLC equation, it determines if the circuit is damped, under-damped or overdamped depending on the capacitor placed in the circuit as shown in Equation 6.1. Where R is resistance, L is inductance and C is capacitance. If the resistance is greater than the resistance of the coil then the circuit is overdamped, if the resistance is less than the circuit then it is under-damped and if the resistance equals the resistance of the circuit then it is critically damped.

Equation 6.1 RLC equation

$$R = \sqrt{\frac{4L}{C}} \qquad (6.1)$$

Fig. 6.50 shows an updated circuit with a capacitor in series. This is a relatively simple approach and reduces circuit complexity to dampen noise and improve signal collection. The AC supply is from the LCR meter, which has a 0.6 voltage output. The capacitor is chosen depending on whether the circuit is under-damped to determine the unknown inductance change as described in (Vincent *et al.*, 2020). Therefore, at 1 kHz frequency the circuit is under-damped using a 100 µF capacitor when using a 100 coil turns inductor which has an inductance of around 190 µH.

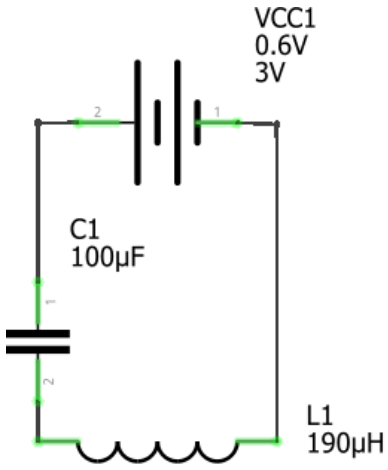

Figure 6.50 Circuit schematic with capacitor in series

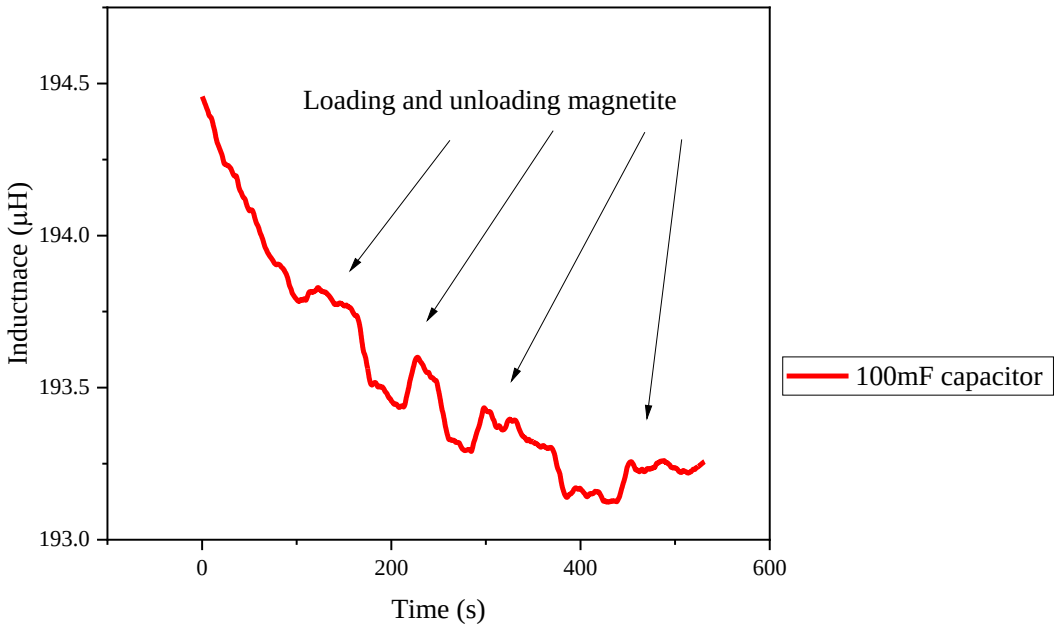

Figure 6.51 LC circuit inductance when loading and unloading magnetite using R100 bend rig and coil 200

Fig. 6.51 shows magnetite loading and unloading in an LC circuit, for a coil with 200 turns and a 100 µF capacitor, to test whether a signal from the magnetite can be seen in the data. The inductance measurement shows that there is a nonlinear decay, as mentioned in (Vincent *et al.*, 2020) where it will decay until it reaches zero. Change of inductance can be clearly seen in Fig. 6.51 where loading and unloading the 20-layered magnetite print using a 100 mm radius bend rig. However, the time taken for the inductance decay to stabilise is around 500 seconds. This must be taken into account when setting up the SHM system as this creates a false reading if not stabilised within the set time.

Fig. 6.52 shows the bending measurement of 20-layered magnetite print using a 100 turns coil in an LC circuit. By selecting a capacitor, Fig.6.52 clearly shows that when using a 100 µF capacitor the signal

is overdamped and when a 10 µF capacitor is used then the circuit has less resistance therefore the signal can be seen more clearly and is under-damped. However, the inductance decay has affected the result slightly as an average was taken from the inductance decay from the null value. In comparison to the result taken for measuring inductance for each 10, 20 and 30-layered magnetite, the LC circuit has improved the inductance to noise as the inductance increases as strain is applied when using the 10 µF capacitor.

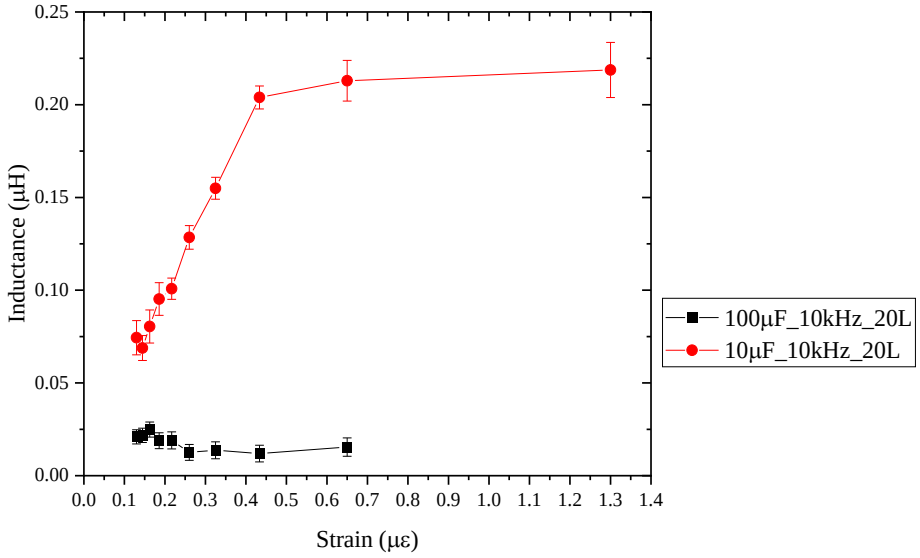

Figure 6.52 inductance of magnetite 20L using 100 coil in an LC circuit

Fig. 6.53 shows the bending measurement of 20 layered magnetite print using a 200-turn coil in an LC circuit. In both cases the signal remains under-damped when using either 100 µF and 10 µF capacitor. The 100 µF capacitor shows a better sensitivity to strain than the 10 µF capacitor. However, in comparison to the 100 coil, both capacitors do not show a distinct difference in relation to the change in inductance. Therefore, a wider range of capacitors could be used in a series with a 200 turns coil.

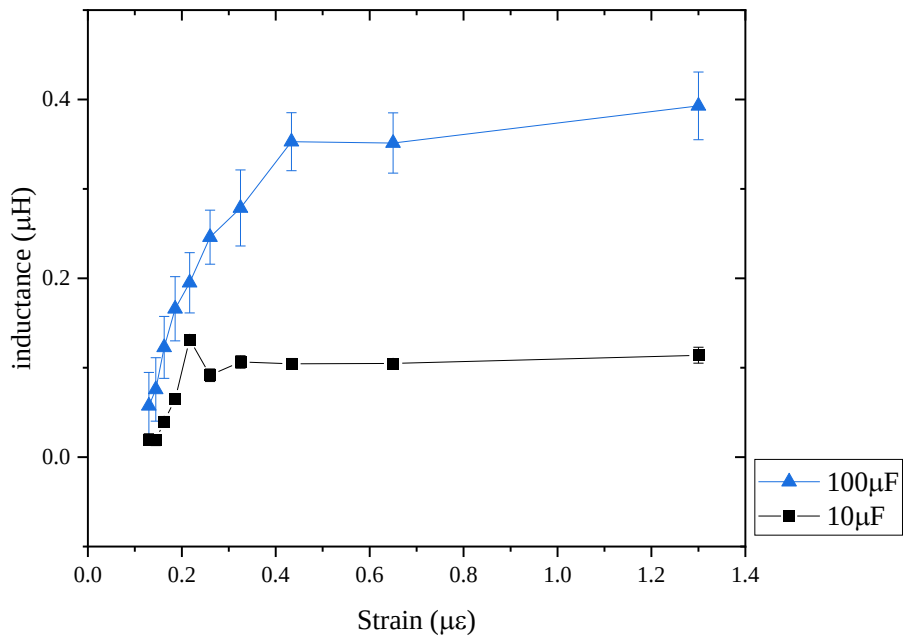

Figure 6.53 Inductance as a function of strain for 20L magnetite using 200 coil inductor with different capacitor

6.9 Summary

Printing magnetic NPs by inkjet printing using a JetLab printing system by Microfab on different substrates was demonstrated. A selection of inks and substrates were tried and tested based on their physical and chemical properties in pre and post processing for SHM applications. For example, photo paper, kapton and glass were available for printing magnetic NPs in inkjet printing. Photo paper was found to be the best for printing NPs as the roughness and porosity of photo paper increased the wetting angle of the droplet and allowed excess solvent to be absorbed through the paper. Magnetite and nickel NPs were able to print via JetLab printer on kapton and glass, however the low wetting angle made it difficult to print accurate structures. Kapton and glass could be printed on, when heated above 373 K to 433 K, as this helped to evaporate excess solvent. However, the kapton and glass substrate in this study were preheated before printing, as the print did not have a heater during jetting process. Nevertheless, kapton and glass substrate demonstrated that magnetite and nickel NPs could be printed on smooth surfaces.

To test the magnetoelastic effect of inkjet-printed designs, COMSOL multiphysics was used to simulate the effect of strain bending and magnetic field response to strain. The effect of gap spacing between each droplet was explored. It was found that the spacing between the droplets had a significant effect on the change in field as a function to strain. Gaps with 0.01 mm or just touching were found to be the best at increasing field due to magnetostatic effect. Simulation results showed that saturation occurs at

100 mm whereas the inductance measurement shows saturation occurs at lower strain (around 300 mm). This may be due to a fault in the simulation as a field is applied in one direction, therefore this could delay the saturation field to higher strain.

The inks were selected based on their properties for example magnetic properties such as saturation magnetisation and printability such as viscosity and composition. Two metal dispersions were selected and purchased from Nanoshel Ltd. Magnetite and Nickel ink dispersions were shown to have good magnetic properties and suitable for inkjet printing. The viscosity for both ink was below 20 cP and were measured to have viscosity around 2 cP at room temperature, this is largely due to the composition of the solvent in the ink. Magnetite ink appeared to be suitable as it had shown higher magnetic properties and printability.

To measure the magneto mechanical sensitivity of the print, first a choice of Hall probe and inductor coil were tested to determine which one was reliable and sensitive to the change in magnetic field/magnetisation when the print was strained. It was found that the inductor coil was better to measure the field as the sensitivity of the coil can be tuned to increase or reduce the sensitivity. However, the SNR for each coil turns when testing bending strain for metglas were different. The 100 coil turns were found to have higher SNR than other coil inductors as the SNR increased as the strain value increased. A bend rig was designed and 3D printed with a known radius of curvature from 1000 mm to 100 mm, so that the printed NPs could be strained while measuring the field. It was found that the sensors were responsive at lower strain as the field changed higher from 1000 mm radius.

Different designs were selected to print, these included coil, uniaxial patch, grid and rectangular block to test the inductance sensitivity as a function to strain. Printing rectangular blocks that were either parallel or perpendicular to the strain direction was to see whether the signal is best in parallel or perpendicular to the strain. Linear fitting using Origin Lab was used to calculate the change of inductance as a function to strain. It was found that coil design had the best sensitivity as strain was increased from 0.13 to 1.3 με using the bending rigs.

The print was analysed in chapter 6.7 by optical microscope, optical profiler, SEM and EDS. Print analysis shows that the print had a resolution of 132 DPI. This was lower than literature studies where they have achieved a resolution of 180 DPI. This is because the jetting parameters were set to print larger droplets to ensure magnetic NPs were jetted and not to let the NPs sink to the bottom of the reservoir. Optical profiler was used and found that the roughness improved depending on the type of substrate used. For example, glass had a roughness Ra of 0.3 μm while photo paper and kapton had a roughness of 0.5 μm. However the peaks Rt, Rp and Rv are higher in paper, which is due to the wetting angle as surface tension on paper is higher than kapton and glass.

The design that was selected was the coil design and the best ink for strain bending was magnetite. The coil design far exceeded other designs that were thought to have anisotropy due to the print design such as in uniaxial patch design. This may be due to the print pattern where the coil design contained larger gaps between the coil turns, therefore may improve the field by increased demagnetisation. It was evident that the greater number of layers of magnetite increased inductance as a function of strain.

Inductance signal enhancement such as coating the print with PDMS, controlling the magnetic moments, further additive layering and circuit design were explored and tested. It was found that the greatest effect, which improved the inductance signal to noise ratio was re-designing the circuit and adding a capacitor in series. The improved sensitivity (depending on the coil copper turns) was observed for all substrates including paper and kapton. Other enhancements did improve the signal but only marginally improved the change in inductance as a function of strain for example layering 20 layers increased the inductance but marginally improved the signal to noise ratio. Coating the paper with PDMS did improve the sensitivity, however this was only noticeable at lower strain values. Placing the coil at the top or bottom did show a difference between measuring the signal from the top or bottom however the sensitivity improved slightly when the coil was placed at the top. Applying a field reduced the print quality as the magnet was placed under the substrate during jetting. Therefore, applying a field would not be beneficial if a design or structure cannot be printed.

Chapter 7

Structural health monitoring evaluation

7 Structural health monitoring evaluation

7.1 Abstract

This chapter evaluates inkjet-printed magnetostrictive sensors for SHM of aircraft grade CFRP. The evaluation consists of impact testing, strain bending and simulations of the sensor attached to the CFRP. It was found that the bending test of magnetite printed sensors directly onto CFRP showed a better response in detecting damage in comparison with magnetite printed sensors on photo paper. A polycarbonate sheet was used to calibrate and measure the noise generated by the vibrations and deformation caused by the imp8act of a dropped weight. CFRP with 4, 5 and 6 layers were tested and compared for damages and defects. A 0.5 kg dropped weight was chosen due to lower error and stable change in inductance, when used in the impact measurements. The CFRP with 4 layers was chosen as it showed higher delamination and defects than the other CFRP samples with higher numbers of layers. An epoxy was used to secure the inductor coil on to the CFRP, this was found to reduce noise and vibration from the impact.

Initial results showed that a 10-layered magnetite line on CFRP, had an increased change in inductance after impact compared to both single layered magnetite line and CFRP without a magnetite line. The single layer magnetite print showed a reduction in inductance compared to the empty CFRP sample. The measured inductance increased when measured on both the front and back of the CFRP for the 10 layered magnetite print. By scanning and measuring the inductance of the magnetite line across the CFRP using an inductor, the change in inductance close to the defect was found to be negligible. Simulations showed that a greater change in magnetic field was present for the magnetite layer on the CFRP with 4 and 5 layers due to an increased damage and defect between the layers. To test the change in magnetic field of a magnetite droplet on the CFRP during impact, a model was created to simulate the moment orientation dynamics during impact, including changing the distance between the droplets.

It was found that magnetic dipoles were formed at the edge of the droplet such that as the gap reduced, the magnetic field increased in the Y direction.

7.2 Introduction to structural and sensor evaluation

The design and selection of a magnetostrictive sensor in chapter 6 showed that the chosen sensor was able to detect the change in strain as a change in the measured inductance. This allows the structural evaluation of aircraft grade CFRP material when a change in strain or defect occurs to be detected by the magnetite sensor. However, direct impact can also occur in the aircraft structure due to projectiles such as debris in service. Therefore, this chapter will focus on impact testing and evaluation of the magnetite sensor for SHM of CFRP samples. To test the magnetostrictive sensor for damage detection of CFRP, a series of mechanical tests were performed such as bending and impact testing. These mechanical testing replicate the force and strains experienced in an aircraft structure.

In the real world, the magnetite sensor would be attached to the CFRP structure, however how the sensor is attached to the CFRP structure is critical to detecting delamination or defects. There are different substrates the sensor can be printed on as seen in chapter 6, which are kapton, paper and glass. The main issue arising when attaching a sensor to the CFRP is the substrate compatibility and whether the sensor is fully in contact with the CFRP. For example, using the same epoxy as used in CFRP is ideal, as both epoxy in CFRP and attached to the substrate will have the same mechanical properties and hence better adhesion. However, as the magnetite NP were printed onto the paper, by applying the epoxy to the back of the paper while the magnetite sensor is in contact to the CFRP, good contact between the magnetite print and CFRP is needed to detect defects and damages on CFRP. Kapton substrate could be heated such as hot pressing onto CFRP as it can withstand higher temperature (beyond the Tg of the epoxy). However, hot pressing kapton could introduce additional flaws on the surface, which is not ideal. Kapton would need to be treated further to reduce surface energy. Printing directly on CFRP and coating is a new technique and would save the need to have an additional layer of substrate. Therefore, bending test and impact testing will be performed on CFRP samples where the SHM magnetite sensor has been directly printed onto it.

Evaluating the sensor for SHM was done by impacting the CFRP sample by dropping a weight at a set height to see if there were any changes in inductance of the sensor, along with scanning the surface for defects or delamination as stated in chapter 4.3.4.2.2. By measuring the change in inductance during an impact, the defect or delamination will cause a torque on the magnetic moment and reorientate it within the printed magnetite. Therefore, placing an inductor to measure the inductance during an impact on CFRP, the change before and after impact will be related to the slight defect and damage within the CFRP. The impact can occur at a distance to the sensor in the real world. Therefore, to test the sensor's

effectiveness in detecting impact from a distance, the inductor or impact will be placed at a distance to see how far the damage or defect can be detected. If for example the sensor cannot detect the damage of CFRP from a certain distance, then another sensor will be placed there to make sure the damage is detected. However, the evaluation will be the distance of detection where if the sensor is not able to pick up a damage that is close such as 5 cm away then it would not be suitable to detect an impact damage. This is because magnetite would need to be printed close together therefore increasing material waste and time taken.

7.3 Mechanical testing result

7.3.1 Bending test

Strain by bending was performed on CFRP with a magnetite sensor, as shown in Fig. 7.1. The same method as shown in chapter 4.3, was used to bend the CFRP, however a higher radius of curvature was used such as from 1000 mm to 200 mm radii. This is due to the strain applied to the CFRP is higher than the paper substrate shown in chapter 6, as the thickness of the substrate is larger. The magnetite sensor has shown change in magnetic field when a higher radius of curvature is used as shown in chapter 6. The issue with bending CFRP by using plastic clamps as shown in Fig.7.2, is that the CFRP may not bend fully over the known radius of the bend rig. Therefore, a higher radius of curvature was used to sufficiently bend the CFRP sample.

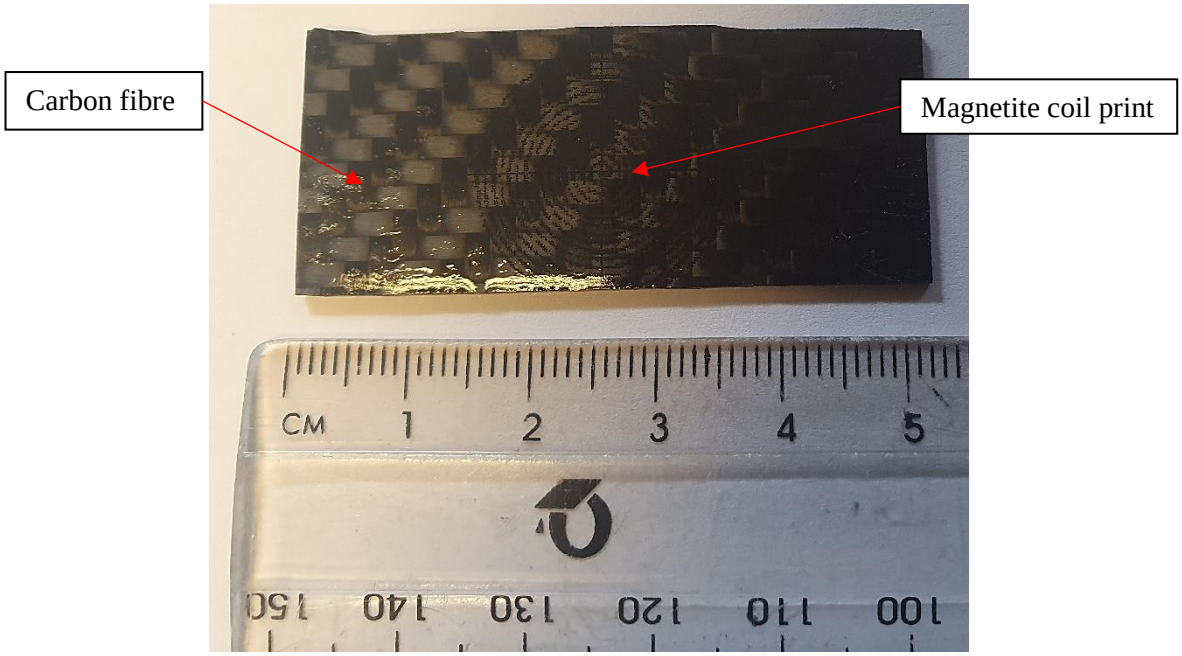

Figure 7.1 magnetite coil print on CFRP

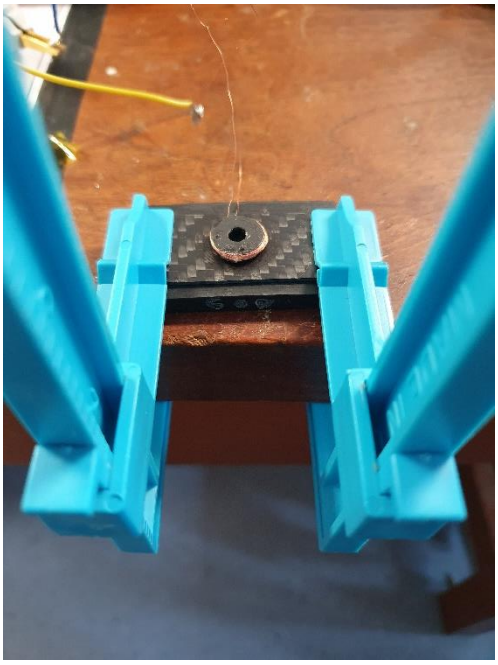

Figure 7.2 Bending CFRP on a bend rig by plastic clamps with 100 turns copper coil inductor

The results shown in Fig. 7.3, shows that the inductance/ strain gradient has increased for the coil design, as the CFRP is strained from 1000 mm to 200 mm radii, measured with a 100 coil turns inductor and 10 µF capacitor. The change in inductance is higher compared to the magnetite coil sensor on photo paper substrate in chapter 6. However, the inductance drifts over time, which is caused by the capacitor. The drift has a larger change in inductance than the signal when measured at lower strain levels but at higher strain level, the change in inductance is greater than the drift from the capacitor. Fig. 7.4 shows the mean inductance to strain, which shows a greater change in inductance, over the radius of curvature range from 1000 mm to 200 mm than magnetite coil on photo paper in chapter 6. This could be due to the substrate, as the photo paper absorbed some of the magnetite material within the paper, whereas on the CFRP, there is little or no absorption of the magnetite NPs. However, there are issues with repeatability for all the coil and patch designs on CFRP, even though the inductance to strain sensitivity is higher than on paper. This could be due to the CFRP substrate adhesion of the magnetite print or straining the CFRP so that crack or defects form, which could affect the reliability of the inductance sensitivity to strain. Coating the magnetite on CFRP could help to increase reliability and performance of the sensor by preventing cracking and improving adhesion of the magnetite NPs to the CFRP.

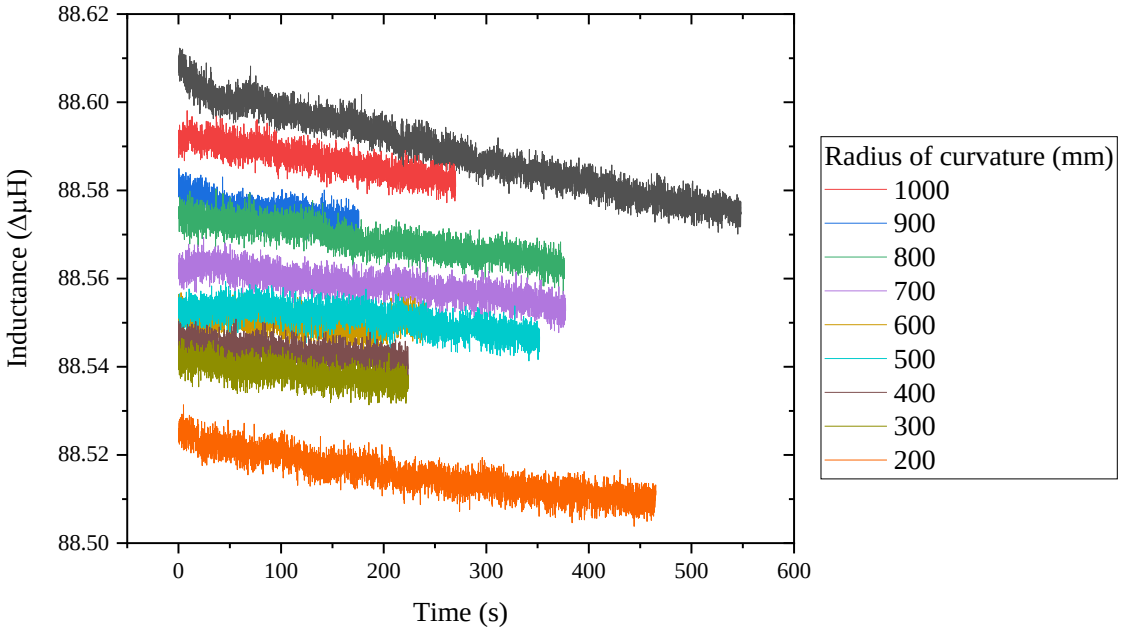

Figure 7.3 Inductance measurement of bending CFRP with printed magnetite coil using 100 coil turns inductor and 10 µF capacitor

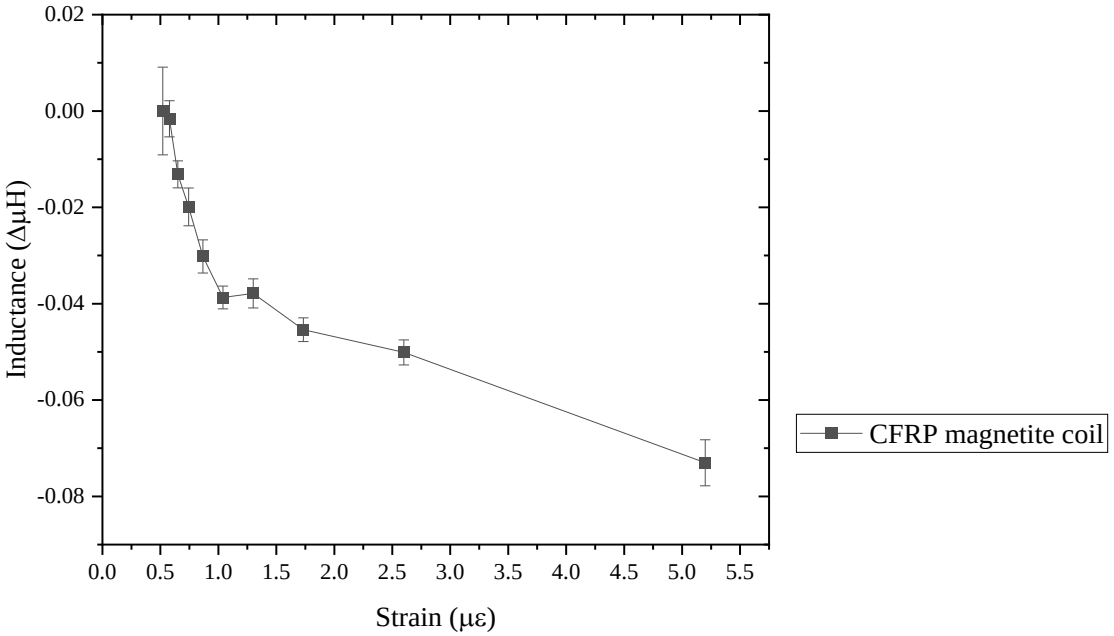

Figure 7.4 Bending CFRP with magnetite print coil design using 100 coil turns inductor and 10 µF capacitor

Fig, 7.5 shows the inductance measurements for magnetite coil sensor, printed on CFRP using a 200 coil turns inductor and a 10 µF capacitor. While the results show that there is a change in inductance as

a function of strain, the initial measurement (baseline) shows that there is a large drift, which could affect the result. However, when the magnetite print was placed under the inductor, the drift reduced and stabilised. This is similar to the 100 turns coil inductor seen in Fig. 7.3, however the drift continues as strain is applied. Therefore, the 100 coil inductor needed longer to stabilise when a capacitor was in series. A lower capacitor in series could be used to reduce the drift to measure the change in inductance with strain.

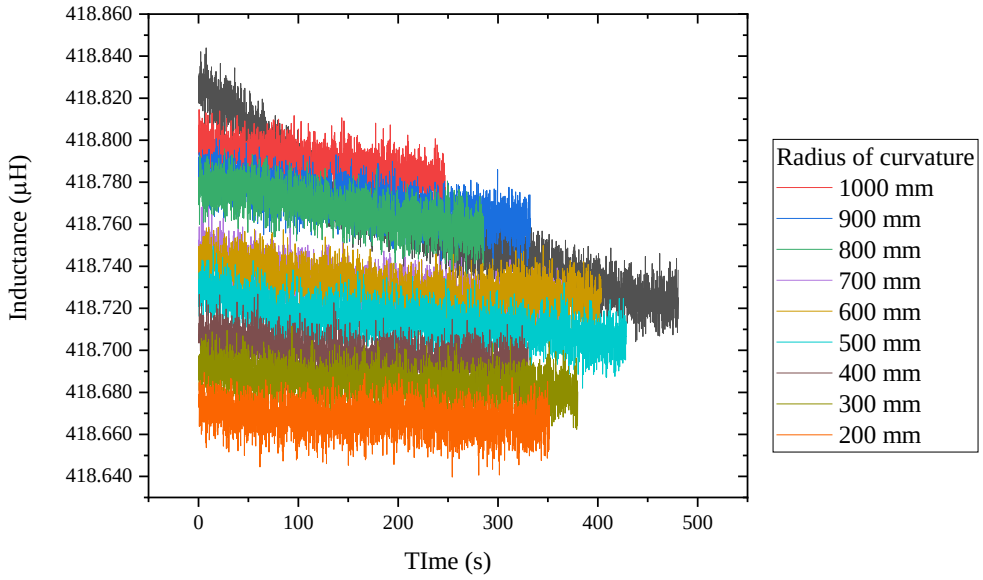

Figure 7.5 Inductance measurement against time of bending CFRP with printed magnetite coil using 200 coil turns, 10 mF capacitor at 20kHz frequency

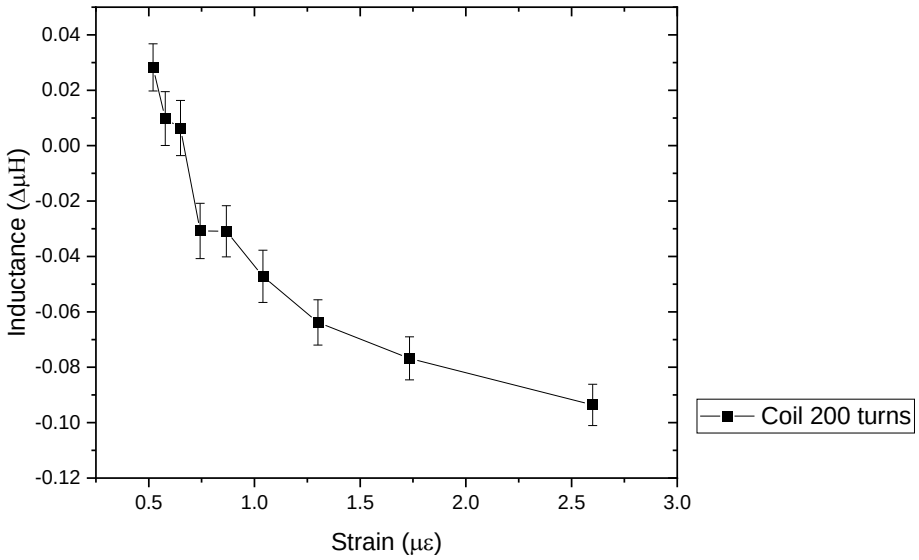

Figure 7.6 Inductance of coil print on CFRP with 200 coil inductor

7.3.2 Impact testing polycarbonate

7.3.2.1 Polycarbonate impact test result

Impact testing was first performed on an empty polycarbonate (PC) sheet (1 mm thick) with an inductor close by as shown in chapter 4.3.4.2.2, where a set of weights was dropped and measured to see the change of inductance without any magnetite NPs sensor on the PC sheet. Therefore, this experiment was performed to see if there was any effect on the change of inductance due to noise and vibrations caused by the weight on impact. To identify a defect or damage on the PC sheet by measuring inductance from the inductor, a time-based measurement was performed to record the inductance value before and after impact. If there was any difference in the inductance measurement between the two events, then that would mean that there was a defect present as the PC sheet deformed and changed the position of the inductor. This is because at the centre of the impact, the deformation is greatest, however as the inductor is placed 5 cm away from the centre which would detect small deformations. Therefore, the larger the weight dropped, the greater the defect will form and change in inductance of the inductor should change significantly. Any anomaly seen in the impact testing with magnetostrictive sensor will be seen here due to noise and vibrations. For example, movement of the plastic tube can cause inductance to change, as the PC sheet would move depending on the force applied to the tube when adjusting, such as loading and unloading the weight. The shock from the drop weight on the PC sheet would cause a change in inductance as the PC sheet would move and deform, causing the inductor to shift and change inductance.

The experiment also allows for examination of the impact and fracture analysis, for example if the impact causes deformation or penetration of the PC sheet. This is useful information as PC sheet is a hard plastic and can be recycled therefore before using CFRP, PC sheet can be used to test dropping weights and detecting change in inductance by shifting of the inductor. The distance from the inductor and the location of impact is somewhat fixed, as the inductor is placed outside the tube to avoid direct impact from the drop weight. Therefore, the inductor is always between 4.5 to 5 cm away from the impact due to limitation of impact base distance and size of the drop weight.

Fig. 7.7 shows the level of damage caused by an impact on the PC sheet from weights ranging from 0.1 kg to 1 kg. From the image, it is clear that 100 g caused minimal damage and would not cause delamination or significant damage to the CFRP, whereas a weight of 1 kg caused fractures and penetrated through the PC sheet. The location of impact is roughly 4.5 to 5 cm away from the inductor therefore the accuracy of the impact depends on a number of factors such as the tube location, angle of

tube and the balance of each weight. The tube is larger than the set of weights, which would cause movement during impact, therefore additional weights that are the same size and shape are used to avoid impact at an angle. The perimeter of the tube is outlined in red as seen in Fig. 7.7, which is used as a guide, therefore any deviation from the line would mean a shift in the impact location on the PC sheet from the dropped weights. The deviation of the impact from the centre is around 0.5 cm as seen in Fig. 7.7. The inductor and PC sheet were held by tape during impact to prevent additional movement.

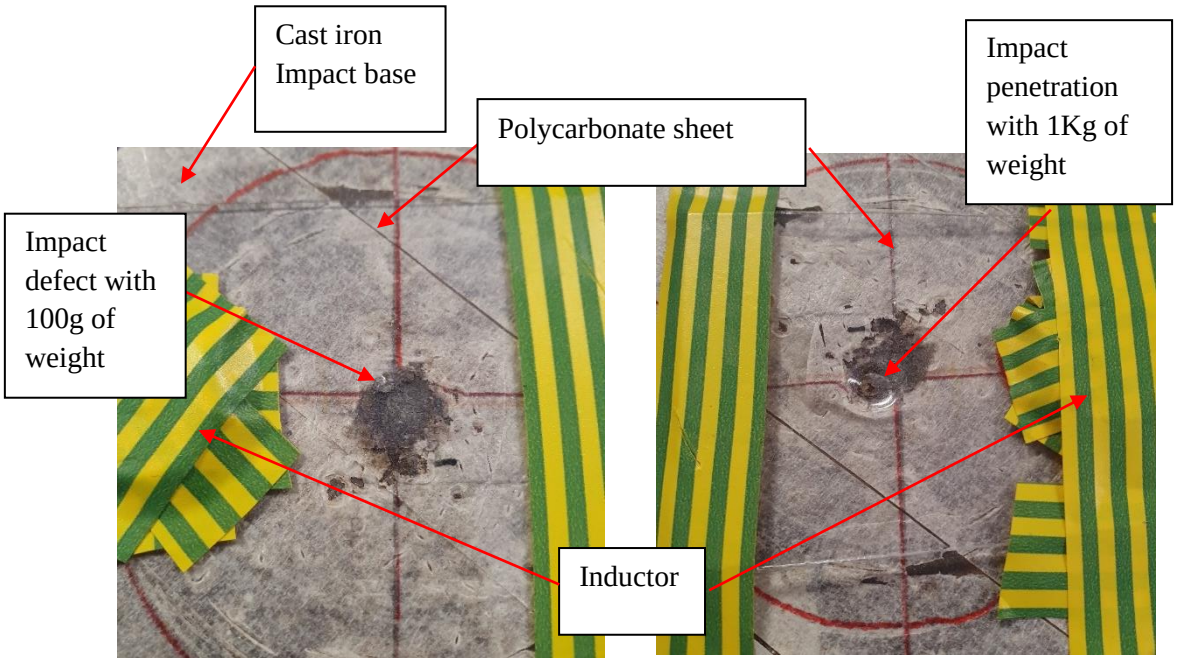

Figure 7.7 Impact with 0.1 kg (Left) and 1 kg (Right) weight on polycarbonate from 1.1m

Fig. 7.8 shows the change in inductance during an impact from a weight of 0.1 kg to an empty PC sheet at a height of 1.1 m. The impact occurred after 80 seconds where a sharp peak can be seen. The inductor placed 5 cm away from the impact resulted in no defect as the inductance before and after the impact are similar to each other, with a value around 483.07 µH. By increasing the weight to 1 kg, penetration occurred as seen in Fig. 7.7, therefore inductance before and after has a measurable difference with a reduction of 3 µH after the impact, as seen in Fig. 7.9. Impact occurred after 15 seconds where the inductance reduced significantly more than 0.1 kg impact. This suggests that without the magnetostrictive material under the inductor, the noise and defect caused by the weight dropped, had an effect on the inductance when the weight was increased to 1 kg. This could be an issue for detecting the change in inductance from the magnetostrictive sensor as the change of inductance is smaller than without the magnetostrictive material under large impact force. Therefore, a weight needs to be selected

to cause enough damage on the PC or CFRP sheet but not to cause large change in inductance before and after impact, to avoid error and inaccuracy of the sensor.

Fig. 7.10 shows the inductance before and after impact from dropping weights of 0.1 kg to 1 kg on to PC sheet. Using equation 4.10 to calculate the kinetic energy of each dropped weight, the overall change has increased slightly from 1 J (0.1 kg) to 10.5 J (1 kg), as seen from the red arrow as a guide to the eye. This suggests that as the defect increases the inductance change from before and after changes and is proportional to the increased weight, as expected. However, some of the data are showing significant change such as from 7 J to 10.5 J. Care was taken to make sure the PC sheet was sufficiently bonded to the impact base to prevent excessive shock to the inductor. Fig 7.11 shows the change in impact peak for each weight dropped on the PC sheet. This data is to confirm that weight dropped on the PC sheet does change the inductance, as greater the weight would cause a larger inductance peak/signal. The energy at 5.4 J (0.5 kg) impact was found to be stable without causing additional noise and is shown to have a good level of deformation on the PC sheet.

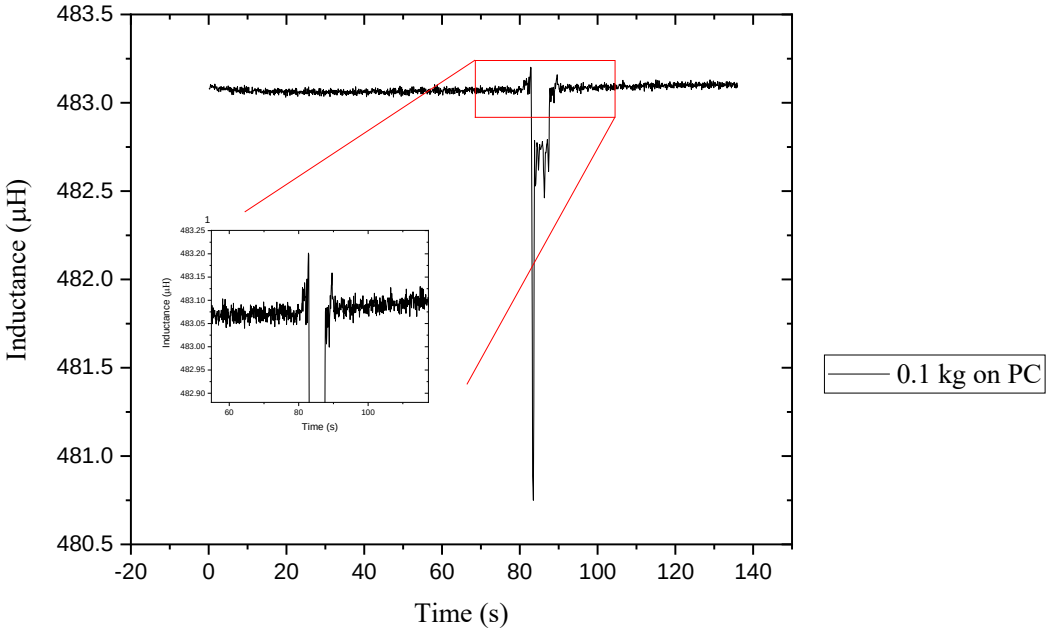

Figure 7.8 Impact testing of empty polycarbonate with weight of 100g and inductor 5cm away

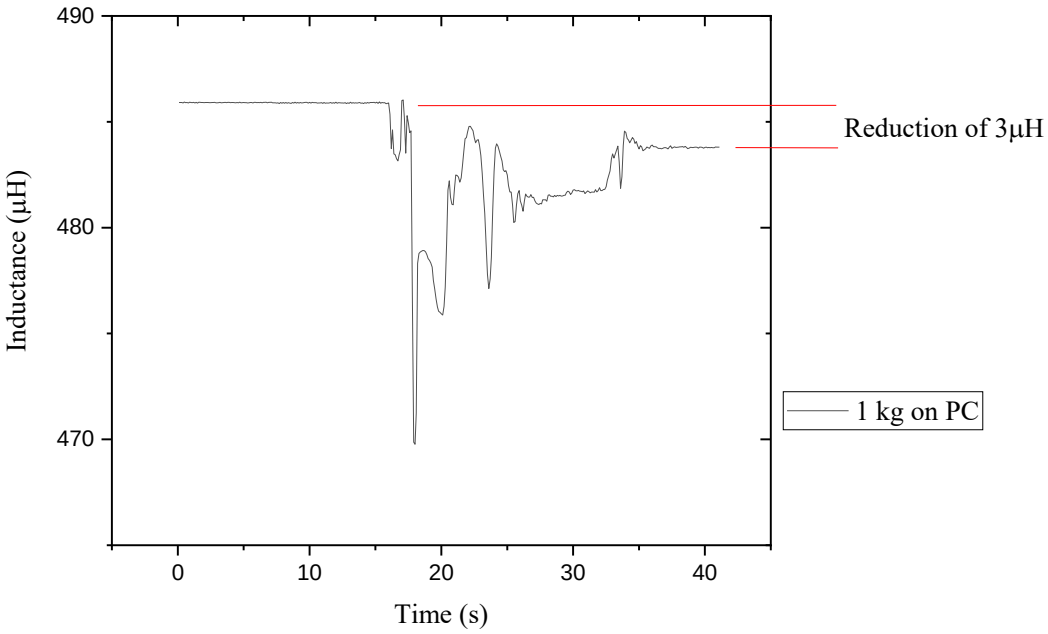

Figure 7.9 Impact testing of empty polycarbonate with weight of 1 kg and inductor 4cm away

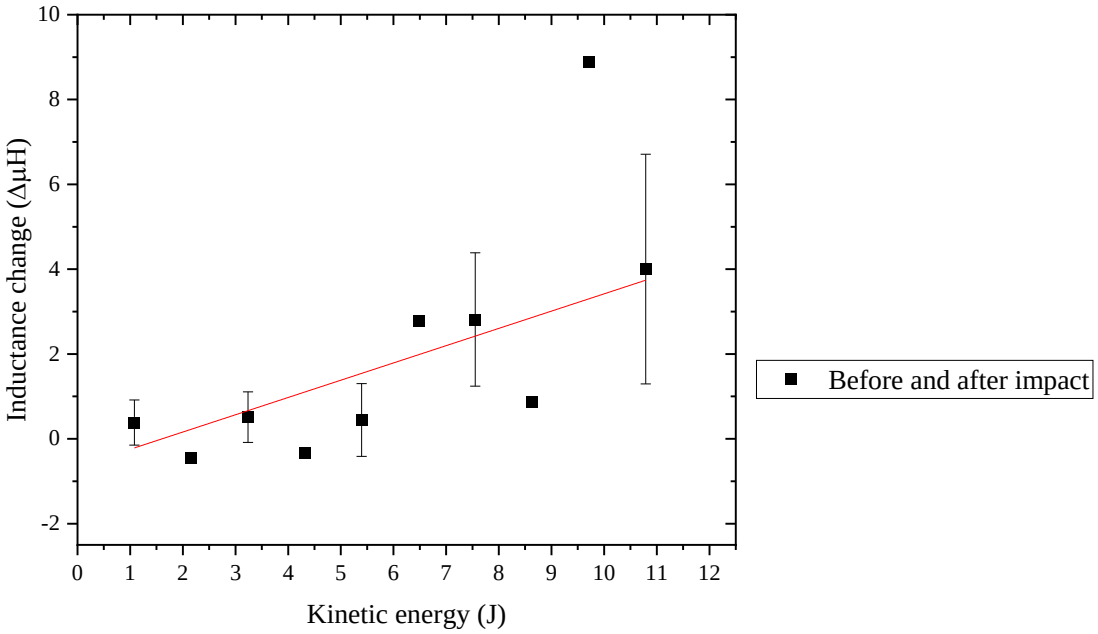

Figure 7.10 Change in inductance before and after impact with fitting (red)

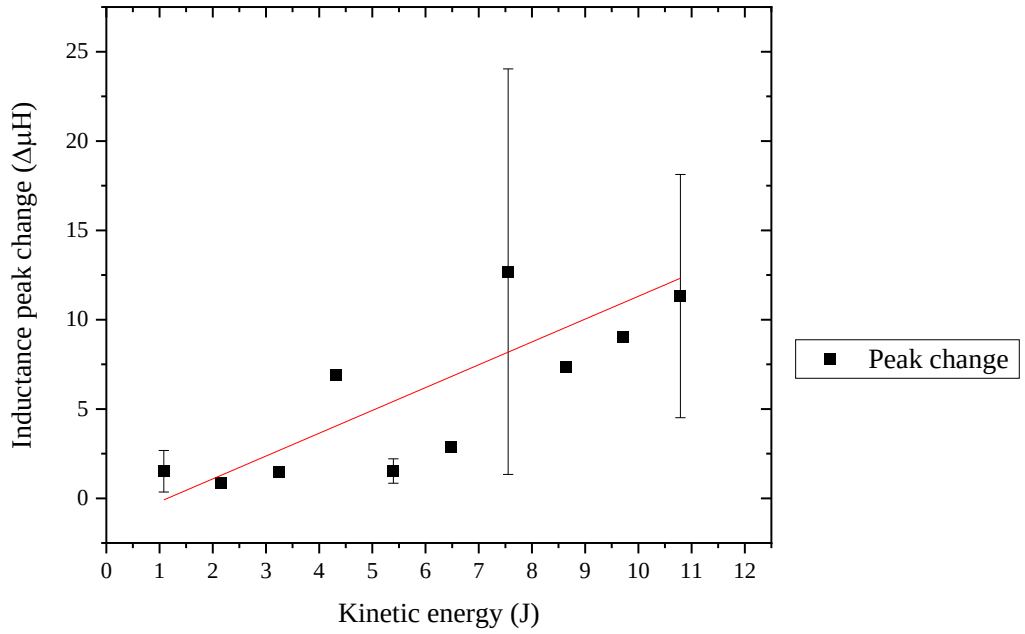

Figure 7.11 Peak inductance impact on polycarbonate with inductor 5cm away with fitting (red)

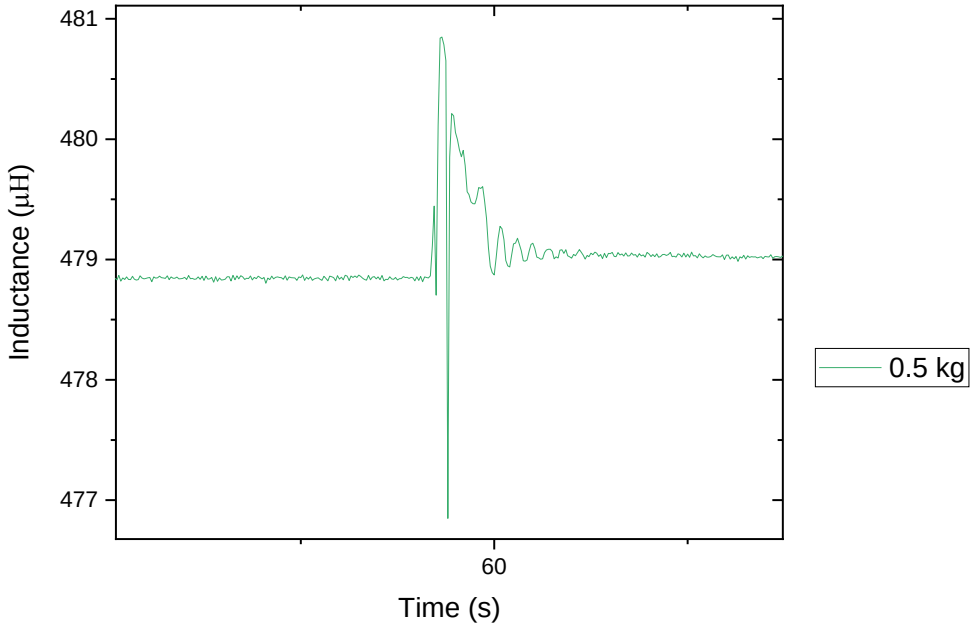

Figure 7.12 Impact test of polycarbonate with inductor and weight of 500g

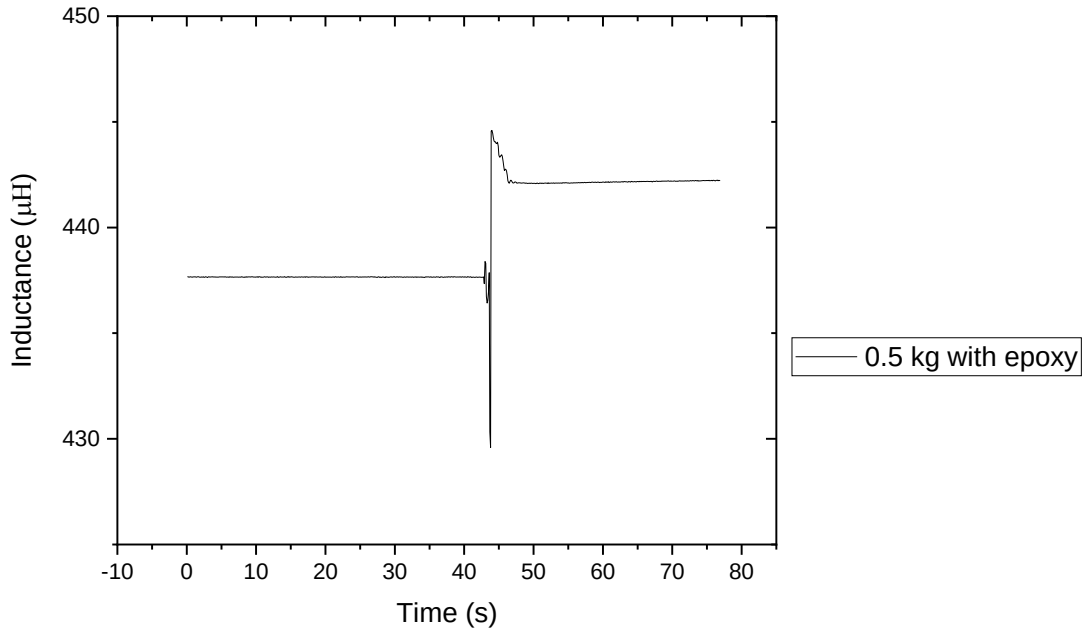

Figure 7.13 Impact test of polycarbonate of 500g weight with inductor fixed by epoxy

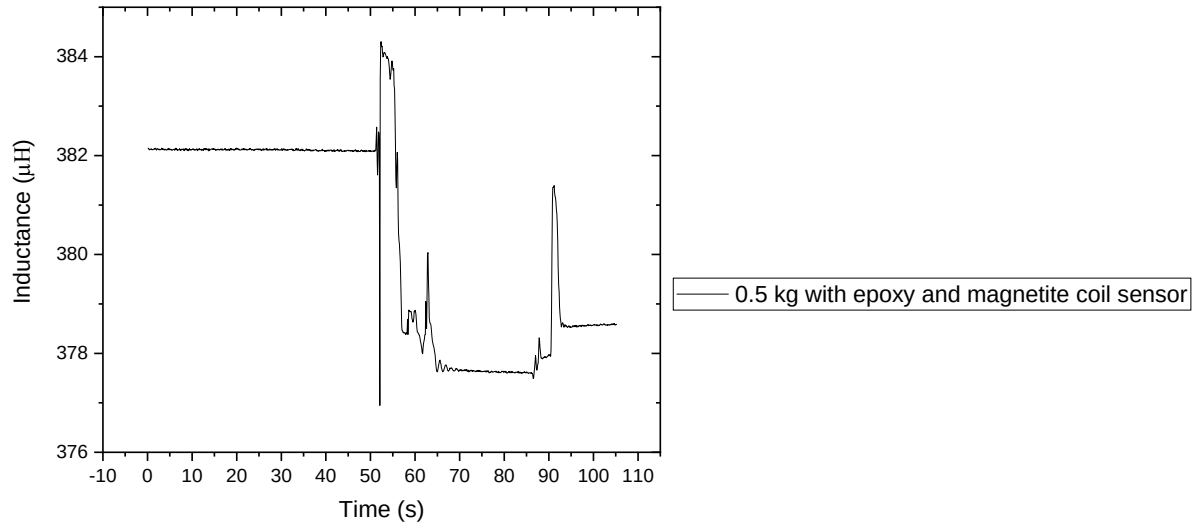

Figure 7.14 Impact test of polycarbonate of 500g weight with inductor and magnetostrictive sensor fixed by epoxy

An effective adhesive was required to bond the inductor coil to the PC sheet, as the inductance oscillated after impact, as seen in Fig. 7.12. The difference in applying an epoxy to fix the inductor to the PC sheet is that it has a 96.4% higher change in inductance in comparison to without epoxy as seen in Fig. 7.12 and Fig. 7.13. The weight dropped from the tube could have an effect on the data as seen in Fig. 7.14, as the oscillation of the sheet and movement of the tube due to impact will increase erratic changes in the inductance measurement. Therefore, clamping the tube above the sheet (not in contact) would reduce the noise from the tube when dropping weights to prevent damping and oscillation effect from impact.

Three tests were done to show the changes of inductance from the inductor attached by tape, by epoxy and by epoxy with magnetite printed coil on paper (magnetite in contact with the PC sheet as seen in Fig. 7.15). The bar chart in Fig 7.16 shows the change in inductance before and after impact from a 0.5 kg weight at a height of 1.1 m onto the PC sheet. The result shows that there is an increase in the change in inductance from an empty coil to an inductor attached by an epoxy onto the PC sheet. This suggests that the epoxy increased adhesion onto the PC sheet and improved the change in inductance from the inductor. However, the magnetite printed coil reduced the change in inductance as seen in the bar chart. This could be due to the paper restricting movement/ absorbing the impact of the dropped weight, therefore no strain was applied to the magnetite print and no significant change was detected by the inductor coil. Fig. 7.17 shows the same test as performed in Fig. 7.16, however the tube was clamped to avoid interference. The result shows that the difference between the empty coil and coil attached by epoxy are roughly similar, whereas the magnetite printed on paper showed a greater reduction of inductance in comparison with without a clamp. The tube had caused an interference by reducing the change in inductance before and after impact. It is shown that magnetite print on photo paper reduces change in inductance, therefore the photo paper could be causing issues by reducing the defect or change in strain around the magnetite sensor.

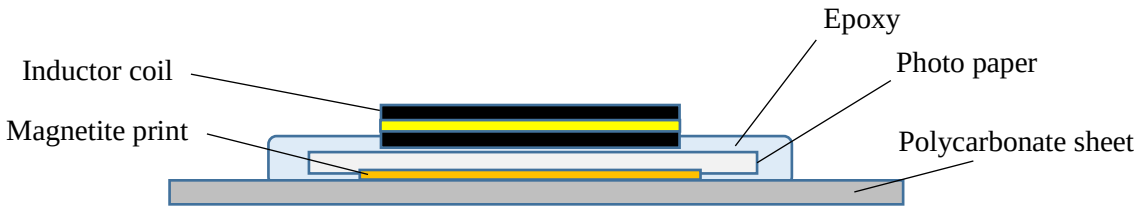

Figure 7.15 Schematic of magnetite printed on photo paper attached to the PC sheet and inductor with epoxy

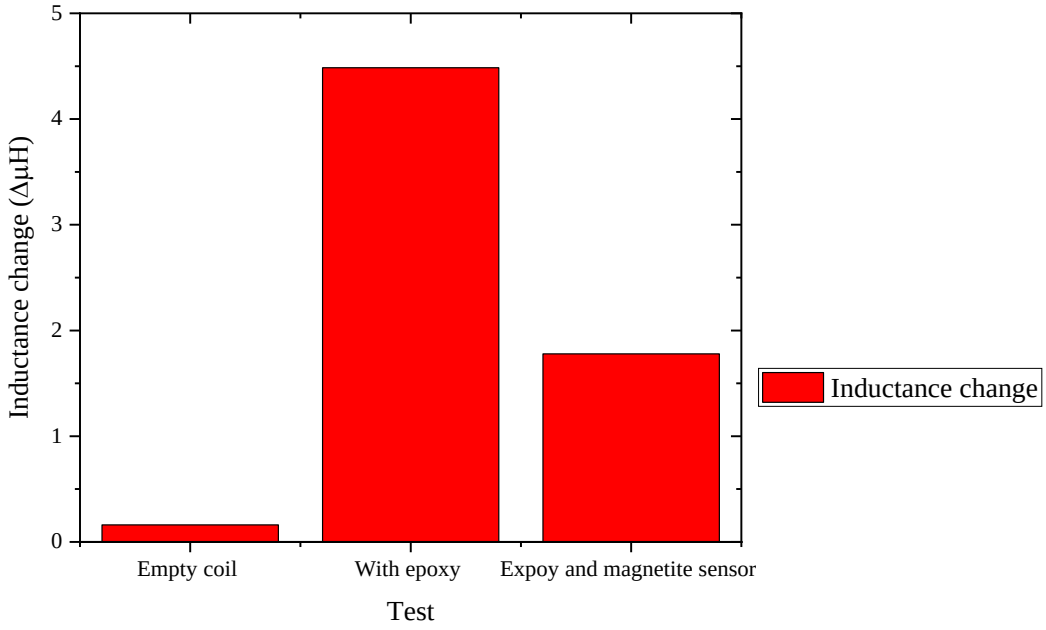

Figure 7.16 Change of inductance before and after impact with 0.5 kg on polycarbonate with empty, epoxy and epoxy/ magnetite coil sensor

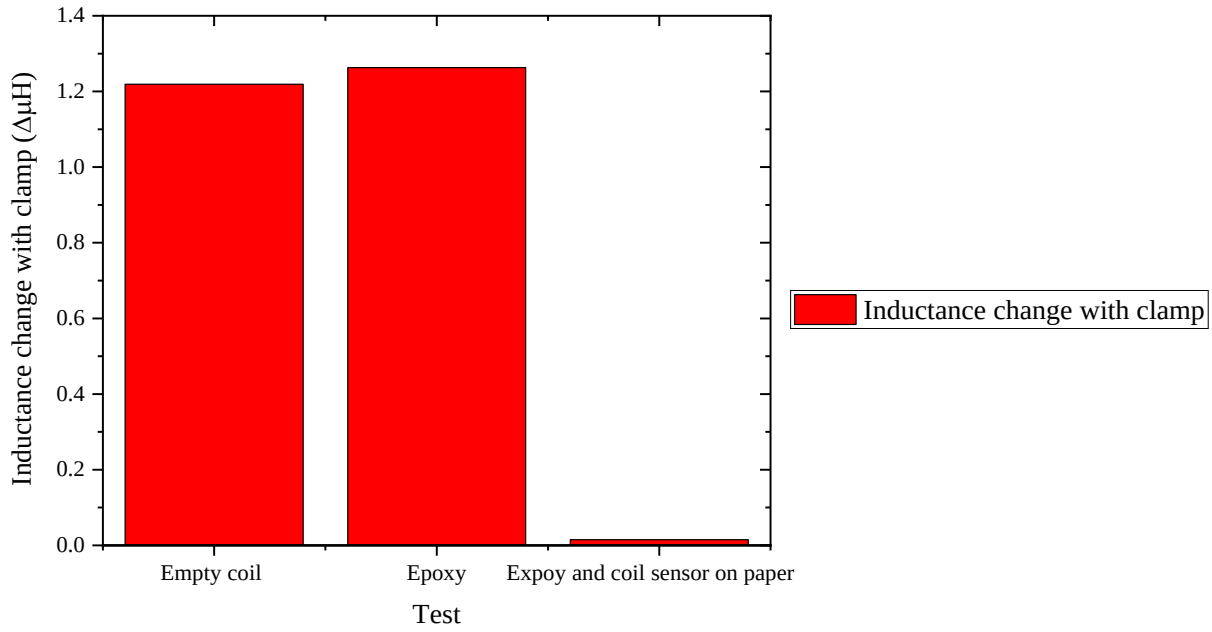

Figure 7.17 Change of inductance before and after impact with 0.5 kg on clamp on polycarbonate with empty, epoxy and epoxy/ magnetite coil sensor

7.3.3 Impact testing CFRP

7.3.3.1 CFRP impact test result

To study impact testing on CFRP, prepreged CFRP with 4, 5 and 6 layers was used. CFRP with 4 layers were used for bending over a known radius of curvature, whereas CFRP with 5 and 6 layers were used to see the extent of delamination and defect caused by the impact. The impact studied used a 0.5 kg weight, with the results seen in Fig. 7.18. A sheet of CFRP measured at 10x10 cm was attached and fixed to the impact base by tape during the experiment as seen in Fig. 7.19.

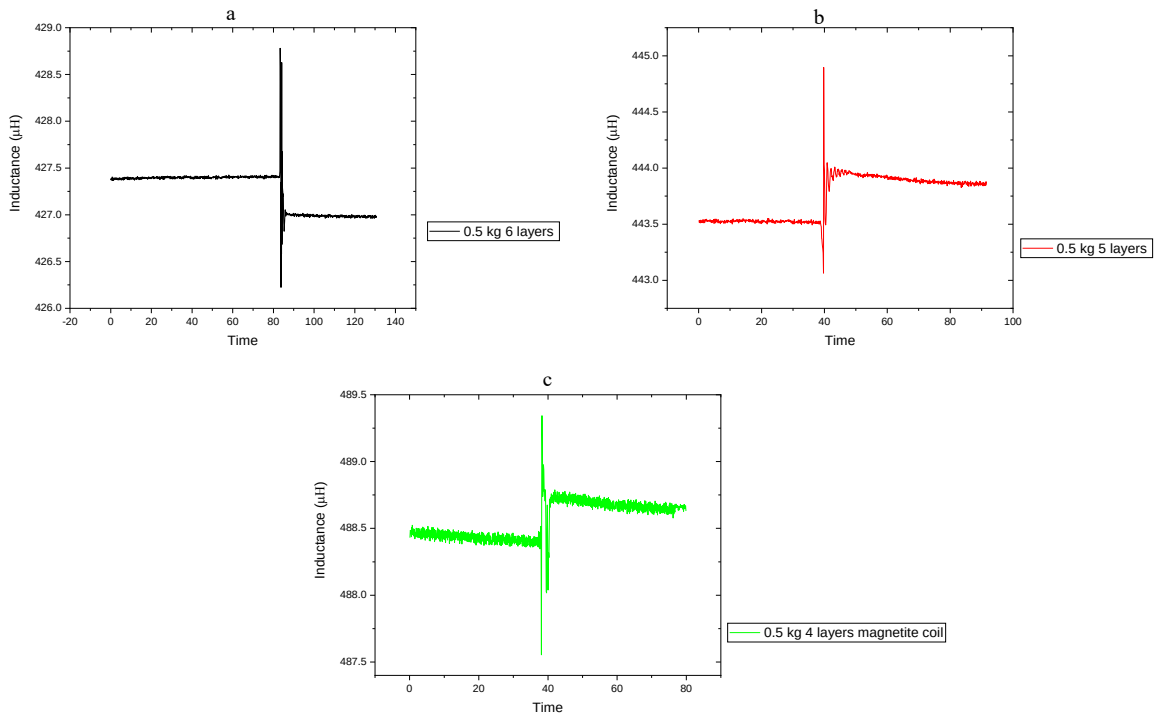

Figure 7.18 Impact test of (a) 6 layers and (b) 5 layers of CFRP sheet with inductor fixed with epoxy and (c) 4 layers of CFRP sheet with inductor and magnetite coil fixed with epoxy

Figure 7.19 CFRP secured on impact base with magnetite coil and inductor fixed with epoxy

The result in Fig. 7.20 shows that there is a decrease in the change in inductance before and after impact as the number of CFRP sheets are reduced. From 6 layers to 5 layers the inductance was decreased by 10% and continues reducing in CFRP sheets with 4 layers. The CFRP sheets with 4 layers and magnetite

sensor (on photo paper) also show a decrease in the change in inductance as expected from previous impact tests on PC. The magnetite printed sensor should have shown a larger change in inductance before and after impact, however this was not the case as the result was within the error of the 4 layered CFRP sheet. Therefore, the addition of magnetite coil on paper did not make any significant difference to the trend. This could be due to the absorption of the paper which may have resulted in lower magnetic field signal of the magnetite printed coil for damage detection, similar to the PC sheet in Fig. 7.16 and Fig. 7.17.

Fig. 7.21 shows the maximum peak change in inductance (at impact) for different layers of CFRP sheet. The result shows that there is an increase in inductance peak from 6 layers to 5 layers but then decreases in 4 layers of CFRP sheet. The results do not follow the same trend as in Fig. 7.20, where there is a reduction in the change in inductance before and after impact from 6 to 4 layers of CFRP sheet. The peak change from 6 to 5 layers could be due to a number of factors such as epoxy or distance of impact from the inductor. However, the 4 layers of CFRP sheet shows a significant reduction of inductance compared to 6 and 5 layers. This could be due to the penetration through the CFRP, therefore most of the energy could be dissipated to the cast iron base. In comparison with a magnetite coil on paper, the change in inductance peak has increased rather than decreased. This could be due to the initial large energy transfer to the magnetite print, changing the magnetic moment briefly and then reducing back to the baseline. The difference in the inductance before and after impact and peak inductance at impact for the magnetite print on paper is the strain and force applied. The paper shows that it restricts the applied strain slightly, therefore reducing the inductance before and after impact, whereas the paper does not absorb or restrict the initial applied force to the magnetite or the CFRP.

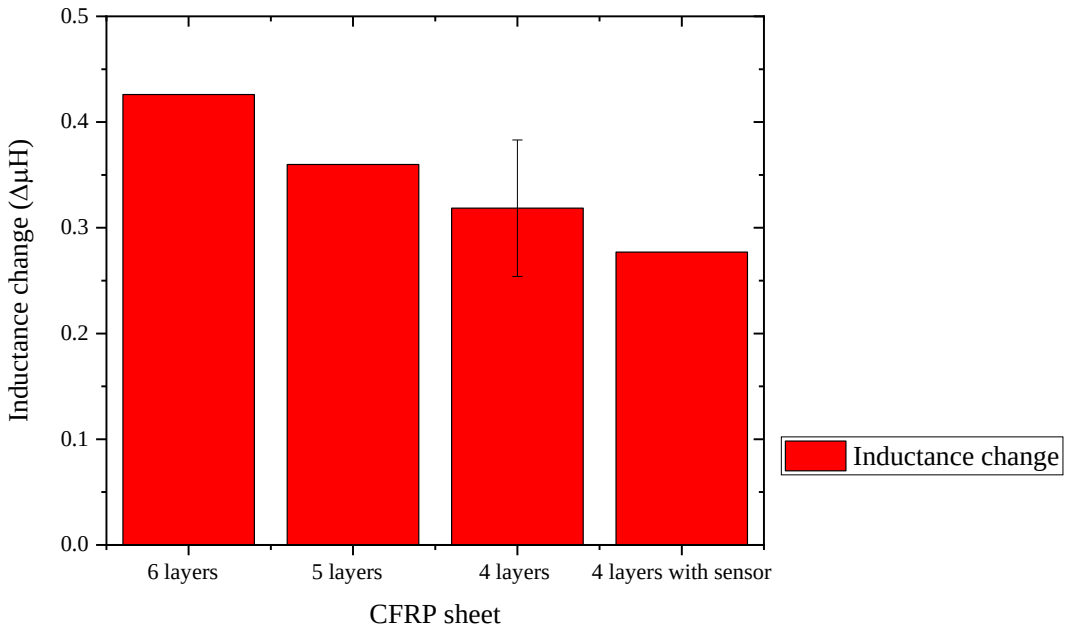

Figure 7.20 Change in inductance before and after 0.5 kg weight impact on CFRP sheet and magnetite sensor

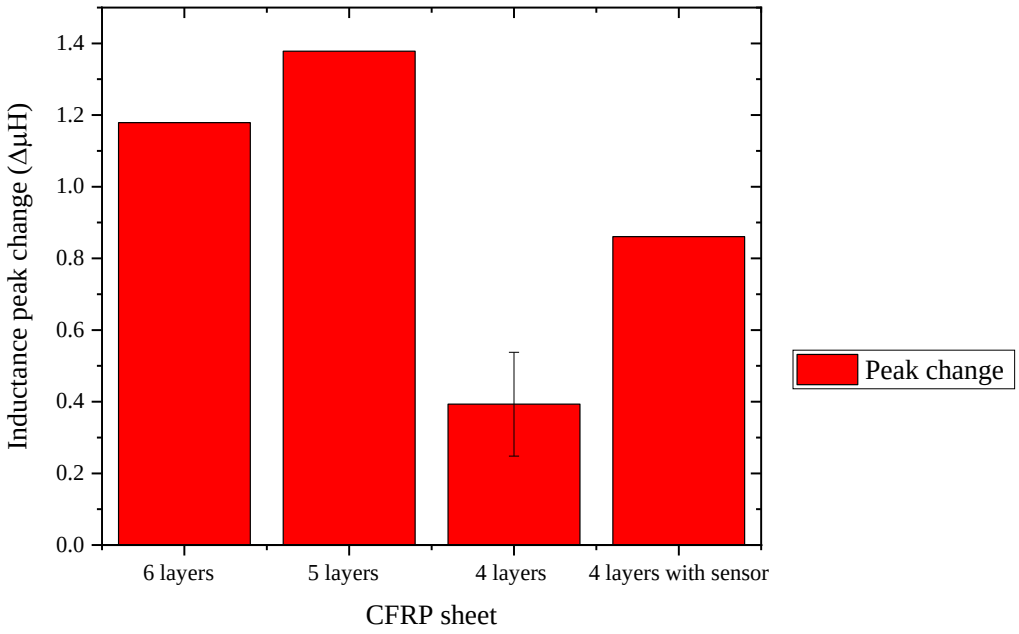

Figure 7.21 Peak inductance of CFRP sheet impact with 0.5Kg for different layers and magnetite sensor

7.3.4 Sensor distance and location

7.3.4.1 Introduction

The sensor location is essential to decide where to install the sensor on the CFRP structure and to scan for defects and damages. There could be areas where CFRP are prone to damages or defects in extreme environments, therefore the location of the sensor is important to detect these defects and damages without interfering with the structural integrity of the CFRP.

7.3.4.2 Magnetite line impact

A magnetite line was printed across the CFRP to detect delamination across the area of impact as shown in Fig. 7.22 and Fig. 7.23 with an inductor fixed with epoxy. Subsequent droplets across the CFRP would in theory detect small defects from the impact by the orientation of magnetic moments. In the previous sections 7.3.3.1 and 7.3.2.1, the magnetite sensor printed onto photo paper did not improve the change in inductance or peak from an impact of 0.5 kg on both CFRP and PC sheet. It was concluded that the paper absorbed or restricted the detection of the defect on CFRP and PC sheet on impact. Therefore, printing a line would provide further analysis of delamination or defect as well as scanning the effective distance of the defect from the impact without paper substrate.

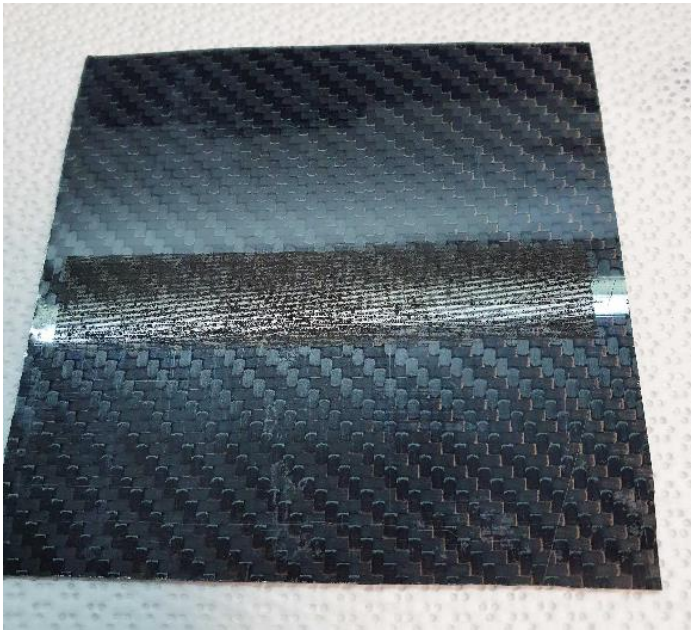

Figure 7.22 Magnetite line printed across CFRP sheet

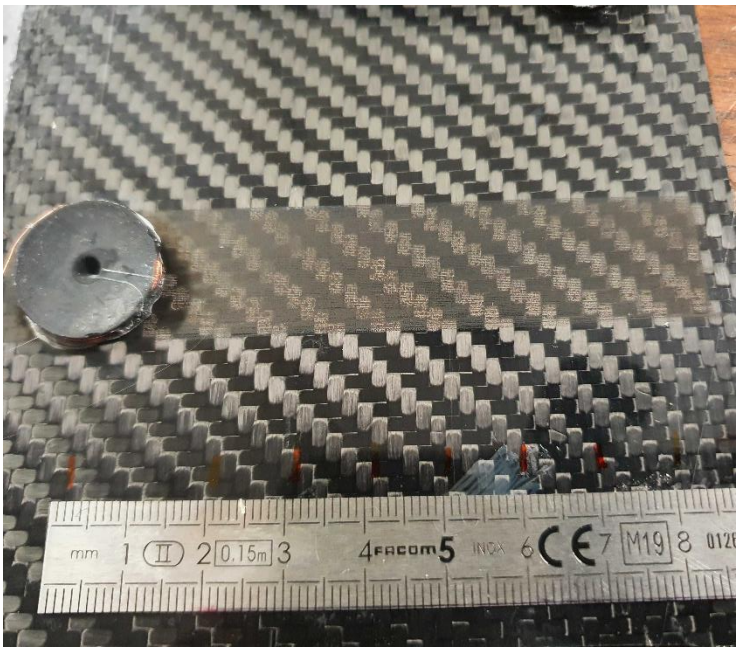

Figure 7.23 Magnetite line with inductor attached by epoxy to CFRP

Two different 200 hand wound coil inductors fixed with epoxy of CFRP sheet were used to detect inductance during the impact. An inductor was placed on top of the single and 10 layered layer magnetite print on CFRP as seen in Fig. 7.23 and one was placed at the back for the 10 layered magnetite print as seen in Fig. 7.22. Therefore, multiple tests and experiments were designed to see the effectiveness of the magnetite layer and placing the inductor on the back or on top of the CFRP. This

was to see the magnetic moment mobility and how the impact would directly change the moment of the magnetite print. A 0.5 kg weight was dropped at a height of 1.1 m for both with single and 10 layers of magnetite line on CFRP. Fig. 7.24 and Fig. 7.25, shows the inductance measurement during the impact experiment for single and 10 layered magnetite line.

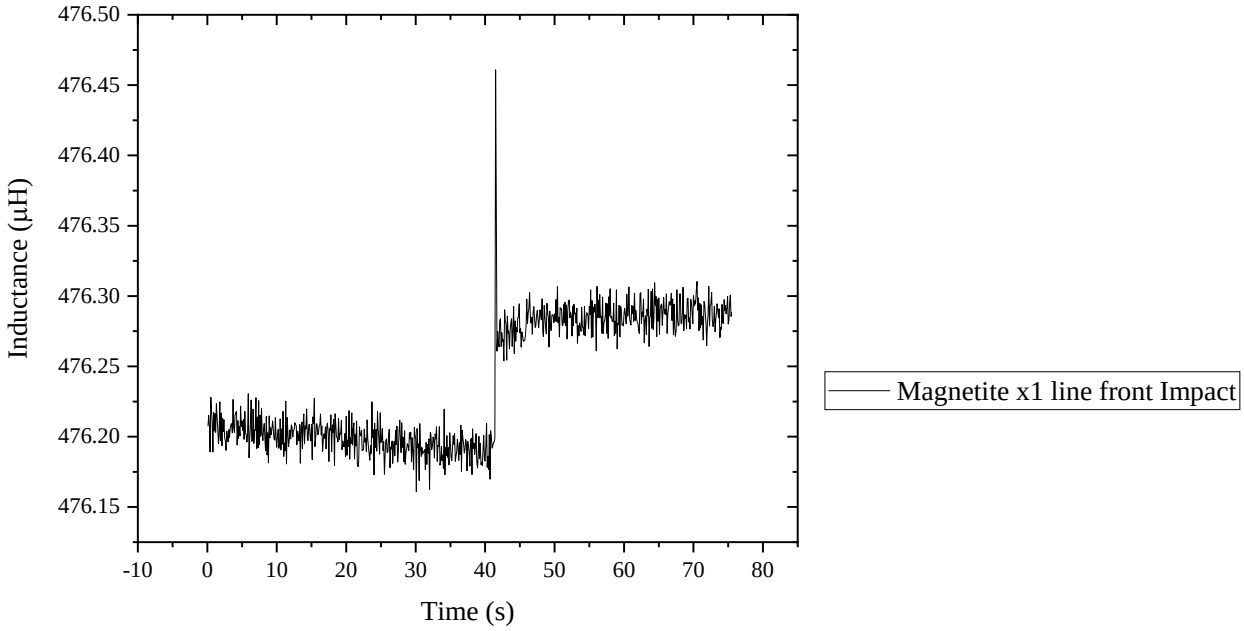

Figure 7.24 Impact test with 500g drop weight on front of CFRP with 1x magnetite line

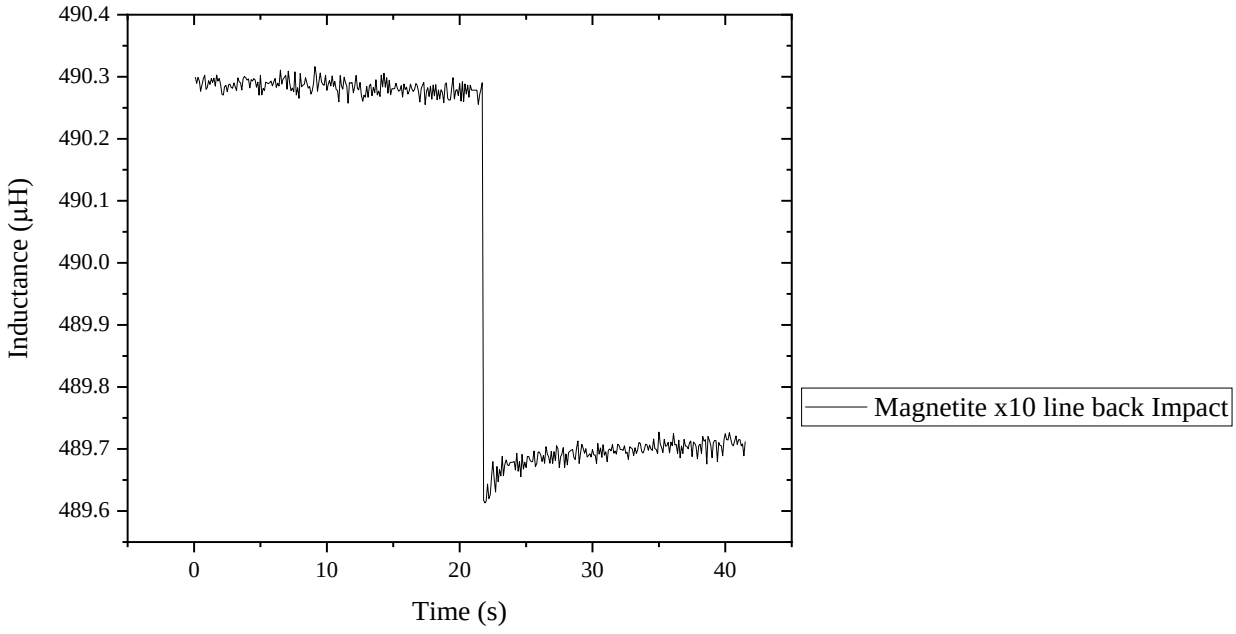

Figure 7.25 Impact test with 500g drop weight on back of CFRP with 10x magnetite line

Fig. 7.26 shows the inductance before and after a dropped weight of 0.5 kg impact on CFRP. Multiple tests were conducted to compare with an empty CFRP i.e. no print on the surface, taken from CFRP with 4 layers. An impact test was done with an inductor fixed by epoxy and the drop tube held by a clamp to reduce noise and vibrations from the impact. Although it did reduce the noise but only around ± 0.01 µH (within error) therefore the influence of the tube affecting the results is removed. In comparison, the single magnetite line shows a decrease in inductance before and after impact compared to the empty CFRP result. The 10 layered magnetite NPs showed a remarkable change of 3.2 µH which is 4600% higher than the single layered magnetite line. However, when the inductor is placed at the back of the 10 layered magnetite line, the inductance increases to almost twice as much as CFRP without magnetite print on the surface. This shows that the 10 layered magnetite line does detect damages and defects on the CFRP by increasing the inductance above the noise generated by the impact.

Fig. 7.27 shows the result for the peak inductance from an impact of 0.5 kg on CFRP. Overall the result shows direct similarity to the result shown in Fig. 7.26. Both 10 layered magnetite with inductor on the front and back show an improved peak inductance than the single layered magnetite line and empty CFRP. While the magnetite line with 10 layers does show an improved inductance peak to the single magnetite line, the single line does show a reduction of inductance to the empty CFRP, similar to the results in Fig. 7.26.

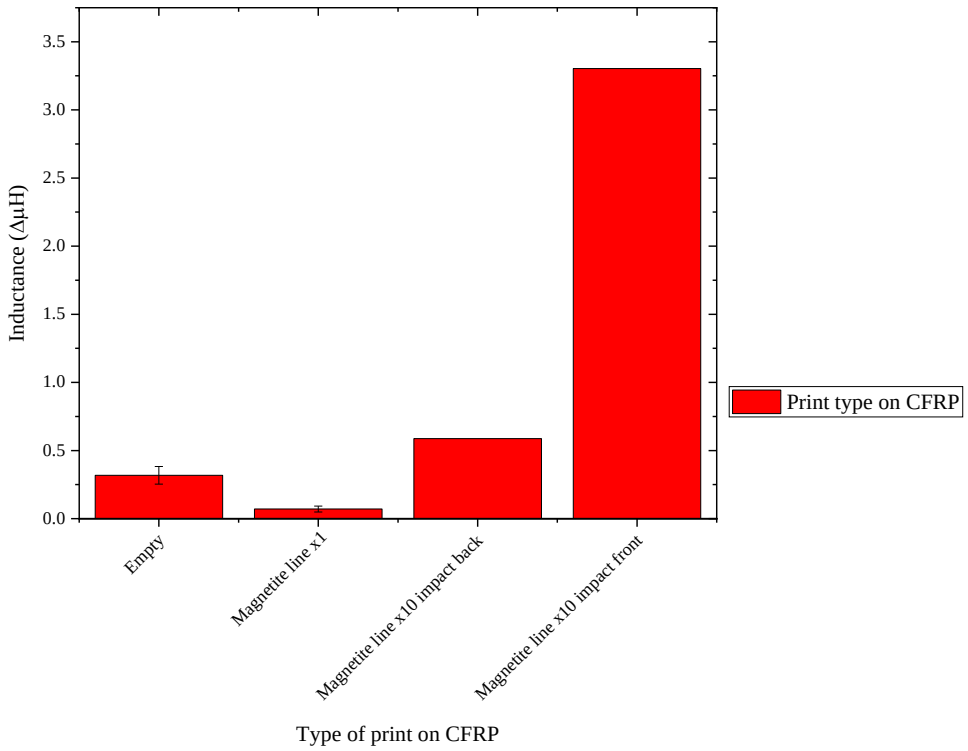

Figure 7.26 Inductance change before and after 0.5 kg impact on CFRP with magnetite line in comparison with empty and sensor printed on photo paper

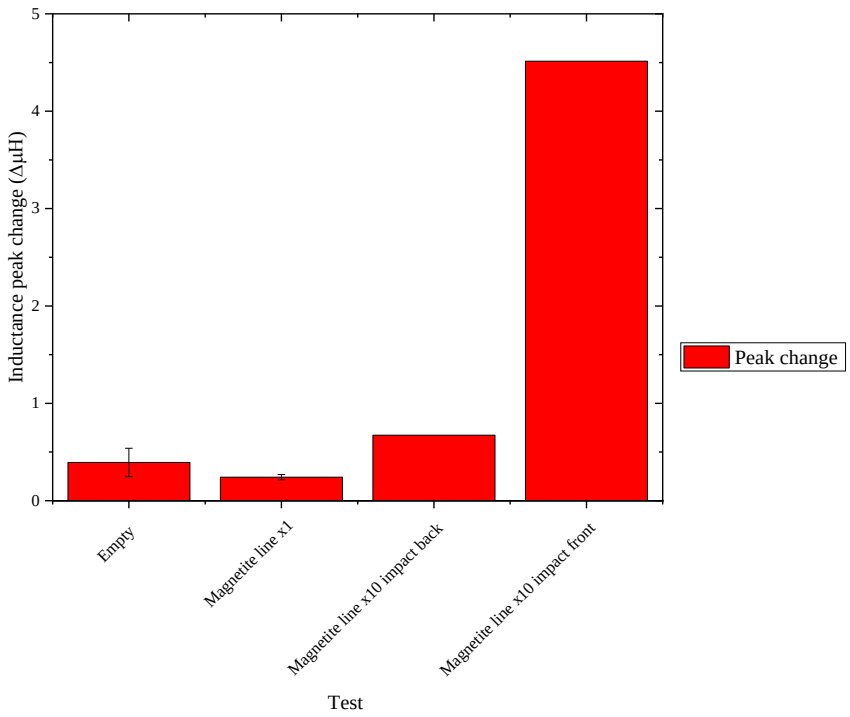

Figure 7.27 Inductance peak change during 0.5 kg impact on CFRP with magnetite line in comparison with empty and sensor printed on photo paper

7.3.4.3 Structural health monitoring of magnetite line

Structural health scan of the CFRP composite with magnetite line was performed by measuring the change in inductance across the surface after impact, as a function of time. The 0.5 kg weight was dropped onto the front of the CFRP where the magnetite was printed on. The baseline/null inductance was measured by placing an inductor on an area of the CFRP with no magnetite print or magnetic material. The inductor was then placed on the magnetite line to start recording the inductance (next to the inductor that was fixed by epoxy to the CFRP). The inductor was then moved across the sample by a plastic tweezer, placing it 1 cm towards the right each time until at the end of the print. An example of the scan can be seen in Fig. 7.28 where the location of the peak inductance, null inductance and 1 cm placement of the inductor. The scan was performed before and after the impact on the front and back. This was to see any differences the impact had made and whether defects could be identified after the impact. The error associated with the scan could be seen in the result. First is the change in distance of the copper wire. As the inductor was moved from left to right, the copper wire moved slightly therefore reducing or increasing the inductance (depending on the direction of scan). This can affect the result, however the reduction of inductance due to the inductor movement was cancelled out by removing the gradient using the plotting software.

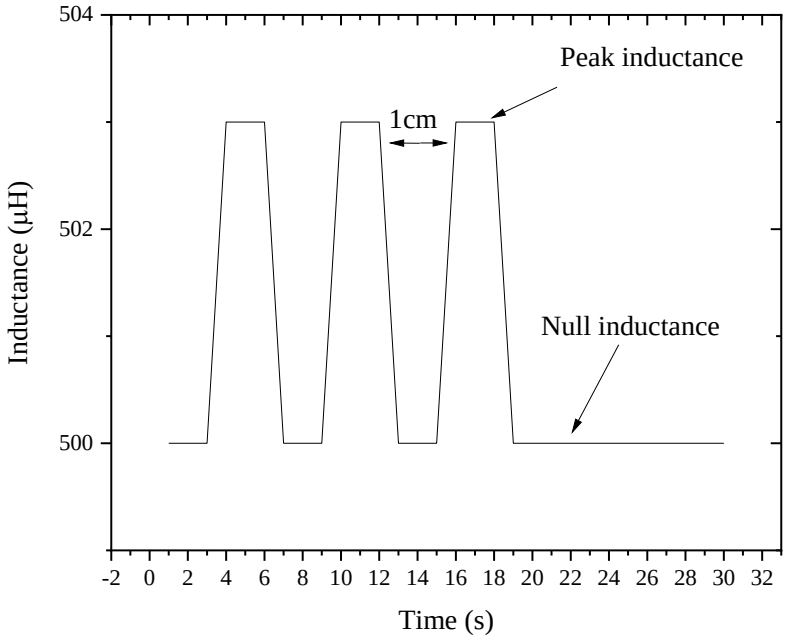

Figure 7.28 Example of scan on magnetite line showing the location of the peak inductance, null inductance and 1cm spacing for each peak

The results in Fig. 7.29 and Fig. 7.30 show that the inductance in both back and front scan had reduced after impact, for both single and 10 layered magnetite lines. However, there is no significant change seen in inductance when moving the inductor across the sample before the impact. For example, in the single magnetite line the peaks (1 cm for each peak), the peaks remain flat across the line. However, the 10 layered magnetite line shows significant improvement to the single magnetite line but shows little deviation from the peak, as expected. Interestingly the null inductance shows to be higher on the back of the CFRP than the front, before impact in the 10 layered magnetite line. This is due to the error of the inductor as this was placed in an area where there was no magnetite print present. The peaks are more definitive i.e. above the null inductance and there seems to be a reduction of inductance near the impact site as shown in Fig. 7.29, where the green line (back of the CFRP) shows variation in peaks and troughs. For example, after 40 seconds or 3 cm across the CFRP, the peak inductance reduces significantly from 501.9 μH to 501.6 μH. This shows that there is some sort of defect present as the inductance from the magnetite reduces. Interestingly the change in inductance peak does not change significantly on the back of the CFRP. This is in direct contradiction to the impact test performed in the previous chapter where an inductor placed during the impact recorded the higher change in inductance on the back for the 10 layered magnetite line. It was expected that the scan from the back of the CFRP would show significant change due to the orientation of the magnetic moment of magnetite at the impact site.

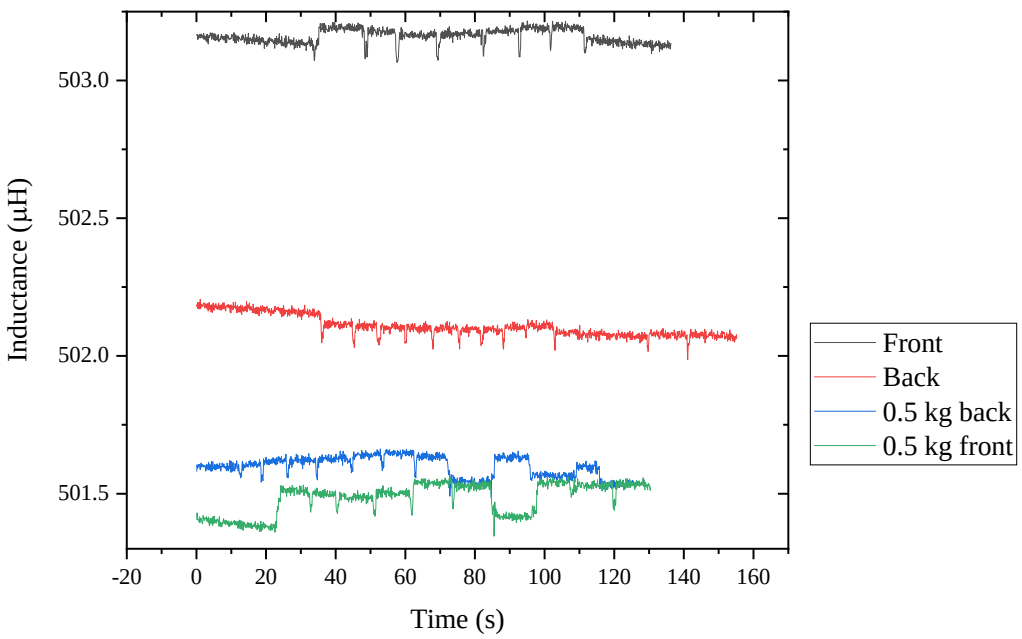

Figure 7.29 Inductance scan before and after impact on front of CFRP with 1x magnetite line

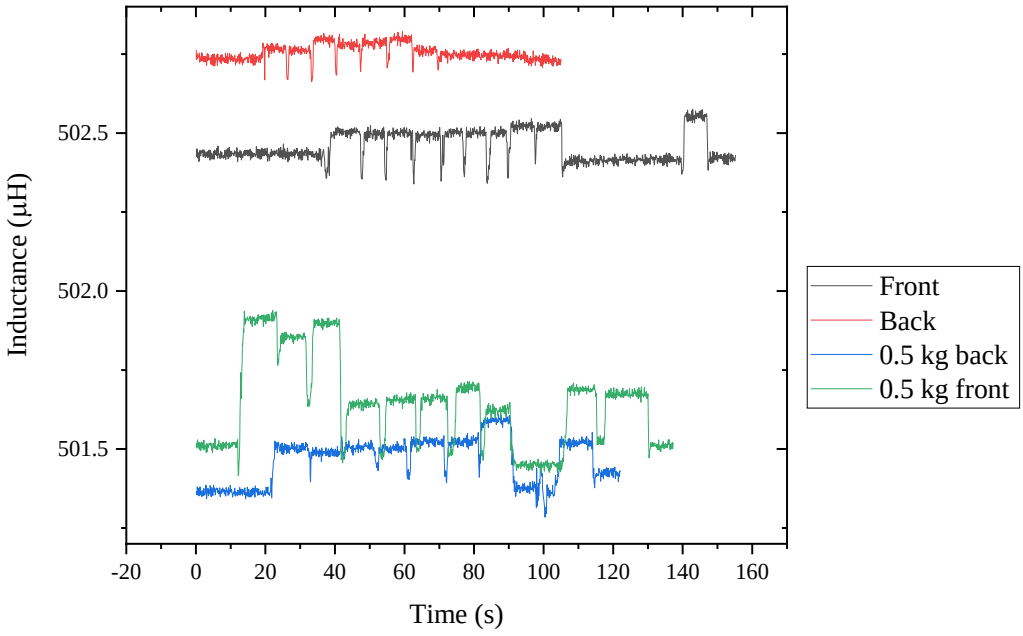

Figure 7.30 Inductance scan before and after impact on back of CFRP with 10x magnetite line

Further analysis of the peaks and distance from the impact (at 0 cm) is seen in Fig. 7.31 and Fig. 7.32 for single and 10-layered magnetite lines. This shows the change inductance peak from the null inductance for both before and after impact. From both magnetite single and 10-layered magnetite lines, the peaks have shown a difference in inductance from the baseline. Before the impact, the peaks are almost in equilibrium across the sample for both front and back of the CFRP. The single layer magnetite line has shown a slight positive and negative inductance as the inductor was moved across the line,

however no significant change is seen. This is maybe due to the inductor coil drift, as the CFRP did not undergo any strain prior to the impact test, therefore the change in inductance before the impact is within error.

After the impact, the inductance is increased and more prominent on the front of the CFRP than the back. However, the distance at the impact is less definitive, for example on the 0 cm mark there is no significant difference or change in peaks than before. There are changes in inductance peak around the impact but only about 2 cm away from the impact. For example, for the 10-layered magnetite line the front of the CFRP scan does show a change in peaks at around -2 cm to -1 cm but does not change significantly when directly on the impact site, where the inductance stabilises after +1 cm and +2 cm as seen in Fig. 7.31. This could mean around the impact site (at 2 cm away) delamination or defects are present. However, past the impact site (at 1 cm to 2 cm) to the edge of the CFRP, the inductance does not change as significantly as before. This would suggest that one side of the impact site had deformed while on the other end, the CFRP had not deformed. As the magnetite deforms, one side would change in polarity in positive and the other in negative however, this would be during the impact and not when the moment has reached equilibrium state. It is clear that there is a defect caused by the impact weight but the defect on a specific side is unusual. It is possible that the dropped weight could have hit the CFRP at an angle or removed some of the magnetite print off the surface. To conclude, further analysis of the impact is needed such as if the defect is seen internally to support the result.

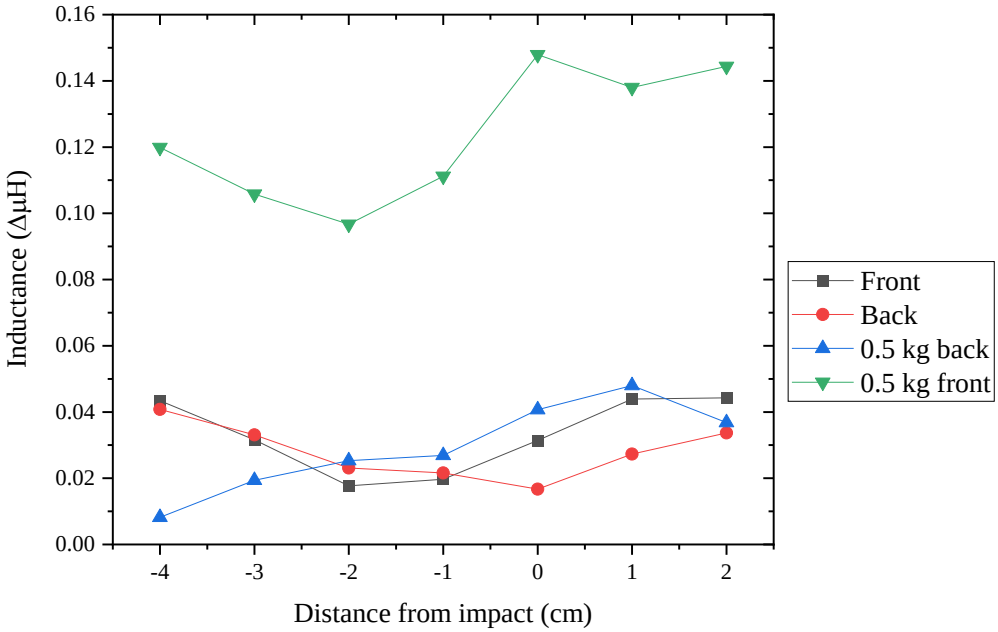

Figure 7.31 Inductance scan and distance from impact of magnetite line x1 before and after impact

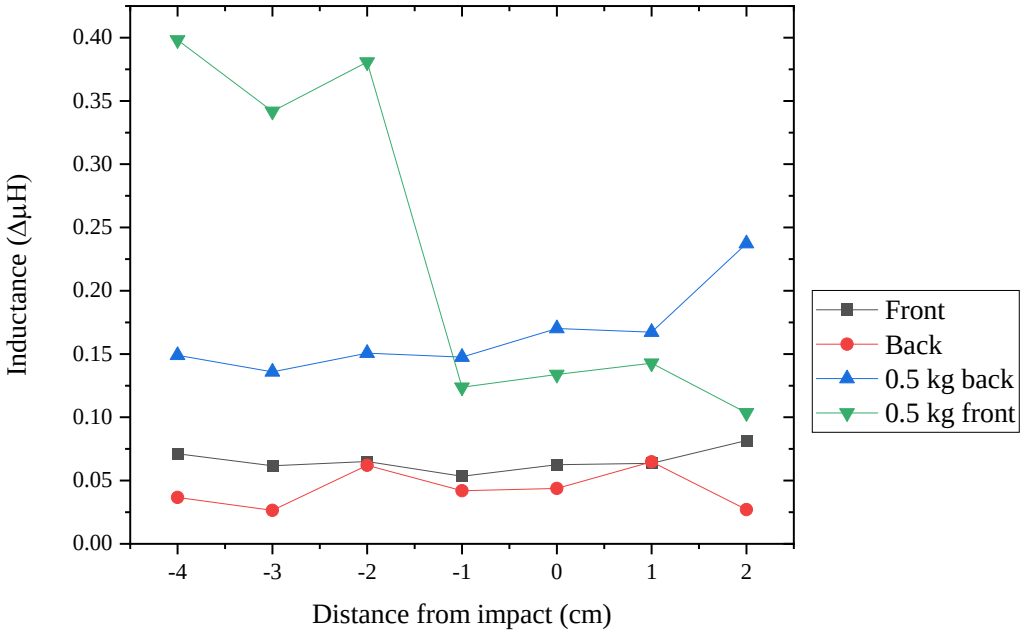

Figure 7.32 Inductance scan and distance from impact of magnetite line x10 before and after impact

7.3.5 Fracture analysis

The CFRP was analysed by optical microscopy analysis and is shown in Fig. 7.33 where a 0.5 kg weight was dropped before (a, b, c) and after impact (d, e, f). Fracture analysis of 4, 5 and 6 layers of CFRP sheet was used, the same that was used in chapter 7.3.3.1 for damage detection. The CFRP was cut using a diamond blade by cutting along the impact site; the cross section of the impact site is shown. For the 4 layers CFRP sheet as seen in (d), had shown significant penetration through the layers in comparison to before impact as seen in (a). Fibre pull out could be seen in (d) and had shown significant delamination and cracking, resulting in a fracture. The structural integrity of the 4 layered CFRP sheet is at risk as further damage could occur due to crack propagation and epoxy debonding in the layers, away from the impact site. The 5 layers of CFRP sheet shows a fracture that was absorbed through the layers and prevented penetration in comparison to the 4 layers of CFRP sheet. While full penetration did not occur, as the CFRP was still intact, each fibre had fractured causing delamination and fibre pull out. The 6 layers of CFRP sheet showed slight delamination and deformation in comparison with before impact, as the layers and structural integrity was still intact. In relation to the results obtained in chapter 7.3.3.1, the inductor had shown an increased inductance, which may be due to excessive noise on the surface and not from delamination or defect within the CFRP. The 4 layers of CFRP sheet shown had reduced change in inductance which could be due to the loss of noise/ energy by penetration through

the layers. In (Leong *et al.*, 2019) they have demonstrated SHM of CFRP using magnetostrictive ribbons. By using 4, 6 and 8 CFRP sheets, they have found that the 6 layers of CFRP sheet have caused a large drop in stress which may have been due to error. 4 CFRP sheets was found to deform and cause damages through the CFRP layers which the magnetostrictive ribbons were able to change in field as stress was applied. This was due to tensile fracture of the fibre at the bottom of the CFRP structure at impact. While higher impact energy of 5 J was used in this work, higher amount of damage and penetration occurred. This was due to the inductor coil placed further away from the impact therefore delamination must occur where the inductor is place on top of the magnetite print.

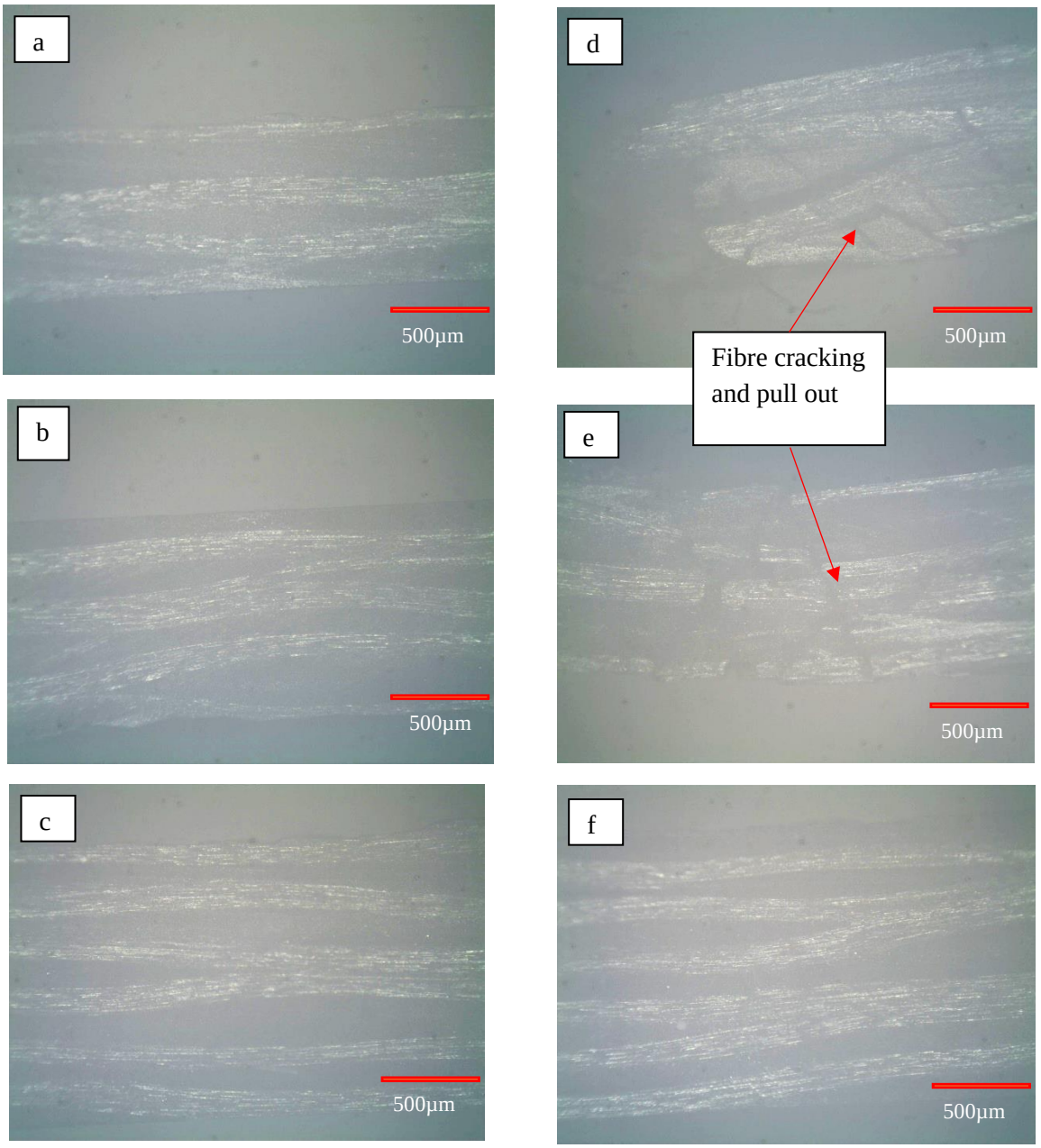

Figure 7.33 Optical microscopy x5 of 4, 5 and 6 layers of CFRP before impact (a, b, c) and after impact (d, e, f) of 0.5kg weight from a height of 1.1m

7.3.6 Impact simulation

To try to understand the magnetic interaction across the magnetite print during impact, a 2D model was created in COMSOL multiphysics to simulate the test, similar to chapter 7.3.4 for different layers of CFRP sheet. The model uses the same method in simulating the magnetic dynamics (non-linear isotropic magnetostriction model) as seen in the experimental method chapter 4.1.1. An example of a model created in COMSOL can be seen in Fig. 7.34, where an object was dropped with a defined weight of 0.5 kg travelling at a velocity of 4m/s and an impact size of 3 mm, collides with a magnetite layer and CFRP sheet. The size has been reduced and refined for easy computation on COMSOL for example, the length of the magnetite and CFRP is kept at 25 mm rather than 100 mm. The thickness of the magnetite layer is kept at 0.2 mm and each layer of CFRP sheet is 0.22 mm, surrounded by air under a field of 10 A/m for model convergence. The magnetite/CFRP and CFRP/CFRP interface is kept as continuous (as one layer), in other words there is no adhesion or friction model between the layers to prevent failure in the computation. The model was set in time domain study with a time stepping of 0.00001 s lasting 0.01 s in total.

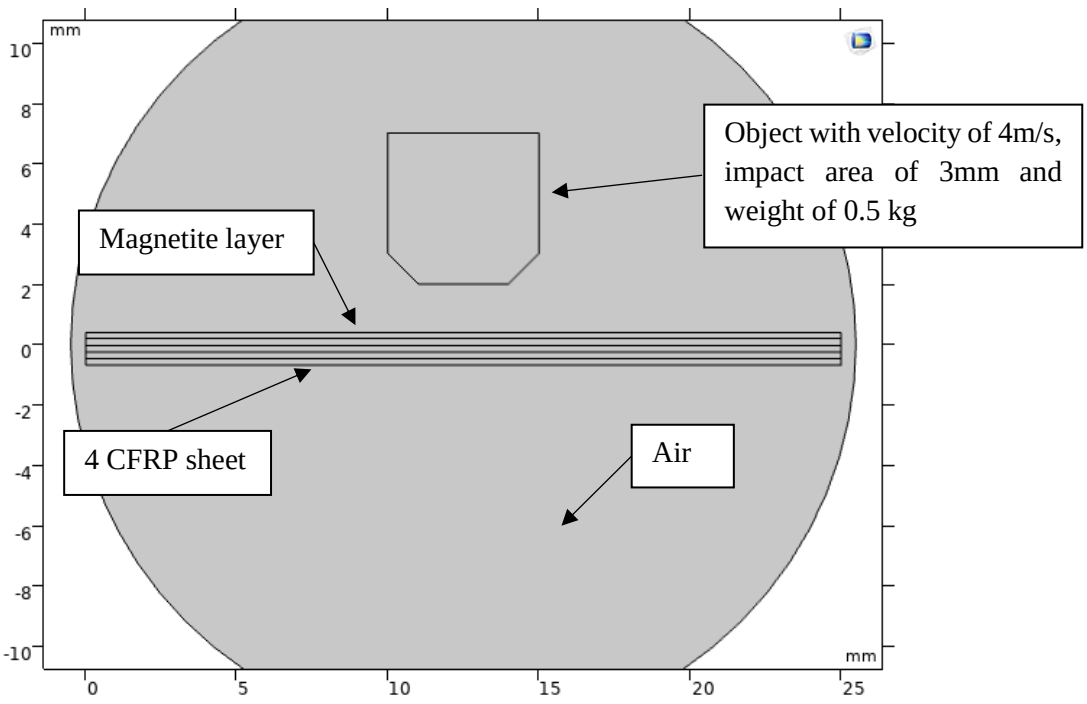

Figure 7.34 Impact COMSOL model with drop weight and magnetite layer and CFRP layer

The magnetisation was measured in the Y direction at the edge of the magnetite layer to simulate the change in field under the inductor, similar to the experimental setup. Fig. 7.35 shows change in field when an object with a total weight of 0.5 kg collides with the magnetite on 4 layers of CFRP at a velocity of 4 m/s. Where (a) is before impact with 10 A/m field, (b) is the magnetic field at impact, (c) is during the impact where the field and stress is applied to the layer and (d) is after the impact where no stress is applied. The 4 stages show the dynamics of the magnetic field across the magnetite layer. At impact, the magnetic field increases exponentially as shown in (b) and (c) and then reaches equilibrium over a short period of time as shown in (d). The short changes in field represent the Villari magnetostriction effect as the strain applied by the object on the magnetite layer, the field orientates into the Y direction while the 10 A/m field is applied in the X direction. The areas of the magnetite layer where the field fluctuates, for example before the impact, the field is confined to the edges of the magnetite layer. After the impact the field increases within the area of impact as seen in (a) then reduces near the edges. This suggests that the load applied by the drop weight deforms the magnetite layer and CFRP layer, therefore creating a change in Y direction, thus the inductor will detect the change in field. The field reduces and stabilises to the edges, shortly after the impact.

a

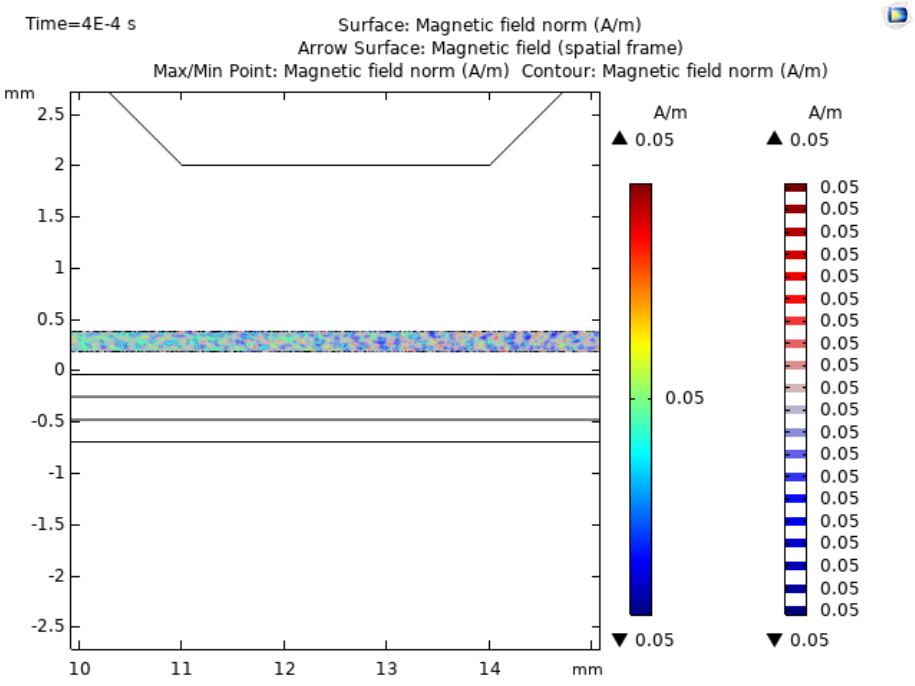

b

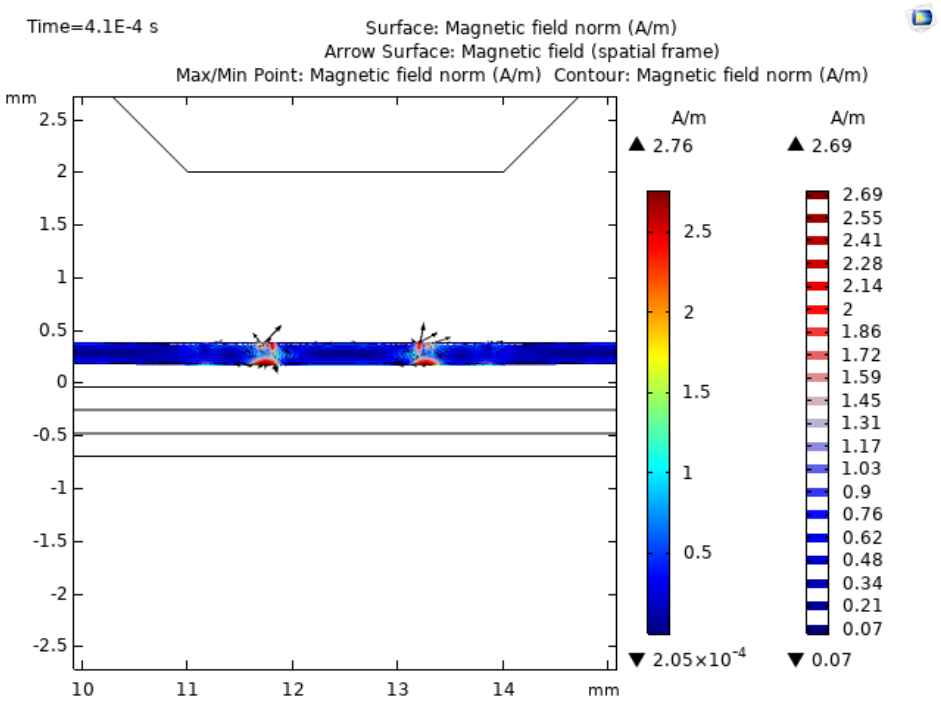
Time=4.1E-4 s
Surface: Magnetic field norm (A/m)
Arrow Surface: Magnetic field (spatial frame)
Max/Min Point: Magnetic field norm (A/m) Contour: Magnetic field norm (A/m)
mm
2.5
2
1.5
1
0.5
0
-0.5
-1
-1.5
-2
-2.5
10
11
12
13
14
mm
A/m
▲ 2.76
2.5
2
1.5
1
0.5
▼ 2.05×10^-4
A/m
▲ 2.69
2.69
2.55
2.41
2.28
2.14
2
1.86
1.72
1.59
1.45
1.31
1.17
1.03
0.9
0.76
0.62
0.48
0.34
0.21
0.07
▼ 0.07

c

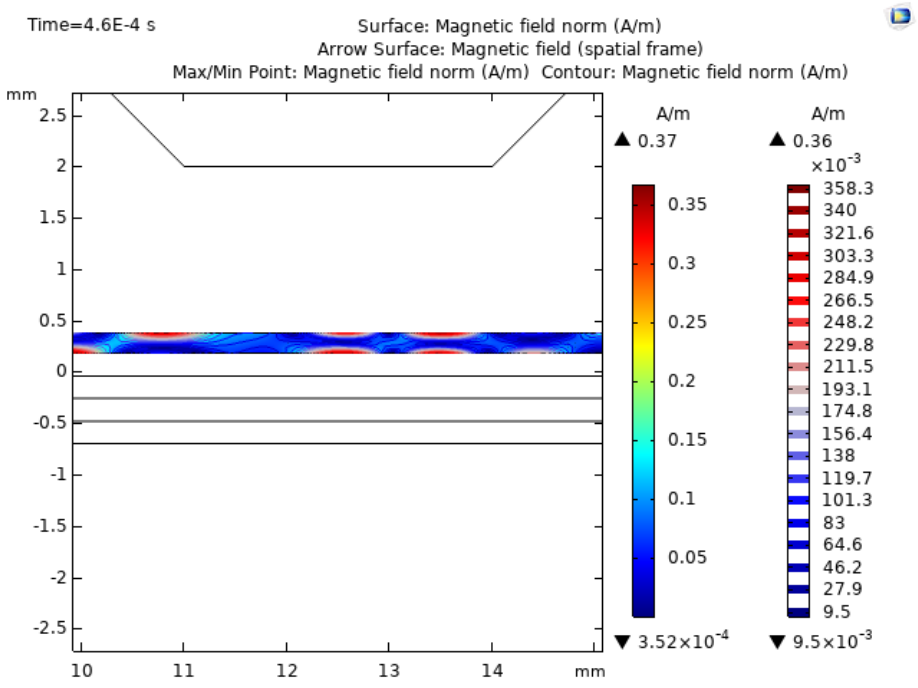
Time=4.6E-4 s
Surface: Magnetic field norm (A/m)
Arrow Surface: Magnetic field (spatial frame)
Max/Min Point: Magnetic field norm (A/m) Contour: Magnetic field norm (A/m)
mm
2.5
2
1.5
1
0.5
0
-0.5
-1
-1.5
-2
-2.5
10
11
12
13
14
mm
A/m
▲ 0.37
0.35
0.3
0.25
0.2
0.15
0.1
0.05
▼ 3.52×10^-4
A/m
▲ 0.36
×10^-3
358.3
340
321.6
303.3
284.9
266.5
248.2
229.8
211.5
193.1
174.8
156.4
138
119.7
101.3
83
64.6
46.2
27.9
9.5
▼ 9.5×10^-3

d

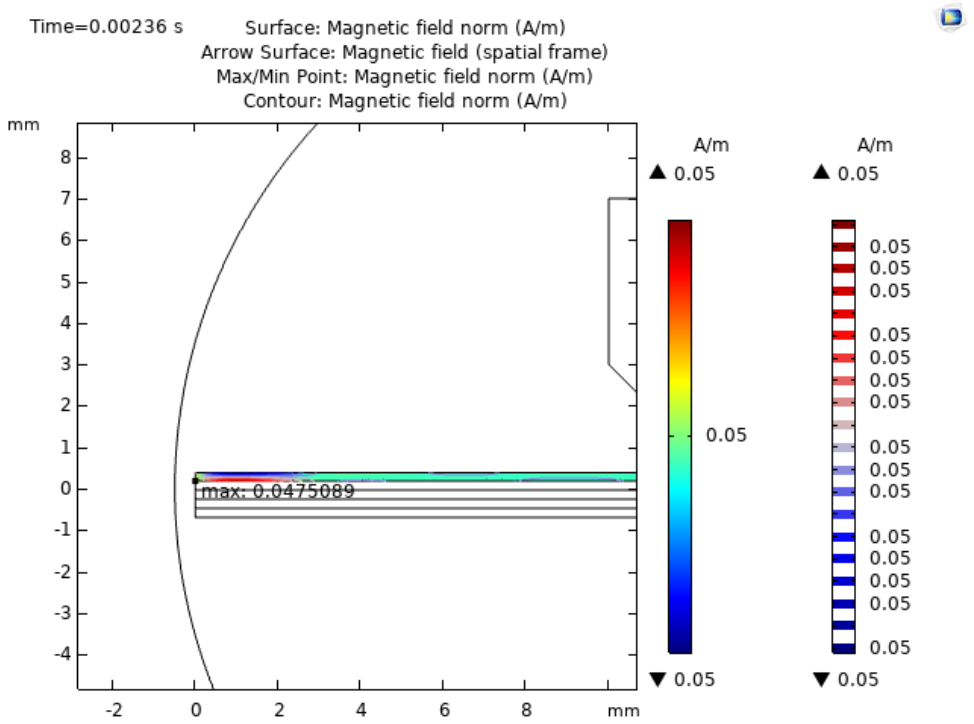

Figure 7.35 Y direction magnetic field area of magnetite in (a)before impact (b) at impact, (c) during impact and (d) after impact

A cut line was taken to show the magnetic field value across the magnetite layer as seen in Fig. 7.36. The cut line shows a broader view of the magnetic field (at the time when the field reached its maximum point) across the layer instead of at a single point. Fig, 7.36 shows the comparison of impacting the magnetite layer and with different layers of CFRP sheet.

The result has shown that for magnetite and CFRP sheet layer, there is a sharp increase in field around the impact site (12.5mm). However, the magnetite layer (with no CFRP layer) and 6 layers of CFRP sheet, shows a reduction in field around the impact site, smaller than the 4 and 5 layers of CFRP sheet. The magnetite layer (on its own) is thought to have an increased change in field, however the result shows that when CFRP layer is added, deformation to the CFRP layer causes a change in field across the magnetite layer. This could mean that the magnetite layer near the impact could not absorb the energy from the impact which could be due to the object penetrating the magnetite layer. Whereas, the 6 layers of CFRP, the impact does not cause enough deformation or damage to the CFRP layer therefore reducing the change in field across the CFRP. However, when the CFRP layer is around 4 or 5, the energy from the drop weight has been absorbed through the CFRP layer and caused a change in field throughout the magnetite layer due to the deformation in the CFRP. This could mean that penetration

has occurred through the magnetite layer but the 4 and 5 layers CFRP sheet has been deformed across the layers therefore increasing the change in field as the magnetite layer is deformed.

This shows that the impact is not the same for all type of CFRP layers as seen in Fig. 7.20 where the 6 layers has shown to have an increase in inductance during impact. In the real world, this would mean assessing the type of damage for each CFRP sheet, for example in 6 layers CFRP sheet, the impact would be higher as the inductance in increased due to the increased deformation and damping effect in the CFRP layers. The sensors placed in close proximity can detect changes for example if one sensors experiences large changes in inductance and another sensor in close proximity experiences small changes, this would mean penetration has occurred. If all sensors in close proximity experiences large change in inductance then this would mean the defect or deformation propagates within the CFRP layers as seen in 6 layers CFRP sheet.

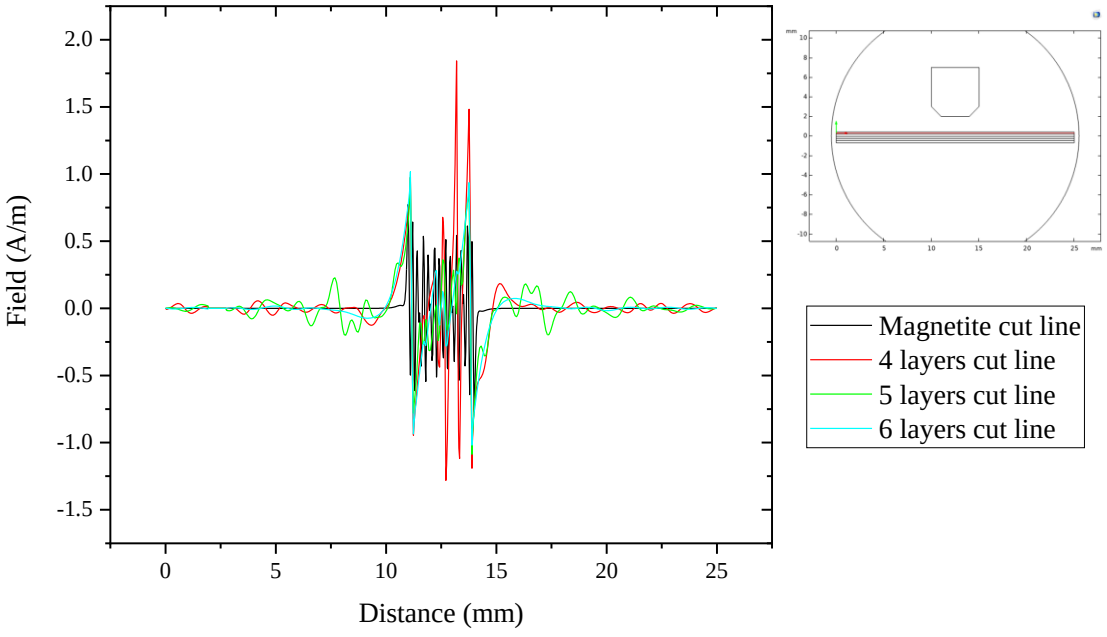

Figure 7.36 Field cut line across the magnetite layer for 4,5 and 6 layers of CFRP

Fig. 7.37 shows that by doubling the thickness of the magnetite from 0.2 mm to 0.4 mm on the 4 layers of CFRP, the field reduces at the site of impact and around the impact site. This could mean that there is less deformation in the magnetite layer as stress is reduced due to the increased resistance to fracture or defects. The 0.2 mm magnetite layer showed an erratic switching of field where the 0.4 mm layer showed a reduced switching of field throughout the layer. This could mean there is lower deformation, as the magnetite layer thickness is increased. Therefore, the change in field due to strain is reduced. The simulation and the experimental work do not follow the same trend as in the experimental work, the increased layer of magnetite shows an increased change in inductance as the magnetic field is increased

on impact. However, the single layer of magnetite in the experimental results showed a reduced inductance, below the noise of CFRP without magnetite layer. Therefore, the simulation and experimental data could be different due to error in both experimental set up and COMSOL model/ boundary conditions.

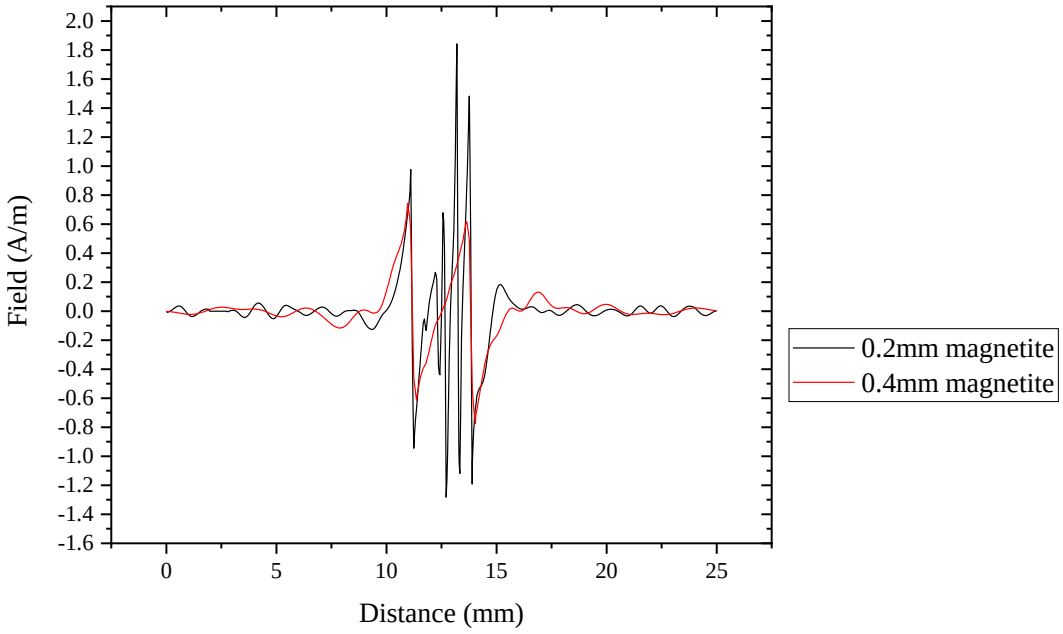

Figure 7.37 Field cut line of double thickness of magnetite on 4 layers of CFRP

Fig. 7.39 compares the field from the magnetite droplet layer with gap distances of 0.1 mm and 0.05 mm between droplets and without gap on 4 layers of CFRP sheet. The field cut line on the magnetite layer shows a distinct difference between both zero and both 0.05 mm and 0.1 mm gap distance. The main difference in field is at the impact site where as the gap increases, the field is reduced sharply as the object is in contact, compared to the magnetite with no gap. However, the field simulated across the sample tells a different story as where there are gaps present, the field is increased sharply compared to the magnetite droplets with no gap in between. This is because there is magnetic dipole interaction, as on the edge of the droplet the polarity orientates in negative or positive on both sides of the droplet, which generates an increase in field in the Y direction as seen in Fig. 7.40. Thus the field picked up by an inductor or a hall probe will be seen better than the magnetite with no gaps. However, the larger the gap in between droplets, caused a greater strain and stress thus increasing the change in field. For example, for the 0.1 mm gap distance, the change in field at the impact site showed a change of 0.6 A/m field while for the 0.05 mm showed a lower change in magnetic field of 0.25 A/m. For both gap distances (0.05 and 0.1 mm), the change in field is different on the magnetite layer between 0 to 10 mm and 15 to 25 mm side as seen in Fig. 7.39. The 0.1 mm gap has an increase between 15 mm and 25 mm side than the 0.05 mm, whereas the 0.05 mm has a higher field between 0 mm and 10 mm side than the 0.1 mm droplet gap. This could be due to the demagnetisation field or magnetic dipole which has a

positive and negative moment on each side. It was thought that 0.05 mm would have twice as many peaks due to the increased gaps and magnetic dipole interaction, however the peaks are similar to the 0.1 mm model.

Unlike the bending strain simulation in chapter 6.3 where it is shown that there is a clear relation between the length of gap in between droplets and field. The dynamics in this simulation is quite different as it is dependent on the gap distance, the ideal gap distance is not when the droplets are touching but rather when they are further apart. However, both models are different, as the droplet dome shape could not be simulated here in the impact model due to computational difficulties, therefore reducing the accuracy of the simulation. Accuracy could be improved by reducing the time stepping on impact but this would increase the computation time and memory in COMSOL software. Overall, both simulations (bending and impact) have shown that the ideal gap between droplets is 0.05 mm as it showed greater change in field when strain is applied and sharp increase in field (similar to 0.1 mm gap) when exposed to an impact.

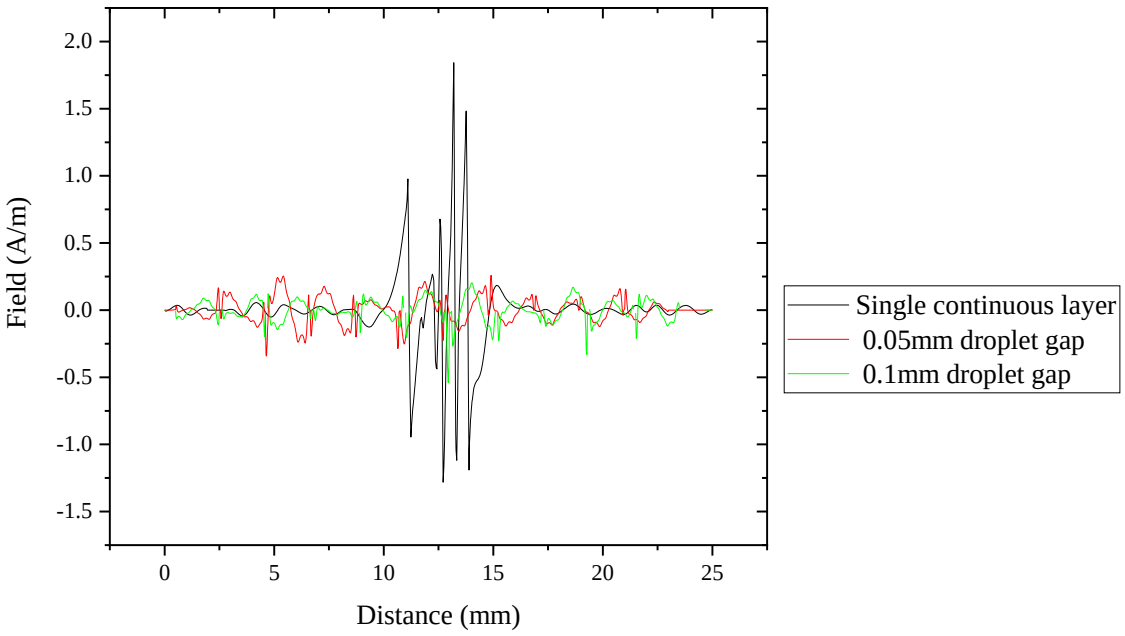

Figure 7.38 field cut line of magnetite droplet gap distance on 4 layers of CFRP

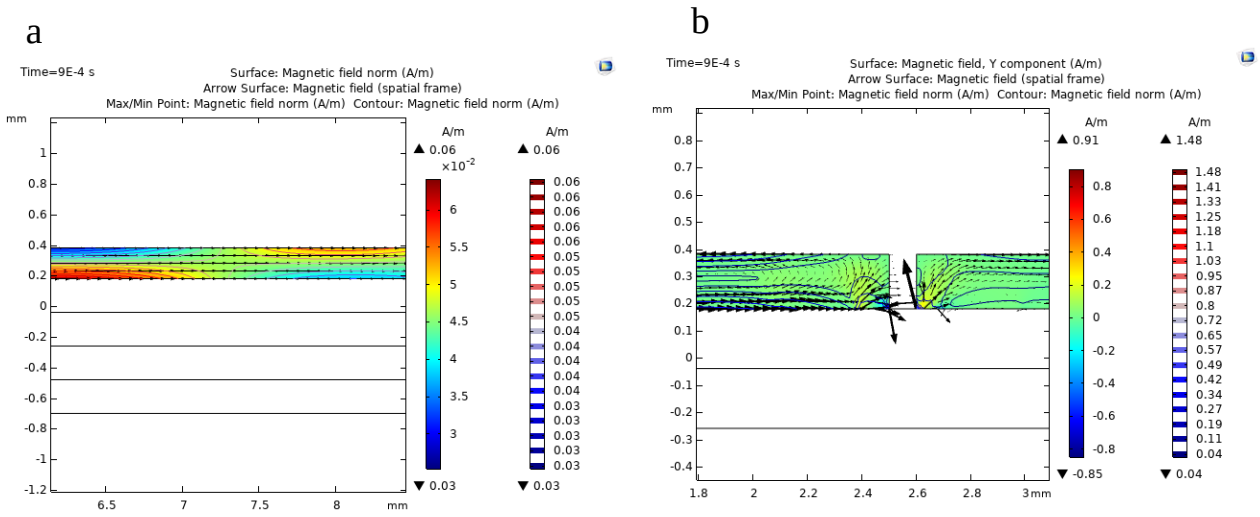

Figure 7.39 Simulated area of field in the Y direction and contours with field direction for magnetite with (a) no gap and (b) droplet gap distance of 0.05mm

In literature (Breen, Guild and Pavier, 2005), they have simulated the stress generated across the CFRP sheets by dropping various weights and from a range of heights. Fig. 7.40 compares the stress generated at the centre and edge of the CFRP after impact. The stress increases sharply at the centre then fluctuates after 2 ms whereas at the edge of the CFRP, the stress is initially lower but then follows the stress generated at the centre after 2 ms. This shows that the elastic behaviour of the CFRP rebounds, for example after 7 ms where the stress increases positively and then decreases into negative stress. Although this work is not directly comparable to literature such as the thickness and weight dropped or the type of CFRP used, the model does show some similarities. This work has shown the same effect where in Fig. 7.41 shows the stress generated from dropping a 0.5 kg weight from 1.1 m height. The stress from the centre on impact shows a sharp increase in stress compared to the stress from 12 mm away. The delay and reduction in stress can be seen in the literature as well as in this work. The short sharp increase in stress is down to the thickness and impact energy, where both model differs as this work has used 1 mm thick CFRP whereas the literature has used CFRP with thickness of 8 mm therefore showing an increased stress from the weight dropped and longer fluctuation in stress over time. Fig. 7.42 shows the strain generated in this work where from 12 mm away from the impact there is an increased delay in strain on the magnetite layer. This results in the change in field as the Villari effect produces a response as strain fluctuates, as seen in Fig. 7.36.

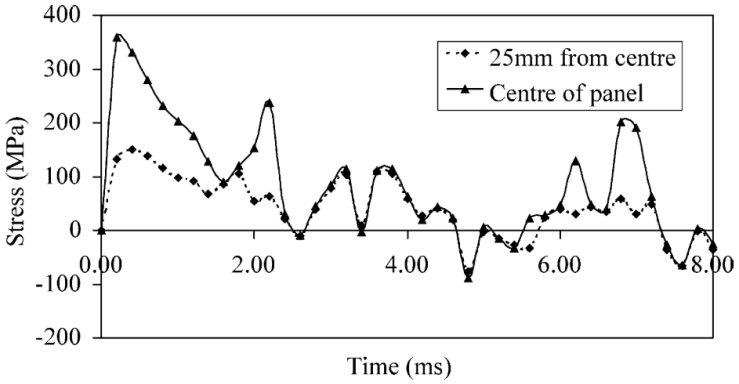

Figure 7.40 Stress at centre and edge of CFRP panel after impact taken from (Breen, Guild and Pavier, 2005)

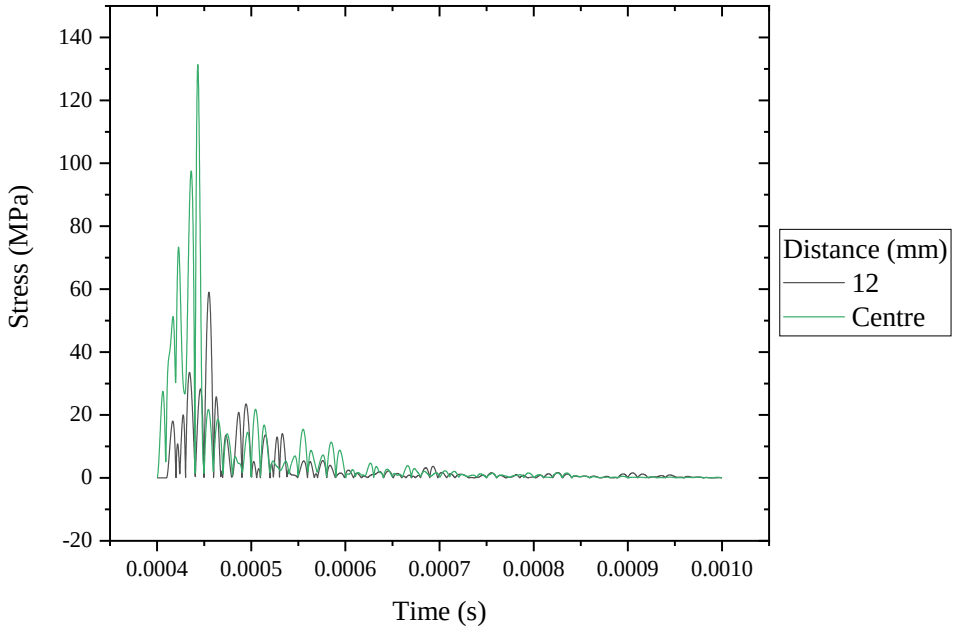

Figure 7.41 Stress on magnetite layer during impact from the centre and 12 mm away

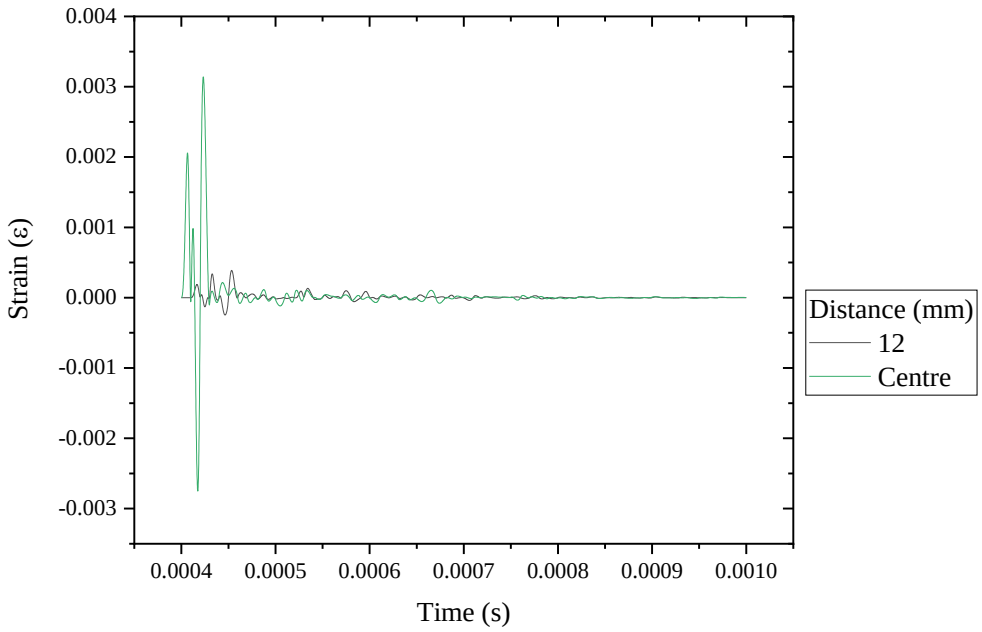

Figure 7.42 Strain on magnetite layer during impact from the centre and 12 mm away

7.4 Summary

In summary, this chapter aimed to evaluate monitoring of strain and defect on CFRP by using inkjet-printed magnetite NP. Strain and defects on CFRP were applied by bending and impact forces respectively. A range of tests were used to evaluate the effectiveness of the inkjet-printed magnetite NP from the bending and impact experiments. For example, eliminating noise, reliability of the sensor, location of the inductor and scan of the CFRP before and after impact. Simulations were employed to compare the field dynamics to the real world test.

By continuing on from chapter 7 (inkjet printing), strain by bending over a known curvature was performed on a CFRP sample with magnetite coil printed directly on top. The results showed that printing directly on the surface of CFRP, performed better than on paper or kapton substrate. This could be due to the paper substrate absorption of the magnetite and higher wetting angle on kapton than CFRP. Acrylic spray or PDMS coating can be used to protect the magnetite print on CFRP and prevent damage from the environment as seen in chapter 6.

The second evaluation of SHM of CFRP was by impact testing and detection of delamination or defects by sensing a change in inductance during impact. Various trial and error measurements were performed such as testing the inductor robustness on PC and fixing the inductor by epoxy to reduce noise. A range of weights from 0.1 kg to 1 kg were dropped on polycarbonate to observe the level of deformation and

inductor signal to noise during impact. It was found that as the weight of the object was increased, the level of inductance increased due to the noise, as the weight was increased however due to the level of noise the trend is erratic and there is a higher level of error in the inductance measurements. The 0.5 kg weight was found to have less noise and provide high damage and defects to the PC sheet.

For CFRP impact testing and simulation, only one weight (0.5 kg) was used throughout the impact tests for consistency. Different layers/ thickness of CFRP were tested for damage analysis and comparison with simulations. It was found that the 4 layers of prepreged CFRP sheets, sustained penetration and excessive delamination/defects whereas the 6 layers of CFRP sheets showed negligible cracking and delamination under an optical microscope. The 6 layers of CFRP sheet showed a greater level of change in inductance than the 4 or 5 layers. This may be due to the noise from impact on the surface. Therefore, 4 layers of CFRP was selected for the impact testing and damage detection. It was also found that the magnetite coil printed on paper did not improve the change in inductance. Therefore, the reduction of inductance may have been due to the contact between the CFRP and magnetite print. The paper as a substrate may have restricted defects or the motion of the CFRP.

To test the sensor for SHM across the CFRP sheet, a line of magnetite was printed directly on the CFRP while an inductor was placed at the edge of the print (5 cm away from the impact site). Single and multiple layers of magnetite were printed to test and compare the change in inductance during impact and whether multiple layers or a single layer were robust for SHM of CFRP. It was found that the multiple layers of magnetite on CFRP was ideal when an inductor was placed directly on top of the magnetite layer, fixed by an epoxy during impact. A scan of the magnetite layer was performed across the CFRP sample by placing an inductor (separate from the one fixed to the CFRP) on top and manually placing it at 1 cm distance at a time. This is to detect any defects or delamination that occurred near the impact site by measuring the inductance peak size. Inductance had increased across the sample after impact as the inductor moved across in front of the 10 layered magnetite line, however defects or any damages were difficult to detect. Although the scan was not clear cut as it thought it would have been, the scan before and after the impact had detected an overall reduction or drifting of inductance across the CFRP sample. This could not be verified if this due to changes of the inductor e.g. wire extension or defect in the inductor or from the magnetite layer as the base line read different levels of inductance before and after the impact.

The impact testing was simulated using COMSOL multiphysics. The results showed that even though the values simulated in COMSOL were inconsistent to the experimental data, some similarities between both test were demonstrated such as the Villari effect from applying stress by impact was shown. For example, 4 layers of CFRP sheet with magnetite layer in both simulation and experimental data was shown to be similar. For example, the COMSOL simulation image in Fig. 7.35 and experimental scan in Fig. 7.32 shows that the field at the edge of the magnetite layer had changed. The simulation showed

a magnetic dipole interaction forming at the edges of the magnetite layer whereas the inductance scan measurement showed an increase change in inductance at both sides of the magnetite print. In Fig. 7.32 the inductance can be seen increased at -4 cm and decreased at +2 cm from the impact at the front for 10 layered magnetite. 4 layers was selected for impact test as simulation has shown that 4 or 5 layers of CFRP sheet was ideal to the magnetite sensor when a weight of 0.5 kg was dropped onto the CFRP composite. It was found that for the 6 layered CFRP sheet and magnetite layer (with no CFRP), the field increased sharply at the point of impact but the field dissipated across the sample, whereas the 4 and 5 layers of CFRP sheet, the magnetic field fluctuated throughout the magnetite layer. This was due to the penetration and defect in the 4 layered CFRP as seen in the experimental setting, therefore the energy and the deformation is transferred to the magnetite layer (around the impact site). Little deformation occurred in the 6 layered CFRP therefore the simulation shows that the field stabilises around the impact as only a small amount of deformation occurred on the magnetite layer. This further demonstrates that the field increases on the magnetite layer when the deformation on the CFRP increases. However, by modelling the increased thickness of magnetite on the surface from 0.2 mm to 0.4 mm, both experimental and simulation do not show any similarities in field. As the experimental test shows the 10 layered magnetite increased in inductance whereas the simulation showed that the field increases in 0.2 mm (reduced thickness) magnetite. This may be due to the magnetite layer increasing the fracture toughness and strength therefore resisting deformation and damages to the CFRP in the simulation. This is not seen in the experimental work where the magnetite layer is removed at the impact site due to the decohesion of the magnetite/ CFRP interface. Therefore, the difference between the experimental and simulations could be due to the large error difference for both real world and computational study.

Chapter 8

Conclusion and future work

8 Conclusion and Future work

8.1 Conclusions

To conclude, this thesis has explored and evaluated different types of magnetostrictive materials and additive manufacturing methods for SHM of CFRP for applications in the aerospace sector and beyond. The two main types of printing used in this project, were the extrusion of steel by using the DMBD printer which consist of extrusion, debinding and sintering. Inkjet printing of magnetite NPs was found to reduce weight and cost more than DMBD printing. The magnetic and structural properties were tested using methods including a SQUID magnetometer to measure the hysteresis loop and SEM/EDS imaging was used to determine the microstructure/porosity and element composition. SHM of these sensors was simulated using the multi-physics software COMSOL and experimentally tested using strain bending and impact testing on CFRP.

Research questions raised at the beginning of the project were:

1. How does printing magnetic materials affect the magneto-mechanical properties of the magnetostrictive sensor?

2. What could improve the magnetic properties during the manufacturing process?

3. Which design is ideal for a sensor?

4. Is a printed magnetostrictive sensor suitable for SHM of aircraft grade CFRP?

Therefore, this work has explored and answered the questions on the effect of printing on magnetoelastic effects on magnetostrictive sensors for each printing method. For example, in chapter 5, it was found that extrusion based printed samples using the DMBD printer showed magnetostrictive properties under bending and on the application of a magnetic field, hence showing the Villari and Joule magnetostriction respectively. Different grid designs with different track spacing showed a difference in their sensing and actuating performance. However, the printing process was unsuitable for sensors

due to warping in the sintering stage limiting the design and thickness of the sensor. Therefore, question 4 could not be answered, as the printing method was unsuitable for SHM of CFRP.

Inkjet printing of magnetostrictive materials was employed to reduce the thickness and weight of the sensor so that the sensor could be used for SHM in CFRP. An off the shelf magnetite NPs ink and the JetLab 4 by Microfab were used to print via the drop on demand technique as shown in chapter 6. The jetting parameters, substrate selection and post processing were configured and optimised to print a sensor best for SHM. It was found that ultra-sonicating and filtering the magnetite ink helped to avoid amalgamation and avoid clogging the nozzle during jetting. Substrates such as photo paper were found to be best at printing metal ink on as it has higher absorption and adhesion due to higher wetting angle than kapton substrate. While kapton film needed to be treated first such as heating to a higher temperature to evaporate the solvent, to avoid a low wetting angle. Post processing of the ink-jet printed samples included heating by UV light and polymer coating. The UV light helped to increase solvent evaporation and curing to maintain print designs. The polymer coating was applied either by spin coating PDMS or spray coating acrylic polymer directly on to the print to protect the sensor from environmental effects.

To measure the Villari effect of the print designs, an inductor was manufactured and used to measure the small changes in magnetic field of the print under strain. This was to test the inkjet printing method and how it affects the magneto-mechanical properties to answer question 1. The printed design was clamped over a bend rig with a known radius of curvature, while the inductor was placed on the top of the print. The result showed that a well-known magnetostrictive material such as metglas had a change in inductance with strain. To answer question 2 and 3, different magnetite and nickel designs were printed including grid, uniaxial patch and coil on photo paper. It was found that the coil design was better as the inductance and strain gradient was found to be higher than other printed designs. In both magnetite and nickel material, the slope of the inductance/strain gradient was found to decrease gradually therefore easier to identify the change in inductance to strain in comparison with other designs. The grid and uniaxial patch showed a near zero gradient in comparison. Whereas the Nickel print showed a greater inductance/ strain gradient in the grid design, however this could be due to the large error in the inductance measurement, therefore magnetite NPs was selected as a sensor for SHM. The printing direction perpendicular to the strain was found to have higher change in gradient than printing in the parallel direction. Additive printing the coil design 10 times was found to have greater inductance/ strain gradient than a single layer of magnetite.

Inductor reliability was tested to improve the signal to noise ratio of the measurement. The coil inductor was tested for a different number of turns of the copper wire. It was found that around 100 coil hand wound were found to have the lowest error and larger gradient change than the 200 and 250 turns coil. However, the signal to noise ratio could be further improved to exploit the use of higher coil turns with

a higher change in inductance to strain gradient. This was achieved by using a capacitor in the circuit, which helped to reduce noise and allowed the use of a 200 turns inductor coil. Coating the magnetite print design with PDMS was found to increase the change in inductance at a lower strain value, then stabilises to the same inductance as the magnetite print without any coating. Therefore, coating magnetite print with PDMS or acrylic would not affect the change in field as a function of strain too much and protect print at the same time. Similar trends are seen with the magnetite coil layered 10 times, however the signal to strain is more erratic than the single layer polymer coated magnetite designs. Controlling and measuring the direction of the magnetic moment of the inkjet-printed magnetite was explored. This was achieved by measuring the inductance at the top and bottom of the magnetite print and controlling the magnetic moment by placing a permanent magnet under the substrate during printing. The inductance measured from the top and bottom showed that the moment was aligned slightly towards the bottom due to higher inductance value but then re-orientate towards the top as the inductance value increased towards the top when higher strain was applied. This means that the moments are aligned in plane when printed and magnetite NP has been absorbed through the paper, which would orientate the moment slightly towards the bottom. By placing a magnet underneath during printing to control the magnetic moment did improve the distribution of magnetite NPs in each droplet, reducing the coffee ring effect; however overall the magnet did not result in good printability, as the coil design failed to print resulting in loss of resolution and definition on the coil structure. Controlling the magnetic moment could be improved in the future by applying a smaller field to improve the printability of magnetite ink.

SHM of CFRP was tested by impact testing to investigate the sensor's performance in a high velocity damage detection. First a polycarbonate sheet was used to test the robustness and reliability of the inductor, placed at 4 or 5 cm away from the impact site. It was found that the inductance peak and change before and after the impact was proportional to the increased weight. The 0.5 kg weight was found to cause significant damage without causing increased error as seen in for 1 kg weight. Different numbers of CFRP layers: 4, 5 and 6 were tested for noise and damage observation. The 4 layered CFRP was found to have greater deformation and penetration than the 5 or 6 layered CFRP without fracture propagation, which was seen in fracture analysis by optical microscope. Printing a magnetite line directly on the CFRP was used to test the magnetite sensor performance by scanning and detecting defects across the CFRP (from the impact site to the edge). In comparison with the empty CFRP sample, the 10 layered magnetite line showed a good change in inductance before and after the impact whereas the single layered magnetite showed a reduction in inductance in both peak and change in inductance before and after impact. It was found that the scan of the magnetite line from the impact had little difference in the change in inductance before and after impact. However, there was a change in inductance peak, before and after the impact on the 10 layered magnetite sensor on 4 layer CFRP sample which could suggest that deformation has occurred but the inductance change over the impact site, did

not change significantly. Therefore, the scan of the magnetite line was found not to be effective in detecting the impact damage and deformation on a 4 layered CFRP. Simulation showed that impact damage on CFRP deforms the layers and applies additional stress/ strain on the magnetite layer, thus changing the field for damage detection. For example, a weight of 0.5 kg caused magnetic field fluctuation for the 4 and 5 layered CFRP whereas a magnetite layer with no CFRP and 6 layered CFRP showed no field fluctuation around the impact site. The mechanism of detecting deformation within the CFRP layers is demonstrated however there is issue in accurate measurement by inductance changes, therefore inkjet printing has shown potential for SHM of CFRP. To answer question 4, inkjet printing magnetite could be used; however, more research is needed to make sure the sensor is reliable and performs well in service.

This project has explored the best route to manufacturing and printing magnetostrictive materials, to exploit the inherent property and mechanism for SHM of CFRP for aircraft or other applications in extreme environments. Even though some methods and measurement used had issues with printability and reliability, this research has shown that there is potential to carry these techniques forward for further improvement. For example, improving data collection over time and alerting the user of the type of damage (bending or impact) which could be done via programmable software or an automated DAQ system for signal processing and online damage detection. Material selection could be improved as printing magnetic materials will be more widely available in the future therefore should improve the resolution and signal to damage detection.

8.2 Future work

8.2.1 Introduction

This project has shown that SHM of CFRP is possible using additive manufactured magnetostrictive materials in simple sensor designs. However, there is still more research that needs to be carried out before being used in service. For example, advancement in additive manufacturing such as developing raw materials at the initiation of the printing process for applications including DMBD or SLM. Inkjet printing has shown that it is possible to be used for SHM however, the reliability and performance of the inkjet-printed magnetostrictive sensor still needs fine tuning. New materials that have shown good response to strain/inductance could be further explored. Further research and development in post treatment and sintering of the 3D printed part would enable control in the microstructure and prevent cracking or warping. Therefore, this would improve the magnetostrictive material's response to external stimuli such as magnetic field or strain, thus improving the sensing and actuating performance. Another research area would be to develop new magnetostrictive materials for additive manufacture. As this

project has shown that while there is some scope for using magnetite for SHM, the response to external stimuli is erratic and would need more work on controlling the signal to noise ratio. Therefore, magnetostrictive materials such as high entropy alloys (HEAs) that have a reduction of rare earth materials show a high magnetostriction constant, that could be developed for AM in the future and will be ideal for sensing and actuating devices.

Another future work is magnetic annealing where controlling the magnetic moment while heating below the Curie temperature (T_c) could improve the magnetostriction constant by re-arrangement of domain and magnetic moment, creating additional strain when field is applied. In theory this technique could be applied to any material in the future, by adjusting the temperature and applied magnetic field. Applying a field during annealing of magnetic materials has shown to increase their magnetic properties. For example, in (Schönrath *et al.*, 2019) they have shown that by applying a field to a 3D printed homogeneous permalloy during annealing, they were able to tune the anisotropy and create a uniaxial anisotropy. Furthermore, it was shown in (Herzer, 2013) that amorphous/ nanocrystalline alloys such as $Fe_{73.5}Cu_1Nb_3Si_{13.5}B_9$ ribbon when subjected to magnetic annealing and showed an improvement in its anisotropy could be tuned to induce directionality in the magnetic moment. If this can be replicated in magnetostrictive material such as metglas (FeCoBSi) then this would be beneficial to be used and tune its performance in the future. SLM or laser based printing can have an effect on grain size and magnetic properties depending on the printing parameters. Amorphous alloys as shown in (Herzer, 2013), have excellent magnetostriction and permeability. Nanocrystalline grain sizes require higher energy to shift domain walls and therefore reduces magnetostriction. Therefore, changing the alloy $Fe_{73.5}\,Cu_1Nb_3Si_{13.5}B_9$ as a function of Si could improve magnetic properties, as zero Si content reduces magnetostriction to zero. This is due to the microstructure phase changes and will be useful for printing alloys that require high magnetostriction constant.

8.2.2 Future additive manufactured magnetostrictive materials

Metglas is a well-known magnetostrictive material as shown in chapter 6.8, which has recently been 3D printed as shown in (Liu *et al.*, 2018) . In this thesis, magnetite was measured to show potential for use in sensor or actuator applications as shown in chapter 6.8, where metglas foil was used to calibrate the inductor for the strain bending measurement (Villari effect). Now that metglas has been developed and is able to be printed on an industrial scale using techniques such as SLM, this means that a change in strain or field can be measured, therefore could be used for future sensing and actuating applications. Metglas has a magnetostriction constant of around 30 ppm, higher than that of stainless steel measured in this project.

Magnetostriction measurement was performed on SLM printed metglas (type 300 for reference). The metglas was printed and measured at the IPCMS research facility in France. The same method was used before when measuring the Joule magnetostriction of stainless steel 17/4 ph by resistance change using

a strain gauge in parallel and perpendicular to the field. The size of the metglas printed was 5 x 10 x 5 mm. The annealing procedure was performed in two ways: conventional (Joule heating) and field annealing. Joule heating was performed by heating via resistive coil and measuring the temperature using a thermocouple attached to the metglas. The metglas was heated to around 600 K for a few seconds before reducing to room temperature as shown in Fig. 8.1. Magnetic annealing was performed in the SQUID magnetometer, the temperature was ramped from room temperature to 400 K at a rate of 0.3 K/s, and under an applied field of 9 T. Magnetostriction was measured before and after heating / annealing.

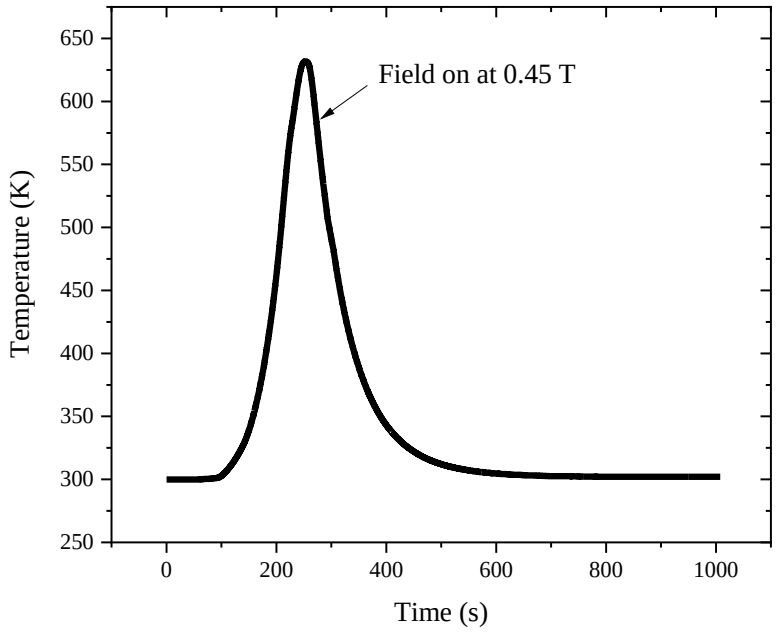

Figure 8.1 3D printed metglas magnetic annealing showing temperature and time at which field was applied

Fig. 8.2 compares the Joule magnetostriction of 3D printed metglas type 300 before and after annealing, showing the change in strain as a function of parallel and perpendicular applied field. For the 3D printed metglas before annealing, the magnetostriction constant is shown to be around 30 ppm. After heating the 3D printed metglas to around 600 K under a magnetic field of 0.45 T (parallel to the build direction), the magnetostriction reduced slightly to 20 ppm and has shown some hysteresis loss, therefore a reduction of magnetostriction has been detected as a result of simple Joule heating under a magnetic field of metglas below the Curie temperature. Fig. 8.3 shows the difference in magnetostriction as Joule heating and magnetic field was applied perpendicular to the build direction. It shows a significant change in strain in the perpendicular direction as a function of the field is changed in comparison with metglas before annealing. The strain has shown an isotropic behaviour in both perpendicular and parallel directions, where the magnetostriction constant is 20 ppm in both directions. This means that

field and annealing in the perpendicular direction has forced a stronger directionality than the original version of metglas. While the magnetostriction reduced in the parallel direction of 10 ppm, the perpendicular direction has shown significant change than before. This could be due to the low field annealing where heating to 600 K has increased grain sizes and reduced stresses and creating a homogeneous structure.

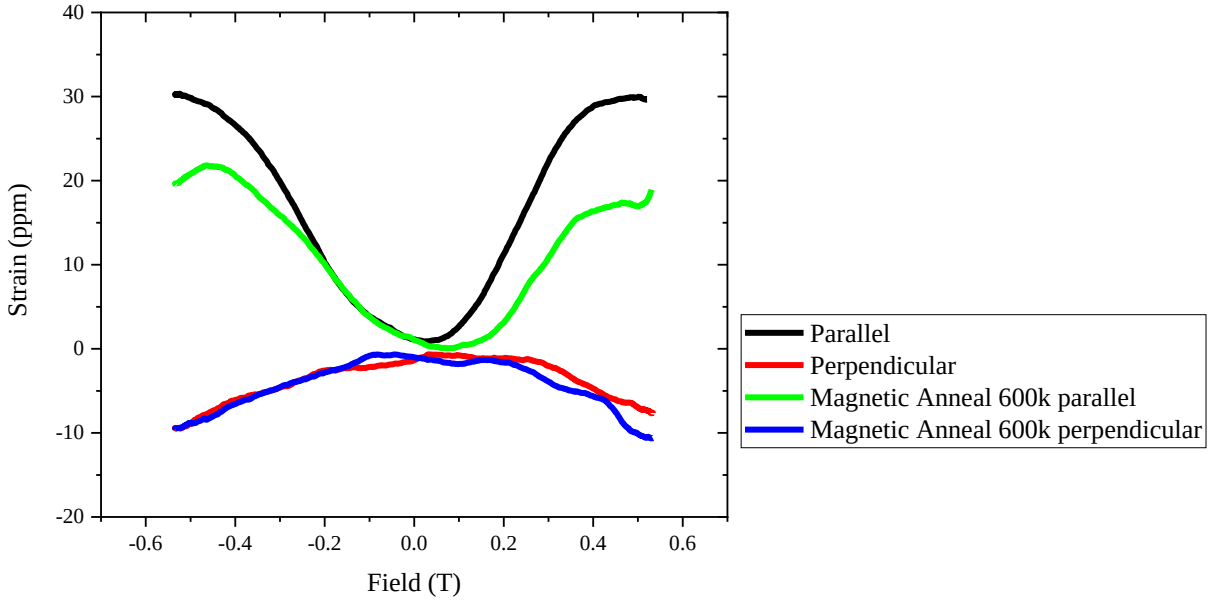

Figure 8.2 3D printed metglas magnetostriction before and after annealing in parallel and perpendicular field direction

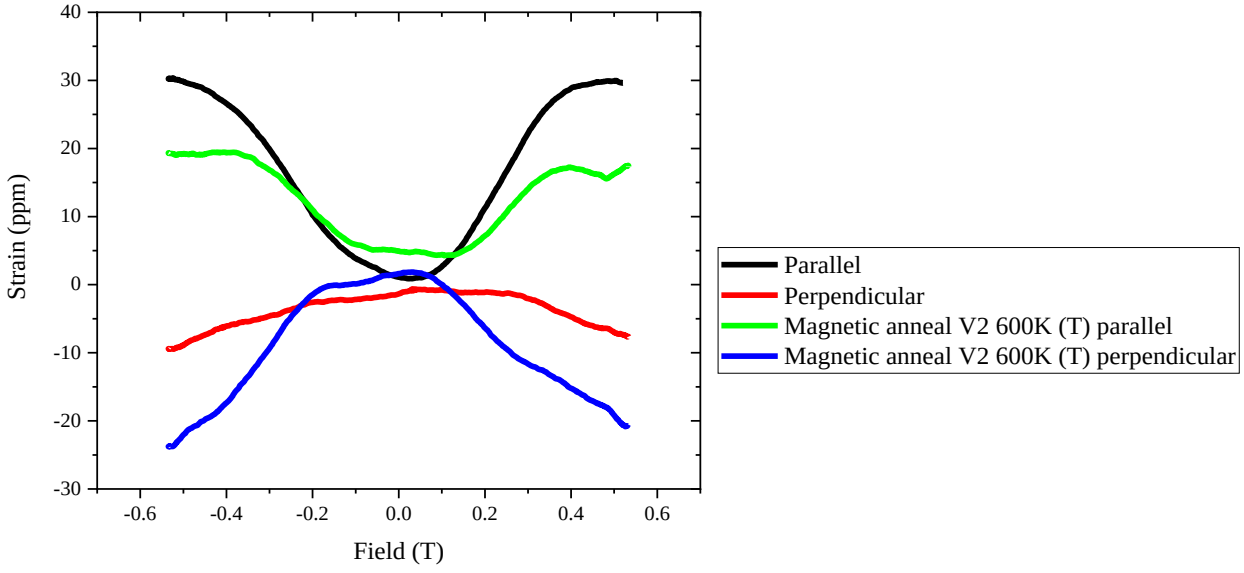

Figure 8.3 Parallel and perpendicular magnetic field direction magnetostriction measurements as a function of magnetic field before and after magnetic annealing (perpendicular to the build direction) for a 3D printed metglas sample

SQUID magnetometer was used to apply a higher field of 6 T and 9 T to see whether the field can rotate the magnetic moment under lower temperatures and increase anisotropy in 3D printed metglas. Fig. 8.4 shows the metglas at 400 K while under 6 T magnetic field in parallel to the build direction. While the results show a slight difference in magnetostriction constant than the original, the increased magnetic field applied was less effective than heating to a higher temperature than at 400K with an applied field of 6 T. The strain parallel to the field formed a broader strain rate as a function of field with a magnetostriction constant 2 ppm less than the original metglas. Whereas the strain in the perpendicular direction showed a greater change in strain with a magnetostriction constant of 5 ppm less than the original version. Fig. 8.5 shows that as the magnetic field is increased to 9T while annealing at 400 K, there is a slight change in strain in the parallel direction where magnetostriction constant has increased to 5 ppm than the original metglas. Similar result is shown when placing the field perpendicular to the field, where the magnetostriction increased by 2 ppm than before.

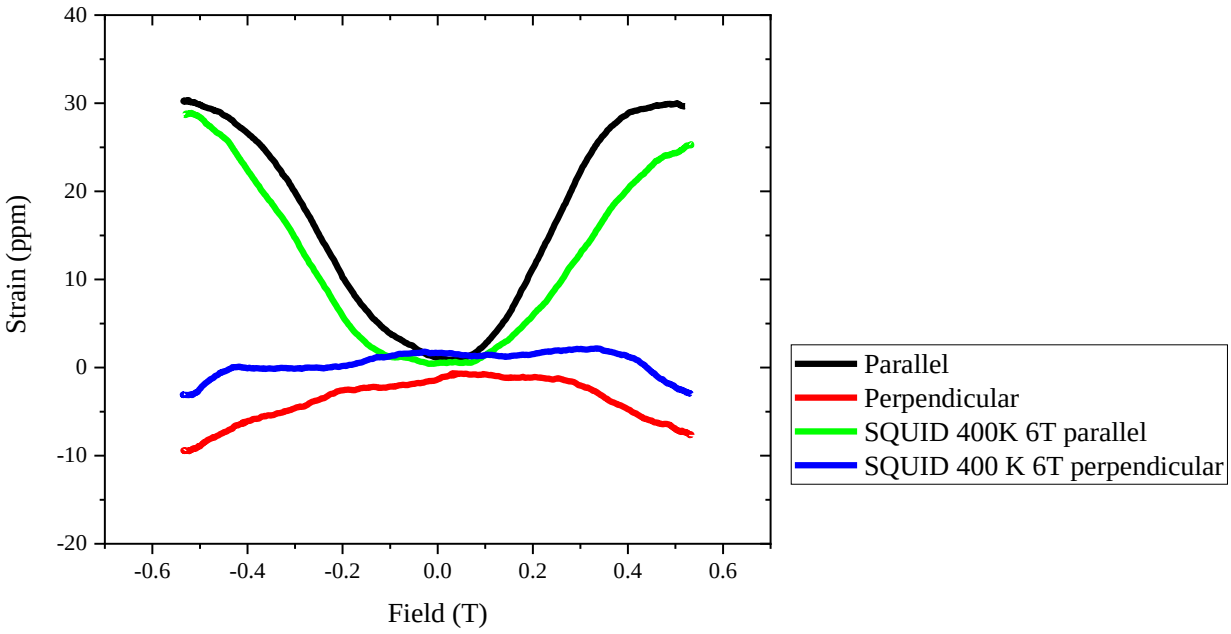

Figure 8.4 3D printed metglas magnetostriction before and after 6T and 400K magnetic annealing in the SQUID magnetometer in parallel and perpendicular direction

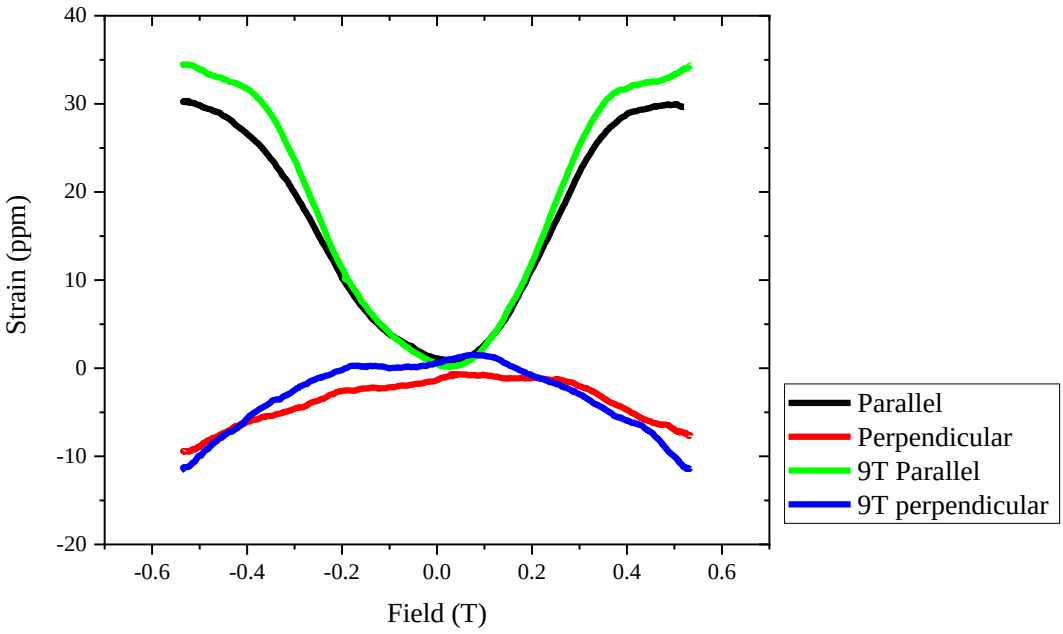

Figure 8.5 3D printed metglas magnetostriction before and after 9T and 400K magnetic annealing in the SQUID magnetometer in parallel and perpendicular direction

Overall it can be said that magnetic annealing does play a role in changing the directionality of the magnetic moment, as shown in Fig. 8.4 and Fig. 8.5. However, a slight improvement on magnetostriction constant was achieved by applying a high magnetic field of 9 T. Further research is needed to increase the temperature beyond 400 K under a high field to see the effect on directionality for 3D printed magnetic materials. Only the temperature and magnetic field direction variables were changed in this work, other variables such as time could be further investigated in the future.

FeGa magnetostrictive materials have been shown to have potential in printing by powder laser bed printing method as seen in (Na, Galuardi and Flatau, 2017). Fig. 8.6 shows magnetostriction measurement of different compositions of FeGa ribbon. While the FeGa ribbons were not printed, it does show that if a thin layer of FeGa is printed using an additive manufacturing technique, the composition of FeGa does have an effect on the magnetostriction constant. $Fe_{79}Ga_{21}$ was shown to have a magnetostriction constant of 50 ppm, higher than other compositions. Although the magnetostriction constant is more than $Fe_{72}Ga_{28}$ which has a higher Ga composition, the magnetostriction saturation in $Fe_{72}Ga_{28}$ takes longer to reach. Therefore, the ideal composition was shown to be $Fe_{79}Ga_{21}$, whereas for $Fe_{19.5}$ $Ga_{17.5}$, the magnetostriction as a function of magnetic field is shown to have less strain gradient (relatively flat). There is a pattern that is present in all the magnetostriction measurements parallel to the field, as there is a sharp increase in strain at low field, which then either stabilises or gently increases. This may be due to the domain wall motion in films and shape effect as the domains are easily orientated

toward the long axis while in the perpendicular field direction the domain wall motion is reduced to near zero magnetostriction. Further analysis is needed such as SEM for microstructural analysis.

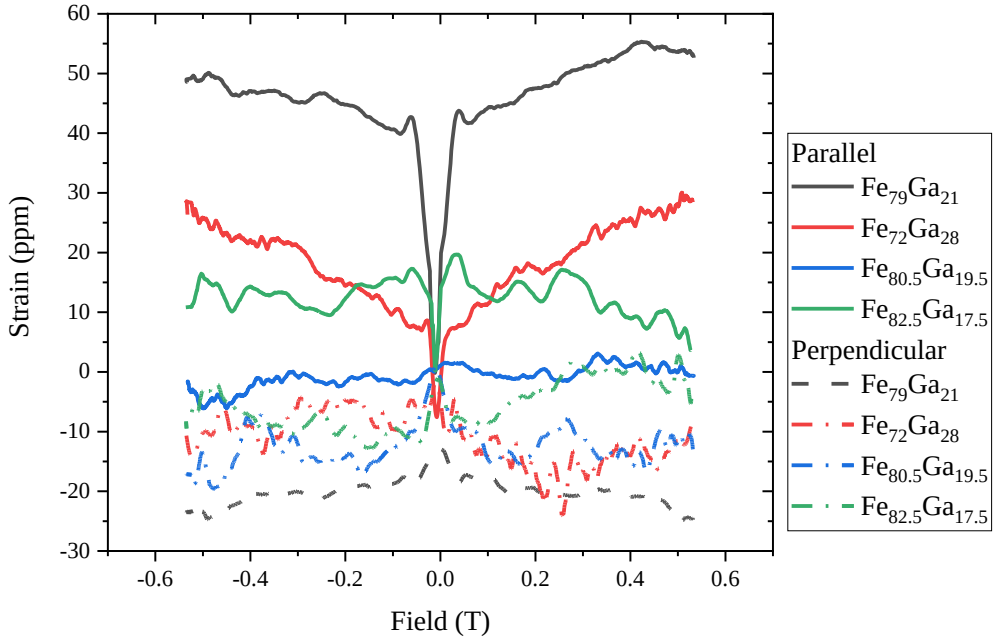

Figure 8.6 FeGa ribbon magnetostriction of different compositions in parallel and perpendicular directions

FeCoNiMo is another magnetostrictive material which could be additive manufactured in the future by laser powder bed technique. Fig. 8.7 shows the magnetostriction of different compositions of FeCoNiMo where transition metals such as Co and Ni are increased and reduction of Fe are tested. Both Co and Ni elements have good magnetostriction values however they are expensive to manufacture at scale (Trading economics, 2023). Therefore, changing the composition of Co ($50 per tonne) and Ni ($30 per tonne) was tested to see the trade off point by obtaining higher magnetostriction at low cost. It was found that the addition of Ni and Co increases the magnetostriction compared to the composition with higher Fe content. The $Fe_{88}Co_9Ni_0Mo_5$ has the lowest magnetostriction constant of around 20 ppm which is not ideal as stainless steel in the project had better magnetostriction than this. The addition of Ni and a reduction of Co content in $Fe_{77}Co_0Ni_{18}Mo_5$ has increased the magnetostriction to around 27 ppm. However, increasing both Co and Ni composition amplifies the magnetostriction to around 40 ppm. Therefore, the work has shown the effects of adding and removing Co and Ni content thus reducing expensive and resource limited material.

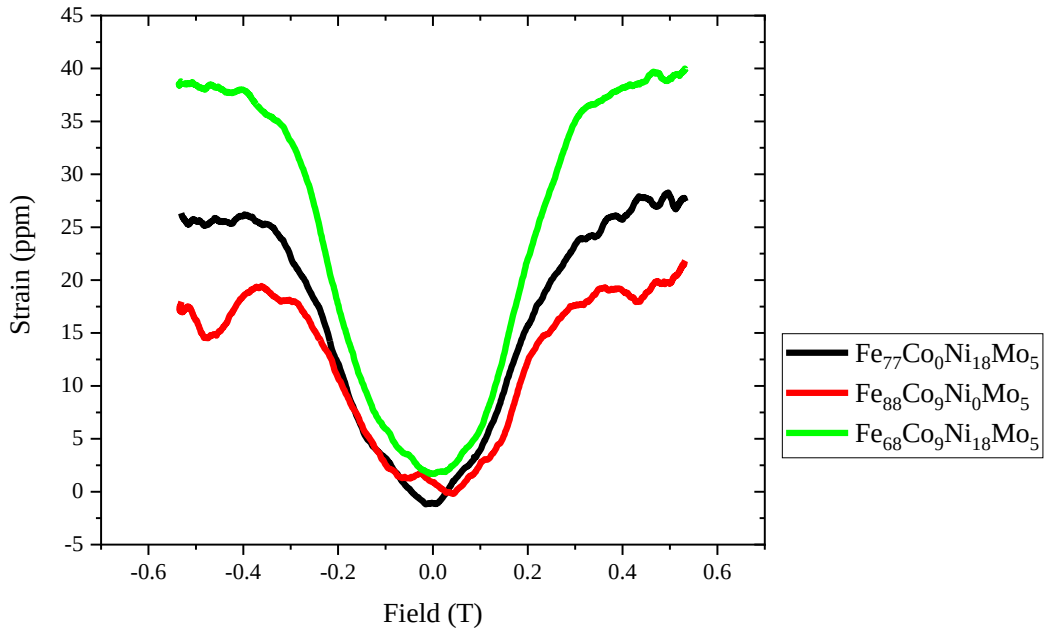

Figure 8.7 FeCoNiMo magnetostriction of different composition in parallel and perpendicular directions

The outlook of developing a better magnetostrictive material for SHM or actuators looks promising as magnetic annealing has shown that manipulation by field annealing can cause changes in the direction of magnetic moments even though the magnitude of magnetostriction was the same in parallel and perpendicular within metglas was observed. Therefore, further development such as higher field and temperature could improve the moment directionality and anisotropy in the future as seen in metglas type 300. FeGa ribbon has shown to have magnetostriction that is composition dependent and large increases in strain at lower applied fields. The difference in thin AM structure and ribbon manufactured FeGa magnetostriction could be interesting to observe in the future. Manipulating Co and Ni content in FeCoNiMo has shown to increase or reduce magnetostriction depending on the composition. This could be useful for developing sensors or actuators that have elements that are expensive or in limited supply, therefore tailoring sensors or actuators in various applications. Therefore, all of these materials have shown potential to be tailored by improving magnetostriction via composition, field annealing and printing therefore opens an exciting area for developing sensors and actuators in the future.

9 References

Abert, C. (2013) *Discrete Mathematical Concepts in Micromagnetic Computations*. Staats- und Universitätsbibliothek Hamburg Carl von Ossietzky. Available at: https://ediss.sub.uni-hamburg.de/handle/ediss/5161 (Accessed: 20 March 2023).

Abert, C. (2021) *Micromagnetism*. Available at: http://micromagnetics.org/micromagnetism/#mjx-eqn-eqllg_explicit (Accessed: 20 March 2023).

Ahmed, N., Deffley, R., Kundys, B. and Morley, N.A. (2023) '3D printing of magnetostrictive property in 17/4 ph stainless steel', *Journal of Magnetism and Magnetic Materials*, 585, p. 171115. Available at: https://doi.org/10.1016/j.jmmm.2023.171115.

Al-Milaji, K.N., Hadimani, R.L., Gupta, S., Pecharsky, V.K. and Zhao, H. (2019) 'Inkjet Printing of Magnetic Particles Toward Anisotropic Magnetic Properties', *Scientific Reports*, 9(1). Available at: https://doi.org/10.1038/s41598-019-52699-0.

Al-Qudsi, A., Kammler, M., Bouguecha, A., Bonk, C. and Behrens, B.A. (2014) 'Comparison between different numerical models of densification during solid-state sintering of pure aluminium powder', *Production Engineering*, 9(1), pp. 11–24. Available at: https://doi.org/10.1007/s11740-014-0574-7.

Al-Taher, A., Reiss, R.W., Lafferty, A.D., Hayes, S.A., Lupu, N., Murgulescu, I. and Morley, N.A. (2017) 'Magnetostrictive Materials for aerospace applications', *Journal of Physics: Conference Series*, 903(1). Available at: https://doi.org/10.1088/1742-6596/903/1/012010.

Alenia Aeronautica (2009) *Induction Heating and Health Monitoring Solutions for Smart Aircraft Maintenance using Adapted Composite Patches*. Available at: https://doi.org/http://cleansky.eu/sites/default/files/documents/Activities/GRA1/INDUCER.pdf.

Altay, B.N. (2018) 'Development and Characterization of Nano Nickel-Based Conductive Inks for Flexographic Printing of Electronics and New Interpretations of Surface Energies of Solids'.

Amafabia, Daerefa-a Mitsheal Montalvão, D., David-West, O. and Haritos, G. (2017) 'A Review of Structural Health Monitoring Techniques as Applied to Composite Structures', *Structural Durability & Health Monitoring*, 11(2), pp. 91–147.

Andò, B. and Marletta, V. (2016) 'An all-Inkjet Printed bending actuator with embedded sensing feature and an electromagnetic driving mechanism', *Actuators*, 5(3). Available at:

https://doi.org/10.3390/act5030021.

Ara, K. (1989) ‘Magnetic Characteristics of Ferromagnetic Stainless Steels’, *IEEE Transactions on Magnetics*, 25(3), pp. 2617–2623. Available at: https://doi.org/10.1109/20.24500.

Ara, K., Yamada, M., Kakuta, T. and Yamagishi, H. (1986) ‘Magnetic characteristics of ferromagnetic stainless steels, SUS 403, SUS 410J1, TAF and SUS 405’, *Japan Atomic Energy Research Inst*, 18(14). Available at: https://inis.iaea.org/search/search.aspx?orig_q=RN:18060028 (Accessed: 10 April 2022).

Archer, E. and McIlhagger, A. (2014) ‘Repair of damaged aerospace composite structures’, in *Polymer Composites in the Aerospace Industry*. Available at: https://doi.org/10.1016/B978-0-85709-523-7.00014-1.

Artero-Guerrero, J.A., Pernas-Sánchez, J., López-Puente, J. and Varas, D. (2014) ‘On the influence of filling level in CFRP aircraft fuel tank subjected to high velocity impacts’, *Composite Structures*, 107, pp. 570–577. Available at: https://doi.org/10.1016/J.COMPSTRUCT.2013.08.036.

B.D.Cullity and C.D.Graham (2009) *Introduction to magnetic materials*. Second Edi. Edited by L. Hanzo. John Wiley & Sons, Inc.

Bakker, H.L.M. (1989) ‘Magnetostriction of duplex stainless steels’, *Materials Science and Technology (United Kingdom)*, 5(11), pp. 1135–1139. Available at: https://doi.org/10.1179/mst.1989.5.11.1135.

Bakker, H.L.M. (2013) ‘Materials Science and Technology Magnetostriction of duplex stainless steels Magnetostriction of duplex stainless steels’. Available at: https://doi.org/10.1179/mst.1989.5.11.1135.

Benyelloul, K. and Aourag, H. (2013) ‘Elastic constants of austenitic stainless steel: Investigation by the first-principles calculations and the artificial neural network approach’, *Computational Materials Science*, 67, pp. 353–358. Available at: https://doi.org/10.1016/j.commatsci.2012.09.005.

Bertotti, G. (1998) ‘Maxwell’s Equations in Magnetic Media’, in *Hysteresis in Magnetism*. Elsevier, pp. 73–102. Available at: https://doi.org/10.1016/B978-012093270-2/50052-0.

Breen, C., Guild, F. and Pavier, M. (2005) ‘Impact of thick CFRP laminates: the effect of impact velocity’, *Composites Part A: Applied Science and Manufacturing*, 36(2), pp. 205–211. Available at: https://doi.org/10.1016/j.compositesa.2004.06.005.

Bruker (2020) *An Overview of Surface Roughness Measurements: Choice of Technique and Analysis | Bruker*. Available at: https://www.bruker.com/en/news-and-events/webinars/2020/an-overview-of-surface-roughness-measurements-choice-of-technique-and-analysis.html (Accessed: 29 July 2022).

Budhe, S., Banea, M.D. and de Barros, S. (2018) ‘Bonded repair of composite structures in aerospace application: a review on environmental issues’, *Applied Adhesion Science*. Springer International Publishing. Available at: https://doi.org/10.1186/s40563-018-0104-5.

Cabrera, L., Gutierrez, S., Menendez, N., Morales, M.P. and Herrasti, P. (2008) ‘Magnetite nanoparticles: Electrochemical synthesis and characterization’, *Electrochimica Acta*, 53(8), pp. 3436–3441. Available at: https://doi.org/10.1016/j.electacta.2007.12.006.

Calkins, F.T., Flatau, A.B. and Dapino, M.J. (2007) ‘Overview of magnetostrictive sensor technology’, *Journal of Intelligent Material Systems and Structures*, 18(10), pp. 1057–1066. Available at: https://doi.org/10.1177/1045389X06072358.

Cawley, P. and Adams, R.D. (1988) ‘The mechanics of the coin-tap method of non-destructive testing’, *Topics in Catalysis*, 122(2), pp. 299–316. Available at: https://doi.org/10.1016/S0022-460X(88)80356-0.

Chaudhary, V., Mantri, S.A., Ramanujan, R.V. and Banerjee, R. (2020) ‘Additive manufacturing of magnetic materials’, *Progress in Materials Science*, 114, p. 100688. Available at: https://doi.org/10.1016/j.pmatsci.2020.100688.

Chen, S.-P., Chiu, H.-L., Wang, P.-H. and Liao, Y.-C. (2015) ‘JSS focus issue on printable functional materials for electronics and energy applications inkjet printed conductive tracks for printed electronics’, *ECS Journal of Solid State Science and Technology*, 4(4), pp. 3026–3033. Available at: https://doi.org/10.1149/2.0061504jss.

Christopoulos, A., Hristoforou, E., Koulalis, I. and Tsamasphyros, G. (2014) ‘Inductive strain sensing using magnetostrictive wires embedded in carbon fibre laminates’, *Smart Materials and Structures*, 23(8). Available at: https://doi.org/10.1088/0964-1726/23/8/085035.

Clark, A.E., Wun-Fogle, M., Restorff, J.B., Dennis, K.W., Lograsso, T.A. and McCallum, R.W. (2005) ‘Temperature dependence of the magnetic anisotropy and magnetostriction of Fe 100-xGa x (x=8.6, 16.6, 28.5)’, in *Journal of Applied Physics*, pp. 10–316. Available at: https://doi.org/10.1063/1.1856731.

Dapino, M.J. (2002) ‘Magnetostrictive Materials’, in *Encyclopedia of Smart Materials*. John Wiley & Sons, Inc. Available at: https://doi.org/10.1002/0471216275.esm051.

Dapino, M.J. (2004) ‘On magnetostrictive materials and their use in adaptive structures’, *Structural Engineering and Mechanics*, 17(4).

Datta, A., Nathasingh, D., Martis, R.J., Flanders, P.J. and Graham, C.D. (1984) ‘Saturation and

engineering magnetostriction of an iron-base amorphous alloy for power applications', *Journal of Applied Physics*, 55(6), pp. 1784–1786. Available at: https://doi.org/10.1063/1.333477.

Datta, S. (2013) *Modeling Magnetostriction Using COMSOL Multiphysics® | COMSOL Blog*, *COMSOL Blog*. Available at: https://uk.comsol.com/blogs/modeling-magnetostriction-using-comsol/ (Accessed: 5 June 2020).

Deepak Dixit, D. and Pattamatta, A. (2019) 'Effect of uniform external magnetic-field on natural convection heat transfer in a cubical cavity filled with magnetic nano-dispersion'. Available at: https://doi.org/10.1016/j.ijheatmasstransfer.2019.118828.

Desktop Metal (2018) *17-4 PH stainless steel data sheet*. Available at: https://www.desktopmetal.com/uploads/Studio-MDS-17-4-PH-stainless-steel.pdf.

DoITPoMS- University of Cambridge (2004) *Ferromagnetic Materials - Types of magnetism*, *TLP Library*. Available at: https://www.doitpoms.ac.uk/tlplib/ferromagnetic/domains.php?printable=1 (Accessed: 12 September 2020).

Downey, P.R. and Flatau, A.B. (2006) 'Bending of iron-gallium (Galfenol) alloys for sensor applications', in *Materials Research Society Symposium Proceedings*, pp. 341–346. Available at: https://doi.org/10.1557/proc-0888-v06-11.

Drahansky, M., Paridah, M.., Moradbak, A., Mohamed, A.., Owolabi, F. abdulwahab taiwo, Asniza, M. and Abdul Khalid, S.H.. (2016) 'Structural Health Monitoring for Composite Materials', *Intech*, i(tourism), p. 13. Available at: https://doi.org/http://dx.doi.org/10.5772/57353.

Duc, N.H. and Brommer, P.E. (2014) 'Magnetoelasticity in rare earth – transition metal thin films and nanoscale heterogeneous magnetic materials', in N.H. Duc (ed.) *Advanced Magnetism and Magnetic Materials*. Hanoi: Vietnam National University Press, pp. 271–418.

Ekreem, N.B., Olabi, A.G., Prescott, T., Rafferty, A. and Hashmi, M.S.J. (2007) 'An overview of magnetostriction, its use and methods to measure these properties', *Journal of Materials Processing Technology*, 191(1–3), pp. 96–101. Available at: https://doi.org/10.1016/j.jmatprotec.2007.03.064.

Elhajjar, R., Law, C.-T. and Pegoretti, A. (2018) 'Magnetostrictive polymer composites: Recent advances in materials, structures and properties', *Progress in Materials Science*, 97, pp. 204–229. Available at: https://doi.org/10.1016/j.pmatsci.2018.02.005.

FBGS (2020) *FBG Principle - FBGS*. Available at: https://fbgs.com/technology/fbg-principle/ (Accessed: 27 January 2020).

Flatau, A.B. (2019) 'Overview of magnetostrictive materials and their use in devices (Conference

Presentation)', in H.E. Naguib (ed.) *Behavior and Mechanics of Multifunctional Materials XIII*. SPIE, p. 28. Available at: https://doi.org/10.1117/12.2518375.

Gasparin, E., Santi, G. and Nussbaumer, A. (2018) 'Eddy Current Crack Monitoring System for Structural Health Monitoring (SHM) Applications', in *68th Int. Inst. Weld. Annu. Assem. Int. Conf*, pp. 1084–1090.

Geng, J., Nlebedim, I.C., Besser, M.F., Simsek, E. and Ott, R.T. (2016) 'Bulk Combinatorial Synthesis and High Throughput Characterization for Rapid Assessment of Magnetic Materials: Application of Laser Engineered Net Shaping (LENS^{TM})', *Jom*, 68(7), pp. 1972–1977. Available at: https://doi.org/10.1007/s11837-016-1918-x.

Giannakeas, I.N., Khodaei, Z.S. and Aliabadi, M.H.F. (2022) 'Structural Health Monitoring Cost Estimation of a Piezosensorized Aircraft Fuselage', *Sensors*, 22(5). Available at: https://doi.org/10.3390/s22051771.

Gilbert, T.L. (2004) 'A phenomenological theory of damping in ferromagnetic materials', *IEEE Transactions on Magnetics*, 40(6), pp. 3443–3449. Available at: https://doi.org/10.1109/TMAG.2004.836740.

Goll, D., Schuller, D., Martinek, G., Kunert, T., Schurr, J., Sinz, C., Schubert, T., Bernthaler, T., Riegel, H. and Schneider, G. (2019) 'Additive manufacturing of soft magnetic materials and components', *Additive Manufacturing*, 27, pp. 428–439. Available at: https://doi.org/10.1016/j.addma.2019.02.021.

Grabham, N.J., Beeby, S.P. and White, N.M. (2001) *The formulation and processing of a thick-film magnetostrictive material Related content The formulation and processing of a thick-film magnetostrictive material, Meas. Sci. Technol.*

Grabham, N.J., White, N.M. and Beeby, S.P. (2000) 'Thick-film magnetostrictive material for MEMS', 36(4). Available at: https://doi.org/10.1049/el:20000264.

Grössinger, R., Turtelli, R.S. and Mehmood, N. (2014) 'Materials with high magnetostriction', *IOP Conference Series: Materials Science and Engineering*, 60(1). Available at: https://doi.org/10.1088/1757-899X/60/1/012002.

Grunwald, A. (2007) *Design and optimization of a magnetostrictive actuator*. Dublin City University. Available at: https://doi.org/54149941.

Güemes, A., Fernandez-Lopez, A., Pozo, A.R. and Sierra-Pérez, J. (2020) 'Structural Health Monitoring for Advanced Composite Structures: A Review', *Journal of Composites Science*, 4(1), p.

13. Available at: https://doi.org/10.3390/jcs4010013.

Gullapalli, A., Beedasy, V., Vincent, J.D.S., Leong, Z., Smith, P. and Morley, N. (2021) 'Flat Inkjet-Printed Copper Induction Coils for Magnetostrictive Structural Health Monitoring: A Comparison with Bulk Air Coils and an anisotropic magnetoresistive sensor (AMR) Sensor', *Advanced Engineering Materials*, p. 2100313. Available at: https://doi.org/10.1002/ADEM.202100313.

Gulmine, J. V., Janissek, P.R., Heise, H.M. and Akcelrud, L. (2002) 'Polyethylene characterization by FTIR', *Polymer Testing*, 21(5), pp. 557–563. Available at: https://doi.org/10.1016/S0142-9418(01)00124-6.

Hamad, A., Archacki, A. and Mian, A. (2020) 'Characteristics of nanosilver ink (UTDAg) microdroplets and lines on polyimide during inkjet printing at high stage velocity', *Materials Advances*, 1(1), pp. 99–107. Available at: https://doi.org/10.1039/d0ma00048e.

Hayward, T. (2019) 'MAT 4111/6390 Lecture 1: Introduction to Magnetic Materials'. Sheffield: University of Sheffield.

Health and Safety Executive (2015) *Inspection/Non Destructive Testing*. Available at: https://www.hse.gov.uk/comah/sragtech/techmeasndt.htm#ProcessManagement (Accessed: 28 January 2020).

Herzer, G. (2013) 'Modern soft magnets: Amorphous and nanocrystalline materials', *Acta Materialia*, 61(3), pp. 718–734. Available at: https://doi.org/10.1016/J.ACTAMAT.2012.10.040.

Honeywell (2018) *Hall effect sensing and application, Micro switch sensing and control*. Illinois: Honeywell Inc. Available at: https://sensing.honeywell.com/hallbook.pdf (Accessed: 31 May 2020).

Hristoforou, E. and Ktena, A. (2007) 'Magnetostriction and magnetostrictive materials for sensing applications', *Journal of Magnetism and Magnetic Materials* [Preprint]. Available at: https://doi.org/10.1016/j.jmmm.2007.03.025.

Hsiao, C.N., Chiou, C.S. and Yang, J.R. (2002) 'Aging reactions in a 17-4 PH stainless steel', *Materials Chemistry and Physics*, 74, pp. 134–142.

Hubert, A., Calchand, N., Gorrec, Y. Le and Gauthier, J.-Y. (2012) 'Magnetic Shape Memory Alloys as smart materials for micro-positioning devices', in *Advanced Electromagnetics Symposium, AES'12*. Paris, France: TELECOM PARISTECH, pp. 1–10. Available at: https://doi.org/hal-00720674.

James, C.J., Mulcahy, D.E. and Steel, B.J. (1984) 'Viscometer calibration standards: viscosities of water between 0 and 60 "C and of selected aqueous sucrose solutions at 25 "C from measurements with a flared capillary viscometer', *Journal of Physics D: Applied Physics*, 17, pp. 225–230.

Jhong, K.J., Huang, W.C. and Lee, W.H. (2016) ‘Microstructure and magnetic properties of magnetic material fabricated by selective laser melting’, in *Physics Procedia*. Available at: https://doi.org/10.1016/j.phpro.2016.08.084.

Jiao, S., Cheng, L., Li, X., Li, P. and Ding, H. (2016) ‘Monitoring fatigue cracks of a metal structure using an eddy current sensor’, *Eurasip Journal on Wireless Communications and Networking*, 2016(1), p. 188. Available at: https://doi.org/10.1186/s13638-016-0689-y.

Jones, N.J., Yoo, J.H., Ott, R.T., Lambert, P.K., Petculescu, G., Simsek, E., Schlagel, D. and Lograsso, T.A. (2018) ‘Magnetostrictive performance of additively manufactured CoFe rods using the LENSTM system’, *AIP Advances*, 8(5), p. 56403. Available at: https://doi.org/10.1063/1.5007673.

Jung, M.R., David Horgen, F., Orski, S. V, Rodriguez, V., Beers, K.L., Balazs, G.H., Jones, T.T., Work, T.M., Brignac, K.C., Royer, S.-J., David Hyrenbach, K., Jensen, B.A. and Lynch, J.M. (2018) ‘Validation of ATR FT-IR to identify polymers of plastic marine debris, including those ingested by marine organisms’, *Marine Pollution Bulletin*, 127, pp. 704–716. Available at: https://doi.org/10.1016/j.marpolbul.2017.12.061.

Khan, U.S., Rahim, A., Khan, N., Muhammad, N., Rehman, F., Ahmad, K. and Iqbal, J. (2017) ‘Aging study of the powdered magnetite nanoparticles’, *Materials Chemistry and Physics*, 189, pp. 86–89. Available at: https://doi.org/10.1016/J.MATCHEMPHYS.2016.12.047.

Khatri, B., Lappe, K., Noetzel, D., Pursche, K. and Hanemann, T. (2018) ‘A 3D-printable polymer-metal soft-magnetic functional composite-development and characterization’, *Materials*, 11(2). Available at: https://doi.org/10.3390/ma11020189.

Kobayashi, M. and Mochizuki, M. (2019) ‘Theory of magnetism-driven negative thermal expansion in inverse perovskite antiferromagnets’, *Physical Review Materials*, 3(2), p. 024407. Available at: https://doi.org/10.1103/PhysRevMaterials.3.024407.

Kohl, M., Gueltig, M., Pinneker, V., Yin, R., Wendler, F. and Krevet, B. (2014) ‘Magnetic shape memory microactuators’, *Micromachines*, 5(4), pp. 1135–1160. Available at: https://doi.org/10.3390/mi5041135.

Kolchanov, D.S., Slabov, V., Keller, K., Sergeeva, E., Zhukov, M. V., Drozdov, A.S. and Vinogradov, A. V. (2019) ‘Sol-gel magnetite inks for inkjet printing’, *Journal of Materials Chemistry C*, 7(21), pp. 6426–6432. Available at: https://doi.org/10.1039/c9tc00311h.

Komagome, R., Katabira, K., Kurita, H. and Narita, F. (2022) ‘Characteristics of carbon fiber reinforced polymers embedded with magnetostrictive Fe–Co wires at room and high temperatures’, *Composites Science and Technology*, 228(July), p. 109644. Available at:

https://doi.org/10.1016/j.compscitech.2022.109644.

de Laire, A. (2020) *The Landau-Lifshitz equation and related models*. Available at: https://hal.science/tel-02985356 (Accessed: 20 March 2023).

de Laire, A. (2022) 'Recent results for the Landau–Lifshitz equation', *SeMA Journal*, 79(2), pp. 253–295. Available at: https://doi.org/10.1007/S40324-021-00254-1/FIGURES/4.

Landau, L. and Lifshitz, E. (1935) 'On the theory of the dispersion of magnetic permeability in ferromagnetic bodies', *Phys. Zeitsch. der Sow*, 8, pp. 153–169.

Lee, E.W. (1955) 'Magnetostriction and magnetomechanical effects', *Reports on Progress in Physics*, pp. 184–229. Available at: https://doi.org/10.1088/0034-4885/18/1/305.

Leong, Z., Chan, L., Walters, N., Clarke, J., Holmes, W. and Hayes, S. (2018) 'Structural health monitoring using magnetostrictive sensors', in *2018 IEEE International Magnetic Conference, INTERMAG 2018*. Singapore: IEEE, p. 6. Available at: https://doi.org/10.1109/INTMAG.2018.8508360.

Leong, Z., Holmes, W., Clarke, J., Padki, A., Hayes, S. and Morley, N.A. (2019) 'Magnetostrictive Sensors for Composite Damage Detection and Wireless Structural Health Monitoring', *IEEE Transactions on Magnetics*, 55(7), pp. 1–6. Available at: https://doi.org/10.1109/TMAG.2019.2899537.

Li, D., Sutton, D., Burgess, A., Graham, D. and Calvert, P.D. (2009) 'Conductive copper and nickel lines via reactive inkjet printing', *Journal of Materials Chemistry*, 19(22), pp. 3719–3724. Available at: https://doi.org/10.1039/b820459d.

Liu, L., Ding, C., Lu, S., Ge, T., Yan, Y., Mei, Y., Ngo, K.D.T. and Lu, G.Q. (2018) 'Design and Additive Manufacturing of Multipermeability Magnetic Cores', *IEEE Transactions on Industry Applications*, 54(4), pp. 3541–3547. Available at: https://doi.org/10.1109/TIA.2018.2819963.

Liu, X., Tarn, T.-J., Huang, F. and Fan, J. (2015) 'Recent advances in inkjet printing synthesis of functional metal oxides', *Particuology*, 19, pp. 1–13. Available at: https://doi.org/10.1016/j.partic.2014.05.001.

Liu, Y. and Derby, B. (2019) 'Experimental study of the parameters for stable drop-on-demand inkjet performance', *Physics of Fluids*, 31(3), p. 032004. Available at: https://doi.org/10.1063/1.5085868.

Ludwig, A. and Quandt, E. (2000) 'Giant magnetostrictive thin films for applications in microelectromechanical systems (invited)', *Journal of Applied Physics*, 87(9 II), pp. 4691–4695. Available at: https://doi.org/10.1063/1.373132.

Mabon, J., Swiech, W., Zhou, H., Chen, C. and Wang, J. (2017) *An Introduction to Scanning Electron Microscopy and Focused Ion Beams, Advanced Materials Characterization*. Illinois.

Mahajan, C., Alfadhel, A., Irving, M., Kahn, B., Borkholder, D., Williams, S. and Cormier, D. (2019) 'Magnetic Field Patterning of Nickel Nanowire Film Realized by Printed Precursor Inks', *Materials*, 12(6), p. 928. Available at: https://doi.org/10.3390/ma12060928.

Mandache, C., Lapointe, J. and Genest, M. (2016) *Mounted Eddy Current Sensors for Monitoring Structural Degradation*.

Marjanović, N., Chiolerio, A., Kus, M., Ozel, F., Tilki, S., Ivanović, N., Rakočević, Z., Andrić, V., Barudžija, T. and Baumann, R.R. (2014) 'Magnetite nanoparticles: Synthesis, thin film properties and inkjet printing of magnetic cores for inductor applications', *Thin Solid Films*, 570(PartA), pp. 38–44. Available at: https://doi.org/10.1016/j.tsf.2014.09.002.

Matrix Inspection and Engineering Services (2017) *Non-Destructive Testing*. Available at: https://doi.org/10.9773/sosei.53.631.

McHugh, W. (2011) *Properties of Nickel as a Magnetostrictive Material for Ultrasonic Conditions*.

Mikler, C. V., Chaudhary, V., Borkar, T., Soni, V., Jaeger, D., Chen, X., Contieri, R., Ramanujan, R. V. and Banerjee, R. (2017) 'Laser Additive Manufacturing of Magnetic Materials', *Jom*, 69(3), pp. 532–543. Available at: https://doi.org/10.1007/s11837-017-2257-2.

Mohaideen, K.K. and Joy, P.A. (2014) 'Studies on the effect of sintering conditions on the magnetostriction characteristics of cobalt ferrite derived from nanocrystalline powders', *Journal of the European Ceramic Society*, 34, pp. 677–686. Available at: https://doi.org/10.1016/j.jeurceramsoc.2013.09.018.

Moskowitz, B.M. (1991) 'Hitchhiker's Guide to Magnetism', *Environmental Magnetism Workshop*, 279(1), p. 48. Available at: https://doi.org/10.1038/nm1005-1051.

Mostafaei, A., Kimes, K.A., Stevens, E.L., Toman, J., Krimer, Y.L., Ullakko, K. and Chmielus, M. (2017) 'Microstructural evolution and magnetic properties of binder jet additive manufactured Ni-Mn-Ga magnetic shape memory alloy foam', *Acta Materialia*, 131, pp. 482–490. Available at: https://doi.org/10.1016/j.actamat.2017.04.010.

Na, S., Galuardi, J.D. and Flatau, A.B. (2017) 'Consolidation of magnetostrictive (001)-oriented Fe-Ga flakes for 3D printing powder materials', *2017 IEEE International Magnetics Conference, INTERMAG 2017*, 53(11), pp. 18–21. Available at: https://doi.org/10.1109/INTMAG.2017.8007895.

Nandakumar, A.P. (2019) *Low Cost Metal Additive Manufacturing by Extrusion using Metal Injection*

Moulding Principles.

Nave, C.R. (2000a) *Hydrogen Fine Structure*. Available at: http://hyperphysics.phy-astr.gsu.edu/hbase/quantum/hydfin.html (Accessed: 15 September 2020).

Nave, C.R. (2000b) *Magnetic forces*. Available at: http://hyperphysics.phy-astr.gsu.edu/hbase/magnetic/magfor.html (Accessed: 7 February 2022).

Nave, C.R. (2000c) *Zeeman effect*. Available at: https://doi.org/10.1007/springerreference_30974.

Nayak, L., Mohanty, S., Nayak, S.K. and Ramadoss, A. (2019) 'A review on inkjet printing of nanoparticle inks for flexible electronics', *Journal of Materials Chemistry C*, 7(29), pp. 8771–8795. Available at: https://doi.org/10.1039/c9tc01630a.

O'Handley, R.C. (1999) *Modern magnetic materials principles and applications*. Canada: John Wiley and Sons Inc.

O'Heir, J. (2018) *3D Printing a Future of New Metal Actuators, The American Society of Mechanical Engineers*. Available at: https://www.asme.org/topics-resources/content/3d-printing-future-new-metal-actuators (Accessed: 6 January 2020).

Olabi, A.G. and Grunwald, A. (2008) 'Design and application of magnetostrictive materials', *Materials and Design*, 29(2), pp. 469–483. Available at: https://doi.org/10.1016/j.matdes.2006.12.016.

Olympus (2017) *Ultrasonic Testing FAQ | Olympus IMS, Olympus*. Available at: https://www.olympus-ims.com/en/knowledge/ultrasound/applications/ultrasonic-faq/ (Accessed: 28 January 2020).

Páez-Pavón, A., Jiménez-Morales, A., Rodriguez-Arbaizar, M., Carreño-Morelli, E. and Torralba, J.M. (2017) 'Powder Metallurgy Sintering optimisation of Fe-Si soft magnetic materials processed by metal injection moulding Sintering optimisation of Fe-Si soft magnetic materials processed by metal injection moulding'. Available at: https://doi.org/10.1080/00325899.2017.1289631.

Park, B.K., Kim, D., Jeong, S., Moon, J. and Kim, J.S. (2007) 'Direct writing of copper conductive patterns by ink-jet printing', *Thin Solid Films*, 515(19 SPEC. ISS.), pp. 7706–7711. Available at: https://doi.org/10.1016/J.TSF.2006.11.142.

Park, S.H. and Kim, H.S. (2014) 'Flash light sintering of nickel nanoparticles for printed electronics', *Thin Solid Films*, 550, pp. 575–581. Available at: https://doi.org/10.1016/j.tsf.2013.11.075.

Pasquarelli, R., Curtis, C. and Hest, M. Van (2008) 'Inkjet printing of nickel and silver metal solar

cell contacts', *U.S. Department of Energy Journal of Undergraduate Research* [Preprint]. Available at: https://www.osti.gov/servlets/purl/1052098 (Accessed: 22 February 2021).

Patton, M. V., Ryan, P., Calascione, T., Fischer, N., Morgenstern, A., Stenger, N. and Nelson-Cheeseman, B.B. (2019) 'Manipulating magnetic anisotropy in fused filament fabricated parts via macroscopic shape, mesoscopic infill orientation, and infill percentage', *Additive Manufacturing*, 27, pp. 482–488. Available at: https://doi.org/10.1016/j.addma.2019.03.026.

Périgo, E.A., Jacimovic, J., García Ferré, F. and Scherf, L.M. (2019) 'Additive manufacturing of magnetic materials', *Additive Manufacturing*, 30. Available at: https://doi.org/10.1016/j.addma.2019.100870.

Quattrone, R.F., Berman, J.B., C, J., Feickert, C.A., Kamphaus, J.M., White, S.R., Giurgiutiu, V. and Cohen, G.L. (2000) 'Investigation of Terfenol-D for Magnetostrictive Tagging of Fiber-Reinforced Polymer Composites', *US Army Corps of Engineers*, pp. 1–80. Available at: http://oai.dtic.mil/oai/oai?verb=getRecord&metadataPrefix=html&identifier=ADA389133.

ramé-hart instrument co. (2019) *ramé-hart Information on Contact Angle*. Available at: http://www.ramehart.com/contactangle.htm (Accessed: 20 September 2021).

Ramos, H.G. and Ribeiro, A.L. (2014) 'Present and future impact of magnetic sensors in NDE', *Procedia Engineering*, 86, pp. 406–419. Available at: https://doi.org/10.1016/j.proeng.2014.11.054.

Raut, N.C. and Al-Shamery, K. (2018) 'Inkjet printing metals on flexible materials for plastic and paper electronics', *Journal of Materials Chemistry C*. Royal Society of Chemistry, pp. 1618–1641. Available at: https://doi.org/10.1039/c7tc04804a.

Roach, D., Neidigk, S., Rice, T. and Duvall, R. (2013) 'Inspection Options for Detecting Various Types of Impact Damage in Composite Structures', *5th European-American Workshop on Reliability of NDE* [Preprint]. Available at: https://www.osti.gov/servlets/purl/1115103 (Accessed: 9 June 2020).

Sabau, A.S. and Porter, W.D. (2008) 'Alloy shrinkage factors for the investment casting of 17-4PH stainless steel parts', *Metallurgical and Materials Transactions B: Process Metallurgy and Materials Processing Science*, 39(2), pp. 317–330. Available at: https://doi.org/10.1007/s11663-007-9125-3.

Saha, T.K., Knaus, T.N., Khosla, A. and Sekhar, P.K. (2018) 'Investigation of Printing Properties on Paper Substrate', *Journal of The Electrochemical Society*, 165(8), pp. B3163–B3167. Available at: https://doi.org/10.1149/2.0211808JES/XML.

Salaoru, I., Maswoud, S. and Paul, S. (2019) 'Inkjet Printing of Functional Electronic Memory Cells: A Step Forward to Green Electronics', *Micromachines*, 10(6), p. 417. Available at:

https://doi.org/10.3390/mi10060417.

Saleh, E., Woolliams, P., Clarke, B., Gregory, A., Greedy, S., Smartt, C., Wildman, R., Ashcroft, I., Hague, R., Dickens, P. and Tuck, C. (2017) '3D inkjet-printed UV-curable inks for multi-functional electromagnetic applications', *Additive Manufacturing*, 13, pp. 143–148. Available at: https://doi.org/10.1016/J.ADDMA.2016.10.002.

Sames, W.J., List, F.A., Pannala, S., Dehoff, R.R. and Babu, S.S. (2016) 'The metallurgy and processing science of metal additive manufacturing', *International Materials Reviews*. Taylor and Francis Ltd., pp. 315–360. Available at: https://doi.org/10.1080/09506608.2015.1116649.

Schönrath, H., Spasova, M., Kilian, S.O., Meckenstock, R., Witt, G., Sehrt, J.T. and Farle, M. (2019) 'Additive manufacturing of soft magnetic permalloy from Fe and Ni powders: Control of magnetic anisotropy', *Journal of Magnetism and Magnetic Materials*, 478, pp. 274–278. Available at: https://doi.org/10.1016/J.JMMM.2018.11.084.

SHD (2022) *Advanced composite prepreg materials by SHD*. Available at: https://shdcomposites.com/ (Accessed: 5 September 2022).

Shieh, J., Huber, J.E., Fleck, N.A. and Ashby, M.F. (2001) 'The selection of sensors', in *Progress in Materials Science*. Available at: https://doi.org/10.1016/S0079-6425(00)00011-6.

Shishkovsky, I. and Saphronov, V. (2016) 'Peculiarities of selective laser melting process for permalloy powder', *Materials Letters*, 171, pp. 208–211. Available at: https://doi.org/10.1016/j.matlet.2016.02.099.

Shokrollahi, H. (2017) 'A review of the magnetic properties, synthesis methods and applications of maghemite', *Journal of Magnetism and Magnetic Materials*, 426, pp. 74–81. Available at: https://doi.org/10.1016/J.JMMM.2016.11.033.

Singh, M., Haverinen, H.M., Dhagat, P. and Jabbour, G.E. (2010) 'Inkjet printing-process and its applications', *Advanced Materials*, 22(6), pp. 673–685. Available at: https://doi.org/10.1002/ADMA.200901141.

Söderberg, O., Sozinov, A., Ge, Y., Hannula, S.-P. and Lindroos, V.K. (2006) 'Giant Magnetostrictive Materials-chapter 1', in K.H.J. Buschow (ed.) *Handbook of Magnetic Materials*. Elsevier, pp. 1–39. Available at: https://doi.org/10.1016/S1567-2719(05)16001-6.

Song, H., Spencer, J., Jander, A., Nielsen, J., Stasiak, J., Kasperchik, V. and Dhagat, P. (2014) 'Inkjet printing of magnetic materials with aligned anisotropy', *Journal of Applied Physics*, 115(17), p. 17E308. Available at: https://doi.org/10.1063/1.4863168.

Sossou, G., Demoly, F., Belkebir, H., Qi, H.J., Gomes, S. and Montavon, G. (2019) ‘Design for 4D printing: Modeling and computation of smart materials distributions’, *Materials and Design*, 181. Available at: https://doi.org/10.1016/j.matdes.2019.108074.

Soutis, C., Fleck, N.A. and Smith, P.A. (1991) ‘Compression fatigue behaviour of notched carbon fibre-epoxy laminates’, *International Journal of Fatigue 13*, (4), pp. 303–312. Available at: https://doi.org/10.1016/0142-1123(91)90357-5.

Spaldin, N.A. (2012) ‘Anisotropy’, in *Magnetic Materials*. Cambridge: Cambridge University Press, pp. 135–144. Available at: https://doi.org/10.1017/cbo9780511781599.011.

Speckmann, H. (2007) ‘Structural Health Monitoring (SHM) Focal Point for SHM’, in *IMRBPB Meeting*. Cologne.

Stashkov, A., Schapova, E., Tsar’kova, T., Sazhina, E., Bychenok, V., Fedorov, A., Kaigorodov, A. and Ezhov, I. (2019) ‘Magnetic, electric properties and hardness of 17-4 PH stainless steel fabricated by selective laser melting’, in *Journal of Physics: Conference Series*. IOP Publishing, p. 12124. Available at: https://doi.org/10.1088/1742-6596/1389/1/012124.

Sundaram, R., Gupta, N., MJ, A. and Datta, A. (2016) ‘Structural Health Monitoring of Aircraft Composite Structures : Offline & Online Approach.’, in *8th International Symposium on NDT in Aerospace (2016)*. Available at: http://www.ndt.net/?id=20623 (Accessed: 14 October 2019).

Tan, H.W., An, J., Chua, C.K. and Tran, T. (2019) ‘Metallic Nanoparticle Inks for 3D Printing of Electronics’, *Advanced Electronic Materials*, 5(5). Available at: https://doi.org/10.1002/aelm.201800831.

Tannous, C. and Gieraltowski, J. (2017) ‘Magnetic properties: from traditional to spintronic’, in *Springer Handbooks*. Springer, p. 1. Available at: https://doi.org/10.1007/978-3-319-48933-9_4.

TDK Corp (2020) *Inductors―Part 1 The Basics of Inductors*. Available at: https://www.tdk.com/en/tech-mag/electronics_primer/1 (Accessed: 22 August 2021).

Tholeke, J.B. (1993) ‘Magnetization and magnetostricion in highly magnetostrictive materials’, *Ames Lab*, pp. 15–38.

Tiberto, P., Barrera, G., Celegato, F., Coïsson, M., Chiolerio, A., Martino, P., Pandolfi, P. and Allia, P. (2013) ‘Magnetic properties of jet-printer inks containing dispersed magnetite nanoparticles’, *European Physical Journal B*, 86(4), p. 173. Available at: https://doi.org/10.1140/epjb/e2013-30983-8.

Trading economics (2023) *Nickel - 1993-2022 -Historical Price, Trading economics*. Available at:

https://tradingeconomics.com/commodity/nickel (Accessed: 9 March 2023).

Tumanski, S. (2016) *Handbook of magnetic measurements*. 1st edn, *Handbook of Magnetic Measurements*. 1st edn. Boca Raton: CRC Press. Available at: https://doi.org/10.1201/b10979.

Utela, B., Storti, D., Anderson, R. and Ganter, M. (2008) 'A review of process development steps for new material systems in three dimensional printing (3DP)', *Journal of Manufacturing Processes*, pp. 96–104. Available at: https://doi.org/10.1016/j.jmapro.2009.03.002.

Vaithilingam, J., Saleh, E., Körner, L., Wildman, R.D., Hague, R.J.M., Leach, R.K. and Tuck, C.J. (2018) '3-Dimensional inkjet printing of macro structures from silver nanoparticles', *Materials and Design*, 139, pp. 81–88. Available at: https://doi.org/10.1016/J.MATDES.2017.10.070.

Vaseem, M., Ghaffar, F.A., Farooqui, M.F. and Shamim, A. (2018) 'Iron Oxide Nanoparticle-Based Magnetic Ink Development for Fully Printed Tunable Radio-Frequency Devices', *Advanced Materials Technologies*, 3(4), p. 1700242. Available at: https://doi.org/10.1002/admt.201700242.

Vincent, J.D.S., Rodrigues, M., Leong, Z. and Morley, N.A. (2020) 'Design and development of magnetostrictive actuators and sensors for structural health monitoring', *Sensors (Switzerland)*, 20(3), p. 711. Available at: https://doi.org/10.3390/s20030711.

Voit, W., Zapka, W., Belova, L. and Rao, K. V. (2003) 'Application of inkjet technology for the deposition of magnetic nanoparticles to form micron-scale structures', *IEE Proceedings: Science, Measurement and Technology*, 150(5), pp. 252–256. Available at: https://doi.org/10.1049/ip-smt:20030692.

Vovrosh, J., Voulazeris, G., Petrov, P.G., Zou, J., Gaber, Y., Benn, L., Woolger, D., Attallah, M.M., Boyer, V., Bongs, K. and Holynski, M. (2018) 'Additive manufacturing of magnetic shielding and ultra-high vacuum flange for cold atom sensors', *Scientific Reports*, 8(1). Available at: https://doi.org/10.1038/s41598-018-20352-x.

Watson, N.D. and von Lockette, P. (2020) 'Deposition controlled magnetic alignment in iron-PLA composites', in *Solid Freeform Fabrication 2018: Proceedings of the 29th Annual International Solid Freeform Fabrication Symposium - An Additive Manufacturing Conference, SFF 2018*, pp. 1145–1151.

Wilson, S.A., Jourdain, R.P.J., Zhang, Q., Dorey, R.A., Bowen, C.R., Willander, M., Wahab, Q.U., Willander, M., Al-hilli, S.M., Nur, O., Quandt, E., Johansson, C., Pagounis, E., Kohl, M., Matovic, J., Samel, B., van der Wijngaart, W., Jager, E.W.H., Carlsson, D., Djinovic, Z., Wegener, M., Moldovan, C., Abad, E., Wendlandt, M., Rusu, C. and Persson, K. (2007) 'New materials for micro-scale sensors and actuators. An engineering review', *Materials Science and Engineering R: Reports* [Preprint].

Available at: https://doi.org/10.1016/j.mser.2007.03.001.

Woon, I.S. (2015) ‘Composite structures in new aircraft-concerns over impact damage and detection’, *The Hong Kong Institution of Engineers*, 43. Available at: http://www.hkengineer.org.hk/issue/vol43-jun2015/notices_others/?id=9706 (Accessed: 31 October 2019).

Wünscher, S., Abbel, R., Perelaer, J. and Schubert, U.S. (2014) ‘Progress of alternative sintering approaches of inkjet-printed metal inks and their application for manufacturing of flexible electronic devices’, *Journal of Materials Chemistry C*. Royal Society of Chemistry, pp. 10232–10261. Available at: https://doi.org/10.1039/c4tc01820f.

Xu, Y., Wu, X., Guo, X., Kong, B., Zhang, M., Qian, X., Mi, S. and Sun, W. (2017) *The Boom in 3D-Printed Sensor Technology*, *Sensors*. Available at: https://doi.org/10.3390/s17051166.

Yap, C.Y., Tan, H.K., Du, Z., Chua, C.K. and Dong, Z. (2017) ‘Selective laser melting of nickel powder’, *Rapid Prototyping Journal*, 23(4), pp. 750–757. Available at: https://doi.org/10.1108/RPJ-01-2016-0006.

Yoo, B., Na, S.M., Flatau, A.B. and Pines, D.J. (2016) ‘Magnetic shape anisotropy effect on sensing performance and directional sensitivity in magnetostrictive nickel patch transducer’, *Journal of Intelligent Material Systems and Structures*, 27(8), pp. 1075–1091. Available at: https://doi.org/10.1177/1045389X15585895.

Yu, G. (2021) *Magnetostriction - Engineering LibreTexts*. Available at: https://eng.libretexts.org/Bookshelves/Materials_Science/Supplemental_Modules_(Materials_Science)/Magnetic_Properties/Magnetostriction (Accessed: 2 October 2019).

Zhang, F., Tuck, C., Hague, R., He, Y., Saleh, E., Li, Y., Sturgess, C. and Wildman, R. (2016) ‘Inkjet printing of polyimide insulators for the 3D printing of dielectric materials for microelectronic applications’, *Journal of Applied Polymer Science*, 133(18), p. n/a-n/a. Available at: https://doi.org/10.1002/app.43361.

Zhang, H.T., Wu, G., Chen, X.H. and Qiu, X.G. (2006) ‘Synthesis and magnetic properties of nickel nanocrystals’, *Materials Research Bulletin*, 41(3), pp. 495–501. Available at: https://doi.org/10.1016/j.materresbull.2005.09.019.

Zhou, L. (2015) *Non-destructive characterisation of steel microstructures using electromagnetic sensor*. The University of Birmingham.

Ziadoon, A.-H.M.R. and Chwei, Z. (2016) *Effect the stacking sequences of composite laminates under low velocity impact on failure modes by using carbon fiber reinforced polymer*, *The International*

Journal Of Engineering And Science (IJES) ||. Available at: www.theijes.com (Accessed: 25 November 2019).

Zou, J., Gaber, Y., Voulazeris, G., Li, S., Vazquez, L., Liu, L.F., Yao, M.Y., Wang, Y.J., Holynski, M., Bongs, K. and Attallah, M.M. (2018) 'Controlling the grain orientation during laser powder bed fusion to tailor the magnetic characteristics in a Ni-Fe based soft magnet', *Acta Materialia*, 158, pp. 230–238. Available at: https://doi.org/10.1016/j.actamat.2018.07.064.

Zub, K., Hoeppener, S. and Schubert, U.S. (2022) 'Inkjet Printing and 3D Printing Strategies for Biosensing, Analytical, and Diagnostic Applications', *Advanced Materials*. John Wiley and Sons Inc. Available at: https://doi.org/10.1002/adma.202105015.

10 Appendix

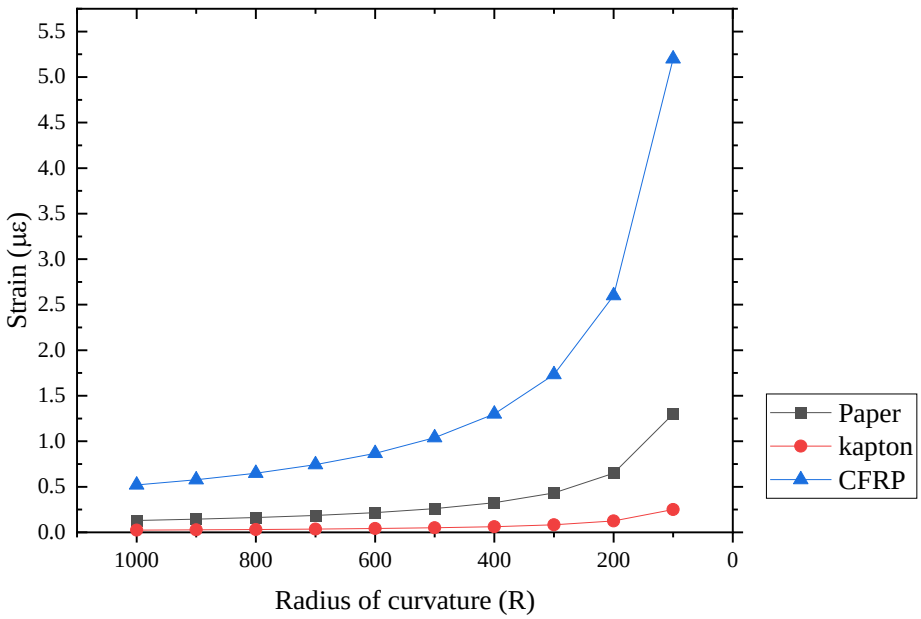

Figure 10.1 Strain calculated values for radius of curvature from 1000 to 100 for paper, kapton and CFRP

Table 10.1 Viscosities of water at various temperatures (James, Mulcahy and Steel, 1984)

Flow times (S)

Temperature (K)	Density (g cm-3)	Upper bulb (cP)	Lower bulb (cP)	Average (cP)
273.15	0.99984	1.789	1.7889	1.7891
278.15	0.99996	1.518	1.5187	1.5187
293.15	0.9982	(1.002)	(1.002)	(1.002)
298.15	0.99704	0.89	0.8903	0.8904
303.15	0.99565	0.7978	0.7977	0.7978
308.15	0.99403	0.7193	0.7193	0.719,
313.15	0.9922	0.6531	0.6531	0.6531
323.15	0.988	0.5475	0.547	0.5475
333.15	0.9832	0.467	-	0.467

Table 10.2 Impact calculation for dropped weight from height of 1.1 m

Impact calculations		
Mass (kg)	**Kinetic energy (J)**	**Impact force (kN)**
0.1	1.0791	335.12
0.2	2.1582	670.24
0.3	3.2373	1005.37
0.4	4.3164	1340.49
0.5	5.3955	1675.62
0.6	6.4746	2010.74
0.7	7.5537	2345.87

0.8	8.6328	2680.99
0.9	9.7119	3016.11
1	10.791	3351.24

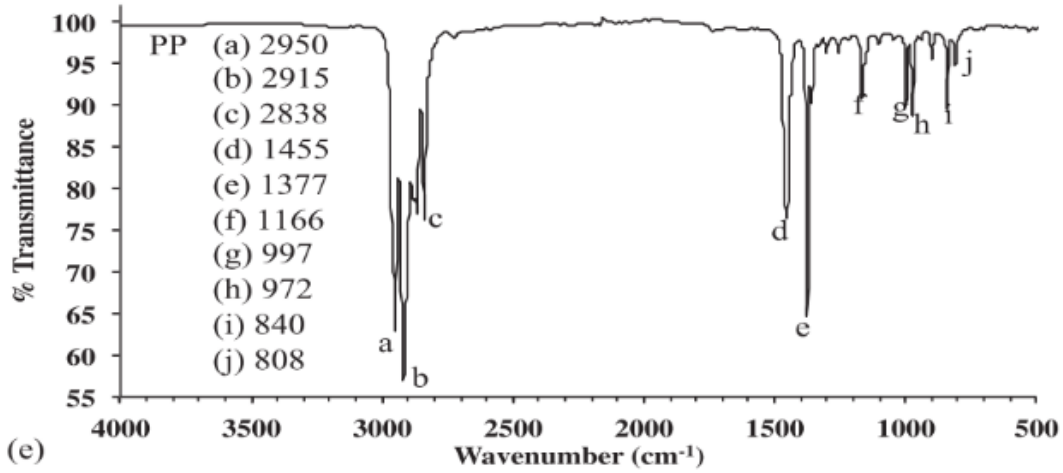

Figure 10.2 FT-IR spectra of polypropylene (Jung *et al.*, 2018)